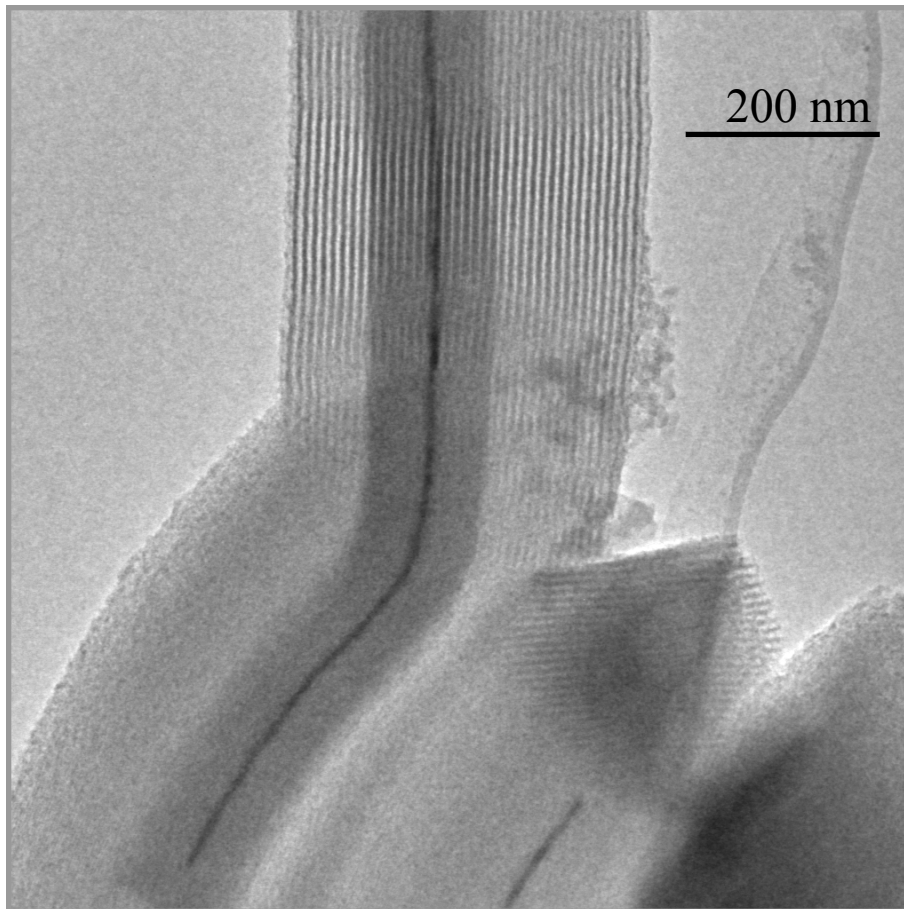


Nanoporous hosts for the encapsulation of conductive nanostructured materials



Nikolay Petkov

Dissertation zur Erlangung des Doktorgrades
der Fakultät für Chemie und Pharmazie
der Ludwig-Maximilians-Universität München

**Nanoporous hosts for the encapsulation of conductive
nanostructured materials**

von
Nikolay Petkov
aus
Sofia
2004

Erklärung

Diese Dissertation wurde im Sinne von § 13 Abs. 3 bzw. 4 der Promotionsordnung vom 29. Januar 1998 von Herrn Prof. Dr. Thomas Bein betreut.

Ehrenwörtliche Versicherung

Diese Dissertation wurde selbständig, ohne unerlaubte Hilfe erarbeitet.
München, am 17. Februar 2004

(Unterschrift des Autors)

Dissertation eingereicht am 17. Februar 2004

1. Gutachter: Prof. Dr. Thomas Bein
 2. Gutachter: Prof. Dr. Helmut Knözinger
- Mündliche Prüfung am 22. März 2004

*For my Grandfather Boris
and my Family*

Contents

Contents	v
Acknowledgements	x
Preface	xi
Chapter 1. Introduction to nanoscience and nanotechnology	1
1.1. Nanoscience and nanotechnology	1
1.2. Nanoelectronics	4
1.2.1. Top-down approach	5
1.2.2. Bottom-up approach	7
1.3. Perspectives	9
References	10
Chapter 2. Introduction to nanoporous materials	11
2.1. Introduction	11
2.2. Surfactant-templated mesoporous materials	12
2.2.1. Definition, nomenclature, and structure	12
2.2.2. Mechanism of formation, properties, and applications	18
2.2.3. Functionalized ordered mesoporous materials	23
2.2.4. Ordered mesoporous films	24
References	29
Chapter 3. Introduction to one-dimensional nanostructures	35
3.1. Introduction	35
3.2. General synthetic routes for the preparation of one-dimensional nanostructures	35
3.3. General properties of one-dimensional nanostructures	38
3.4. Synthesis and properties of carbon nanotubes	40
References	44

Chapter 4. Characterisation techniques for nanostructured materials	47
4.1. Introduction	47
4.2. X-ray diffraction (XRD)	47
4.3. Infrared and Raman spectroscopy	53
4.4. Nitrogen-sorption measurements	54
4.5. Electron microscopy	58
4.6. Other characterization techniques	60
4.6.1. Dynamic light scattering (DLS)	60
4.6.2. Thermogravimetric analysis (TGA)	61
References	61
Chapter 5. Synthesis and characterization of mesoporous powders with different morphologies	63
5.1. Introduction	63
5.2. Experimental	65
5.2.1. Synthesis of MCM-48 spheres	65
5.2.2. Synthesis of SBA-15 rods	66
5.2.3. Synthesis of mesostructured monoliths	66
5.2.4. Calcination procedures	67
5.2.6. Characterization	68
5.3. Results and Discussion	68
5.3.1. Mesophase structure and thermal stability	68
5.3.2. Sorption properties and surface morphology	80
5.4. Conclusions and perspectives	87
References	88
Chapter 6. Preparation and characterization of ordered mesoporous films	90
6.1. Introduction	90
6.2. Experimental	91

6.2.1. Preparation of ordered mesoporous films	91
6.2.2. Characterization of the mesoporous films	92
6.3. Results and discussion	93
6.3.1. Mesophase structure - influence of the relative humidity, composition of the coating solution and post-synthesis thermal treatments	93
6.3.1.1. CTABr-templated mesoporous films	93
6.3.1.2. Pluronic123-templated mesoporous films	105
6.3.2. Sorption properties of the mesoporous films – N ₂ -sorption studies with a QCM device	111
6.3.3. Surface morphology and thickness of the mesoporous films	115
6.4. Conclusions and Perspectives	118
References	119
Chapter 7. Growth of carbon nanotubes by catalytic decomposition of acetylene on Fe-containing mesoporous films	120
7.1. Introduction	120
7.2. Experimental	121
7.2.1. Preparation of Fe-containing mesoporous films and monoliths	121
7.2.2. Growth of carbon nanotubes	123
7.2.3. Characterization	123
7.3. Results and Discussion	123
7.3.1. Nature of precursor species in Fe-containing coating solutions	123
7.3.2. Mesophase structure and surface morphology of Fe-containing mesoporous films and monoliths	126
7.3.3. Growth of carbon nanotubes	132
7.4. Conclusions and Perspectives	139
References	140
Chapter 8. Growth of carbon filaments in ferrocene-modified SBA-15 rods and mesoporous thin films	141
8.1. Introduction	141

8.2. Experimental	142
8.2.1. Modification of the SBA-15 rods and mesoporous films	142
8.2.2. Growth of carbon filaments	145
8.2.3. Characterization	145
8.3. Results and Discussion	146
8.3.1. Amino- and ferrocene-modified SBA-15 rods	146
8.3.2. Carbon filaments in ferrocene-modified SBA-15 rods	156
8.3.3. Carbon filaments in ferrocene-modified mesoporous films	161
8.4. Conclusions and Perspectives	169
References	170
Chapter 9. Gold nanostructures in mesoporous SBA-15 rods and mesoporous films prepared by electroless reduction	172
9.1. Introduction	172
9.2. Experimental	175
9.2.1. Modification of the SBA-15 rods and mesoporous films	175
9.2.2. Preparation of gold nanoparticles	176
9.2.3. Assembly of gold nanoparticles on MPS- and AEPMS-modified mesoporous materials and electroless reduction	178
9.2.4. Characterization	179
9.3. Results and Discussion	180
9.3.1. MPS- and AEPMS-modified SBA-15	180
9.3.2. Preparation of gold nanoparticles	188
9.3.3. Assembly of gold nanoparticles and electroless reduction of gold in SBA-15 rods	191
9.3.4. Au nanostructures in MPS-modified mesoporous films	206
9.4. Conclusions and Perspectives	213
References	215
Chapter 10. Preparation of semiconductor PbS nanostructures in functionalized mesoporous SBA-15 rods and mesoporous thin films	217

10.1. Introduction	217
10.2. Experimental	219
10.2.1. Synthesis of PbS nanostructures in functionalized mesoporous materials	219
10.2.2. Characterization	221
10.3. Results and Discussion	222
10.3.1. PbS nanostructures in SBA-15 rods	222
10.3.2. PbS nanostructures in mesoporous films	225
10.4. Conclusions and Perspectives	229
References	229
Conclusions and Outlook	231
Curriculum Vitae	236
List of Publications	237

Acknowledgements

I would like to acknowledge the people who made this work possible and gave me the opportunity to experience the freedom to explore, to chase ideas, to be excited and disappointed at the same time.

Prof. Dr. Thomas Bein has provided guidance, ideas, and concepts without interference, and encouraged creativity and self-confidence that were necessary for the research work. He also thought me to gain much criticism and scientific liability to my and other people's results, and for that I am truly grateful.

The person without whom I would probably never have had a chance to start a research career is Dr. Svetlana Mintova; for that I am gratefully thankful.

Enjoyable work is never a lonely task. For that one needs not only good colleagues but also friends. And my list of colleagues that became my friends is long. I would start with Jake Reder, Ken Yasuda, Norbert Stock, and Jürgen Sauer that were my lab-teachers and who stayed behind where I was making my first failures and successes. Martin Kuba, Barbara Fieres, Sing-Jin, and Lea Mühlstein were there to share knowledge, ideas, and results on our common project. Alex Darga, Stephan Angloher, Sebastian Bauer, Enrica Biemmi, Manoel Vega, and others with whom I shared creative discussions, cases of beer, long-drinks, and emotions.

I'd like to thank Prof. Dr. H. Knözinger for being my second reviewer.

Finally, I thank my parents for their love, patience, and reliance. I like to thank my sister for her intelligence and understanding.

Thanks to all people that believed in me!

Preface

Nanoscience and nanotechnology are multidisciplinary fields of science where traditional physics, chemistry, biology, medicine, engineering, and even social sciences meet to create a crossover that will revolutionize industries, such as pharmacy, microelectronics and optics, energy production, communications, and many others. The subject of this Thesis is to understand nanoporous systems, learn to control their design, and to explore potential functionality. It is aimed to show that such systems can serve as host matrixes for incorporation of conducting materials at the nanometer scale. By designing nanoporous host structures we are trying to manipulate the growth process and the properties of the embedded conductive nanostructures.

The focus is on liquid-crystal templated silica-based mesoporous materials prepared under different sol-gel synthetic conditions and characterized by a variety of physico-chemical methods. Morphologies include bulk materials and thin mesoporous films on different substrates; the latter may offer potential as components for the construction of molecular electronic devices. It was aimed to gain knowledge of the physico-chemical characteristics of the mesoporous solids and to access differences in their bulk and surface properties that can be essential for further functionalization and modification (Chapters 5 and 6).

The encapsulation of conductive nanostructures in ordered mesoporous hosts is exemplified with several distinct cases by developing new synthetic methods for selective confinement of the guest structures. Namely, carbon filaments and nanotubes, metal nanowires and nanoarrays, and semiconducting nanoparticles and wires (Chapters 7, 8, 9 and 10) are prepared in the mesoporous systems by selective functionalization of the host matrix followed by restricted growth in the nanosized porous system.

Chapter 1. Introduction to nanoscience and nanotechnology.

1.1. Nanoscience and nanotechnology

1.2. Nanoelectronics

1.2.1 Top-down approach

1.2.2. Bottom-up approach

1.3. Perspectives

1.1. Nanoscience and nanotechnology

When it comes to nanoscience the scale matters. Prof. Richard Feynman, a Nobel Prize-winning physicist, in his famous lecture in 1959 called “There is a plenty of room at the bottom” gave the boundaries of the unexplored science at the smallest realm of physical existence. At that time most scientists were thinking big about interplanetary space travel, but Feynman awakened them to possibilities of controlling single molecules or even atoms and creating machines with them. Talking about nanoscience we usually address to the area of science where dimensions in the range of 0.1 nm to 100 nm play a critical role (we recognize the overlap in dimensions with molecular chemistry). Nanoscience is based on the fact that properties of materials change drastically as a function of the physical dimensions at the length scales where the Newtonian and quantum physics coexist to some extent. Is nanoscience a science fiction, a myth that is propagated to fascinate the academic, industrial and some social circles? Is the prefix “nano” just a fashionable word nowadays? People already imagine the future when the technology would be based on the word “nano”.

“ Imagine a technology so powerful that it will allow such feats as desktop manufacturing, cellar repair, artificial intelligence, inexpensive space travel, clean and abundant energy, and environmental restoration; a technology so portable that everyone can reap its benefits; a technology so fundamental that it will radically change our economic and political systems; a technology so imminent that most of us will see its impact within our lifetimes. Such is the promise of Nanotechnology.” Kai Wung

This all seems very promising but let us take a look at the real “macroscopic” world. Nanoscience and nanotechnology attracted considerable research and scientific attention during the last ten years; more than 2000 publications containing as keywords “nanoscience” and “nanotechnology” were issued and cited in the scientific community (according to SciFinder). Among them around 700 are review articles and only 35 patents. The distribution of the published articles among the 10 years period clearly shows that the interest in nanoscience is growing exponentially; only during the last year the number of the published articles increased twice in comparison to the previous year (Figure 1.1).

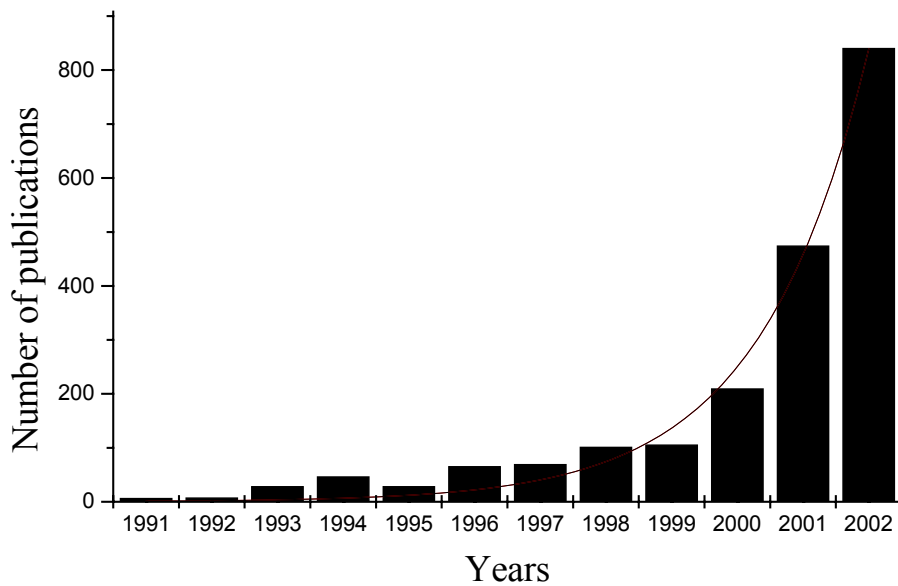


Figure 1.1. Published articles containing as keywords “nanoscience” and “nanotechnology” for the last ten years (SciFinder).

The U.S. National Science Foundation (NSF) and other agencies, for a number of years, have been funding a variety of programs in support of nanoscale science and engineering. The goal of these programs is to catalyze synergistic science and engineering research in emerging areas of nanoscale science and technology, including: bio-systems at nanoscale; nanoscale structures, novel phenomena, and quantum control; device and system architecture; design of tools and nanosystems specific software; nanoscale processes in the

environment; multi-scale and multi-phenomena modeling and simulation at the nanoscale; and studies on societal implications of nanoscale science and engineering. This in fact encircles the whole field that could be referred to as nanoscience and that gives the birth of a new technology called nanotechnology. The NSF project is alone supported by \$600 million in funding over five-year period and is estimated to create nanotechnology markets that will be worth \$ 1 trillion by 2015.

In the European community, through the 6th Framework Programme, nanotechnology is presented as the third thematic priority area called “Nanotechnologies and Nanosciences, knowledge-based multifunctional materials and new production processes and devices”. Funding for nanotechnology under this programme may be estimated to mobilize funds in the range of € 1 billion over the next four-year period. Two global objectives are defined: first, to stimulate the introduction of innovative nanotechnologies in existing industrial sectors; second, to stimulate breakthroughs, which can lead to entirely new materials, new devices, new products and finally new industries. The programme will cover essentially all nanomaterials types and related devices as well as societal implications that were already mentioned to be enclosed in the term nanoscience. Countries in Asia, South America and Australia are also showing increased scientific and technological activity in the nanoscale field by founding their own national nanotechnology projects and organizations.

It is clear that nanoscience and nanotechnology is a multidisciplinary field, an area of science where traditional physics, chemistry, biology, medicine, engineering and even social sciences meet to create a crossover that will revolutionize industries such as pharmaceuticals, microelectronics and optics, energy production, communications and many others. As a multidisciplinary field, research in nanoscience is unified to share knowledge, tools and techniques on atomic and molecular interactions. These will enable the researchers working in nanoscience to expand their expertise into new application fields.

A typical example for cooperative research work in nanoscience is the Center for NanoScience (CeNS) established in 1998 in our university; based at the beginning on the department of physics, CeNS now consists of a large number of working groups from the departments of physics, chemistry and biology of LMU.

We can clearly say that the word is moving steadily towards nanoscience, nevertheless the boundaries and priorities of this field are still not fully defined and debatable, but it might

be that this is inherent in its nature. Certainly it is an extremely broad field which makes it necessary to divide the subject into suitable parts according to the applicational areas such as nanobiology, nanomedicine, nanoelectronics or molecular electronics, nanomaterials, nanomachinery and others. The topic of this Thesis is focused on nanostructured materials as building units for molecular electronics and therefore the rest of this introductory Chapter will provide an introduction to nanomaterials for molecular electronics, also called nanoelectronics.

1.2. Nanoelectronics

Nowadays microelectronics is based, as the word suggests, on components roughly one micron (10^{-6} m) on a side. The relentless miniaturization of the microelectronic devices will promote shrinkage of the components by a factor of 10 to 1000 and will lead us to the nanoworld (10^{-9} m) which involves a paradigm shift to the question how to deal with these “new” dimensions and to put everything together. Let us first explain the organization of the components in the modern microelectronic and future nanoelectronic devices.

Microelectronics and nanoelectronics both entail three levels of organization¹. The basic building block is usually a transistor with its nanoequivalent – a switch that can turn an electric current on or off as well as amplify signals. In microelectronics, transistors are made of bulky semiconducting material. In nanoelectronics, transistors might be organic molecules or nanoscale inorganic structures that can flip between conducting and nonconducting states. A typical example is a molecular switch. The next level of organization is the interconnections - the wires that link transistors together in order to perform arithmetic or logical operations. In microelectronics, wires are metal lines typically hundreds of nanometers to tens of microns in width deposited onto silicon. In nanoelectronics the wires might be nanotubes, such as carbon nanotubes, or other wires prepared with nanodimensions. The top level of organization is the integration of the electronic devices to the macro world – the overall way the transistors are interconnected, so that the circuit can plug into a computer or other system and perform logical operations. At this time, nanoelectronics have not gotten to the point where real testing of different components can be achieved. There are several examples proposing different ways for testing the components for nanoelectronics but still the boundaries and concepts at this

level of organization are controversial. Nevertheless the general concept of microelectronics and nanoelectronics might not be much different; one needs to find a way for miniaturization of the electronic devices and integration of the components at different levels of organization.

Two fundamentally different approaches to nanoelectronics are graphically termed as top-down and bottom-up (Figure 1.2). The next part of this introductory chapter will focus on the basic principles of top-down and bottom-up approaches for the preparation of nanoscale devices for electronics.

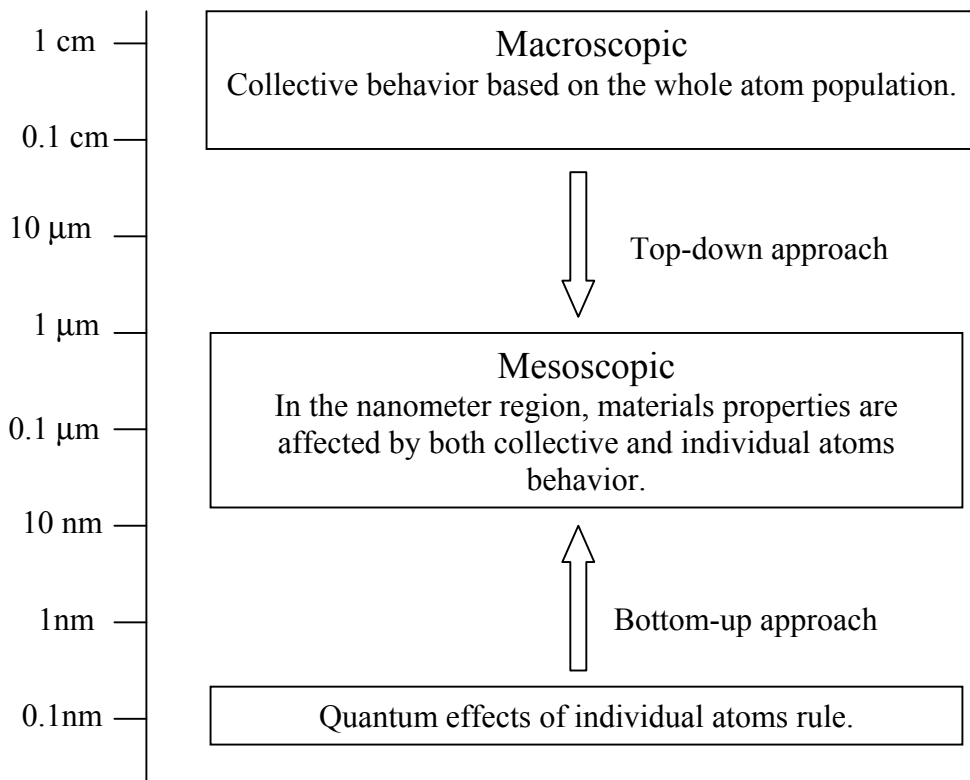


Figure 1.2. Schematic representation of the principles of top-down and bottom-up approaches. In principle, the bottom-up approach could also be used to create macroscopic objects.

1.2.1. Top -down approach

It is convenient to start with the top-down approach because it is traditional for microelectronics. To build a silicon chip today, fabrication plants start with a silicon crystal, lay down a pattern using a photographic technique known as lithography, and etch away the unwanted material using liquid etching or plasma treatment. Usually the top-down approach is

defined as one in which macroscale components are utilized to create nanoscale structures. All processes that include etching, molding or sculpting away material together with methods used to design spatially defined patterns such as photolithography, microcontact printing and to some extent dip-pen lithography fall into this category.

The need for miniaturization of the components for microelectronics is recognized by the microelectronic industry itself². Nowadays the rates of increase of devices per chip already exceed Moore's predictions wherein there is a doubling of devices per chip every 18 – 24 months. The state-of-the-art of the microprocessor industry today has advanced to the point where engineers can now put on a sliver of silicon of just a few square centimeters some 100 million transistors, with key features measuring 0.18 micron³. Yet within the next two decades this dramatic march will run up against scientific, technical and economic limits. The application of lithographic processes to nanoscale electronics is limited simply because they do not provide the precision for devices that are mere nanometers in width, nevertheless there are examples where mask processes can now define components less than 100 nm on a side. Indeed, various nagging (though not yet fundamental) problems in the fabrication of efficient smaller silicon transistors and their interconnections are becoming increasingly bothersome. Many experts expect these challenges to intensify dramatically as the transistors approach the 100 nm level. Because of these and other difficulties, the exponential increase in transistor densities and processing rates of integrated circuits is being sustained only by a similar exponential rise in the financial outlays necessary to build the facilities that produce these chips. Eventually the drive to downscale will run headlong into these extreme facility costs, and the market will reach equilibrium. Many experts project that this will happen around or before 2015, when a fabrication facility is projected to cost nearly \$200 billion. When that happens, the long period of breathtaking advances in the processing power of computer chips might have run its course. Further increases in the power of the chips will be prohibitively costly. Certainly new approaches and ideas for achieving nanoscale devices for electronics have to be discovered and applied.

1.2.2 Bottom-up approach

As mentioned above, the simple shrinkage of the electronic components to meet the demands of nanoscale electronics might not be feasible until a fundamental breakthrough into the manner these systems are approached is discovered. Researchers use the methods of synthetic chemistry to produce building blocks and assemble them into progressively larger structures atom by atom, molecule by molecule. In other words, the fundamentals of the bottom-up approach lie in the preparative materials chemistry and the principles of self-assembly. It is clear that if the building blocks can be guided and self-assembled into desired patterns, this will solve many manipulations and manufacture problems typical for the top-down approach. As discussed earlier, the building blocks for nanoelectronics can be considered to be every organic or inorganic molecular object with nanoscale dimensions that can act as transistor – switching off and on the flow of electrons by flipping between conductive and nonconductive state⁴. Typical examples are π -conjugated organic molecules, semiconducting nanoparticles or wires, carbon nanotubes, metal nanowires, etc. An active device such as a transistor, however, has to do more than merely allow electrons to flow - it has to somehow control that flow. Thus, the task of the molecular device engineer is to exploit the quantum world's discrete energy levels, specifically, by designing molecules whose orbital characteristics achieve the desired kind of electronic control.

Building up an arsenal of molecular and nanoscale devices by self-assembly is just the first step in the organization of the components for nanoelectronics. Interconnecting and integrating these devices is perhaps the much greater challenge. To date, molecular switches or inorganic solids that can as transistors have been hooked to conventional wires created by lithography. In many cases, the molecular “glue” is represented by thiol-terminated organic molecules attached to gold electrodes forming self-assembled monolayers (SAM)⁵. Thinking about wiring of the components for molecular electronics, we should not neglect carbon nanotubes that are believed to play in principle the same role as silicon does in electronic circuits, but at a molecular scale where silicon and other standard semiconductors cease to work⁶. A more detailed discussion on the synthesis and properties of the building blocks for nanoelectronics - carbon nanotubes, semiconductor and metal nanoparticles and nanowires that are the objects of this Thesis, will be given in Chapter 3.

Once the components for molecular electronics are connected to nanowires, the wires themselves must be organized into multidimensional arrays and integrated to the macro environment for testing. This seems to be the most difficult task to solve for the construction of molecular electronic devices. The first successful demonstration of the testing of components of nanoelectronic systems occurred just several years ago, in 1996, when Paul S. Weiss's group at Pennsylvania State University started from self-assembled conductive molecules that were sparsely dispersed among insulating ones, and by positioning an STM tip directly over one of the isolated conducting molecules, they could qualitatively measure the conductivity⁷. As expected, the conductivity was significantly greater than that of the surrounding molecules. Research groups in the University of California – Los Angeles and at Hewlett Packard are using more deterministic way; they are trying to create arrays of the elements for nanoelectronics with a certain predictable behavior. Similar results were also obtained by the group of Prof. Charles M. Lieber at Harvard University, where they were able to create interconnections of semiconducting wires in the direction of a fluid flow⁸. These examples and some more show that we are approaching the ability to create reliable nanoelectronic building blocks; nevertheless, real molecular computing is still a vision rather than reality.

It is clear that there are a lot of challenging problems to be overcome till first examples of molecular electronic devices are realized. Among them, the addressability of the conductive structures, the arrangement of the conductive molecules in a three-dimensional array and the encapsulation of the conductive structures in a way to be easily accessible and isolated from each other are of special interest to nanotechnology. Another challenge is to develop a method for rapid screening and electrical characterization of new candidates for molecular electronic devices. This requires special techniques that can link the nanoscale world of molecular devices to the macroscopic world of conventional electronic circuits.

An assembly of molecular wires, switches or connections could be addressed by constructing an ordered channel matrix of insulating material of metal oxide in which these structures are encapsulated and therefore isolated^{9, 10}. On the other hand, solid supports with ordered porosity can offer a template matrix for the guided growth for a variety of conductive structures, giving patterned arrays of aligned nanowires and connections. Such solid supports with ordered porosity ranging from several Angstroms to several nanometers can be silica-

based micro- or mesoporous materials, also called molecular sieves. Sol-gel chemistry provides different approaches for the preparation of such structures in a variety of special morphologies ranging from bulky materials to thin films and fibers. A detailed discussion on the nanoporous materials, specifically molecular sieves that can be used as building units in molecular electronics, will be given in Chapter 2.

Although, the two concepts for “making-things-smaller”, the top-down and bottom-up approaches, are inherently opposing it seems that there might be important common ground. In particular, top-down structures and methods might help with the interfacing of bottom-up structures into a system. Useful means of positioning and interconnecting molecular structures might be created in the near term that could serve as a proof-of-principle, showing that more ambitious molecular manufacturing may be possible. The current development of micro-electromechanical systems (MEMs) for nanoscience (e.g. in the AFM) may open avenues for incorporating molecular nanoelectronic components into widely used systems. The MEMs themselves can also have a nanometer-sized component, e.g., a sharp tip in the case of the scanning probe microscopes. A good example is the Millipede storage device of IBM (Vettiger et al., 1999) where a whole array of 32 x 32 cantilevers with small tips is used to write pits 40 nm in size into a polymer¹¹.

1.3. Perspectives

Nanoscience and nanotechnology are undergoing a rapid development. Past experience with translating science into practical technology provides cautionary examples as well as successes. In principle, civilization could make use of controlled nuclear fusion as an immense source of energy in analogy with nature’s application of various fusion reactions to power stars. However, in reality achieving this has been much more difficult than originally anticipated. Similarly, achieving the manufacture and control of sophisticated molecular nanodevices based on current conceptual designs may be much more difficult than anticipated. Looking at the problem more optimistically we can say that there has been much encouraging theoretical and conceptional study as foundation for achieving nanoscale manufacturing. It might be that broader pool of ideas and concepts coming from different fields of natural

sciences is essential for the fulfillment of the tasks of nanotechnology, but certainly the first steps are made starting from known concepts in physics, chemistry and biology.

The aim of the project that inspired this Thesis was to understand nanoporous systems, learn to control their design, and to explore potential functionality. It has been outlined that such systems can serve as host matrixes for the incorporation of conducting materials at the nanometer scale. By designing nanoporous host structures, we are trying to manipulate the growth process and the properties of embedded conductive nanostructures. The next Chapter will focus on the basic properties and characteristics of the nanoporous materials.

References

- ¹ C. M. Lieber, *Scientific American* **2001**, 285, 58-64.
- ² P. A. Packan, *Science* **1999**, 285, 2079.
- ³ M. A. Reed, and J. M. Tour, *Scientific American*; **2000**, 282, 86-93.
- ⁴ J. M. Tour, *Acc. Chem. Res.* **2000**, 33, 791-804
- ⁵ D. S Everhart, *Handbook of Applied Surface and Colloid Chemistry* **2002**, 2, 99-116.
- ⁶ H. Dai, *Acc. Chem. Res.* **2002**, 35, 1035-1044.
- ⁷ G. S. McCarty, P. S. Weiss, *Chemical Reviews* **1999**, 99, 1983-1990.
- ⁸ Y. Huang, X. Duan, Q. Wei, C. M. Lieber, *Science* **2001** 26, 291, 630-633.
- ⁹ T. Bein, *Stud. Surf. Sci. Catal.* **1996**, 101, 1303.
- ¹⁰ D. J. Cardin, *Adv. Mater.* **2002**, 14, 553.
- ¹¹ G. K. Binnig, W. Haeberle, P. Vettiger, In *PCT Int. Appl.*; (International Business Machines Corporation, USA): Wo, 2002.

Chapter 2. Introduction to nanoporous materials.

2.1. Introduction

2.2. Surfactant-templated mesoporous materials

2.2.1. Definition, nomenclature, and structure

2.2.2. Mechanism of formation, properties, and applications

2.2.3. Functionalized ordered mesoporous materials

2.2.4. Ordered mesoporous films

2.1. Introduction

Nanostructured materials play a central role in nanoscale science and technology. Among them, nanoporous materials have attracted considerable attention within the last few years as building units for designing molecular architectures by applying bottom-up strategies. There are a variety of nanoporous solids, such as porous carbons, porous inorganic oxides, zeolites and zeolite-like materials, pillared clays, porous polymeric materials, and others, that possess high surface areas as a common feature. High surface areas in all these materials can be attained either by fabricating small particles and clusters where the surface-to-volume ratio of each particle is high, or by creating materials where the void surface area (pores) is high compared to the amount of bulk support material.

Let us define the term nanoporous materials. The pore systems of solids can be of many different kinds. The individual pores may vary both in size and in shape within a given solid, and between one solid and another. A feature of special interest for many purposes is the width of the pores, e.g., the diameter of a cylindrical pore or the distance between the walls of a slit-shape pore. A convenient classification of pores according to their average width originally proposed by Dubinin¹ and now officially accepted by the IUPAC² is summarized in Table 2.1. As can be seen from this classification, the term nanoporous materials does not exist. Nevertheless, here we define all materials with pores in the nanometer range as nanoporous.

Associated with the porosity of solids is the term “molecular sieve”. In 1932 McBain proposed the term “molecular sieve” to describe a class of materials that exhibited selective

sorption properties³. He proposed that for a solid to be a molecular sieve it must separate components of a mixture on the basis of molecular shape and size. Chart 2.1 represents all materials that are considered to have molecular sieve properties. Among those of special interest to this work are peri-crystalline MS41 materials (surfactant-templated mesoporous molecular sieves) that are described in the next parts of this introductory Chapter.

Table 2.1. Classification of the pores according to the pore width.

Width	
Micropores	Less than 2 nm
Mesopores	Between 2 and 50 nm
Macropores	More than 50 nm

Another important classification that should be considered refers to the dimensions of the particles. In this work we will discuss particles (for example semiconducting or noble metal particles) that have strictly nanometer-range diameters. They will be referred to as nanosized materials.

2.2. Surfactant-templated mesoporous materials

2.2.1. Definition, nomenclature, synthesis, and structure

In 1992, researchers of the Mobil Corporation discovered a new class of inorganic porous solids called M41S family of mesoporous materials and since then considerable research and characterization effort has been devoted to this class of solids⁴. According to the IUPAC nomenclature this class of materials belongs to the porous solids that have pore sizes in the mesoporous region. Mesoporosity is not something new. There is a large number of porous solids, such as mesoporous silica, alumina, and polymeric materials, that show mesoporosity; the unique feature of the aforementioned class of porous solids is that they all show ordered mesoporosity with narrow pore-size distribution, and sometimes they are more correctly referred to as mesostructured materials. Ordered mesoporosity of this class of solids is given by the specific mechanism of formation that employs the intriguing interaction of liquid-crystal templating and the cooperative self-assembly of inorganic and organic (micellar)

species. This is the reason why some authors prefer to use the term surfactant-templated mesoporous materials when they are referring to this class of solids.

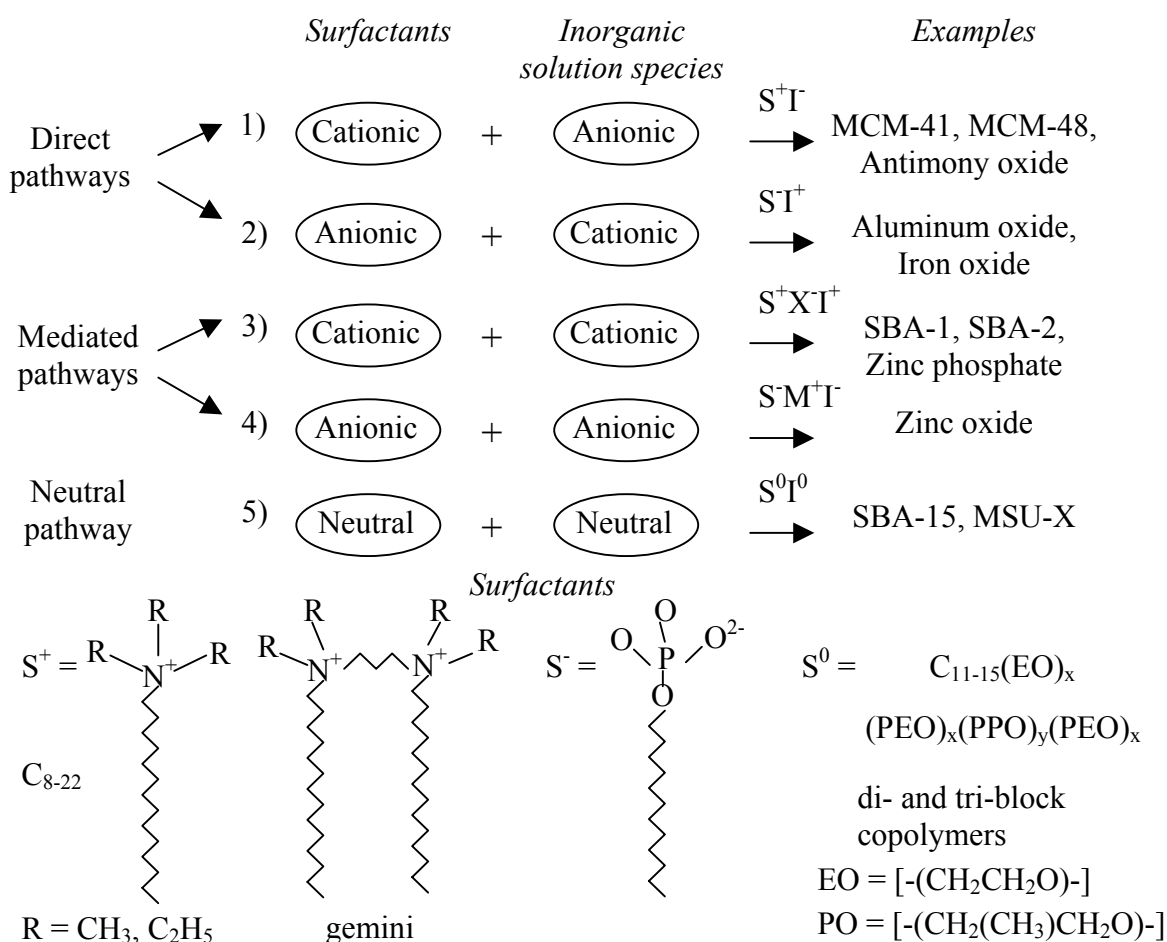
Mesoporous materials with ordered porosity were first prepared as pure silicates or aluminosilicates^{5,6,7}, but now a large number of metal oxides are readily synthesized^{8,9}. Recently, mesostructured carbons (CMK) were also prepared as replicas of the silica-based mesoporous materials¹⁰. In this Thesis silica-based mesostructured materials will be discussed in more detail.

The common features that distinguish this class of nanoporous solids from zeolites and other mesoporous supports are the long-range order of mesopores with defined and controllable pore sizes, extremely high surface areas obtained after removal of the template molecules, and various types of mesophase structures that could be obtained by simply choosing proper structure directing agents (surfactant) and/or co-surfactant molecules. In contrast to the zeolites, the wall structure of these materials is essentially amorphous; this is expected to limit some of the potential industrial applications. Only recently, it has been claimed that the wall structure of these materials may be made zeolitic^{11,12}.

A strict nomenclature has not been adopted for the mesoporous materials. The literature on mesoporous materials is replete with acronyms, such as MCM-41, SBA-15, FSM-16, FDU, MSU-X, and many others, that are usually associated with specific mesophase structures. The first to be discovered was the MCM family of materials by the researchers at the Mobil Corporation⁴. Later on, researchers from Santa Barbara prepared a broad class of materials made under acidic conditions, so-called SBA family¹³.

At present, periodic mesoporous materials can be readily synthesized in a wide range of pH, at temperatures ranging from ambient to approximately 150°C, and using a variety of surfactants and polymers as structure directing agents, thus leading to different mesophase structures and morphologies. Usually in the literature five different synthetic pathways are outlined (Scheme 2.1)^{14,15}. Route 1 involves the direct co-condensation of anionic inorganic species with a cationic surfactant (S^+T), the synthesis of the M41S family is a prototypic example. A similar route to ordered non-silica mesoporous structures has been found involving the cooperative condensation of a cationic inorganic species with an anionic surfactant (ST^+), route 2. In contrast, routes 3 and 4 involve the condensation of ionic inorganic molecules in the presence of similarly charged surfactant molecules. These

pathways are mediated by counter-ions of opposite charge (to that of the surfactant head group) thus giving rise to completely new pathways schematically represented as (S^+X^-), where $X^- = Cl^-, Br^-$; or (S^-M^+) where $M^+ = Na^+, K^+$. Routes 1 and 3 are most often used to prepare silica-based mesoporous materials. The fifth synthetic route employs hydrogen bonding between non-ionic surfactants and neutral inorganic precursors (S^0I^0) to prepare ordered mesoporous materials and is a good alternative to electrostatic charge - matching routes 1 to 4. Applying the last synthesis route, a large number of ordered and disordered mesoporous materials were prepared^{16,17}.



Scheme 2.1. A general scheme for the self-assembly reaction of different surfactant and inorganic species. Some surfactants, other than alkyltrimethylammonium ions, such as gemini surfactants or block copolymers, are also good templates for mesoporous materials.

Most often cited and certainly well-known is the two-dimensional hexagonal mesophase structure with ($p6m$) space group symmetry that is typical for MCM-41 and SBA-15 materials. The structure resembles mesoporous tubes (channels) that are assembled in hexagonal order and indexed in the ($p6m$) space group. These tubes are not always straight but can wind like a bunch of ropes. The structure viewed by electron microscopy in the direction along the tubes (in a narrow section where the tubes are essentially straight) resembles an image of a honeycomb net (Figure 2.1C).

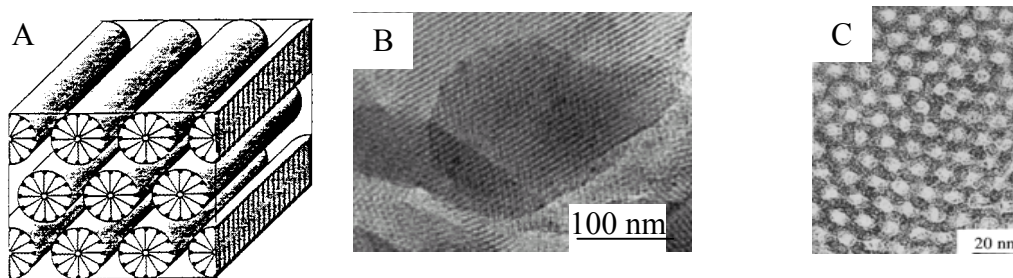


Figure 2.1. (A) Schematic representation of the hexagonally ordered mesoporous material, (B) TEM image of MCM-41 material with the electron beam perpendicular to the direction of the main channels (reprinted from Ref. 20), (C) TEM image of the SBA-15 material with the electron beam parallel to the direction of the main channels (reprinted from Ref. 24).

Nevertheless, the difference between MCM-41 and SBA-15 materials, having one and the same overall mesophase structure, is profound. For example, MCM-41 materials are synthesized with cationic surfactants (most commonly cetyltrimethylammonium cationic surfactant, following the first synthetic route) under basic conditions, and commonly have $d_{(100)}$ spacing of about 4 nm, which after calcination yield a hexagonally ordered porous solid with uniform pore sizes of 2 to 3 nm^{18,19,20}. Using different swelling agents, such as trimethylbenzene or co-surfactants, the pore size can be expanded up to 10 nm; this is usually associated with a considerable decrease of the mesostructural order^{21, 22}. In contrast, the SBA-15 material is synthesized under acidic conditions by use of amphiphilic tri-block copolymers as an organic structure directing agents^{23,24}. The pore size is usually 6 nm after calcination and can be tuned up to 30 nm. In contrast to MCM-41 materials, SBA-15 possesses thicker uniform walls (3 to 6 nm) with disordered microporosity that is attributed to the specific interaction of

the amphiphilic copolymer molecules and the silica wall²⁵. The connectivity between the channels of the SBA-15 material is identified by TEM measurements of platinum replicas prepared in the channels. The thicker silica walls of the SBA-15 material provide an explanation for the increased hydrothermal stability of this material in comparison to MCM-41. Another feature that is worth mentioning here is the difference in the surface area and pore volume of the MCM-41 and SBA-15 materials. Despite of the bigger pore size of the SBA-15 material it usually shows lower surface area and pore volume. This fact is explained and modeled by the increased wall thickness of the SBA-15 material²⁶.

Three-dimensional cubic mesophase structures showing a variety of space group symmetries are gaining much attention due to the increased diffusion and pore accessibility. Among them the first to be prepared was the MCM-48 mesophase structure, a member of the M41S family discovered by the scientists of the Mobil Corporation⁴. MCM-48 has a cubic structure with space group $(Ia3d)^{27,28}$. It is a bicontinuous mesoporous net of two channel systems that are interwoven (Figure 2.2A).

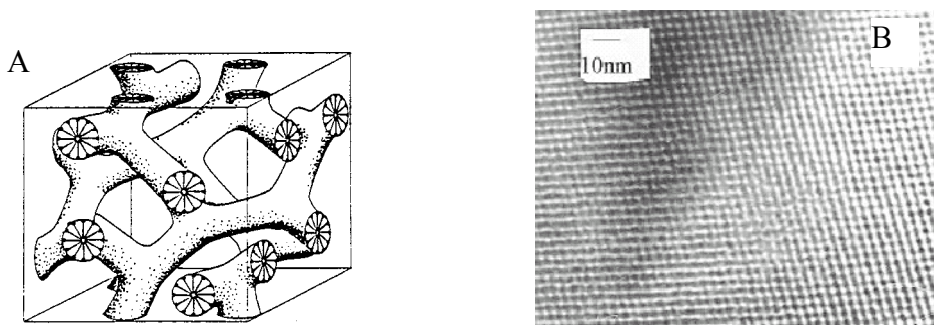


Figure 2.2. (A) Schematic representation of the cubic MCM-48 mesoporous material, (B) TEM image of MCM-48 material with the electron beam parallel to the (110) cubic plane (reprinted from Ref. 27).

It has been shown that the structure of MCM-48 fits very well with the gyroid minimal surface as evidenced from a comparison of experimental transmission electron micrographs with simulations based on the gyroid surface^{29,30}. Recently a mesophase structure showing the same $(Ia3d)$ bicontinuous symmetry has been observed for a material prepared under acidic conditions with tri-block copolymer as the structure directing agent³¹. The structure was deduced from careful electron microscopy imaging although the X-ray diffraction results do

not correspond to the one expected for the traditional ($Ia3d$) mesophase structure of MCM-48 material.

A large group of cubic phase mesoporous materials having different space group symmetries have been prepared under acidic conditions^{32,33}. The space group of some of them is easily deduced by a large number of diffraction peaks³⁴. For some of them, recently, electron diffraction was used to clarify the real three-dimensional structure^{35,36}. A common feature for all of them is that the three-dimensional mesophase order is obtained by self-assembly of spherical micelles rather than micellar rods that are typical for hexagonally ordered MCM-41 materials or cubic MCM-48 material. For example, SBA-1 and SBA-6 materials have a cubic mesophase structure with space group ($Pm3n$) that is suggested to be of a cage type with open windows connecting the cavities, thus giving a bimodal pore size distribution (Figure 3A).

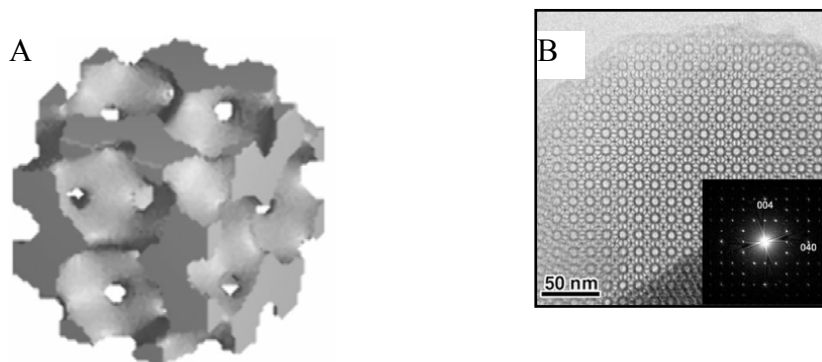


Figure 2.3. (A) Schematic representation of the SBA-6 cubic mesoporous material with ($Pm3n$) symmetry, (B) TEM image of SBA-6 material with the electron beam parallel to the [100] plane (reprinted from Ref. 35).

The synthesis of those mesoporous materials employs acidic conditions and cationic surfactant with bigger head groups (alkyltriethylammonium surfactant). Other cubic mesoporous structures were obtained using di- and triblock copolymer structure directing agents in acidic media, such as SBA-16 ($Im3m$), SBA-11 ($Pm3m$), or FDU-1 ($Im3m$), that reached pore sizes of more than 10 nm^{37, 38}.

Similar to the cubic mesoporous materials prepared under acidic conditions is a group of acidic materials that show three-dimensional order of hexagonally packed spherical cages

(*P6/mmc*); these are prepared with gemini cationic surfactants or di-block copolymers. These are SBA-2 and SBA-12 materials showing pore sizes of 3 and 4.5 nm, respectively. As for the SBA-15 material, this group of acidic materials when prepared with non-ionic surfactants such as block copolymers shows increased wall thickness and thermal stability in comparison to the M41S group.

There is a group of mesoporous molecular sieves that does not show diffraction patterns that can be attributed to any of the foresaid mesophase configurations^{39,40}. They are prepared under slightly acidic conditions with neutral surfactants and identified by only one single, broad reflection but still showing all other typical characteristics of ordered mesoporous materials. These materials are not always correctly referred to as disordered mesoporous materials and a typical example is the MSU-X group of materials. The mesophase structure is usually presented as worm- or spaghetti-type, and the lack of higher order reflections is explained by smaller scattering-domain sizes (Figure 2.4). As typical for the acidic materials prepared with non-ionic surfactants, MSU-X materials show thicker pore walls and improved thermal stability.

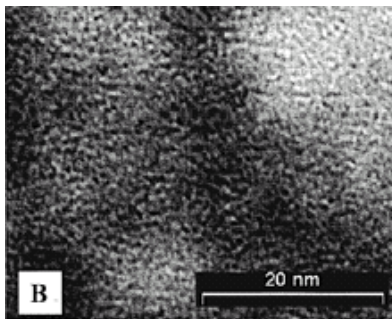


Figure 2.4. TEM image of disordered MSU-X material with worm-like structure.

Finally, it should be mentioned just for consistency that layered mesophase structure can also be prepared. A typical example is the MCM-50 lamellar mesophase that is not thermally stable and collapses under the calcination conditions⁴.

2.2.2. Mechanism of formation, properties, and applications

The formation mechanism of mesoporous materials relies on the concepts of supramolecular chemistry where self-assembly, electrostatic interactions, or hydrogen-

bonding play decisive roles. Much of the interest, beauty, and potential in this field comes from the motivation provided by the many intricate architectures of organic/inorganic biphasic structures that exist in nature. A biomimetic approach relies on the existence or construction of an organized organic surface that controls the subsequent nucleation and growth of the inorganic species around it⁴¹. Following these analogies, the scientists of the Mobil Corporation in their early article on the M41S mesoporous family outlined two possible mechanisms for the formation of this class of inorganic solids⁴. The first model assumes the central theme of biomimetics and postulates that the primary structure-directing element is the water-surfactant liquid-crystal mesophase around which the inorganic framework is formed. The second one suggests that addition of the silicate orders the subsequent silicate-encased surfactant micelles. These general models can be used as a foundation to understand the formation mechanism of the surfactant-templated mesoporous inorganic solids. At the same time they are not sufficient for establishing a mechanistic understanding needed for better control of the synthesis process where the specific features of the surfactant molecules, inorganic species, and solvents, and the interactions between them could be crucial for the final mesophase structure.

Lately, the cooperative formation mechanism of inorganic-organic interfaces was accepted. In this mechanism the multidentate charge density matching between soluble inorganic species and surfactant molecules determines the initial interaction between them^{42, 43}. Within this charge density matching constraint, hydrophobic parts of the surfactant molecules reorganize (form micelles) by minimizing the van der Waals interaction and inorganic/organic charge energies to form final hybrid organic/inorganic mesophase structures. It should be recognized that phase transitions can take place that are associated with changes in the curvature of the organic/inorganic interface. Hence, the size, charge, and shape of surfactants are important structure-directing parameters. The surfactant organization in amphiphilic liquid-crystal arrays is described in terms of the local effective surfactant packing parameter,

$$g = V/a_0l \quad (2.1)$$

where V is the total volume of the surfactant chains plus any co-solvent organic molecules, a_0 is the effective head group area at the micelle surface, and l is the kinetic surfactant tail length.

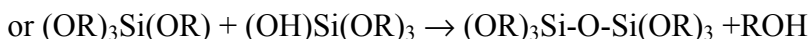
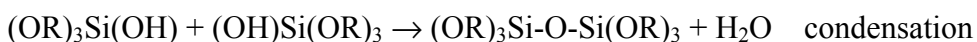
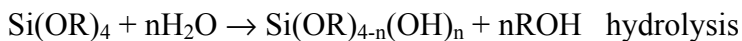
The expected mesophase sequence as a function of the packing parameter is shown in the Table 2.2.

The value of g increases as: a_0 or l decreases or V increases. These transitions reflect a decrease in surface curvature from cubic ($Pm3n$) through vesicular ($p6m$) and lamellar. For surfactants to associate in a spherical structure such as ($Pm3n$) the surface area occupied by the surfactants polar group should be large, as for example in $C_nH_{2n+1}(C_2H_5)_3NBr$, or gemini surfactants.

Table 2.2. Mesophase structures as a function of the surfactant packing parameter.

g	mesophase
1/3	Cubic ($Pm3n$)
1/2	Hexagonal ($p6m$)
1/2- 2/3	Cubic ($Ia3d$)
1	lamellar

However, the formation of the final mesophase structure under the charge-density matching constraint is strictly affected not only by the character of the surfactant molecules but also by the nature of the silica precursors⁴⁴. The nature of the silica species that are presented and participate in the multidentate bonding with the surfactant molecules depends on various synthesis conditions, such as pH, dilution, silica source, etc. In many cases, metal alkoxides are popular precursors because they react readily in the acid- or base-catalyzed process of hydrolysis-condensation.



The hydrolysis-condensation of silica precursors coming from different silica sources was thoroughly studied with in-situ NMR, Raman, and mass spectrometry and the precursors were identified to be various silica oligomers (cyclic rings, branched silica species, etc.)⁴⁵. The

charge, geometry, and association of the molecular silica species in solution can be adjusted through the choice of pH, co-solvent, counter ions, and temperature.

The model of charge-density matching has been shown to be successful in explaining the formation mechanism of mesophase structures prepared by the first four synthetic pathways. The fifth synthetic pathway is explained by hydrogen-bonding between the neutral surfactant molecules and neutral inorganic species, and it seems that the inorganic structure fully mimics the organized liquid-crystalline mesophase. Because of the weaker repulsive interactions between the metal oxide precursors at the surfactant-solution interface, compared to those between charged metal oxide precursors, this synthetic pathway usually affords thicker framework walls as outlined before.

The unusual properties of the ordered mesoporous materials have intrigued the zeolite community for more than ten years and have opened avenues to many desirable applications. Nevertheless, it should be noted that to date no real industrial application of mesoporous materials has been recorded. Obvious applications of ordered mesoporous materials were seen first in catalysis, where a need for zeolite-like materials with bigger pore sizes was identified in order to process heavier residues more efficiently^{46,47}. However, since the acidity of ordered mesoporous materials does so far not substantially exceed that of amorphous aluminosilicates, the high expectations could not be met. Many authors point out that the other basic problem for applications of ordered aluminosilicate mesoporous materials as catalysts lies in the low hydrothermal stability of the materials. Recently much effort has been extended to improve the hydrothermal stability of these materials, for example, by applying colloidal zeolite seeds as precursors for the synthesis (recrystallization) of ordered mesoporous materials^{48,49}. These materials possess remarkable hydrothermal properties and in some cases they show advantageous performance in a number of catalytic reactions⁵⁰.

Recently ordered mesoporous materials were targeted as supports for organic-inorganic hybrid catalysts^{51,52}. Much is known about organic catalysts working in solution and the immobilization of these entities into solids creates organic-inorganic hybrid catalysts where the organic moiety works as an active site and the solid provides avenues to recovery of the organic active sites. In other words, the ordered mesoporous structure can be used as a nanoreactor for interesting catalytic reactions.

In addition to the catalyst field, other novel applications seem to be coming of age. Thiol-, amino-, or benzoylthiourea-functionalized ordered mesoporous materials have been shown to have excellent sorption properties for heavy metals, which by far exceed those of commercial adsorbents^{53,54,55}. Ammonium-functionalized mesoporous silica was also used as sorbent for dangerous pollutants such as arsenate and chromate anions⁵⁶. The usage of such modified mesoporous silica sorbents in “green” chemistry has been recently reviewed⁵⁷.

A more recent development is the employment of the ordered mesoporous materials in optics and electronics^{58,59,60}. These novel applications are the basic topic of this Thesis and will be discussed in details in Chapter 3. Recently synthetic methods were suggested for preparation of macrostructures as fibers, rods, thin films, self-standing membranes, and spheres of highly ordered mesoporous materials, some of these morphologies are of interest for applications in optics and electronics.

Another potential application in future microelectronics is the usage of mesoporous thin films as low-k dielectric coatings. It is desirable to produce materials that possess good mechanical strength, large break-down voltage, small leakage current, and a dielectric constant (k) as low as 2. First reports on the dielectric constant of ordered mesoporous silica films by Zhao et al. gave values between 1.45 and 2.1 depending on the exact nature of the film⁶¹. This is smaller than values that can be obtained with many organic films. It is expected that modifying the internal surface of the mesoporous films with proper molecular functionality can make them highly hydrophobic, thus reaching even lower dielectric constants⁶². However, the ability to precisely control pore architecture and orientation in the mesoporous films might be the significant advantage in the construction of low dielectric constant films. There are strong indications that this will be the first real industrial implication of this class of porous solids.

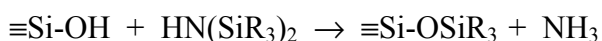
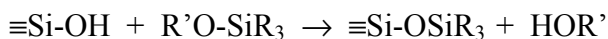
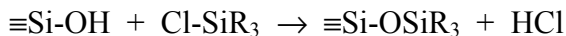
Mesoporous materials are considered to be very promising materials for sensing applications because they permit the confinement of different molecular functionalities and active molecules that can operate as sensors. Optical sensing techniques have been used that rely on the ability to incorporate dye molecules in the mesoporous hosts. The detection is done by a change in fluorescence or coloration of a dye in the presence of the species to be detected. Thus pH sensors were developed by inclusion of pH-sensitive dyes in the mesoporous films⁶³. Mesoporous layers prepared over carbon paste electrodes and modified with amine

functionality have been used for sensing heavy metals such as Cu(II) and Hg(II)⁶⁴. Mesoporous films prepared on surface photo-voltage semiconductor devices have been used as NO and NO₂ gas sensors⁶⁵. The sensing is possible due to physical adsorption of the target gases in the porous system that causes a shift of the bias-voltage dependent characteristics. It has been shown that the sensor properties are dependent on the structure and pore accessibility of the mesoporous films. Another approach is to prepare the mesostructured film itself as an electrochemically active material⁶⁶. This led to the synthesis of a tin oxide mesoporous material that was used as hydrogen gas sensor⁶⁷.

2.2.3. Functionalized ordered mesoporous materials

Incorporation of organic functionalities, either on the silicate surface, as part of the silicate walls, or trapped within the channels, gives opportunities for modifying the physical and chemical properties of the ordered mesoporous materials. The inorganic component of such hybrid inorganic/organic structures can provide mechanical, thermal, or structural stability, whereas the organic features can introduce flexibility into the framework, increase hydrothermal stability, or change the optical properties. The topic of modification of the ordered mesoporous materials with organic functionalities has been reviewed in a number of publications^{68, 69}.

It is well-known that ordered mesoporous materials possess hydroxyl-covered surfaces that can be exposed to reactive silane coupling agents that will provide a variety of organic functionalities on the mesoporous surface or will be intermediate for further attachments. Post-synthesis inclusion of molecular functionalities through covalent bonding to the surface silanol groups is referred to as grafting. This process is most commonly carried out by silylation by one of the following procedures.



Silylation can occur on terminal ($\equiv\text{Si-OH}$) and geminal ($=\text{Si}(\text{OH})_2$) silanol groups, but it is well known that only silanol groups that are not hydrogen-bonded are accessible to modification, otherwise they form hydrophilic networks among themselves and are not reactive to silane coupling⁷⁰. In this respect surface pre-treatments like template removal by solvent extraction, rehydration in boiling water, or rehydroxylation by acid hydrolysis can minimize loss of surface silanols⁷¹.

The second alternative for the preparation of hybrid organic/inorganic mesoporous structures is a co-condensation reaction of the tetralkoxysilane and an organosilane with hydrolyzable groups and Si-C bonds. The process is performed by applying the sol-gel reaction conditions and following the synthesis pathways for preparation of surfactant-templated mesoporous silica. The template removal is usually done by solvent extraction under acidic conditions.

A difficult problem to be answered in many surface modifications of mesoporous solids is whether the functional groups are located on the internal pore surface, the external particle surface, or within the walls. Attempts have been made to selectively modify only the internal surface of the mesoporous materials by passivation of the external surface but the selectivity of such strategies is difficult to ascertain.

2.2.4. Ordered mesoporous films

Originally synthesized as powders that have no alignment of the pores over a macroscopic length scale, mesoporous materials can now be prepared as film architectures on a variety of substrates in a thickness range of nanometers to micrometers. The inspiration for creating such architectures comes from the fact that many of the envisioned industrial applications of the mesoporous materials, such as separation membranes, chemical sensors, surfaces for heterogeneous catalysis, optoelectronic devices, or low dielectric constant layers, could benefit from growing thin films of mesoporous silicates at surfaces or interfaces. A promising issue is the formation of mesoporous silica films that possess accessible pores with preferable orientation that allows direct interaction with a substrate. Ordered mesoporous films are characterized by the same properties typical for the powdered mesoporous materials, such as mesophase structure, pore diameter, surface area, and stability, as well as parameters

that are relevant in the thin film geometry. These include pore alignment with respect to the interfacial plane, film thickness, continuity, pore accessibility, and surface roughness.

Ordered mesoporous films have been prepared as free-standing membranes on the air/liquid interface or as supported layers on a variety of substrates such as silicon wafers, glass, mica, stainless steel, etc. In the first case, the films were observed to grow by transport of material from the homogeneous solution prepared under acidic conditions in the presence of a cationic surfactant towards the air/liquid interface. The mesophase structure, homogeneity, and the thickness of the free-standing films depends on the growth period, surface-to-volume ratio of the reaction vessel, acidity, and silica-to-surfactant ratio in the synthetic mixture^{72,73,74}. For example, free-standing films prepared from tetramethoxysilane (TMOS) and cetyltrimethylammonium bromide (CTABr) showed that the formation mechanism is concentration- and time-dependent⁷⁵. By the use of gemini surfactants a three-dimensional hexagonal mesophase structure ($P6_3/mm$) has been obtained similar to that observed for the bulk SBA-2 material⁷⁶. That kind of a structure when prepared as a thin interfacial layer is assumed to enhance pore accessibility and give an opportunity for the incorporation of guest molecules.

Relatively more research effort has been devoted to mesoporous films prepared on solid supports. Generally, two preparation methods can be recognized for the synthesis of supported ordered mesoporous films according to the role played by the solid surface in the growth process. Thus, we distinguish between surfaces that nucleate mesoporous film growth and surfaces that are coated with the film.

The first process uses heterogeneous nucleation at the solid - liquid interface during the course of the direct mesoporous film growth on the substrate surface. In this approach, silica precursor concentrations are purposefully kept dilute in order to decrease the rate of homogeneous nucleation to such an extent that the heterogeneous nucleation is predominant. The structure of the resulting film is found to depend on the specific interactions of the substrate with the organic surfactant molecules from the silica-surfactant solution^{77,78,79}. Of primary concern here is the structure of the first adsorbed layer at each surface. Preferred orientation of the mesoporous films was observed on the (110) plane of single crystal silicon wafers⁸⁰. Besides the ability of the substrate to guide the orientation of the grown mesoporous films, other macroscopic actions, such as a shear flow field together with topological defects

in the grown film, or covering the original substrate with polymer film and one-directional rubbing have been tried to align the mesochannels in the surface plane⁸¹. These and several more examples show that in most of the cases the grown mesoporous films have been successfully prepared as continuous (although sometimes uneven and granular) layers with a thickness of more than 0.5 μm , exhibiting hexagonal order of channels aligned parallel to the interface surface. A considerable disadvantage of this deposition method is the slow rate of the process and dependence on the specific hydrothermal conditions applied for silica condensation.

The spin- or dip-coating technique is a well-developed method for the formation of thin films and is widely used in the industry for preparation of polymeric thin films. Recently, dip- and spin-coating techniques have been developed for the preparation of continuous thin mesoporous films by applying an elegant and simple evaporation-induced self assembly (EISA) process^{82,83}. This approach employs homogeneous silica/surfactant/alcohol/water coating solutions with surfactant concentrations below the critical micellar concentration ($c_0 \ll \text{cmc}$) and silica precursors obtained by acid-catalyzed hydrolysis of TEOS that are spin- or dip-coated to give preferential evaporation of the co-solvent (alcohol). The dynamic conditions concentrate the depositing film in water and the non-volatile components surfactant, silica species, and acid. The progressively increasing surfactant concentration drives the self-assembly process towards the critical micellar concentration and the formation of the liquid-crystal mesophase. On the other hand, the rapid solvent evaporation induces silica condensation through the increased concentration of the silica oligomers that are simultaneously self-assembled in the final mesophase structure (Figure 2.5). The result is the rapid formation of thin mesophase films that are highly oriented with respect to the substrate surface.

Having in mind these specific features of the mesoporous films prepared by EISA, we can summarize that this method is strongly dependent on parameters, such as initial silica-to-surfactant ratio, nature of the prehydrolyzed silica species, type of surfactant used, dilution of the initial solution, humidity in the deposition chamber, deposition speed, and post synthesis treatments, that can influence the mesophase structure, pore size and accessibility, stability of the films, and film thickness and roughness. For example, the pore size of the mesoporous

films and the mesophase structure can be controlled by using different structure-directing agents as templates - cationic surfactants or amphiphilic di- or tri-block copolymers. Thus, mesoporous films showing two-dimensional hexagonal arrangement of the channels oriented parallel to the interface surface have been prepared but three-dimensional hexagonal or cubic mesophase structures were also obtained with mesophase structures similar to SBA-1 and SBA-2 powdered materials^{84,85,86,87}.

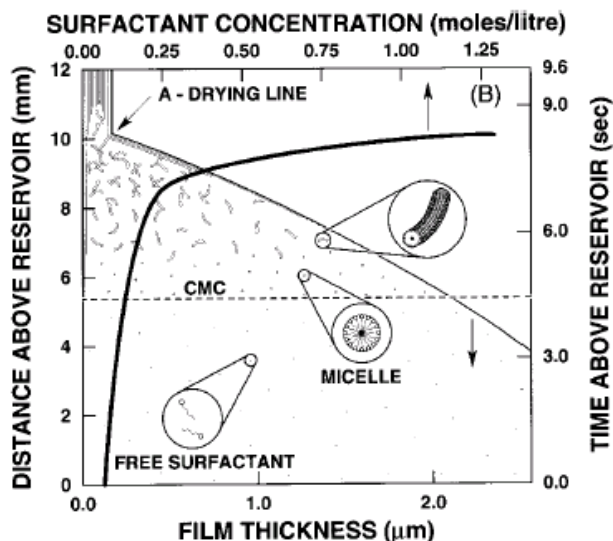


Figure 2.5. Formation of the mesoporous thin film via dip-coating of a mixture containing silica/CTABr/alcohol/water. The initial surfactant concentration is $c_0 \ll \text{cmc}$; it increases with the distance above the reservoir surface (reprinted from Ref. 80.).

The nature of the prehydrolysed silica species, easily changed by the conditions of the hydrolysis of TEOS, also plays a dramatic role in the final order and the thickness of the mesoporous films⁸⁸. Nevertheless, the most extensively studied parameter that influences the final mesophase structure is the surfactant-to-silica ratio. For the CTABr-templated mesoporous films it has been shown that by increasing the silica-to-surfactant ratio three-dimensional hexagonal ($P6/mm$), three-dimensional cubic ($Pm3n$), two-dimensional hexagonal ($p6m$), and lamellar phases can be prepared⁸⁹. Phase diagrams for CTABr-silica mesoporous film have been prepared and thoroughly examined by plan-view or cross-section TEM images

and SAXS measurements. Relatively less characterization effort has been devoted to the di- or tri-block copolymer-templated mesoporous films. Nevertheless, it has been outlined that by changing the tri-block copolymer (Pluronic 123)-to-silica ratio, a three-dimensional cubic ($Im3m$) mesophase, similar to SBA-16 powder material, one-dimensional hexagonal ($p6m$), and lamellar phases can be prepared in the forms of films⁸⁷. Recently, it has been shown that one very important parameter that influences the structure and order of the mesoporous films prepared by EISA is the relative humidity during the deposition process. Humidity-controlled mesostructuration in the CTABr-templated mesoporous silica films showed that the water content is a critical parameter, as poorly ordered, two-dimensional hexagonal, or three-dimensional cubic structures can be obtained, depending on the relative humidity⁹⁰. Another critical factor that can change the final mesophase structure of the mesoporous films is the post-synthetic treatment. As-deposited films show less condensation of the silica framework, therefore processes that increase cross-linking of the silica, such as basic- or acid-catalyzed silica condensation or thermal treatment, can stabilize the final mesophase structure⁹¹.

The dynamic conditions for the preparation of mesoporous films by the EISA method imply difficulties with respect to mechanistic studies because the film deposition proceeds for no more than about one minute. Nevertheless, by applying time-resolved SAXS measurements using a two-dimensional CCD camera, high-flux synchrotron radiation, and in-situ interferometry measurements, it was possible to follow the formation mechanism and the kinetics of film formation^{92,93,94}. A model has been proposed for the CTABr-templated mesoporous films, postulating that the organization at the mesoscale takes place at the final stage of liquid-phase evaporation and involves formation of micelles at both film/air and substrate/film interfaces in the early stages of the film formation. In some cases, the formation of intermediate phases or a mixture of phases existing at the same time can be observed. Here it should be noted that such kind of investigation was done only for dip-coated films for a couple of surfactant/silica/solvent systems and no systematic examination of the formation mechanism of spin-coated films was performed so far. Certainly the explanation of the formation mechanism of these systems lacks additional characterization and we are just in the beginning of the understanding and controlling the formation of the mesoporous films by EISA.

The EISA method was also used for the preparation of a variety of transition metal oxide mesoporous films, such as titania, alumina, zirconia, vanadium oxide films, having in most cases two-dimensional (*p6m*) hexagonal mesophase structure^{95,96,97}. Furthermore, different organosiloxane precursors were mixed with the silica source to give organically functionalized mesoporous films⁹⁸. Another advantage of the EISA method is the facile introduction of molecular functionality in the mesoporous channels by simply dissolving the organic molecules into the surfactant part of the hybrid organic/inorganic composite film. Thus dye molecules or photo-acid generator molecules have been introduced in the liquid-crystal interiors⁹⁹.

The application of the EISA process in the rapid fabrication of hierarchical structures exhibiting form and function on multiple length scales and at multiple locations can be performed by soft lithography techniques such as pen printing or microcontact printing^{100,101,102}. Here the rapid patterning is done using stable homogeneous ink in the form of a surfactant/silica/solvent coating mixture used for dip- or spin-coating.

References

- ¹ M. M. Dubinin, *Chem. Rev.*, **1960**, 60, 235.
- ² IUPAC Manual of Symbols and Terminology, Appendix 2, Colloid and Surface Chemistry. *Pure Appl. Chem.*, **1972**, 31, 578.
- ³ J. M. McBain, *The Sorption of gases and vapors by solids*, **1932**, Rutledge and Sons, London, Chapter 5.
- ⁴ J. S. Beck, J. C. Vartuli, W. J. Roth, M. E. Leonowicz, C. T. Kresge, K. D. Schmitt, C. T-W. Chu, D. H. Olson, E. W. Sheppard, S. B. McCullen, J. B. Higgins, J. L. Schlenker, *J. Am. Chem. Soc.*, **1992**, 114, 10834.
- ⁵ C. Y. Chen, H. X. Li, M. E. Davis, *Microporous Materials*, **1993**, 2, 17.
- ⁶ M. Janicke, D. Kumar, G. D. Stucky, B. F. Chmelka, *Stud. Surf. Sci. Catal.*, **1994**, 84, 243.
- ⁷ C. T. Kresge, J. C. W. J. Vartuli, Roth, M. E. Leonowicz, J. S. Beck, K. D. Schmitt, C. T-W. Chu, D. H. Olson, E. W. Sheppard, *Stud. Surf. Sci. Catal.*, **1995**, 92, 11.
- ⁸ F. Schüth, *Chem. Mater.*, **2001**, 13, 3184.

- ⁹ P. Yang, D. Zhao, D. I. Margolese, B. F. Chmelka, G. D. Stucky, *Nature*, **1998**, 396, 152.
- ¹⁰ S. Jun, S. H. Joo, R. Ryoo, M. Kruk, M. Jaroniec, Z. Liu, T. Oshuma, O. Teresaki, *J. Am. Chem. Soc.*, **2000**, 122, 10712.
- ¹¹ K. R. Kloetstra, H. van Bekkum, J. C. Jansen, *Chem. Commun.*, **1997**, 2281.
- ¹² Y. Liu, W. Zhang, T. J. Pinnavaia, *Angew. Chem.*, **2001**, 113, 1295.
- ¹³ Q. Huo, D. I. Margolese, G. D. Stucky, *Chem. Mater.*, **1996**, 8, 1147.
- ¹⁴ A. Monnier, F. Schüth, Q. Huo, D. Kumar, D. Margolese, R. S. Maxwell, G. D. Stucky, M. Krishnamurty, P. Petroff, A. Firouzi, M. Janicke, B. F. Chmelka, *Science*, **1993**, 261, 1299.
- ¹⁵ Q. Huo, D. I. Margolese, U. Ciesla, P. Feng, T. E. Gier, P. Sieger, R. Leon, P. M. Petroff, F. Schüth, G. D. Stucky, *Nature*, **1994**, 368, 317.
- ¹⁶ P. Tanev, T. J. Pinnavaia, *Science*, **1995**, 267, 865.
- ¹⁷ S. A. Bagshaw, E. Prouzet, T. J. Pinnavaia, *Science*, **1995**, 269, 1242.
- ¹⁸ J. C. Vartuli, C. T. Kresge, W. J. Roth, S. B. McCullen, J. S. Beck, K. D. Schmitt, M. E. Leonowicz, J. D. Lutner, E. W. Sheppard, *Advanced Catalysts and Nanostructured Materials* **1996**, 1-19.
- ¹⁹ J. S. Beck, J. C. Vartuli, G. J. Kennedy, C. T. Kresge, W. J. Roth, S. E. Schramm, *Stud. Surf. Sci. Catal.*, **1995**, 98, 15.
- ²⁰ J. P. M. Niederer, A. B. J. Arnold, W. F. Holderich, B. Spliethof, B. Tesche, M. Reetz, H. Bonnemann, *Topics in Catalysis*, **2002**, 18, 265-269
- ²¹ J. L. Blin, C. Otjacques, G. Herrier, Bao-Lian. Su, *Langmuir*, **2000**, 16, 4226.
- ²² A. Sayari, ; M. Kruk, M. Jaroniec, I. L. Moudrakovski, *Adv. Mater.*, **1998**, 10, 1376.
- ²³ D. Zhao, J. Feng, Q. Huo, N. Melosh, G. H. Fredrickson, B. F. Chmelka, G. D. Stucky, *Science*, **1998**, 279, 548.
- ²⁴ D. Zhao, J. Sun, Q. Li, G. D. Stucky, *Chem. Mater.*, **2000**, 12, 275.
- ²⁵ J. Fan, Ch. Yu, L. Wang, B. Tu, D. Zhao, Y. Sakamoto, O. Terasaki, *J. Am. Chem. Soc.*, **2001**, 123, 12113.
- ²⁶ F. di Renzo, A. Galarneau, P. Trens, N. Tachoux, F. Fajula, *Stud. Surf. Sci. Catal.*, **2002**, 142, 1057.
- ²⁷ V. Alfredsson and M. Anderson, *Chem. Mater.*, **1996**, 8, 1141.
- ²⁸ M. Hartmann, C. Bischof, *J. Phys. Chem. B*, **1999**, 103, 6230.

- ²⁹ K. Schumacher, P. I. Ravikovitch, A. Du Chesne, A. V. Neimark, K. K. Unger, *Langmuir*, **2000**, 4648.
- ³⁰ M. Kurk, M. Jaroniec, R. Ryoo, S. H. Joo, *Chem. Mater.*, **2000**, 12, 1414.
- ³¹ X. Liu, B. Tian, C. Yu, F. Gao, S. Xie, B. Tu, R. Che, L-M. Peng, *Angew. Chem.*, **2002**, 114, 4032.
- ³² D. Zhao, Q. Huo, J. Feng, B. F. Chmelka, G. D. Stucky, *J. Am Chem. Soc.*, **1998**, 120, 6024.
- ³³ M. J. Kim, R. Ryoo, *Chem Mater.*, **1999**, 11, 487.
- ³⁴ J. M. Kim, G. D. Stucky, *Chem. Commun.*, **2000**, 1159.
- ³⁵ Y. Sakamoto, M. Keneda, O. Terasaki, D. Y. Zhao, J. M. Kim, G. D. Stucky, H. J. Shin, R. Ryoo, *Nature*, **2000**, 408, 449.
- ³⁶ Y. Sakamoto, I. Diaz, O. Terasaki, D. Y. Zhao, J. Perez-Pariente, J. M. Kim, G. D. Stucky, *J. Phys. Chem. B*, **2002**, 3118.
- ³⁷ C. Yu, Y. Yu, D. Zhao, *Chem. Commun.*, **2000**, 575.
- ³⁸ C. Yu, Y. Yu, L. Mao, D. Zhao, *Micropor. Mesopor. Mater.*, **2001**, 44-45, 65.
- ³⁹ P. Tanev, T. J. Pinnavaia, *Science*, **1995**, 267, 865.
- ⁴⁰ G. Herrier, J.-L. Blin, B.-L. Su, *Langmuir*, **2001**, 17, 4422.
- ⁴¹ C. T. Kresge, *Adv. Mater.*, **1996**, 8 181.
- ⁴² Monnier, F. Schüth, Q. Huo, D. Kumar, D. Margolese, R. S. Maxwell, G. D. Stucky, M. Krishnamurty, P. Petroff, A. Firouzi, M. Janicke, B. F. Chmelka, *Science*, **1993**, 261, 1299.
- ⁴³ Q. Huo, D. I. Margolese, U. Ciesla, D. G. Demuth, P. Feng, T. E. Gier, P. Sieger, A. Firouzi, B. F. Chmelka, F. Schüth, G. D. Stucky, *Chem. Mater.*, **1994**, 6, 1176.
- ⁴⁴ N. K. Raman, M. K. Anderson, C. J. Brinker, *Chem. Mater.*, **1996**, 8, 1682.
- ⁴⁵ C. J. Brinker and G. W. Scherer, "Sol-gel science: the physics and chemistry of sol-gel processing" *Academic Press, Inc.*, **1990**, Chapter 3.
- ⁴⁶ F. Schüth, *Stud. Surf. Sci. Catal.*, **2001**, 135, 1.
- ⁴⁷ A. Corma, M. T. Navarro, *Stud. Surf. Sci. Catal.*, **2002**, 142A, 147.
- ⁴⁸ Y. Liu, W. Zhang, T. J. Pinnavaia, *J. Am. Chem. Soc.*, **2000**, 122, 8791.
- ⁴⁹ Y. Liu, T. J. Pinnavaia, *Chem. Mater.*, **2002**, 14. 3.
- ⁵⁰ Z. Zhang, Y. Han, F.-S. Xiao, S. Qiu, L. Zhu, R. Wang, Y. Yu, Z. Zhang, B. Zou, Y. Wang, H. Sun, D. Zhao, Y. Wei, *J. Am. Chem. Soc.*, **2001**, 123, 5014.

- ⁵¹ A. P. Wight and M. E. Davis, *Chem. Rev.*, **2002**, 102, 3589.
- ⁵² A. Stein, B. J. Melde, R. C. Schroden, *Adv. Mater.*, **2000**, 12, 1403.
- ⁵³ L. Mercier and T. J. Pinnavaia, *Micropor. Mesopor. Mater.*, **1998**, 20, 101.
- ⁵⁴ V. Antochushuk, O. Olkhovyk, M. Jaroniec, I.-S. Park, R. Ryoo, *Langmuir*, **2003** in press.
- ⁵⁵ A. M Liu, K. Hidajat, S. Kawi, D. Y. Zhao, *Chem. Commun.*, **2000**, 13, 1145.
- ⁵⁶ H. Yoshitake, T. Yokoi, T. Tatsumi, *Chem. Mater.*, **2002**, 14, 4603.
- ⁵⁷ J. H. Clark, *Acc. Chem. Res.*, **2002**, 9, 791.
- ⁵⁸ M. E. Davis, *Nature*, **2002**, 417, 813.
- ⁵⁹ R. C. Hayward, P. Alberius-Henning, B. F. Chmelka, G. D. Stucky, *Micropor. Mesopor. Mater.*, **2001**, 44-45, 619.
- ⁶⁰ S. J. Brian, G. Wirnsberger, G. D. Stucky, *Chem. Mater.*, **2001**, 13, 3140.
- ⁶¹ D. Zhao, P. Yang, N. Melosh, J. Feng, B. F. Chmelka, G. D. Stucky, *Adv. Mater.*, **1998**, 10, 1380.
- ⁶² S. Seraji, Y. Wu, M. Forbess, S. J. Limmer, T. Chou, G. Cao, *Adv. Mater.*, **2000**, 12, 1695.
- ⁶³ G. Wirnsberger, B. J. Scott, G. D. Stucky, *Chem. Commun.*, **2001**, 119.
- ⁶⁴ A. Walcarius, C. Despas, P. Trens, M. J. Hudson, J. Bessiere, *J. Electroanal. Chem.*, **1998**, 453, 249.
- ⁶⁵ T. Yamada, H.-S. Zhou, H. Uchida, M. Tomia, Y. Ueno, T. Ichino, T. Honma, K. Asai, T. Katsube, *Adv. Mater.*, **2002**, 14, 812.
- ⁶⁶ G. J. Li, S. Kawai, *Mater. Lett.*, **1998**, 99, 34.
- ⁶⁷ G. S. Attard, P. N. Bartlett, N. R. B. Coleman, J. M. Eliot, J. R. Owen, J. H. Wang, *Science*, **1997**, 278, 838.
- ⁶⁸ K. Moller, T. Bein, *Chem. Mater.*, **1998**, 10, 2950.
- ⁶⁹ A. Sayari, S. Hamoudi, *Chem. Mater.*, **2001**, 13, 3151.
- ⁷⁰ X. S. Zhao and G. Q. Lu, *J. Phys. Chem. B*, **1998**, 102, 1556.
- ⁷¹ X. Feng, G. E. Fryxell, L.Q. Wang, A. Y. Kim, J. Liu, K. M. Kemner, *Science*, **1997**, 276, 923.
- ⁷² H. Yang, N. Coombs, Ö. Dag, I. Sokolov, G. Ozin, *J. Mater. Chem.* **1997**, 7, 1755.
- ⁷³ J. L. Ruggels, S. A. Holt, P. A. Reynolds, A. s. Brown, D. C. Creagh, J. W. White, *Phys Chem Chem Phys.*, **1999**, 1,323.

- ⁷⁴ K. J. Edler, A. Goldar, A. V. Hughes, S. J. Roser, S. Mann, *Micropor. Mesopor. Mater.*, **2001**, 44-45, 661.
- ⁷⁵ T. Brennan, A. V. Hughes, S. J. Roser, S. Mann, K. J. Edler, *Langmuir*, **2002**, 18, 9838.
- ⁷⁶ S. H. Tolbert, T. E. Schäfer, J. Feng, P. K. Hansama, G. D. Stucky, *Chem. Mater.*, **1997**, 9, 1962.
- ⁷⁷ S. Manne, H. E. Gaub, *Science*, **1995**, 270, 1480.
- ⁷⁸ S. Manne, J. P. Cleveland, H. E. Gaub, G. D. Stucky, P. K. Hansma, *Langmuir*, **1994**, 10, 4409.
- ⁷⁹ M. Jascjke, H. J. Butt, H. E. Gaub, S. Manne, *Langmuir*, **1997**, 13, 1381.
- ⁸⁰ H. Miyata and K. Kuroda, *J. Am. Chem. Soc.*, **1999**, 121, 7618.
- ⁸¹ H. Miyata and K. Kuroda, *Chem. Mater.*, **1999**, 11, 1609
- ⁸² M. Ogawa, *Chem. Commun.*, **1996**, 1149.
- ⁸³ C.J. Brinker, Y. Lu, A. Sellinger, H. Fan, *Adv. Mater.*, **1999**, 11, 579.
- ⁸⁴ D. Zhao, P. Yang, N. Melosh, J. Feng, B. Chmelka and G. D. Stucky, *Adv. Mater.*, **1998**, 10, 1380.
- ⁸⁵ M. Ogawa and N. Masukawa, *Micropor. Mesopor. Mater.*, **2000**, 38, 35.
- ⁸⁶ D. Zhao, P. Yang, D. I. Margolese, B. F. Chmelka, G. D. Stucky, *Adv. Mater.*, **1998**, 2499.
- ⁸⁷ P. C. Albers, K. L. Fridell, R. C. Hayward, E. J. Kramer, G. D. Stucky, B. F. Chmelka, *Chem. Mater.*, **2002**, 14, 3284.
- ⁸⁸ M. Klotz, P.-A. Albouy, A. Ayrat, C. Menager, D. Grosso, A. Van der Lee, V. Caballero, F. Babonneau, C. Guizard, *Chem. Mater.* **2000**, 12, 1721.
- ⁸⁹ S. Besson, T. Gacoin, C. Ricolleau, C. Jacquiod, J.-P. Boilot, *J. Mater. Chem.*, **2003**, 13, 404.
- ⁹⁰ F. Cagnol, D. Grosso, G. J. De A. A. Soler-Illia, E. L. Crepaldi, F. Babonneau, H. Ametisch, C. Sanchez, *J. Mater. Chem.*, **2003**, 13, 61.
- ⁹¹ Y. Lu, R. Ganguli, C.A. Drewien, M.T. Anderson, C.J. Brinker, W. Gong, Y. Guo J.I. Zink, *Nature* **1997**, 389, 364.
- ⁹² D. Grosso, F. Babonneau, P.-A. Albouy, H. Ametisch, A. R. Balkenende, A. Brunet-Bruneau, J. Rivory, *Chem. Mater.*, **2002**, 14, 931.

- ⁹³ D. Grosso, A. R. Balkenende, P.-A. Albouy, A. Ayral, H. Amentisch, F. Babonneau, *Chem. Mater.*, **2002**, 14, 931.
- ⁹⁴ D. Grosso, F. Babonneau, G. J. De A. A. Soler-Illia, P.-A. Albouy, *Chem. Mater.*, **2002**, 14, 931.
- ⁹⁵ E. L. Crepaldi, G. J. De A. A. Soler-Illia, D. Grosso, P.-A. Albouy, C. Sanchez, *Chem. Commun.*, **2001**, 1582.
- ⁹⁶ E. L. Crepaldi, G. J. De A. A. Soler-Illia, D. Grosso, C. Sanchez, *New. J. Chem.*, **2003**, 27, 9.
- ⁹⁷ L. Pidol, D. Grosso, G. J. De A. A. Soler-Illia, E. L. Crepaldi, C. Sanchez, P.-A. Albouy, H. Amentisch, P. Euzen, *J. Mater. Chem.*, **2002**, 12, 557.
- ⁹⁸ B. Alonso, A. R. Balkenende, P.-A. Albouy, H. Amentisch, M.-N. Rager, F. Babommeau, *J. Sol-Gel Sci. Tech.*, **2003**, 26, 587.
- ⁹⁹ D. A. Doshil, N. K. Huesing, M. Lu, H. Fan, Y. Lu, K. Simmons-Potter, B. G. Potter Jr., A. J. Hurd, C. J. Brinker, *Science*, **2000**, 290, 107.
- ¹⁰⁰ H. Fan, Y. Lu, A. Stump, S. T. Reed, T. Baer, R. Schunk, V. Perez-Luma, G. P. Lopez, C. J. Brinker, *Nature*, **2000**, 405, 56.
- ¹⁰¹ H. Fan, S. T. Reed, T. Baer, R. Schunk, G. P. Lopez, C. J. Brinker, *Micropor. Mesopor. Mater.*, **2001**, 44-45, 625.
- ¹⁰² M. Trau, N. Yao, E. Kim, Y. Xia, G. M. Whitesides, I. A. Aksay, *Nature*, **1997**, 390, 674.

Chapter 3. Introduction to one-dimensional nanostructures.

3.1. Introduction

3.2. General synthetic routes for the preparation of one-dimensional nanostructures

3.3. General properties of one-dimensional nanostructures

3.4. Synthesis and properties of carbon nanotubes

3.1. Introduction

Nanostructures – structures that are defined as having at least one dimension between 1 and 100 nm – have received steadily growing interest as a result of their peculiar and fascinating properties that often differ substantially from their bulk counterparts. The necessity and ability to fabricate such structures is essential to much of modern science and technology, and has resulted in the establishment of a separate scientific field called nanoscience (see Chapter 1).

Two-dimensional nanostructures (quantum wells) have been extensively studied by the semiconductor community and their manufacture is already mature technology. Considerable research effort has also been dedicated to quantum dots in the past two decades. For example, a rich variety of chemical methods have already been developed for generating quantum dots with well-controlled dimensions and from a broad range of materials. Recently, one-dimensional nanostructures, such as wires, rods, and tubes, have also become the focus of intensive research owing to their unique potential applications in mesoscopic physics and the fabrication of nanoscale devices^{1,2,3}. They are also expected to play an important role as both interconnections and functional units in fabricating electronic, optoelectronic, electrochemical, and electromechanical devices^{4,5}.

3.2. General synthetic routes for the preparation of one-dimensional nanostructures

The methods for the manufacture of one-dimensional nanostructures can be divided into two basic groups. The first group of methods relies on fabrication processes typical for the top-down approaches (Figure 1A), such as electron-beam writing, proximal-probe patterning, X-ray or extreme-UV lithography, etc. In contrast, the second group of methods

based on bottom-up approaches provides an alternative and intriguing strategy because of the versatility of the chemical synthesis methods applied therein. Figure 3.1 summarizes the different possible synthetic strategies for achieving one-dimensional growth of nanostructures.

Some solids naturally grow as one-dimensional nanostructures, and this habit is determined by the highly anisotropic bonding in the crystallographic structure (Figure 3.1.B). Typical examples are carbon nanotubes, molybdenum chalcogenides, selenium, and tellurium nanowires. The growth and properties of carbon nanotubes will be discussed in a separate part of this Chapter. For many solids that are characterized by isotropic crystal structures symmetry breaking is required in the nucleation step to induce anisotropic growth. Many strategies have been explored to produce nanostructures with one-dimensional morphologies. Methods that are relevant to this work are shown in Figure 3.1.C and D, and will be discussed in more detail. Another possible strategy is a vapor-liquid-solid process in which the symmetry is broken through the introduction of a flat solid-liquid interface, or vapor-phase methods where supersaturation of the system can be controlled below a certain level to effectively induce and maintain one-dimensional growth.

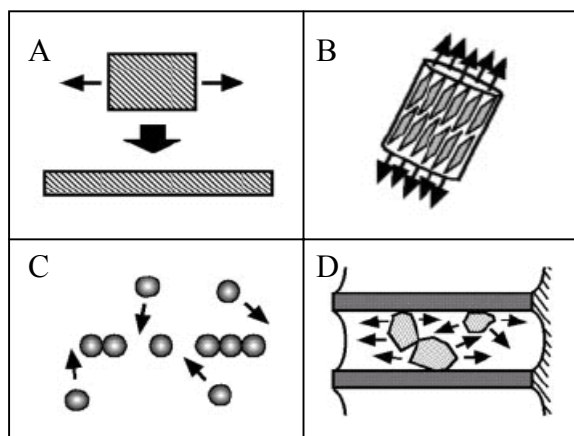


Figure 3.1. Schematic illustration of different approaches that have been applied for one-dimensional growth of solids: A) size reduction achieved by different top-down strategies, B) growth dictated by the anisotropic crystallographic structure, C) assembly of nanoparticles, D) directed growth through the use of a template.

Monodispersed colloids have been pursued as building blocks for the formation of wire-like structures through self- or externally manipulated assembly (Figure 1C). Most often metallic nanoparticles have been used to assemble continuous one-dimensional nanostructures. For example, it has been demonstrated that gold clusters such as $\text{Au}_{55}(\text{PPh}_3)_{12}\text{Cl}_6$ can assemble into chains at the water-dichloromethane interface as induced by poly(p-phenyleneethynylene) dissolved in the liquid phase⁶. Another group has investigated the selective self-assembly of metal nanoparticles on the surfaces of thin films formed from diblock co-polymers and found that gold nanoparticles aggregate into chains inside the polystyrene block with a selectivity approaching 100%⁷. In addition to self-assembly, external manipulation with a field or a mechanical probe has also been explored to induce or direct the organization of nanoparticles into arrayed structures. Velez and co-workers have shown that metallic nanoparticles suspended in a liquid assembled into microwires under dielectrophoresis⁸. Here an alternating electric field was used to induce the mobility and attractive interaction of the nanoparticles. In another approach, a scanning force microscope was used to assemble linear chains and other structures from individual gold nanoparticles⁹. A variety of other examples using capillary forces¹⁰, magnetic fields¹¹, or electrostatic interactions¹² can be found in the literature.

Template-directed growth is another possibility for the synthesis of one-dimensional nanostructures (Figure 1D). In this approach, the template simply serves as a scaffold within or around which different material is generated. A variety of templates have been successfully demonstrated with notable examples including step edges on solid surfaces, mesoscale structures self-assembled from organic surfactants or block copolymers, biological macromolecules, such as DNA strands or rod-shaped viruses, existing nanostructures synthesized using other approaches, and lastly channels of porous materials (the last approach will be exemplified and discussed in detail in the next parts of the Thesis).

The nature of the one-dimensional materials prepared by this approach is versatile ranging from conductive metal nanowires and semiconductor structures to conductive polymers. For example, electrochemical step-edge metal decoration employs selective deposition of a metal at atomic step edges of a single crystal surface^{13,14,15}. The wire-thickness in the direction normal to the substrate is only several atomic layers. The

electrochemical template synthesis of metal nanowires in porous materials, established by Martin, Moskovits, and Searson, involves electrochemical deposition of metal into cylindrical pores of an inert, nonconductive host material - usually porous alumina or polycarbonate membranes with pore sizes ranging from tens of nanometers to several hundred nanometers^{16,17,18,19,20}. Electroless reduction methods use metal catalyst nanoparticles to nucleate and guide the growth of continuous metal nanowires. It has been shown that chiral lipid tubules can be metallized by electroless reduction giving nanometer thin metal wires.²¹ Metallized DNA molecules were also subjected to electroless reduction resulting in a metal nanowire between two metal electrodes²². Mesophase structures self-assembled from surfactants can be directly used as soft templates to promote the formation of nanorods when coupled with an appropriate chemical or electrochemical reaction. Using this approach, the synthesis of gold nanorods by templating against rod-like micelles²³ or semiconductor nanowires by use of mixed surfactants has been demonstrated²⁴. Existing nanostructures such as carbon nanotubes have also been used as hard templates to generate nanorods or tubes of many materials²⁵. More details on nanowires in mesoporous hosts will be covered in later Chapters dealing with specific systems.

3.3. General properties of one-dimensional nanostructures

It is generally accepted that low-dimensional nanoscale structures in comparison with the bulk materials show interesting quantum confinement effects with distinct electronic, optical, chemical, and thermal properties. It is obvious that one-dimensional nanostructures with well-controlled dimension, composition, and crystallinity represent a new class of intriguing systems for the investigation of structure-property relations and related applications. The properties that are attractive and dependent on the nanosized dimensions are: thermal, mechanical, phonon transport, optical, field emission, and, of primary interest for this work, electronic properties.

The thermal stability of the one-dimensional nanostructures is of critical importance for their implementation as building units in nanoelectronics. The melting point of a solid formed as a nanostructure is significantly reduced^{26,27} in comparison to the bulk materials. It

was found that the lowering of the melting point is inversely proportional to the diameter of the nanowire²⁸.

The investigation of the mechanical properties of nanostructures is essential for the atomic-scale manipulation of these materials in constructing composites with improved mechanical properties. Single-crystalline, one-dimensional nanostructures are expected to be significantly stronger than their bulky counterparts. This is explained by the reduction in the number of the defect sites per unit length as a result of decreased lateral dimensions. Measurements of the mechanical properties of one-dimensional nanostructures were performed by attaching the nanowires to STM tips²⁹. This approach can be further extended to examine the atomic events during the mechanical deformations of nanosized structures.

As for quantum dots, size-confinement also plays an important role in determining the energy levels of a nanowire once its diameter has been reduced below a critical value (the Bohr radius)³⁰. In this way, one-dimensional nanosized semiconductor structures usually exhibit a so-called blue-shift of the absorption or photoluminescent spectra as compared to the bulk materials. In contrast to quantum dots, light emitted from nanowires is highly polarized along their longitudinal axes³¹. For nanorods of noble metals, their surface plasmon resonance (SPR) properties are shown to be different from those of the corresponding spherical nanoparticles³². The one-dimensional noble-metal nanowires show two SPR modes, corresponding to the transverse and longitudinal excitations. Nonlinear optical properties and lasing properties of one-dimensional nanostructures have also been studied intensively in the last few years because of the possibility to integrate them as logic/routing elements in optoelectronic circuits³³.

Nanowires with sharp tips are promising candidates for applications related to cold cathode, field emission of electrons. Carbon nanotubes, Si and SiC nanowires have been shown to possess promising field-emission properties³⁴.

Electronic properties of one-dimensional nanowires are of primary interest nowadays because it is believed that there is a potential to go beyond the traditional microelectronic approaches. As the critical dimensions of an individual device become smaller and smaller, the electron transport properties of their components become an important issue to study. Quantization due to the transverse confinement and the resulting finite level spacing of

electronic and phononic states are responsible for some novel effects. When a nanowire or nanotube diameter becomes small, singularities in the electronic density of states develop at special energies, called van Hove singularities, where the electronic density of states becomes very large resembling more closely the case of molecules and atoms but appearing to be very different from the case of crystalline solids or even two-dimensional systems (Figure 3.2). Among one-dimensional nanowires, carbon nanotubes exhibit remarkable electronic properties and will be discussed separately.

The electron transport properties of metallic or semiconductor nanowires prepared have been studied by measuring the current/voltage characteristics at different temperatures and show that some metal nanowires can become semiconducting as their diameters are reduced to below certain values. For semiconductor nanowires such as GaN it has been shown that they still could function properly as a semiconductor as their dimensions are decreased to several nanometers³⁵.

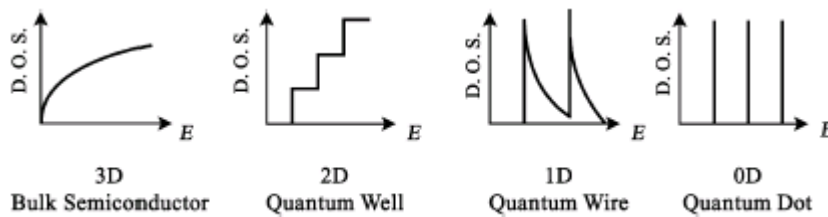


Figure 3.2. Electronic density of states for a) 3-D crystalline semiconductor, b) 2-D quantum well, c) 1-D nanowire or nanorod, c) 0-D quantum dot.

3.4. Synthesis and properties of carbon nanotubes

During the last decade, carbon nanotubes have attracted considerable attention due to their unique electronic properties^{36,37,38}. As far as theoretical calculations are concerned, a carbon nanotube is assumed to be an infinitely long cylinder with a monolayer of hexagonally ordered carbon atoms in the tube wall³⁹. One could start with a sheet of graphene (single layer of graphite) and fold it into a cylinder such that the open edges match perfectly to form a seamless structure. This operation will result in an open ended tube (Figure 3.3.). The tubes have to be closed at the both ends, which means that at some stage in

the growth process pentagons are nucleated to initiate the closure mechanism. Thus, in a general nanotube structure, on the curved surface of the tube, the hexagonal arrays of carbon atoms wind around in a helical fashion introducing helicity to the structure (Figure 3.3A).

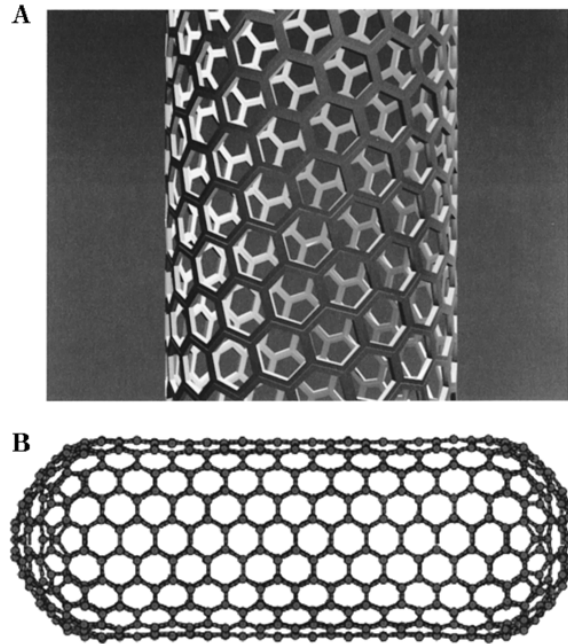


Figure 3.3. Schematic representation of a single-walled carbon nanotube.

It is convenient to specify a general carbon nanotube in terms of the tubule diameter d_t and the chiral angle θ . The chiral vector R is defined in terms of the integers (m, n) and the basis vectors a_1 and a_2 of the honeycomb lattice (Figure 3.4.). The integers (m, n) uniquely determine tube diameter and the chiral angle. In general the $(m, 0)$ nanotubes are called zigzag nanotubes, all (m, m) are called armchair and all others will be helical. This scheme of indexing the symmetry of carbon nanotubes is very important because it relates directly the diameter of individual nanotube to its helicity and expected properties. For example, calculations predict that carbon nanotubes are either semiconducting or metallic depending on their diameter and helicity³⁸. Concerning the electronic properties of carbon nanotubes it has been found by theoretical predictions that for all armchair and for all nanotubes with $m - n$ multiple of 3, the nanotubes will be metallic, otherwise they will exhibit semiconducting behavior.

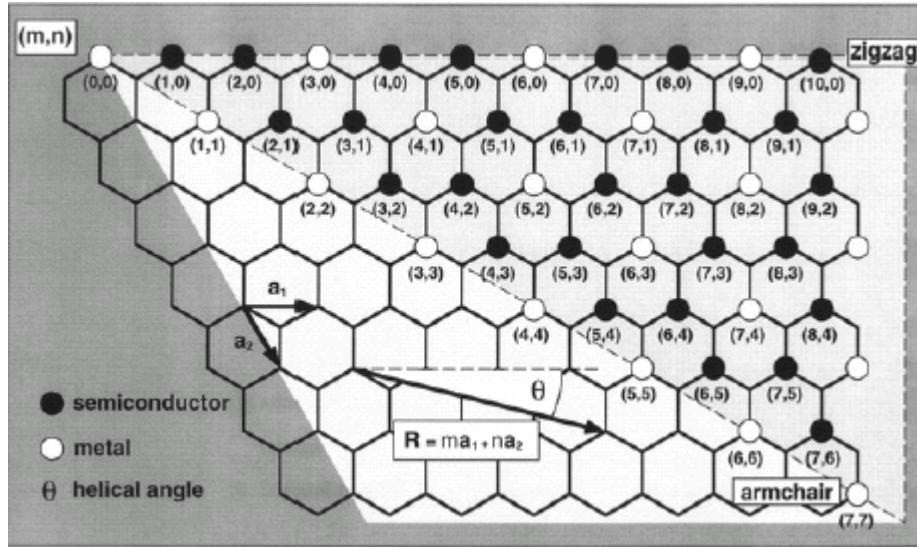


Figure 3.4. Indexing scheme that shows the folding procedure to create nanotube cylinders from planar graphene sheets by rolling in perpendicular direction to the chiral vector R ($0 \leq R \leq 30^\circ$).

It should be outlined that till now there is no evidence that the helicity of the nanotubes can be controlled systematically by the synthetic procedure used for their growth. Recently, clear images by scanning tunneling microscopy (STM) of atomically resolved structures of the nanotube surface have revealed the helicity and simultaneously gave information about the electronic properties of these structures⁴⁰. It was possible to record well-spaced and symmetric structures in the local density of states called van Hove singularities that arise, as depicted before, from the one-dimensional nature of the conduction electron states in nanotubes.

Nanotubes of carbon are synthesized in two categories – single-walled carbon nanotubes (SWNT) and multiwalled carbon nanotubes (MWNT). The latter consist of concentric cylinders placed around a hollow center, with spacing between the layers close to that in graphite. Carbon nanotubes are prepared by arc-discharge, catalytic decomposition of hydrocarbons, or laser-assisted methods, and today's synthetic strategies permit the preparation of three-dimensionally organized arrays of carbon nanotubes^{41,42,43,44,45}. Generally, all methods for the synthesis of carbon nanotubes suffer from one big

disadvantage – usually a mixture of carbon material is obtained including carbon nanoparticles, carbon rods, graphite, glassy carbon, and in many cases a mixture of SWNT and MWNT. This is true to a large extent for arc-discharge and laser ablation methods. In the laser ablation technique, a metal containing graphite sample is placed in an oven and ablated with strong laser pulses under inert atmosphere. Catalytic vapor deposition at relatively lower temperatures has also been used for the synthesis of carbon nanotubes. In general, catalytic metal nanoparticles are exposed to a medium containing gaseous hydrocarbon species. Clear evidence for the formation mechanism during this process is not available but it is believed that the size of the catalyst seed particles and their distribution controls the uniformity and size of the resulting carbon nanotubes.

Another interesting characteristic of carbon nanotubes are the vibrational modes since the spectrum varies as a function of the nanotube diameter and the number of atoms in the unit cell. The so-called radial breathing mode associated with a radial vibration of the carbon atoms is very sensitive to the tube diameter. The frequency of the radial breathing mode is independent of the integers (m,n) and is roughly inversely proportional to the tube radius.

The electronic conduction process in carbon nanotubes is unique since the radial direction of the electrons is confined in the singular plane of the graphene sheet. The conduction occurs in the metallic tubes through gapless modes as the valence and conduction bands always cross each other at the Fermi energy. In most helical nanotubes that contain large numbers of atoms in their unit cell, the one-dimensional band structure shows an opening of the gap at the Fermi level and this leads to semiconducting properties. In a MWNT, the electronic structure of the smallest inner tubes is superimposed by the outer, larger planar graphene-like tubes. This has been substantiated by experiments where the band structure obtained from individual MWNT resembles that of graphite^{46, 47}.

The topic of synthesis and characterization of carbon nanotubes is well studied and attracts enormous scientific interest reflected in more than 5000 publications to date and many reviews. Since the aim of this Thesis is not solely restricted to carbon nanotube synthesis and application, a full coverage of this field will not be given here. Nevertheless, it should be emphasized that most of the nanotechnology applications of carbon nanotubes will require a fabrication method capable of producing uniform carbon nanotubes with well-

defined and controllable properties. In addition, electronic and photonic devices such as field emission displays and data storage devices would need high density, well-ordered nanotube arrays. Certainly, the incorporation of the carbon nanotubes with their remarkable one-dimensional electronic properties in an insulating matrix can open new opportunities for investigation of isolated carbon nanotubes and for the construction of novel composite materials.

References

- ¹ Special issue of *Advanced Materials*, **2003**, 15, 5, 341 - 468.
- ² Y. Xia, P. Yang, Y. Sun, Y. Wu, B. Mayers, B. Gates, Y. Yin, F. Kim, H. Yan, *Adv. Mater.*, **2003**, 15, 353.
- ³ S. Banerjee, A. Dan, D. Chakravorty, *J. Mater. Sci.*, **2002**, 37, 4261
- ⁴ S. Ciraci, A. Buldum, I. P. Batra, *J. Phys: Condens. Matter.*, **2001**, 13, R537.
- ⁵ J. Hu, T. W. Odom, C. J. Lieber, *Acc. Chem. Res.*, **1999**, 32, 435.
- ⁶ D. Wyrwa, N. Beyer, G. Schmid, *Nano Lett.*, **2002**, 2, 419.
- ⁷ W.A. Lopes, *Phys. Rev.*, **2002**, 65, 031606
- ⁸ K. D. Hermason, S. O. Lusdon, J. P. Williams, E. W. Kaler, O. D. Velev, *Science*, **2001**, 294, 1082.
- ⁹ R. Resch, C. Baur, A. Bugacov, B. E. Keol, A. Madhukar, A. A. G. Requicha, P. Will, *Langmuir*, **1998**, 14, 6613.
- ¹⁰ A. S. Dimitrov, T. Miwa, K. Nagayama, *Langmuir*, **1999**, 15, 5257.
- ¹¹ M. Tanse, L. A. Bauer, A. Hultgren, D. M. Silevitch, L. Sun, D. H. Reich, P. C Searson, G. J. Meyer, *Nano Lett.*, **2001**, 1, 155.
- ¹² M. Trau, D. A. Saville, I. A. Aksay, *Langmuir*, **1997**, 13, 6375
- ¹³ P. Gambardella, M. Blanc, H. Brune, K. Kuhnke, K. Kern, *Phys. Rev. B*, **2000**, 61, 2254.
- ¹⁴ S. Morin, A. Lachenwitzer, O. M. Magnussen, R. J. Behm, *Phys. Rev. B*, **1999**, 83, 5066.
- ¹⁵ M. P. Zach, K. H. Ng, R. M. Penner, *Science*, **2000**, 290, 2120.
- ¹⁶ C. A. Foss, M. J. Tierney, C. R. Martin, *J. Phys. Chem.*, **1992**, 96, 9001.

- ¹⁷ T. M. Whitney, J. S. Jiang, P.C. Searson, C. L. Chien, *Science*, **1993**, 261, 1316.
- ¹⁸ C. K. Preston, M. Moskovits, *J. Phys. Chem.*, **1993**, 97, 8495.
- ¹⁹ G. Schmidt, *J. Mater. Chem.*, **2002**, 12, 1231.
- ²⁰ C. R. Martin, *Chem. Mater.*, **1996**, 8, 1739.
- ²¹ M. S. Spector, R. R. Price, J. M. Schnur, *Adv. Mater.*, **1999**, 11, 337.
- ²² E. Braun, Y. Eichen, U. Sivan, G. Ben-Yoseph, *Nature*, **1998**, 391, 775.
- ²³ Y.-Y. Yu, S. S. Chang, C.-L. Lee, C. R. C Wang, *J. Phys. Chem. B*, **1997**, 101, 6661.
- ²⁴ L. Manna, E. C. Scher, A. P. Alivisatos, *J. Am. Chem. Soc.*, 122, 12700.
- ²⁵ Y. Zhang, H. Dai, *Appl. Phys. Lett.*, **2000**, 77, 3015.
- ²⁶ P. Buffat, J.-P. Borel, *Phys. Rev.*, **1976**, 13, 2287
- ²⁷ S. Link, C. Burda, M. B. Mohamed, B. Nikoobakht, M. A. El-Sayed, *Phys. Rev.*, **2000**, 61, 6086.
- ²⁸ Y. Wu, P. Yang, *Adv. Mater.*, **2001**, 13, 520.
- ²⁹ G. Rubio-Bollinger, S. R. Bahn, N. Argrait, K. W. Jacobsen, S. Vieira. *Phys. Rev. Lett.* **2001**, 87, 026 101.
- ³⁰ M. V. Wolkin, J. Jorne, P. M. Fauchet, G. Allan, C. Delerue, *Phys. Rev. Lett.*, **1999**, 82, 197.
- ³¹ J. F. Wang, M. S. Gudixsen, X. F Duan, Y. Cui, C. M. Lieber, *Science*, **2001**, 293, 1455.
- ³² M. A. El-Sayed, *Acc. Chem. Res.*, **2001**, 34, 257.
- ³³ M. Huang, S. Mao, H. Feick, H. Yan, Y. Wu, H. Kind, E. Weber, R. Russo, P. Yang, *Science*, **2001**, 292, 1897.
- ³⁴ X. T. Zhaou, H. L Lai, H. Y. Peng, F. C. K. Au, L. S Laio, N. Wang, I Bello, C. S. Lee, S. T. Lee, *Chem. Phys. Lett.*, **2000**, 318, 58.
- ³⁵ Y. Cui, C. M. Lieber, *Science*, **2001**, 291, 851.
- ³⁶ M. S. Dresselhaus, G. Dresselhaus, M. Pimenta, *Eur. Phys. J. D*, **1999**, 9, 69.
- ³⁷ P.C. Eklund, J. M. Holden, R. A. Jishi, *Carbon*, **1995**, 33, 959.
- ³⁸ P. M. Ajayan, *Chem. Rev.*, **1999**, 99, 1787.
- ³⁹ R. A. Jishi, M. S. Verkatarmn, M. S. Dresselhaus, G. Dresselhaus, *Chem. Phys. Lett.*, **1993**, 77, 209.

- ⁴⁰ J. W.G. Wilder, L. C. Venema, A. G. Rinzler, R. E. Smalley and C. Dekker, *Nature*, **1998**, 391, 59.
- ⁴¹ S. Iijima, *Nature*, **1991**, 354, 56.
- ⁴² R. Andrews, D. Jacques, A. M. Rao, F. Derbyshire, D. Quan, X. Fan, E. C. Dickey, J. Chen, *Chem. Phys. Lett.*, **1999**, 303, 467.
- ⁴³ L.-C. Qin, X. Zhao, K. Hirahara, Y. Miyamoto, Y. Ando, S. Iijima, *Nature*, **2000**, 408, 50.
- ⁴⁴ B. Q. Wei, R. Vajtai, Y. Jung, J. Ward, R. Zhang, G. Ramanath, P. M. Ajayan *Nature*, **2002**, 416, 495.
- ⁴⁵ V. Derycke, R. Martel, J. Appenzeller, Ph. Avouris, *Nano Lett.*, **2001**, 1, 453.
- ⁴⁶ C. H. Olk, J. P. Heremans, *J. Mater. Res.*, **1994**, 9, 259.
- ⁴⁷ D.L. Carroll, Ph. Redlich, P. M. Ajayan, J.-C. Charlier, X. Blase, A. De Vita, R. Car, *Phys. Rev. Lett.*, **1997**, 78, 2811.

Chapter 4. Characterisation techniques for nanostructured materials.

- 4.1. Introduction
- 4.2. X-ray diffraction (XRD)
- 4.3. Infrared and Raman spectroscopy
- 4.4. Nitrogen-sorption measurements
- 4.5. Electron microscopy
- 4.6. Other characterization techniques
 - 4.6.1. Dynamic light scattering (DLS)
 - 4.6.2. Thermogravimetric analysis (TGA)

4.1. Introduction

Nanostructured materials are characterized by a variety of instrumental methods. No single technique is capable of providing complete characterization of a specific material. There are three main categories of physical techniques that may be used to characterize nanostructured materials; these are diffraction, microscopic, and spectroscopic techniques. In addition others, such as sorption of gases, thermal analysis, or physical property measurements, may give valuable information.

The purpose of this Chapter is to summarize different characterization techniques that have been used in this study with emphasis on the characterization methods used for thin films and nanostructured materials. It is assumed that the fundamental knowledge behind all the methods is well known.

4.2. X-ray diffraction (XRD)

An X-ray powder diffraction pattern of a crystalline substance is a set of lines, each of different intensity and position (d-spacing or Bragg angle, θ). For a given substance the line positions and intensities are fixed and characteristic and can be used as a finger print to identify that substance. The basic equation of the X-ray diffraction is the Bragg law. It is defined as:

$$n\lambda = 2d\sin\theta \quad (4.1.)$$

where λ is the wavelength of the X-rays, n is an integer number, d is the distance between the adjusted crystal planes and θ the Bragg angle. At the Bragg conditions (conditions satisfying the Bragg law), a constructive interference occurs between the reflected incoming X-ray beams, which results in an increase in the intensity called reflection.

In a common powder set up with the diffractometer (in $\theta - \theta$ geometry), the source of monochromatic X-rays (usually X-ray tube) and the detector (scintillator or semiconductor detector) will scan along θ degrees (giving a plot of intensities against $2\theta^\circ$) to record the so-called XRD pattern (Figure 4.1). Because a powder is usually randomly oriented and the various lattice planes are also presented in every possible orientation, cones of diffraction are created rather than “spots”. Nevertheless, with the usage of the diffractometer, because of the one-dimensional detection, only well resolved lines (Bragg peaks, reflections) are recorded when the Bragg conditions are fulfilled.

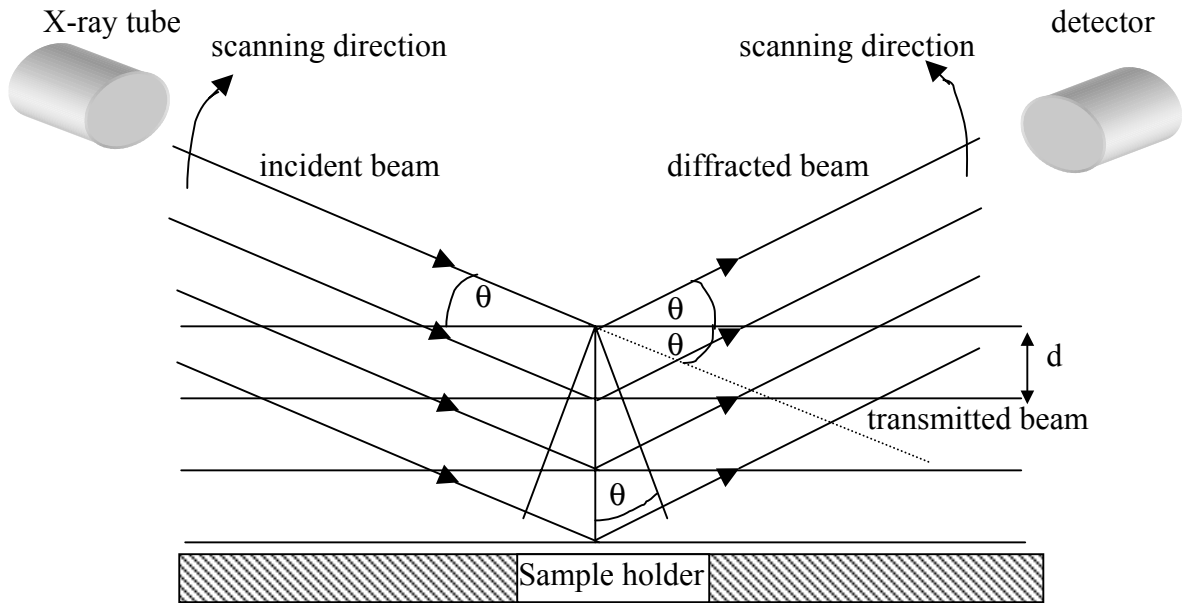


Figure 4.1. Schematic representation of the reflection XRD experiment ($\theta - \theta$ geometry).

All powder diffraction studies in the course of this work were obtained using a Scintag XDS 2000 reflection ($\theta - \theta$) diffractometer with a Cu K_α source, a stationary sample

positioned horizontally, and a solid-state, liquid-nitrogen-cooled germanium semiconductor detector. The powder XRD pattern was used to identify the structure of powdered mesoporous materials and crystalline nanostructured materials prepared in the course of this study. The XRD patterns of mesoporous thin films positioned horizontally were also measured with the same set-up, and are referred to films measured in reflection-XRD (RXRD) geometry.

The X-ray powder diffraction data may be used to calculate the average crystal size in a powder sample provided that the average diameter is less than about 200 nm. The lines in the powder diffraction pattern are of finite width; additional broadening of the diffracted X-ray beams occurs when the particle size approaches the nanometer region. The commonly accepted equation to calculate particle sizes from the X-ray diffraction data is Scherrer's formula:

$$T = 0.9\lambda/B\cos\theta_B \quad (4.2.)$$

T is the thickness of the crystal in Angstrom, λ the X-ray wavelength, θ_B the Bragg angle. The line broadening, B, is measured from the extra peak width at the half peak height and is obtained from the formula:

$$B^2 = B_m^2 - B_s^2 \quad (4.3)$$

where B_m is the measured peak width in radians at the half peak height and B_s is the corresponding width of the peak of a standard material of high crystallinity and micron crystal size. The lower limit of detection with XRD occurs when the peaks become so broad that they disappear in the background radiation.

It is necessary to make an important comment about the evaluation of the diffraction data from the RXRD experiment for thin mesoporous films. The RXRD geometry in many cases is not useful to directly identify the mesophase structure because only the structural information in the direction perpendicular to the film plane (in the direction of the specularly reflected X-ray beam, see below) can be obtained. For example, in numerous publications it has been shown that the two-dimensional hexagonally ordered mesoporous films with channels aligned parallel to the film surface show only two reflections (first and second order

peaks of the 100 planes) instead of three reflections typical for the hexagonally ordered MCM-41 or SBA-15 materials (see Chapter 2.2. and references therein). The absence of the (110) reflection in the RXRD comes from the orientational alignment of the mesoporous channels¹. Only the (100) face is parallel to the surface and can therefore be recorded in reflection geometry, and the (110) face in this case does not contribute to the observed diffraction pattern (see Figure 4.2b). The (110) reflection could be observed if a different arrangement of the mesoporous channels in respect to the substrate surface is obtained (see Figure 4.2c). Full disappearance of any structural information in the RXRD experiment would correspond to complete alignment of the mesoporous channels perpendicular to the substrate surface (see Figure 4.2a). Of course, in many cases the lack of structural information cannot be directly accepted as proof for the mesochannel-alignment; other reasons, such as distortion of the mesophase structure or complete loss of mesophase order, are also possible. Similar problems hinder the direct identification of the mesophase structure for other known structural configurations. For example, the three-dimensional hexagonal (similar to SBA-2 material, see Chapter 2.2.) structure or several different three-dimensional cubic mesophase structures could be indexed because usually only one or several (not well-resolved) reflections were obtained in the RXRD geometry².

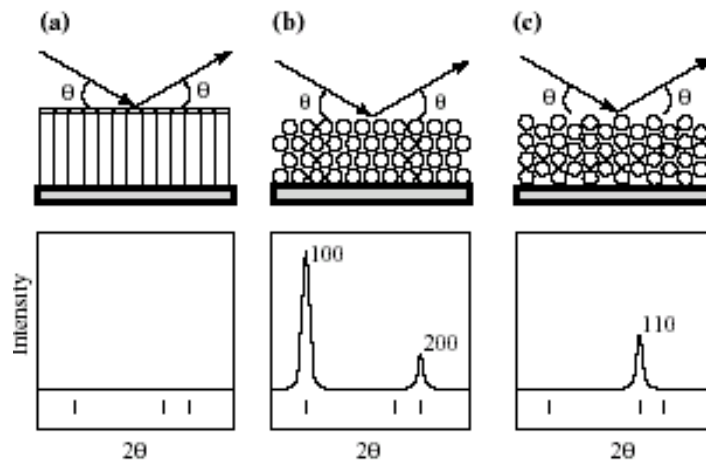


Figure 4.2. Schematic representation of the alignment of the channels in the two-dimensional hexagonally ordered ($p6m$) mesoporous film with the corresponding RXRD patterns¹.

Summarizing, the need to use diffraction measurements in other geometries (for example, grazing-incidence) instead of conventional reflection-mode X-ray diffraction to determine the mesophase structure of the films is important because in oriented films all the crystallographic planes may not be oriented in a way that the diffracted beam is detectable in the RXRD experiment. In this study, grazing-incident diffraction (GID) with 2D detection (CCD camera) was used to identify the mesophase structure and to determine the orientation of the mesoporous channel system.

Grazing-incidence diffraction (GID) is a scattering geometry combining the Bragg condition with the conditions for X-ray total external reflection from surfaces when the incident angle of the X-rays is small enough (typically $0.05 - 3^\circ$, depending on the substrate electron density and the X-ray energy), close to the so called critical angle α_c . At this point the surface is not entirely invisible to the X-rays, but only an evanescent wave penetrates and scatters from it³. Let some set of crystallographic planes be oriented perpendicular to the substrate surface and fulfill the Bragg condition (forming a Bragg angle θ between the plane of the incident beam and the crystallographic planes), thus preserving the small grazing-exit angle α_f ; this will generate a diffraction wave in the plane of the substrate. These conditions provide superior characteristics of GID as compared to other diffraction schemes in the studies of thin surface layers^{4,5,6}. In order to perform grazing-incidence diffraction, a highly intense, parallel, and stable X-ray beam is desirable that can be obtained only by using Synchrotron radiation.

The geometry of the GID experiment with 2D detection is shown in Figure 4.3. The 6-circle diffractometer at beam-line ID01 at the ESRF (www.esrf.fr) in Grenoble, France, was used for all GID experiments. The X-ray beam is focused on the film surface with the help of the single crystal monochromator at an incident-angle of $\alpha_i = 0.3$ degrees, which is higher than the critical angle for silica ($\alpha_c = 0.1$), where the total external reflection is observed. The structural information as a function of the film thickness depends on the penetration depth of the X-rays at constant incidence angle. It was calculated that at this incident angle the whole film thickness was scanned. In forward direction the specularly reflected beam is observed at the grazing exit angle α_f , together with the diffracted wave (out

of plane diffraction) coming from the planes that are parallel to the substrate surface (as in the RXRD experiment where the specularly reflected and diffracted beams are overlapping).

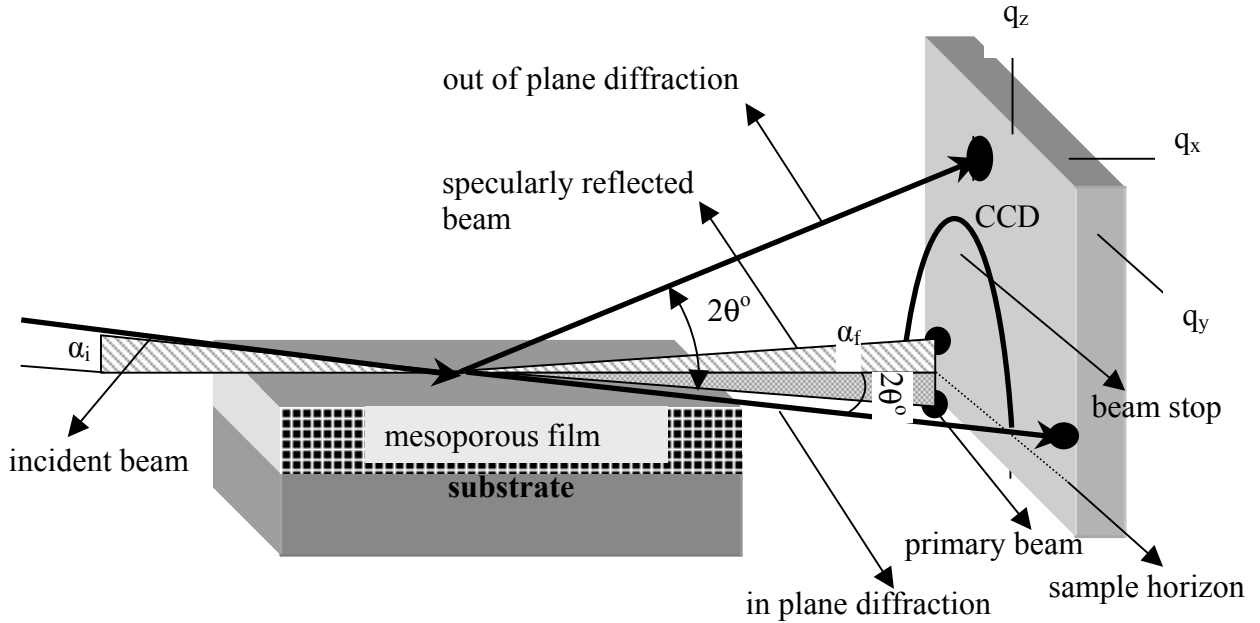


Figure 4.3. Schematic representation of the scattering geometry of GID in real space.

As explained earlier at these incident angles it is possible to have total external reflection and to obtain in-plane diffraction from planes oriented perpendicular to the substrate surface (grazing-incident diffraction). With the help of a 2D detector (CCD camera) set perpendicular to the incident beam and the grazing incident geometry, it was possible to obtain structural information from both the q_z and q_y components of the structural vector Q at the same time. Thus, correct indexing of the mesophase structure and determination of the orientation of the mesoporous system is possible. The distance between the sample and the recording plane was 650 mm. The resolution of the measurement is given by the number of pixels of the CCD camera per degree, which was 0.005 degree per pixel. Alignment of the X-ray beam to the sample surface was performed before every measurement. The specular reflectivity was masked with a circular beam stop to avoid saturation of the detector. The positions of the Bragg spots were calculated from the position of the primary beam in the CCD camera taking into account that one pixel corresponds to 0.005 2θ degrees.

4.3. Infrared and Raman spectroscopy

FT-IR and FT-Raman spectroscopies can be used to investigate solid materials by excitation of the vibrational modes, involving pairs or groups of bonded atoms, to higher energy states by absorption of radiation of appropriate frequency. In order to absorb infrared radiation, a molecule must undergo a net change in dipole moment as a consequence of its vibration or rotation, while in Raman spectroscopy the molecules undergo a change in the bond polarizability. In Raman spectroscopy the sample is illuminated with monochromatic light, usually generated by a laser. Two types of scattered light are produced from the sample: elastically scattered light (Rayleigh scattering) and Raman-scattered light (inelastic scattering), which is much less intense than the incident light.

IR and Raman spectra of solids are complex with a large number of peaks, each corresponding to particular vibrational transitions. Both techniques are much used for the straightforward identification of specific functional groups, especially in organic molecules. In inorganic solids, species, such as hydroxyl groups, trapped water, or grafted molecular functionalities, can be successfully studied. Furthermore, solid state spectroscopy has been effectively used for the determination of the degree of crystallisation, geometry of the dominant structural species in the crystalline inorganic solids, small-scale defects, and the degree of disorder^{7,8}.

Most often FT-IR and Raman spectroscopies are used to investigate powdered materials pressed in pellets in transmission and backscattering geometry, respectively. An alternative set-up that allows examination of thin layers of organic or inorganic matter on metal surfaces was developed, i.e., reflection-adsorption IR spectroscopy (RA-IR)⁹. The application of this technique for the characterization of the surface modifications with molecular functionalities of the thin mesoporous films is presented in this Thesis. Figure 4.4 shows the geometry of the reflection-absorption FT-IR experiment. Infrared (IR) radiation is directed onto the sample and reflected from an underlying reflective surface. The signal is modulated by the mesoporous film where absorption of the IR radiation occurs and further reflected from the underlying surface. If the reflection layer is a noble metal, only those vibrations whose dipole moments lie perpendicular to the reflection surface can be observed. This is because the incident and reflected p-polarised components of the radiation

superimpose constructively (add together), enhancing the signal, whereas the s-polarised components cancel each other out, (as they undergo a phase change on reflection from the reflection surface). This technique was successfully applied to study monomolecular layers and thin films up to 2 μm thickness on gold surfaces. As a reflection surface in this study, sputtered gold or polished silicon were used with incident angles of 75° and 45° to the surface normal, respectively. In the latter case in the region of about 1100 cm^{-1} an artefact appeared due to the absorption of the signal on the thin oxidized silicon layer.

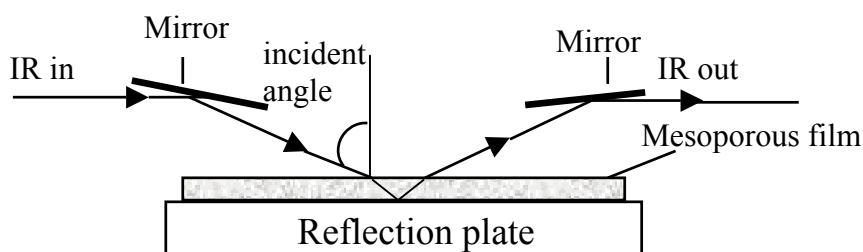


Figure 4.4. Schematic representation of the geometry of the reflection-absorption FT-IR measurement.

4.4. Nitrogen-sorption measurements

Nitrogen sorption is commonly used in the characterization of porous solids, allowing one to determine the specific surface area, pore volume, and pore size distribution¹⁰. With the discovery of the ordered mesoporous materials, the theoretical models for estimation of the aforementioned parameters have been successfully proven¹¹. A result of the gas sorption measurement is a plot of the volume of gas absorbed/desorbed vs relative pressure P/P_0 (P is the absolute pressure, P_0 is the saturation vapor pressure) at constant temperature, called sorption isotherm. Nitrogen-sorption instruments present an important characterization tool for many laboratories dealing with nanoporous materials.

Experimental gas-adsorption isotherms usually fall into six categories according to the IUPAC classification¹² (Figure 4.5.A). The most important for gas absorption in mesoporous solids are Type IV, V, and IV_c isotherms. The gas absorption proceeds via multiplayer adsorption followed by capillary condensation (steep steps in the isotherms).

Capillary condensation and capillary evaporation often do not take place at the same relative pressures, which leads to the appearance of hysteresis loops. This phenomenon is usually attributed to thermodynamic or pore connectivity problems; the latter may be more prominent^{10, 13}.

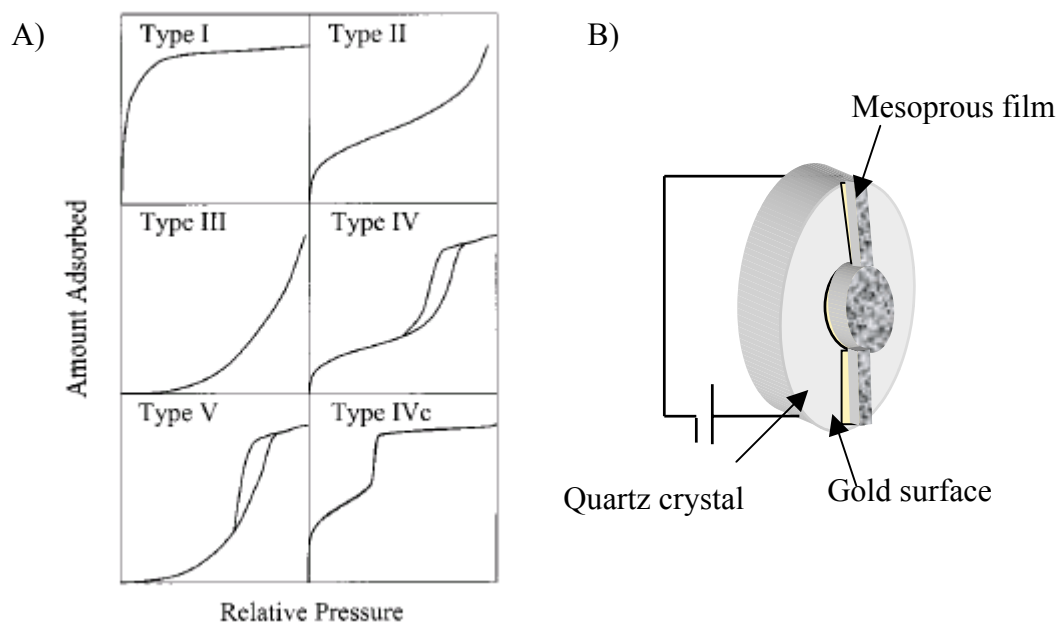


Figure 4.5. (A) Classification of gas adsorption isotherms and (B) schematic representation of the QCM device with a mesoporous film.

The thermodynamic effects are related to the metastability of adsorption or desorption (or both) branches of the isotherm. Namely, the capillary condensation or evaporation may be delayed and take place at higher or lower pressures, respectively, in comparison to the pressure of coexistence between the gas-like or liquid-like phases in the pore. Pore-connectivity (network) effects play an important role when, for example, larger pores have access to the surrounding only through narrower pores, the former cannot be emptied at the relative pressures corresponding to their capillary evaporation since the latter are still filled with the condensed adsorbate. So the larger pores may actually be emptied at a relative pressure corresponding to the capillary evaporation in the smaller pores (or at the relative pressure corresponding to the lower limit of adsorption-desorption). However, it was

confirmed many times that capillary condensation/evaporation can also be reversible as in Type IV_c isotherms¹⁴.

The adsorption isotherm may be used to calculate the surface area of the sample. The procedure known as the BET model was introduced by Brunauer, Emmett, and Teller¹⁰. It is based on the evaluation of the monolayer capacity (the number of the absorbed molecules in the monolayer on the surface of a material). The monolayer capacity is multiplied by the cross-sectional area of the absorbed molecules in the monolayer formed on a given surface. The derivation of the BET model is based on the Langmuir equation relating the number of molecules adsorbing on the surface with the number of molecules evaporating (desorbing) from the sample, involving several assumptions, such as a flat surface, equivalence of all the adsorption sites, and the absence of lateral interactions between absorbed molecules. In the case of adsorption on real solids, these assumptions often do not hold. Therefore caution must be exercised regarding the interpretation of the specific surface area of the solids derived from the BET model. Despite all of these issues, the BET model is currently a standard method for the specific surface area evaluation, and relative comparisons provide valuable information.

For the evaluation of the pore size distribution, a number of models have been suggested that are usually based on the Kelvin equation. Assuming that the vapor side of the meniscus formed in a pore behaves as an ideal gas at constant temperature, the general form of the Kelvin equation for the determination of the radius of the hemispherical meniscus may be derived

$$\ln[P/P_0] = -2\sigma VL / R_k RT \quad (4.4.)$$

where VL is the molar volume, R is the gas constant, T is the temperature, R_k is Kelvin radius (the mean radius of curvature of the meniscus at which capillary condensation occurs). The most commonly used model to calculate pore size distribution that is often integrated in the sorption apparatus software is the BJH model (Barett, Joyner, Halenda method)¹⁵. It has recently been confirmed using MCM-41 with approximately cylindrical pore geometry that this model reflects the actual nature of adsorption in mesopores¹⁶. More theory on the sorption of gases in porous hosts can be found elsewhere^{10, 17}.

In this thesis, the nitrogen-sorption measurements on powdered mesoporous materials were performed with a NOVA 4000e Surface area & Pore Size Analyser after evacuation of the samples at 120°C. Unfortunately, nitrogen-sorption experiments on thin films are very difficult or even impossible to obtain with this technique because of the small amount of the adsorbent (less than 0.1 $\mu\text{g}/\text{cm}^2$ of the film surface). Here, an alternative technique to estimate the amount of the sorbed gas that relies on the high gravimetric sensitivity of the quartz crystal microbalance (QCM) is described.

The QCM detection is a variant of acoustic wave microsensors that is capable of ultrasensitive mass measurements. Under favorable conditions, a typical QCM can measure a mass change of 1-10 ng/cm^2 . The QCM oscillates in a mechanically resonant shear mode under the influence of a high-frequency AC electric field that is applied across the thickness of the crystal. The central portions of the top and bottom sides of the crystal are coated with thin films of gold or other metals that are typically of disk shape. The mass sensitivity of the QCM originates from the relationship between the oscillation frequency on the total mass of the crystal and the adlayers of material residing on the metal-coated crystal faces, the Sauerbrey equation, as shown below.

$$\Delta f = -2f_0^2 \Delta m / [A \sqrt{\mu\rho}] \quad (4.5.)$$

where f_0 is the resonant frequency of the fundamental mode of the crystal, A is the area of the gold disk coated onto the crystal, ρ is the density of the crystal ($= 2.684 \text{ g}/\text{cm}^3$), and μ is the shear modulus of quartz ($= 2.947 \times 10^{11} \text{ g}/\text{cm}\cdot\text{s}^2$). Using a crystal with a 10 MHz fundamental frequency (as used in our measurements), a net change of 1 Hz corresponds to 26.4 ng of materials adsorbed or desorbed onto a crystal surface of 1 cm^2 .

In a typical measurement, the gold surface of the QCMs modified with linking molecules (see Chapter 6.2.) were covered with mesoporous film (Figure 4.5B) and after calcination the mass of the film was measured by recording the frequency of the QCM before and after deposition of the film. The mesoporous film was dehydrated in flowing helium at 120°C for 24 h and the measurement chamber was cooled to liquid-nitrogen temperature. A gas flow of water-free nitrogen in helium was conducted by a computer-controlled gas-flow

system (MKS Instruments) in the range of 0 – 95 %. Using digital mass-flow controllers and a calibrated gas-flow system it was possible to finely control the partial pressure of the sorbed gas (N₂) at every sorption step. The nitrogen adsorption/desorption isotherm was obtained by measuring the frequency of the QCM at every adsorption/desorption step (every partial pressure of N₂) and recalculating the amount of the nitrogen adsorbed by using the Sauerbrey equation.

4.5. Electron microscopy

Exceeding the resolution limits given by the wavelength of light that restricted the applicability of optical microscopy to objects smaller than about 1-2 μm, electron microscopy offers extremely versatile structural information over a broad range of magnifications using a beam of accelerated electrons. Electrons emitted from a filament (electron gun) are accelerated through high voltage. Their wavelength is related to the accelerating voltage, V by the equation:

$$\lambda = h(2meV)^{-1/2} \quad (4.6.)$$

where m and e are the mass and charge of the electron. In order to be able to focus the electron beam, electromagnetic lenses are used. For example, the condenser lens in the TEM is used to control the size and the angular spread of the electron beam that is incident on the sample.

Electron microscopy is used basically in reflection (SEM) or transmission (TEM) mode. The first one relies on the reflected (or backscattered) electrons that are used to build up a three-dimensional image of the sample surface giving information on the sample texture, topography, and surface features. This type of electron microscopy covers the magnification range between the lower resolution limit of optical microscopy (~1 μm) and the upper practical limit of TEM. At the other extreme, high-resolution transmission electron microscopy (HREM) is capable of giving information on an atomic scale, by direct lattice imaging. The TEM gives information on the crystallographic arrangement of atoms in the specimen and their degree of order, detection of atomic-scale defects in areas a few nanometers in diameter, and indexing crystalline materials. In principle, the resolution in the

TEM is given by the ability to accelerate electrons. The higher the voltage to accelerate electrons the greater the resolving power of the TEM. Nevertheless, the practical resolving limit is governed by the imperfection of the lenses and for the current microscopes is in the of range 0.1 - 0.2 nm (Figure 4.6). The contrast in electron microscopy is given by the relative difference in the observed intensities between atoms with different scattering behavior. For example, heavy elements are good electron scatterers and appear darker in the TEM bright-field image (image taken when the directly transmitted electron beam is recorded).

TEM offers another possibility when the diffracted rather than transmitted beam is selected to be recorded. The electron wavelengths are much smaller than the X-ray wavelengths used in typical diffraction experiments, as a result the diffracted beams are concentrated into a narrow cone centered on the non-diffracted beam.

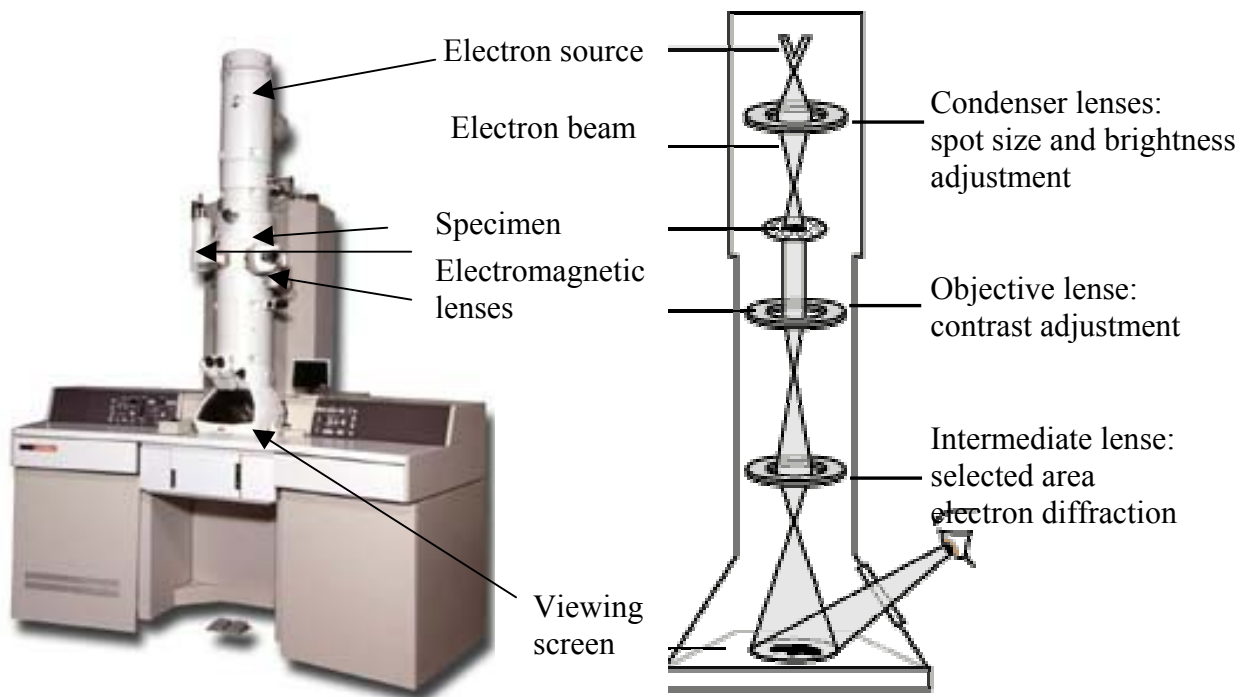


Figure 4.6. Schematic representation of the basic components of a TEM.

The region of illumination that is chosen for diffraction can be selected by appropriate lenses giving rise to the so-called selected-area diffraction that is very important for polycrystalline materials.

Some SEM or TEM instruments have a very valuable additional feature providing the elemental analysis of sample composition. It takes advantage of the fact that when a sample is placed in the microscope and bombarded with high energy electrons, electronic transitions can occur that result in the generation of X-rays. These X-rays are characteristic emission spectra of the elements present in the sample. By scanning the energy (energy dispersive, ED) of the emitted X-rays it is possible to identify the elements. If a suitable calibration is carried out, a quantitative elemental analysis can be performed. With this technique, only elements heavier than including sodium can be detected. In this Thesis, SEM investigations were performed with the Philips XL 40 microscope and with the field emission JEOL, JSM 65007 microscope. The TEM images were obtained with the JEM 2010 transmission electron microscope operating at 200 kV. The elemental analysis was performed with the JSM 65007, field emission SEM equipped with an Oxford EDX detector.

4.6. Other characterization techniques

4.6.1. Dynamic light scattering (DLS)

In the DLS measurement, the rate of the intensity fluctuations in the light caused by the random movement (Brownian motion) of particles are detected after illuminating colloidal particles in liquid with known viscosity. An important feature of Brownian motion for DLS is that small particles move quickly and large particles move more slowly. The relationship between the size of the particle and its speed due to the Brownian motion is defined in the Stokes-Einstein equation.

In a real measurement, this will mean that the rate of the intensity fluctuations will be low if large particles are measured and high if bigger particles are detected. By extracting different decay rates, distribution of particle classes are formed (autocorrelation function). A typical size distribution graph shows on the X-axis a distribution of size classes and on the Y-axis the intensity of the scattered light.

4.6.2. Thermogravimetric analysis (TGA)

Thermogravimetry is a technique for measuring the change in weight of a substance as a function of temperature or time. The sample is usually heated at a constant rate and has a constant weight until it begins to decompose at a certain temperature. The difference in the weights and the slopes of the decomposition steps are characteristic for the decomposition process and can be used for quantitative calculations of compositional changes.

References

- ¹ H. W. Hillhouse, J. W. van Engmond, M. Tsapatsis, J. C. Hanson, J. Z. Larese, *Micropor. Mesopor. Mater.*, **2001**, 44-45, 639.
- ² S. Besson, T. Gacoin, C. Jacquiod, C. Ricolleau, D. Babonneau, J.-P. Boilot, *J. Mater. Chem.*, **2000**, 10, 1331.
- ³ P. Dutta, *Curr. Sci.* **2000**, 78, 1478.
- ⁴ T. H. Metzger, I. Kegel, R. Paniago, A. Lorke, J. Peisl, J. Schulze, I. Eisele, P. Schittenhelm, G. Abstreiter, *Thin Solid Films*, **1998**, 336, 1.
- ⁵ T. H. Metzger, S. Mintova, T. Bein, *Micropor. Mesopor. Mater.*, **2001**, 43, 191.
- ⁶ N. Petkov, S. Mintova, B. Jean, T. H. Metzger, T. Bein, *Chem. Mater.*, **2003**, 15, 2240.
- ⁷ S.K. Sharma, J.F. Mammone, M.F. Nicol, *Nature*, **1981**, 292, 140.
- ⁸ S. Mintova, B. Mihailova, V. Valtchev and L. Konstantinov, *J. Chem. Soc., Chem. Commun.*, **1994**, 1791.
- ⁹ T. Michael, *Annual Review of Physical Chemistry* **2000**, 51, 381.
- ¹⁰ F. Rouquerol, J. Rouquerol, K. Sing, *Adsorption by Powders and Porous Solids*; Academic Press: San Diego, **1999**.
- ¹¹ M: Kruk and M. Jaroniec, *Chem. Mater.*, **2001**, 13, 3169.
- ¹² K. S. W. Sing, D. H. Everett, R. A. W. Haul, L. Moscou, R. A. Pierotti, J. Rouquerol, T. Siemieniewska, *Pure Appl. Chem.*, **1985**, 57, 603.
- ¹³ P. C. Ball, R. Evans, *Langmuir*, **1989**, 5, 714.

¹⁴ O. Franke, G. Schulz-Ekloff, J. Ratousky, J. Starek, A. Zukal, *J. Chem. Soc., Chem. Commun.*, **1993**, 724.

¹⁵ E. P Barrett, L. G. Joyner, P. P. Halenda, *J. Am. Chem. Soc.*, **1951**, 73, 373.

¹⁶ M. Kurk, M. Jaroniec, *Chem. Mater.*, **2000**, 12, 222.

¹⁷ M. Jaroniec and R. Madey, *Physical Adsorption on Heterogeneous Solids*, Elsevier, Amsterdam, **1988**.

Chapter 5. Synthesis and characterization of mesoporous powders with different morphologies.

5.1. Introduction

5.2. Experimental

5.2.1. Synthesis of MCM-48 spheres

5.2.2. Synthesis of SBA-15 rods

5.2.3. Synthesis of mesostructured monoliths

5.2.4. Calcination procedures

5.2.5 Characterization

5.3. Results and Discussion

5.3.1. Mesophase structure and thermal stability – XRD, FT-IR, and TG studies

5.3.2. Sorption properties and surface morphology – N₂ sorption, TEM, SEM, and DLS studies

5.4. Conclusions and perspectives

5.1. Introduction

A general introduction to the periodic mesoporous materials was given in Chapter 2. Although all ordered mesoporous materials prepared as powders are relatively well studied and characterized, there are still distinct differences in their bulk synthesis, structure, and surface chemistry that are reflected in their chemical behavior, thermal stability, surface properties, and morphology. The goal of this Chapter is to present synthetic methods for the preparation of two well-known powdered mesoporous materials, such as MCM-48 and SBA-15, with emphasis on their surface morphology and thermal stability, and to use different physico-chemical methods to characterize those solids. It was intended to gain basic knowledge of the physico-chemical characteristics of the mesoporous solids and to access differences in their bulk and surface properties that can be essential for further functionalization and modification. Bridging powder mesoporous materials to mesoporous films, mesostructured monoliths have also been prepared and their characterization is presented in this Chapter.

The synthesis of MCM-48 materials has been a matter of debate for some time. Essentially, it utilizes the same synthetic conditions as for the hexagonal member of the MCM-family of mesoporous solids, basic media and cationic surfactant under room or elevated temperatures. Unfortunately, sometimes it is just “synthetic luck” that one is able to observe this phase (see Chapter 2.2.1.). Various synthesis routes to MCM-48 mesophase were developed in order to overcome those synthetic shortcomings^{1,2,3,4,5}. It has been shown that the MCM-48 phase can be obtained as an intermediate in the process of transformation from a hexagonally-ordered or disordered (spaghetti-like) silica mesophase to a more thermodynamically favorable lamellar mesophase. Those difficulties in the synthesis of MCM-48 material motivate the establishment of a reliable preparation procedure for MCM-48 material. Furthermore, MCM-48 solids prepared as uniform spheres are intriguing candidates for adsorbents in separation techniques, e.g., column chromatography, or as a catalyst supports⁶. It is believed that due to its interwoven and branched pore structure (see Chapter 2.2.1), which provides more facile mass transfer than in the one-dimensional hexagonal structure of MCM-41 material, the catalytic and separation applications would be facilitated.

Here, a modification of the synthetic method for the preparation of MCM-48 spheres⁷ is presented, aiming to find optimal synthesis conditions for high quality (best mesostructural order) of the MCM-48 solid, high reliability of the synthetic procedure, and spherical particle morphology with a sharp particle-size distribution.

Mesoporous materials templated by nonionic amphiphilic surfactants, such as di- or tri-block copolymers, have attracted considerable attention during the last few years because of their structural properties that can be easily tuned by adjusting the molecular weight of the copolymer, hydrophobic to hydrophilic molar ratios of the copolymer blocks and copolymer molecular architecture. The discovery of the SBA-type materials templated by tri-block copolymers led to a new class of acidic materials (materials synthesized through acid-catalyzed hydrolysis-condensation of TEOS) with remarkably increased pore sizes and thermal properties (see Chapter 2.2.1. and references therein). The SBA-15 material with its one-dimensional hexagonally ordered channel structure provides an ideal host system for the incorporation of nanometer-sized wires and tubes (see Chapter 3.1.1).

Here, the preparation of SBA-15 mesoporous rods with channels oriented parallel to the long axis of the rod is presented⁸. The aim was to investigate the thermal stability of this material and to find a thermal procedure for the stabilization of the mesoporous host that makes the material suitable for high-temperature manipulations, e.g., growth of carbon nanotubes by catalytic decomposition of hydrocarbons at 700 °C or by pyrolysis of hydrocarbons at 850 °C (see Chapters 7 and 8).

Mesoporous free-standing monoliths are host materials for optical devices and other potential applications⁹. Monolithic mesoporous silica has been prepared through complete removal of the residual solvent of silica/surfactant containing sols. The synthesis procedure adopted in this work for the preparation of mesoporous monoliths uses similar conditions as those used for deposition of thin mesoporous films by the EISA method (see Chapter 2.2.4.) and therefore the obtained powder material is considered to have comparable physico-chemical properties as the mesoporous films.

5.2. Experimental

5.2.1. Synthesis of MCM-48 spheres

The preparation of MCM-48 spheres employs a synthetic approach that is based on a Stöber synthesis of non-porous silica spheres¹⁰ combined with the room-temperature synthesis of mesoporous materials¹¹. In a typical synthesis batch 0.217 g of cetyltrimethylammonium bromide (CTABr – Aldrich) was dissolved in 30 mL of double distilled water and 12.5 mL of technical ethanol (98%), and 3 mL of 26 wt% aqueous ammonia was added to the surfactant solution. The solution was stirred (250 rpm) for 5 min, and 0.45 g of tetraethoxy orthosilicate (TEOS - Aldrich) was added at one time. Finally the gel was stirred (200 rpm) for 5 h at room temperature and the product was recovered by centrifugation. Dry mesoporous material was obtained by freeze drying. In order to investigate the influence of the silica to surfactant ratio on the final mesophase structure, different gel compositions were prepared. The final molar ratios of the gels are shown in Table 5.1.

Table 5.1. Molar ratio of the synthesis gels used for the preparation for MCM-48.

Sample	TEOS	CTABr	EtOH	NH ₃	H ₂ O
MCM-48-1	1	0.1	54	12.5	410
MCM-48-2	1	0.13	54	12.5	410
MCM-48-3	1	0.2	54	12.5	410
MCM-48-4	1	0.4	54	12.5	410

5.2.2. Synthesis of SBA-15 rods

Mesoporous SBA-15 rods were prepared according to the methods described in the literature⁸. In a typical synthesis 2.0 g of PEO-PPO-PEO Pluronic 123 triblock copolymer (BASF) was dissolved under stirring in 30 g of 4 M HCl and 45.0 g water, followed by addition of 3.1 g tetramethoxy silane (TMOS - Aldrich). This mixture was homogenized and stirred at 40 °C for 20 h and then kept at 100 °C for an additional 24 h without stirring. The final product was recovered by filtration and dried at room temperature without washing.

5.2.3. Synthesis of mesostructured monoliths

Clear precursor solutions were prepared by addition of ethanol solutions of PEO-PPO-PEO triblock copolymer (Pluronic 123 - BASF) or ethanol solutions of CTABr to polymeric silica sols in a two step process. First acid-hydrolyzed silica was prepared by mixing of 2.08 g TEOS (Aldrich), 3 g 0.2 M HCl, 1.8 g H₂O, and 5 mL EtOH at room temperature and heated at 60°C for 1 h. For the preparation of MM1 solution, 15 mL of 5% Pluronic 123 were added to the silica solution and diluted with 10 mL EtOH. Similarly, 0.682 g of CTABr were dissolved in 25 mL EtOH and added to the prehydrolyzed silica solution (MM2). The molar ratios of the solutions that were used to prepare monoliths are:

MM1: 1 TEOS: 0.013 Pluronic 123: 0.06 HCl: 48.8 EtOH: 26.6 H₂O.

MM2: 1 TEOS: 0.18 CTABr: 0.06 HCl: 48.8 EtOH: 26.6 H₂O.

Mesostructured monoliths were prepared by slow evaporation of the solvent in a Teflon holder or glass petri-dishes at room temperature for 24 h. The samples were calcined following the procedure described in Figure 5.1B.

5.2.4. Calcination procedures

In order to investigate the thermal stability of the mesoporous powder materials, the template removal was done following four different calcination procedures shown schematically in Figure 5.1.

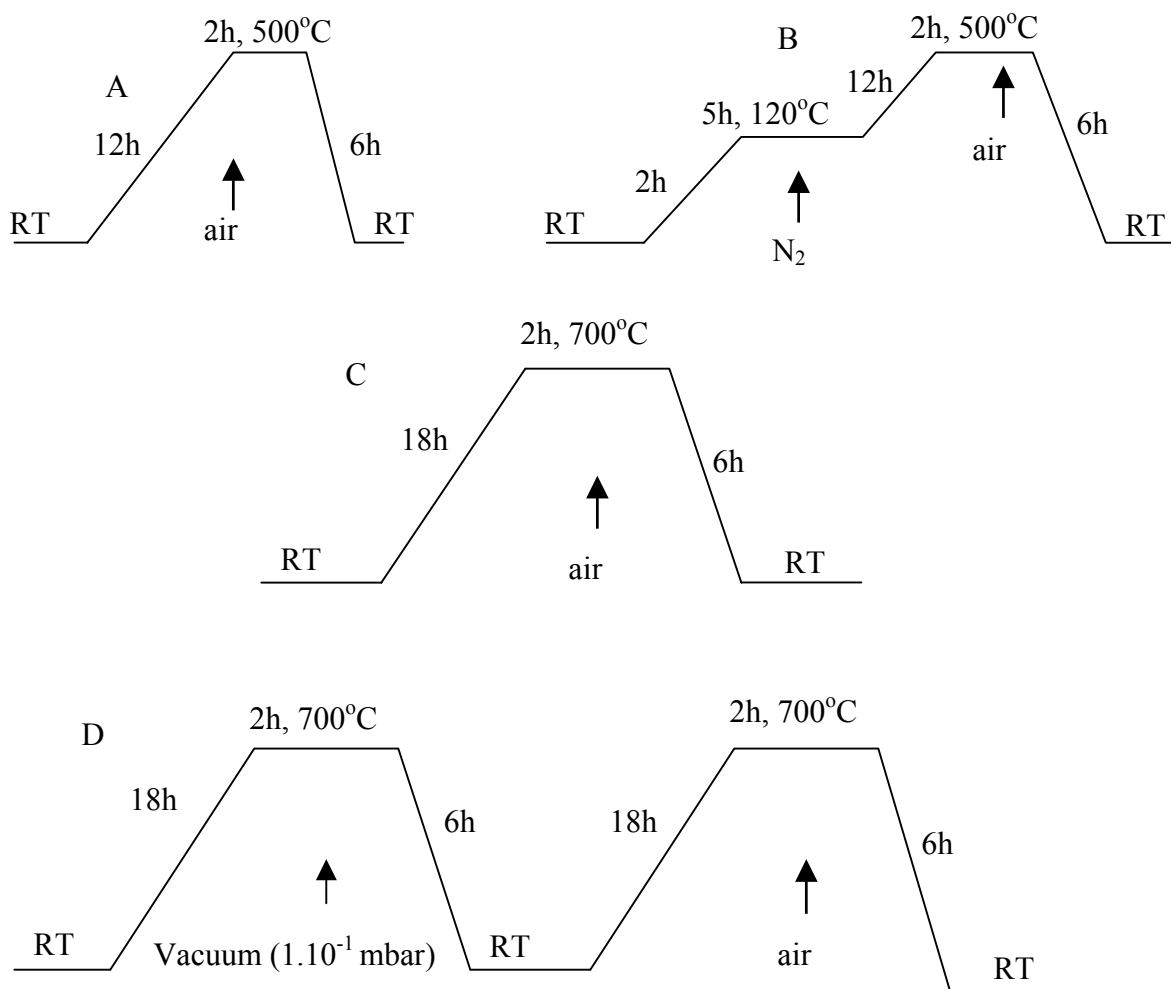


Figure 5.1. Schematic representation of the calcination procedures used in the study.

5.2.5. Characterization

The mesophase structure of all the samples was determined by powder X-ray diffraction with a Scintag XDS 2000 instrument (CuK_α radiation). TEM images of the mesoporous solids were obtained with a JEM 2010 TEM operating at 200 kV. Nitrogen adsorption-desorption isotherms of the mesoporous solids were measured with a NOVA 4000e Surface area & Pore Size Analyser after evacuation of the samples at 120 °C. The calcination process was followed by FT-IR spectroscopy with Bruker Equinox 55 - 106v/S spectrometer. The powder was molded in KBr-supported disks and measured in transmission mode. Thermogravimetric analysis of the as-prepared samples was performed with a thermal analyzer (DuPont Instruments – 951 TA). The surface morphology of the mesoporous materials was determined with scanning electron microscopy (Philips XL 40).

5.3. Results and discussion

5.3.1. Mesophase structure and thermal stability - XRD, FT-IR, and TG studies

Figure 5.2 shows the XRD patterns of the mesoporous material prepared from different synthesis gels as depicted in Table 5.1. The XRD pattern of the mesoporous material prepared using synthesis gel MCM-48-1 (Figure 5.2.a) shows one broad reflection at $2.42^\circ 2\theta$ with relatively small intensity that cannot be assigned to any particular type of ordered mesophase structure. Usually the broadening of the XRD reflections in the pattern of the mesoporous materials is attributed to the decreased mesostructural order and comes from the scattering of the micelles that have characteristic dimensions but are not ordered in any known liquid-crystal mesophase structure. It is usually accepted to call this type of mesophase structure spaghetti- or worm-like mesophase structure. The XRD pattern that corresponds to the material obtained from the MCM-48-2 synthesis gel (Figure 5.2.b) shows two reflections at 2.34° and $2.72^\circ 2\theta$ that are indexed as (211) and (220) reflections of the cubic ($Ia3d$) mesophase structure. The expected higher order reflections appear as an unresolved increase in the diffraction intensity, which is an indication of low quality MCM-48 material with a short range of mesoporous order. The sample prepared from the MCM-48-3 synthesis gel shows six distinct reflections at 2.42, 2.82, 3.68, 3.94, 4.4 and 4.6 degrees 2θ that are indexed as (211), (220), (321), (400), (420) and (332) reflections of the

cubic ($Ia3d$) symmetry of the MCM-48 structure³. The appearances of well-resolved higher order reflections indicate high-quality MCM-48 material with long range mesophase order. The product obtained after synthesis using MCM-48-4 gel shows an XRD pattern that possesses several reflections at 4.42, 2.88, 4.38, 4.6 and 5.74 degrees 2θ that come from a mixture of two phases, MCM-48 and lamellar mesophase (Figure 5.2.d)¹. A strong indication for this interpretation is the superposition of the (220) reflection of the MCM-48 phase with the (100) reflection of the lamellar phase and the appearance of the second-order reflection of the lamellar phase at $5.74^\circ 2\theta$.

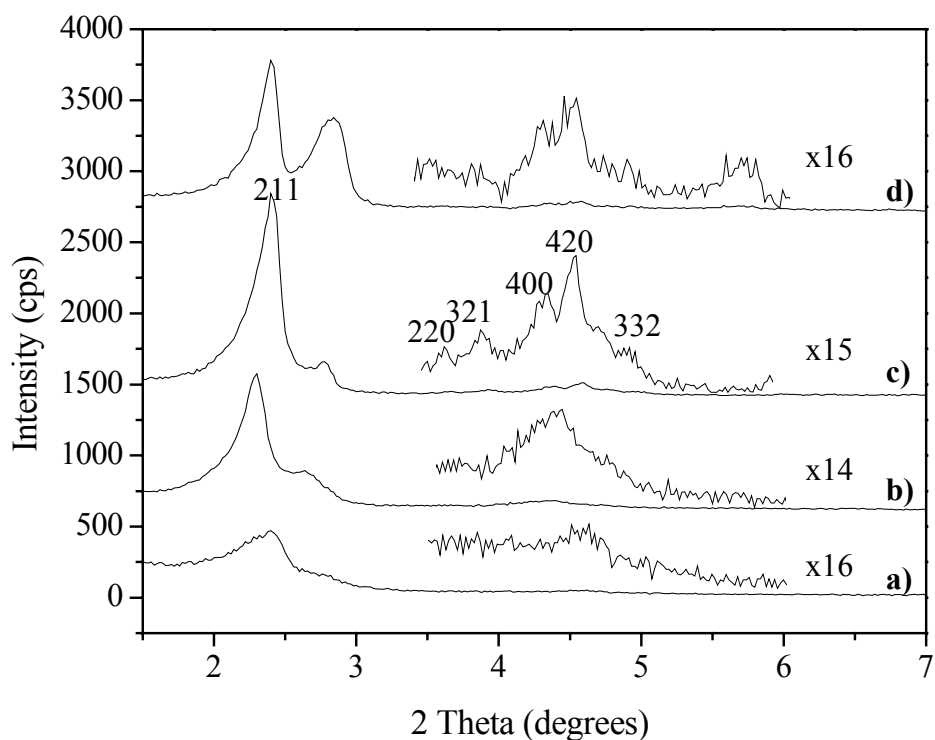


Figure 5.2. XRD patterns of mesoporous powders prepared from different synthesis gels; a) MCM-48-1, b) MCM-48-2, c) MCM-48-3, and d) MCM-48-4 (the diffraction patterns are offset with 500 cps).

Apparently, there is a profound influence of the surfactant-to-silica ratio on the mesophase structure for this sequence of synthesis gels. The change of the mesophase structure is explained by the effect of the surfactant concentration, where the increased surfactant concentration drives the structure form disordered through cubic MCM-48 to bilayered lamellar. This is in agreement with the water-CTABr phase diagrams at room temperatures where the general tendency of the H \rightarrow Q \rightarrow L phase transitions is observed with decreasing surface curvature around the surfactant micelles (H, Q, L refer to the hexagonal ($p6m$), cubic ($Ia3d$), and lamellar mesophases, respectively). The absence of the hexagonal ($p6m$) mesophase structure in the sequence of the synthesis gels used here is explained by the high ethanol concentration in the synthesis sols. Usually synthetic mixtures giving hexagonal ($p6m$) mesophase do not require additional co-solvent apart from water. Taking into account the cooperative self-assembly mechanism and the surface charge matching constraint it can be argued that the ethanol molecules increase the effective surfactant parameter g by enlarging the total volume of the surfactant chains V ($g = V/a_0l$, see Chapter 2.2.2.) due to the swelling effect, and thus induce formation of mesophase structures with decreased curvature such as cubic ($Ia3d$) structure. The possibility to tune the mesophase structure through phase transitions and the role of the ethanol to preferentially promote formation of the cubic ($Ia3d$) mesophase suggest that the cooperative self-assembly mechanism is leading the formation process of the mesoporous materials synthesized with the examined gels.

The effect of the calcination process on the mesophase structure is examined using two different calcination procedures shown on Figure 5.1.A and B. The XRD patterns of the as-prepared MCM-48-3 sample and the samples calcined according to procedures A and B are shown on Figure 5.3. The XRD patterns of the MCM-48-3 samples calcined following procedures A and B show that the mesophase structure is preserved after the template removal. The corresponding cubic unit cell calculated from the equation:

$$a = 6^{1/2} \cdot d_{211} \quad (5.1)$$

is $a_{\text{as-deposited}} = 8.96$ nm, $a_{\text{calcined A}} = 7.42$ nm, and $a_{\text{calcined B}} = 8.06$ nm. The position of the (211) reflection for the calcined samples is shifted to higher 2θ values; a fact that is explained by the increased siloxane condensation at the high calcination temperatures that induces shrinkage of the mesophase structure. Calcination procedure A gives higher shrinkage of the silica framework. The shrinkage calculated from the equation:

$$\delta H = (a_{\text{as-deposited}} - a_{\text{calcined}}) / a_{\text{as-deposited}} \times 100 \quad (5.2)$$

is 17.2% for the sample calcined with calcination procedure A and 10.1% for the sample calcined with calcination procedure B. The decreased shrinkage of the mesophase structure following calcination procedure B is explained by the additional thermal step at 120 °C that stabilizes the structure and prevents rapid template removal. Furthermore, the sample calcined with calcination procedure B suggests higher mesostructural order based on the presence of well-resolved higher order peaks. These results support the fact that the choice of an accurate calcination procedure for template removal is essential for the preparation of mesoporous solids with improved mesostructural order and thermal stability.

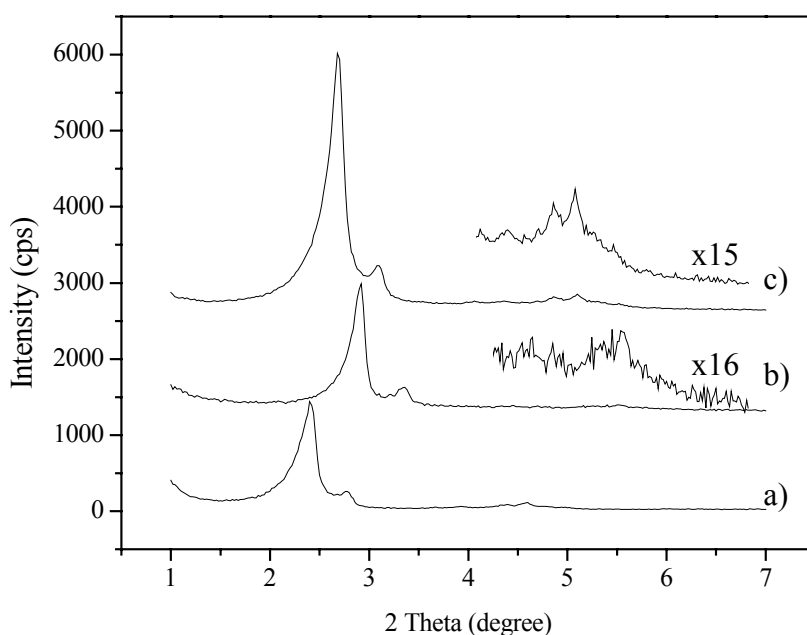


Figure 5.3. XRD patterns of a) as-prepared MCM-48-3, calcined with b) procedure A and c) procedure B (the diffraction patterns are offset with 1200 cps).

In order to prove full template removal after calcination, FT-IR spectra of the as-synthesized and calcined samples were compared. Figure 5.4 shows the FT-IR spectra of the as-synthesized and calcined (procedure B) mesoporous MCM-48-3 samples. The peak assignment of the FT-IR spectra of the as-synthesized and calcined MCM-48 can be made based on literature results and is as following¹². The broad band between 3700 and 3100 cm^{-1} is attributed to the hydrogen-bonded silanol groups with adsorbed molecular water (note that the spectra are taken in air at room temperature, H_2O bending at 1660cm^{-1} is also to be noted)¹³. The nature of this broad band comes from geminal and vicinal silanols, which participate in H-bonding among themselves, and molecularly adsorbed water, and are not accessible for further chemical modification¹⁴. The strong and narrow peaks at 2920 and 2850 cm^{-1} in the spectrum of the as-synthesized sample are characteristic for the aliphatic symmetric and anti-symmetric stretching vibrations of CTABr surfactant molecules.

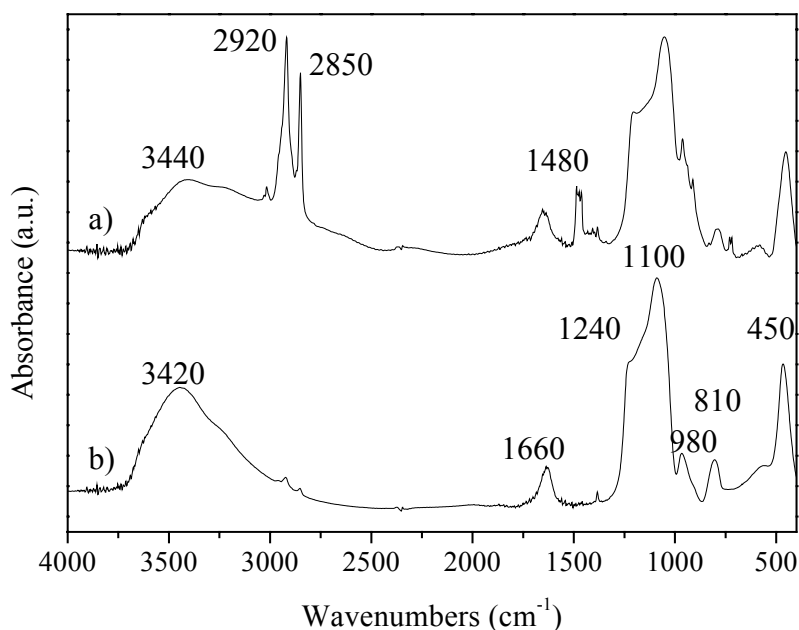


Figure 5.4. FT-IR spectra of a) as-synthesized and b) calcined MCM-48-3 mesoporous powder.

After calcination the characteristic bands for the organic template almost disappear, indicating complete removal of the surfactant (Figure 5.4.b). At lower frequencies two broad bands at 1240 and 1100 cm^{-1} are observed and assigned to the Si-O-Si asymmetric stretching vibrations¹. The band at 1480 cm^{-1} is attributed to the C-H banding vibrations and is also not seen in the spectrum of the calcined sample. The band at 810 cm^{-1} is attributed to the Si-O-Si symmetric stretching vibrations, while the band at 980 cm^{-1} is ascribed to the Si-OH stretch. The band at 450 cm^{-1} is assigned to the SiO_4 non-structural banding vibration and is typical for amorphous silica materials. As expected, bands around 550 cm^{-1} that are ascribed to the structural vibrations in zeolites are not observed confirming the amorphous character of the material¹⁵.

As discussed in Chapter 2.2., the preparation of the ordered mesoporous materials can be controlled by choosing specific surfactant or co-surfactant agents. In order to explore the formation of large pore size mesoporous material, SBA-15 (see Chapter 2.2.1.) mesoporous solid was prepared. Figure 5.5 shows the XRD patterns of the as-synthesized and calcined (procedure B) SBA-15 mesoporous material prepared with tri-block copolymer surfactant under acidic conditions. The as-synthesized sample shows a first order reflection at $0.81^\circ 2\theta$ and two very low-intensity second-order reflections at 1.37° and $1.63^\circ 2\theta$ that are indexed as (100), (110), and (200) reflections of the (*p6m*) hexagonal mesophase structure with a unit cell of $a = 12.6 \text{ nm}$ ¹⁶. The unit cell of the one-dimensional hexagonal mesophase structure is calculated from the position of the (100) reflection according to the following formula:

$$a = 2/3^{1/2} \cdot d_{100} \quad (5.3)$$

After calcination following procedure B the mesophase structure is preserved and the diffraction peaks appear with increased intensity and at higher 2θ values. The increased intensity of the reflections after calcination is explained by the increased mesostructural order and higher X-ray contrast due to template removal while the shift in the position of the diffraction peaks to higher 2θ values is due to the shrinkage of the silica framework. The hexagonal unit cell of the calcined sample is $a = 11.5 \text{ nm}$; this corresponds to 8.7% shrinkage of the mesophase structure.

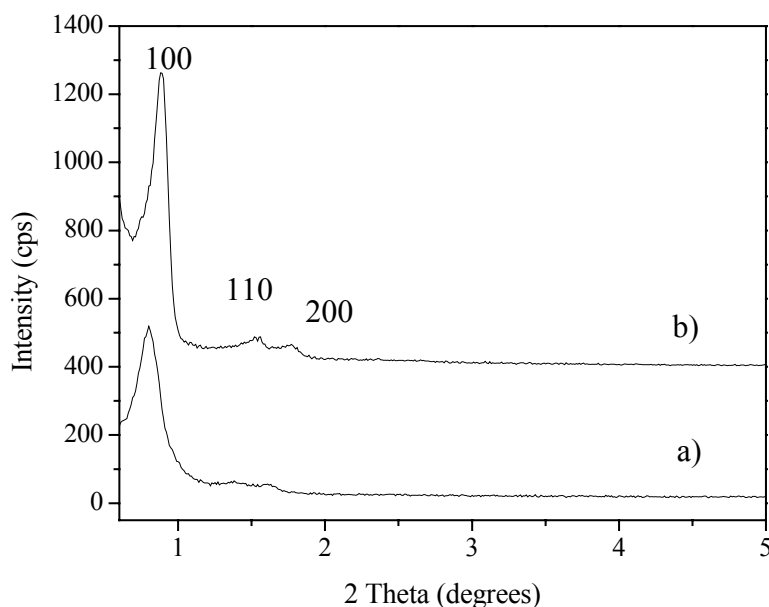


Figure 5.5. XRD patterns of a) as-synthesized and b) calcined (procedure B) SBA-15 mesoporous material (diffraction patterns are offset with 500 cps).

The temperature stability of the SBA-15 mesoporous support was further investigated aiming to prepare host structures that can withstand relatively high temperatures of about 700 – 900 °C desirable for a variety of catalytic applications, including the growth of carbon nanotubes. Two types of calcination procedures (Figure 1C and D) were applied and the corresponding XRD patterns are shown in Figure 5.6. Both calcination procedures give hexagonally ordered SBA-15 material even after calcination at 700 °C. The material obtained after calcination procedure C shows one, low-intensity first-order diffraction peak, while the material calcined following procedure D (with additional temperature stabilization step - see Figure 1D) possesses several well-resolved high-intensity reflections indicative for highly ordered SBA-15 material. The hexagonal unit cell is $a = 11.2$ nm in both cases. Apparently, the more complicated two-step calcination procedure D does not cause any additional shrinkage of the silica framework.

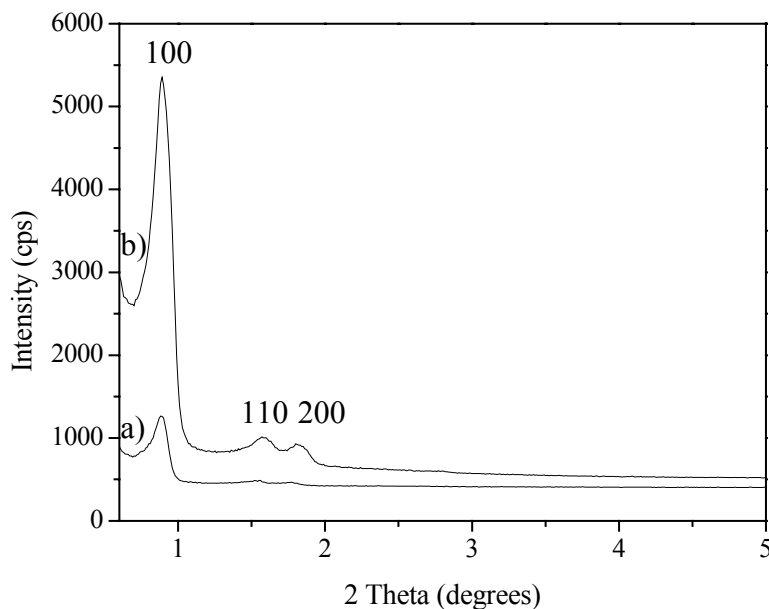


Figure 5.6. XRD patterns of a) calcined (procedure C) and b) calcined (procedure D) SBA-15 mesoporous material.

Attempts to stabilize the MCM-48-3 material using calcination procedure D gave poorly ordered mesoporous material with one very broad diffraction peak. The higher thermal stability of the SBA-15 material in comparison to the MCM-48 solid is explained by the thicker mesoporous walls (see Chapter 2.2.1. and references therein). The SBA-15 material obtained following calcination procedure D shows promising thermal stability and is a good candidate for a host support that can be used for templated growth of carbon materials at high temperatures, such as carbon nanotubes or carbon filaments.

Figure 5.7. shows the FT-IR spectra of the as-synthesized and calcined (procedure D) mesoporous SBA-15 samples. The assignment of the bands is similar to that in the FT-IR spectra of the MCM-48 material with some differences in the aliphatic stretching vibration region that come from the different templating agent, namely Pluronic 123. Most importantly, after calcination the C-H stretching vibrations completely disappear, thus confirming the removal of all template from the mesoporous material.

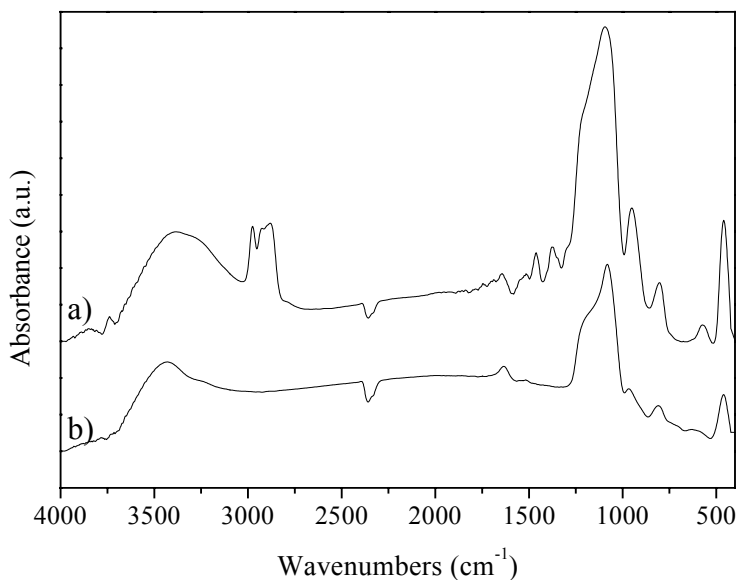


Figure 5.7 The FT-IR spectra of the as-synthesized and calcined (procedure D) mesoporous SBA-15 samples is shown.

Mesostructured monoliths have been prepared using synthesis solutions MM1 and MM2 (see above) with different structure directing agents (CTABr and Pluronic123). The XRD patterns of the as-prepared and calcined (procedure B) CTABr-templated mesostructured monoliths are shown in Figure 5.8. The pattern of the as-prepared monolith (Figure 5.8a) shows two reflections at 2.6 and $5.1^\circ 2\theta$ that are assigned to the (100) and (200) reflections of the one-dimensional hexagonal mesophase structure with mesoporous channels oriented parallel to the plane surface of the monolith^{17,18}. The hexagonal unit cell of the as-deposited sample is 3.91 nm (calculated from 5.3.). After calcination the mesophase structure is preserved and the Bragg peaks appear at higher 2θ values (Figure 5.8.b) in correspondence with the shrinkage of the silica framework at the high calcination temperatures. The calculated contraction of the silica framework is 4%. The first-order reflection (100) of the calcined sample shows considerable broadening, probably due to the decreased size of the ordered domains.

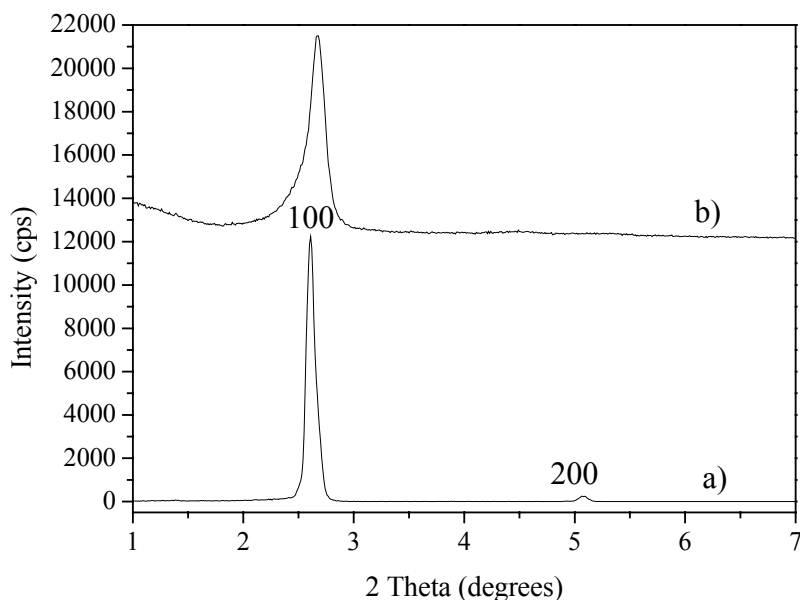


Figure 5.8. XRD patterns of a) as-prepared and b) calcined (procedure B) CTABr-templated mesostructured monoliths.

The XRD patterns of the as-prepared and calcined mesostructured monoliths deposited from coating solution MM2 are shown in Figure 5.9. The templating agent in the coating solution MM2 is a tri-block copolymer (Pluronic123) that gave a highly ordered mesophase structure as seen from the very intense first-order reflection at 1.05° 2θ with its less intense second-order reflection at 1.97° 2θ . These two diffraction peaks in the XRD pattern of the as-deposited sample are assigned to the one-dimensional hexagonal ($p6m$) mesophase structure with unit cell parameter of $a = 9.8$ nm (5.3). After calcination (procedure B) the hexagonally ordered mesophase structure is preserved as indicated by the well-resolved first- and second-order diffraction peaks (Figure 5.9.b). The contraction of the silica framework is estimated to be around 14% (5.2). The absence of the (110) reflection, typical for the hexagonally ordered mesophase powders like SBA-15 material (see above), in the XRD patterns of the MM1 and MM2 mesostructured monoliths is due to the preferential alignment of the mesoporous channels parallel to the surface of the monolith.

Further discussion of the preferred alignment and orientation of the mesophase channels will be given in the part covering mesostructured films (Chapter 6). By applying different synthesis solutions and under the conditions of the slow evaporation of the solvent, mesostructured monoliths having a one-dimensional hexagonal mesophase structure were prepared. The difference in the hexagonal unit cell of the as-deposited samples, namely 3.9 and 9.8 nm for the MM1 and MM2 materials, respectively, suggest that mesoporous monoliths with different pore sizes can be synthesized under conditions similar to those used by the EISA method.

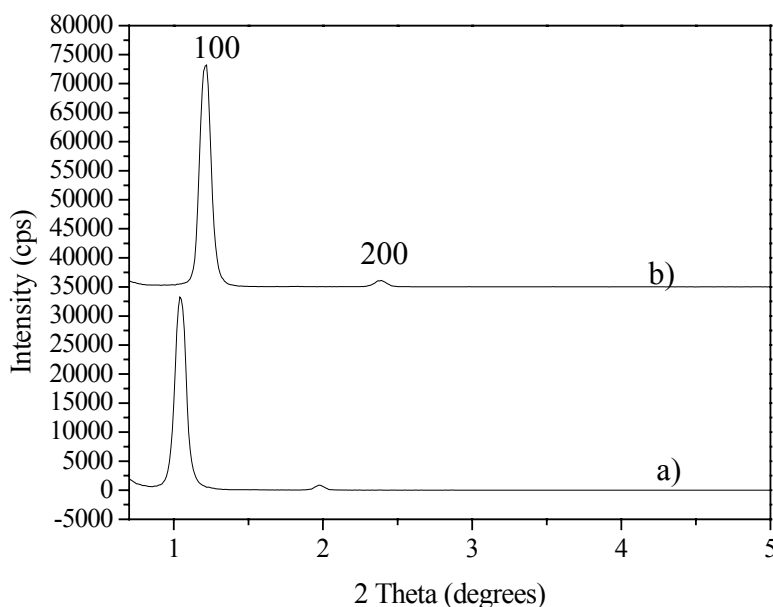


Figure 5.9. XRD patterns of a) as-prepared and b) calcined (procedure B) mesostructured silica monoliths prepared with coating solution MM2 (diffraction patterns are offset with 35000 cps).

Figure 5.10 shows the TG curves of MCM-48-3, SBA-15, as well as CTABr- and Pluronic123-templated monoliths. In all of them three distinct regions of weight loss can be distinguished. The first one (I) starts at about 50 °C up to 160 °C, and is associated with the desorption of physically adsorbed water¹. It accounts for a weight loss of 2 - 5% depending

on the type of the mesoporous material. The highest weight loss in this region is observed for the CTABr-templated materials such as MCM-48 (see Figure 5.10.a). The second region (II) in the TG curves is associated with the desorption, combustion, and decomposition of the organic template¹. The shape and position of this region strongly depend on the type of organic template. For example, SBA-15 (Figure 5.10.b) and Pluronic-123-templated monoliths (Figure 5.10.d) show a steep weight loss step between 160 and 220 °C that accounts for about 44% weight loss. The MCM-48-3 sample shows a weight loss of 31% in the interval 140 – 240 °C, while CTABr-templated monoliths show only 28% weight loss starting at a much higher temperature of about 235 °C. The third region (III) in the TG curves is related to water loss *via* condensation of silanol groups to form siloxane bonds and continuing loss of hydrocarbons. It starts at considerably higher temperatures and gives a weight loss between 10 – 15%.

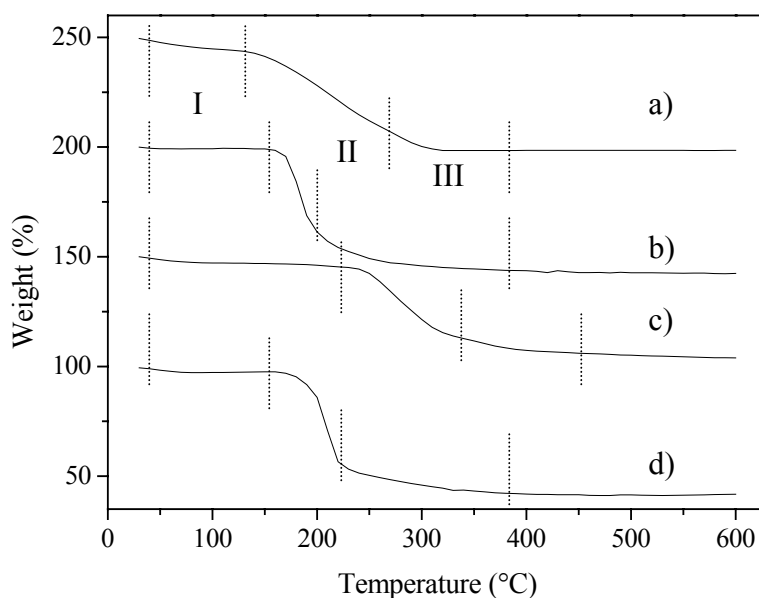


Figure 5.10. TG curves of a) MCM-48-3, b) SBA-15, c) CTABr-templated, and d) Pluronic123-templated mesoporous materials (the curves are offset with 50%).

Summing the weight loss from the second and third region, the overall weight loss is obtained, which stands for 43% in MCM-48-3, 56% in SBA-15, 40% in CTABr-templated monoliths, and 55% in Pluronic123-templated monoliths. The difference in the shape of the TG curves for CTABr and Pluronic123-templated materials may be related to the different behavior of the organic templates towards desorption and combustion, and the different type of the silica mesophase. Most importantly, in all cases, inorganic materials showing high weight loss during calcination were prepared that can provide high porosity suitable for a variety of applications in the field of inclusion chemistry.

5.3.2. Sorption properties and surface morphology – N₂-sorption, SEM, DLS, and TEM studies

N₂-sorption measurements were performed to determine specific surface areas (S_{BET}), pore-size distributions (D_{BJH}), and total pore volumes (V_t) of the calcined mesoporous solids (Table 5.2.). The application of the BET model for the calculation of the specific surface area and the BJH model for the calculation of the pore-size distribution was discussed in Chapter 4. Figure 5.11 presents N₂-sorption isotherms of the calcined (procedure B) CTABr-templated monoliths, MCM-48-3, and SBA-15 materials.

The isotherm obtained for the CTABr-templated monolith and MCM-48-3 material show distinct adsorption/desorption steps (capillary condensation in mesopores, see Chapter 4) between relative pressures of 0.1 and 0.3 with no hysteresis loop. Both are type IV isotherms showing ordered mesoporosity¹⁹. The adsorption/desorption step in the MCM-48-3 isotherm is steeper than that of the CTABr templated monolith; this can be explained by the existence of more uniform mesopores in the MCM-48-3 material. The obtained specific surface areas (S_{BET}) for both samples are more than 1200 m²/g (see Table 5.2.), which is in a good agreement with the published results for the MCM-type materials¹. Pore-size-distribution curves calculated from the BJH model from the desorption branch of the isotherms are shown in Figure 5.12. Calculated mean pore size for the CTABr-templated monolith and MCM-48-3 material are 2.13 and 2.19 nm, respectively, which corresponds to the values obtained for the CTABr-templated mesoporous materials¹⁹.

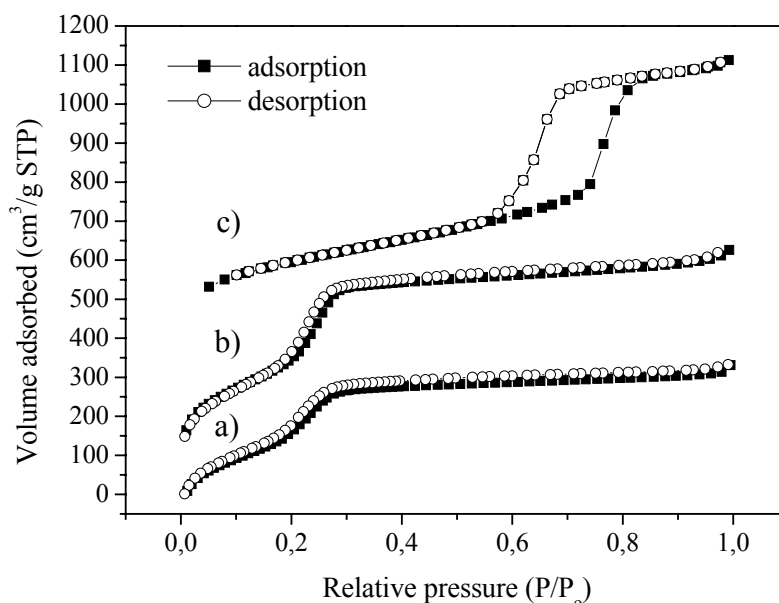


Figure 5.11. N₂-sorption isotherms of the calcined a) CTABr-templated monolith, b) MCM-48-3, and c) SBA-15 materials (the isotherms are offset with 200 cm³/g).

Table 5.2. N₂ sorption data for different mesoporous solids

Sample	a(nm)	S _{BET} (m ² g ⁻¹)	V _t (cm ³ g ⁻¹)	D _{BJH} (nm)
CTABr-templated monolith	3.83	1291	0.724	2.13
MCM-48-3	8.06	1574	0.963	2.19
SBA-15	11.5	856	1.17	5.74

The unit cell parameter is calculated from the XRD experiments, the surface area is calculated from the BET model, the total volume adsorbed is calculated from single point measurement at $P/P_0 = 0.994$, and the pore size is determined by the BJH model applied to the desorption branch of the isotherm.

The N₂ sorption isotherm of the SBA-15 material shows a sharp adsorption/desorption step between relative pressures of 0.6 and 0.8 with a distinct hysteresis loop. This kind of isotherm is again considered a type IV isotherm; as expected the desorption branch of the isotherm lies above the adsorption branch at the capillary condensation step (at any given relative pressure the amount adsorbed is always greater along the desorption branch than along the adsorption branch).²⁰ The reasons for this phenomenon are discussed in Chapter 4. The specific surface area (S_{BET}) for the SBA-15 material is much lower than that of the CTABr-templated materials (see Table 5.2.). This result is explained by the thicker walls of the SBA-15 material compared with those of the

CTABr-templated materials.²¹ The calculated mean pore size for the SBA-15 material is 5.74 nm; this is higher than that of the CTABr-templated materials in agreement with the literature results (see Chapter 2.2.1. and references therein).

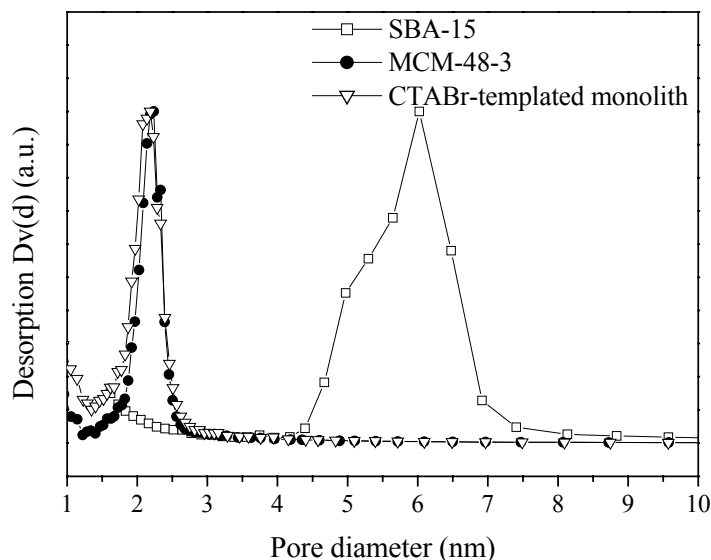


Figure 5.12. Pore size distribution curves for different mesoporous solids.

Knowing the pore size estimated from the BJH model and the hexagonal unit-cell size calculated from the XRD measurements, it is possible to calculate the wall thickness of the mesoporous materials. For example, the CTABr-templated hexagonally ordered mesoporous monolith with unit cell size of 3.83 nm and mean pore size of 2.13 nm will have a wall thickness of about 1.7 nm calculated using the formula:

$$T = a_{\text{XRD}} - D_{\text{BJH}} \quad (5.4.)$$

In comparison, the SBA-15 material shows wall thickness of about 5.76 nm.

Figure 5.13 shows an SEM image of the uniform spheres of MCM-48-3 material having a diameter of about 300 nm. The spheres are not completely isolated and form bigger aggregates. No special crystallographic planes or facets (typical, for example, for crystalline zeolites) can be observed, as MCM-48 is amorphous silica material.

The particle size distribution of the as-synthesized and washed suspensions of MCM-48-3 material was examined by DLS. Figure 5.14 shows the DLS data of the 3 wt% suspension of washed MCM-48 spheres. The mean particle radius is 250 nm with a broad particle size distribution of about 200 to 500 nm.

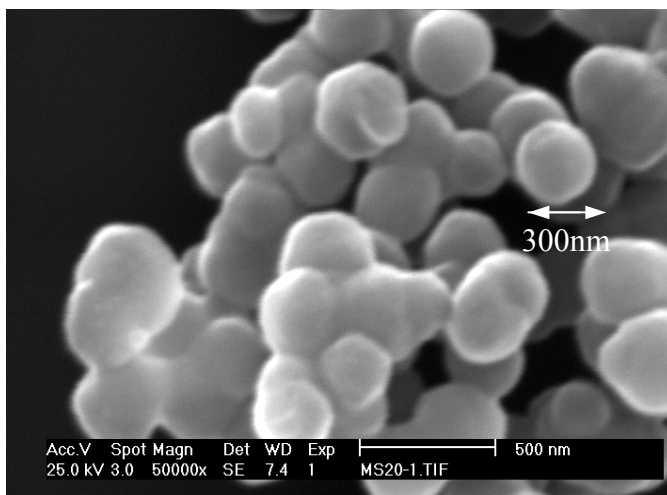


Figure 5.13. SEM image of calcined MCM-48-3 material.

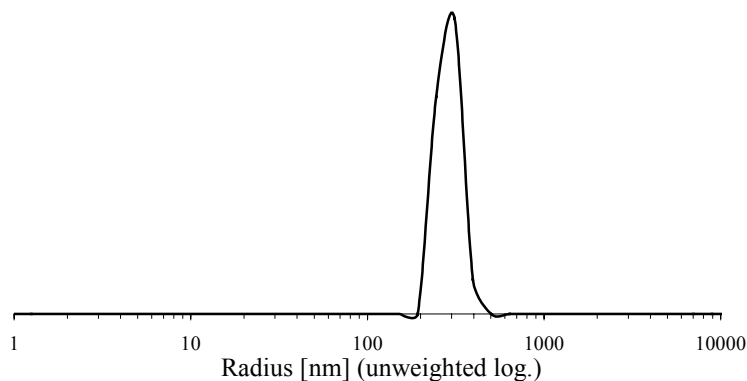


Figure 5.14. DLS data of a 3% water suspension of MCM-48 spheres.

The bigger particle size detected with DLS in comparison to SEM results is explained by the formation of bigger aggregates of MCM-48 particles as opposed to isolated and strictly monodisperse MCM-48 spheres. Attempts to obtain isolated MCM-48

spheres by repeated centrifugation and re-dispersion in water or other solvents were not successful.

Figure 5.15 shows the TEM images of the MCM-48-3 materials. The spherical morphology of 300 nm particles is confirmed from the low-resolution TEM image. The cubic ($Ia3d$) structure of the mesoporous materials is seen in Figure 5.15.b, c, and d and corresponds to the structure observed during TEM investigations of the MCM-48 material.

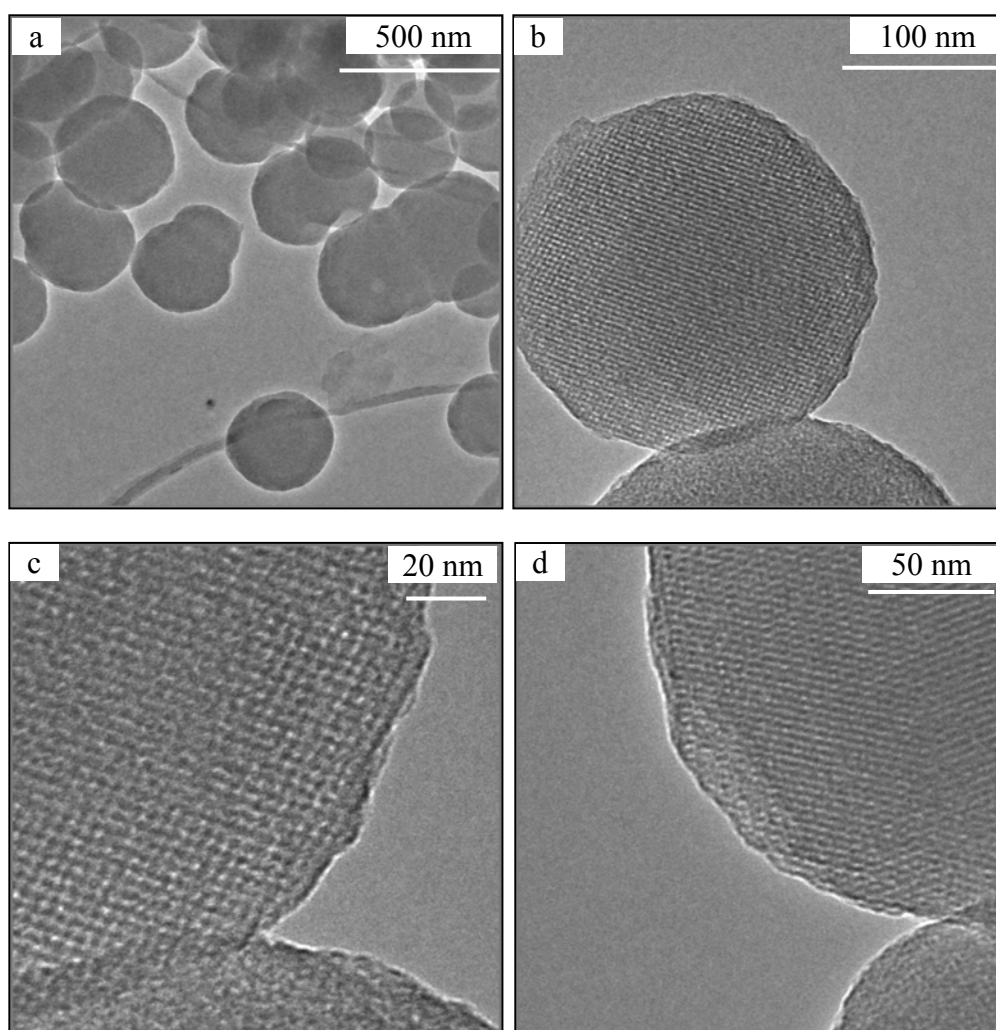


Figure 5.15. TEM images of MCM-48-3 material a) along the [110] direction and b) along the [311] direction.

The high degree of mesostructural order is clearly visible in Figure 5.15.b where it is seen that the whole particle is “crystalline” (better expression would be: well organized in a periodic silica/surfactant mesophase). The following images show the particles viewed along the [110] and [311] directions of the MCM-48 mesophase. The TEM results are in good agreement with the literature results²². These results together with the XRD measurements confirm the cubic (*Ia3d*) mesophase structure of the MCM-48-3 material and prove its excellent mesostructural order.

The calcined SBA-15 material contains rods with a typical diameter of 10-30 μm and lengths of up to 150 μm (Figure 5.16). The rods are assembled from small (several micrometer long) worm-like structures that are running or curling along the long axes of the rod (inset in Figure 5.16). The diameter of the worm-like structures is less than 1 μm . It has been observed by TEM investigations that the hexagonally ordered channels of the SBA-15 material are preferentially aligned with the long axes of the worm-like structures (Figure 5.17). Thus SBA-15 rods can be considered as coaxial cables showing a hierarchical structure with more than 100 μm length.

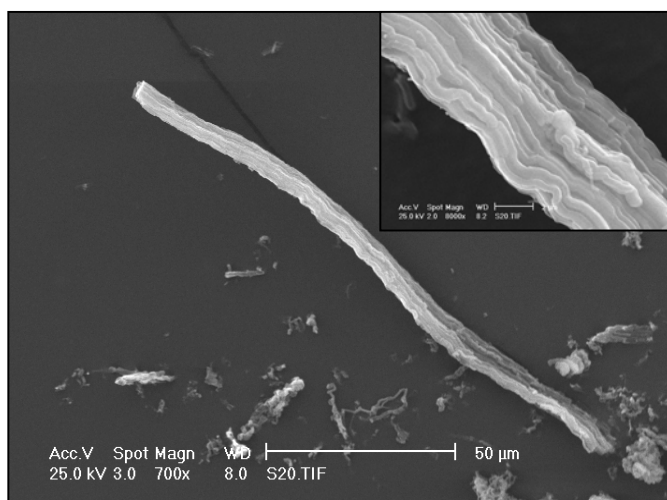


Figure 5.16. SEM image of calcined SBA-15 rods (inset: higher-magnification SEM image - scale bar 2 μm).

The TEM images of the calcined SBA-15 material are shown in Figure 5.17. Figure 5.17.a shows a TEM image in the direction parallel to the hexagonally ordered channels with the typical well-ordered honeycomb structure.

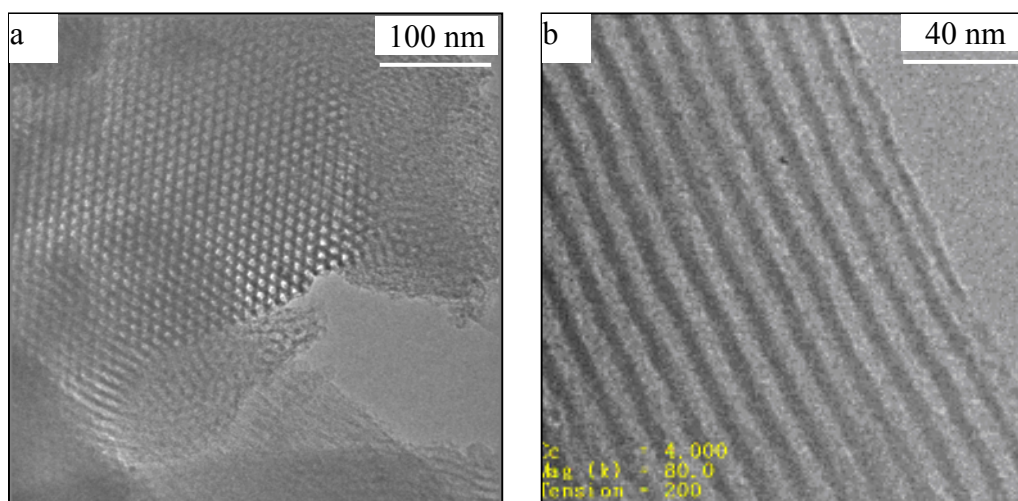


Figure 5.17. TEM images of SBA-15 material a) along the channels direction and b) perpendicular to the channel direction.

Well-ordered mesoporous channels running parallel to the long axes of the worm-like structures are seen in the high-resolution TEM image (Figure 5.17.b). The pore-to-pore distance calculated from the high-resolution TEM image is around 11.7 nm with a pore diameter of about 6.2 nm and is in a good agreement with that determined from the BJH analysis of the N₂-sorption data (5.74 nm). The wall thickness is estimated to be 5.5 nm and corresponds to that determined from the XRD and N₂-sorption results.

Figure 5.18 shows a side-view SEM image of the calcined Pluronic123-templated monolith. The thickness of the monolith is about 25 μm and can be tuned by changing the amount of the deposited synthesis sols and by controlling the solvent evaporation rate. Before calcination, deposited monoliths show homogeneity and uniformity over centimeter ranges. After calcination, micrometer-long scratches were observed in the monoliths giving delaminated pieces with different dimensions. Further synthetic effort is needed to obtain homogeneous, free of template, centimeter-sized mesostructured monoliths.

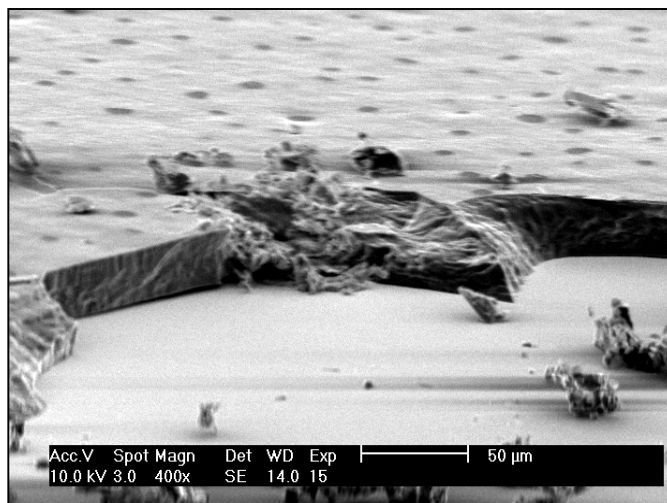


Figure 5.18. Side-view SEM image of the calcined Pluronic123-templated mesostructured monolith deposited on Si wafer.

5.4. Conclusions and Perspectives

The structural analysis of different examples of powdered mesoporous materials prepared in the course of this study shows that in most cases highly ordered mesoporous solids can be prepared using different surfactants, cationic or nonionic, under basic or acidic conditions. Two different types of mesophase structure have been prepared showing three-dimensional cubic or two-dimensional hexagonal structures that were characterized by powder XRD, FT-IR, N₂-sorption, and SEM measurements. For all materials it was demonstrated that the calcination procedure used to obtain template-free porous supports is critical for the preservation of the mesophase structure.

It has been shown that the preparation of MCM-48 material is very sensitive and depends on a variety of synthetic parameters. Among them, the silica-to-surfactant ratio is critical and determines the final mesophase structure. Applying the proposed procedure for the preparation of MCM-48 material, spherical particles with several hundred nanometers in diameter can be prepared. SBA-15 rods having hierarchical structure composed of nanometer-sized worm-like structures have also been prepared. Applying an additional thermal curing step during the calcination process, SBA-15 rods with improved thermal stability were obtained. Mesostructured monoliths showing two-dimensional hexagonal

structures have been deposited by using a simple solvent-evaporation method. The characterization of the mesostructured monoliths gave additional information that was very useful as starting point for the characterization of thin mesoporous films.

Calcined MCM-48 mesoporous spheres can be used as supports for a variety of catalytic and chromatographic applications after introduction of desirable surface modifications with molecular functionality or transition metal nanoparticles. Additionally, the uniform MCM-48 spheres showing mono-dispersed particle size distribution and dimensions around 300 nm can be used to prepare uniform monolayers of nanoparticles by applying spin-coating or pen-printing techniques. In the latter case, hierarchically patterned nanostructures can be prepared.

Thermally stable SBA-15 material is suitable for variety of catalytic applications that require extremely high temperatures. Furthermore, when loaded with conductive nanostructures SBA-15 rods can be contacted to gold electrodes and can serve as coaxial cables to study the electrical properties of different conductive nanostructures.

References

- ¹ J. S. Beck, J. C. Vartuli, W. J. Roth, M. E. Leonowicz, C. T. Kresge, K. D. Schmitt, C. T.-W. Chu, D. H. Olson, E. W. Sheppard, S. B. McCullen, J. B. Higgins, J. L. Schlenker, *J. Am. Chem. Soc.*, **1992**, 114, 10834.
- ² K. W. Gallis and C. C. Landry, *Chem. Mater.*, **1997**, 9, 2035.
- ³ J. M. Kim, S. K. Kim, R. Ryoo, *Chem. Commun.*, **1998**, 259.
- ⁴ K. Schumacher, C. F. von Hohenesche, K. K. Unger, R. Ulrich, A. du Chesne, U. Wiesner, H. W. Spiess, *Adv. Mater.*, **1999**, 11, 1194.
- ⁵ R. Ryoo, S. H. Joo, J. M. Kim, *J. Phys. Chem. B*, **1999**, 103, 7435.
- ⁶ D. Kumar, K. Schumacher, C. F. von Hohenesche, M. Grün, K. K. Unger, *Colloids Surf. A*, **2001**, 187-188, 109.
- ⁷ K. Schumacher, P. I. Ravikovitch, A. Du Chesne, A. V. Neimark, K. K. Unger, *Langmuir*, **2000**, 4648.

- ⁸ D. Zhao, J. Sun, Q. Li, G. D. Stucky, *Chem. Mater.*, **2000**, 12, 275.
- ⁹ B. J. Scott, G. Wirnsberger, G. D. Stucky, *Chem. Mater.*, **2001**, 13, 3140.
- ¹⁰ W. Stöber, A. Fink, E. Bohn, *J. Colloid Interface Sci.*, **1968**, 26, 62.
- ¹¹ K. Schumacher, M. Grün, K. K. Unger, *Microporous Mater.*, **1999**, 27, 201.
- ¹² M. S. Morey, S. O'Brien, S. Schwarz, G. D. Stucky, *Chem. Mater.*, **2000**, 12, 898.
- ¹³ E. F. Vansant, P. van der Voort, K. C. Vrancken, *Stud. Surf. Sci. Catal.*, **1995**, 93, 97.
- ¹⁴ A. Jentys, K. Kleestorfer, H. Vinek, *Micropor. Mesopor. Mater.*, **1999**, 27, 321.
- ¹⁵ J. C. Jansen, F. J. van der Gaag, H. van Beckum, *Zeolites*, **1984**, 4, 369.
- ¹⁶ D. Zhao, Q. Huo, J. Feng, B. F. Chmelka, G. D. Stucky, *J. Am. Chem. Soc.*, **1998**, 120, 6024.
- ¹⁷ M. Ogawa, *J. Am. Chem. Soc.*, **1994**, 116, 7941.
- ¹⁸ B. Lebeau, C. F. Fowler, S R. Hall, S. Mann, *J. Mater. Chem.*, **1999**, 9, 2279
- ¹⁹ M. Kurk and M. Jaroniec, *Chem. Mater.*, **2001**, 13, 3169.
- ²⁰ D. Zhao, J. Feng, Q. Huo, N. Melosh, G. H. Fredrickson, B. F. Chmelka, G. D. Stucky, *Science*, **1998**, 279, 548.
- ²¹ F. di Renzo, A. Galarneau, P. Trens, N. Tachoux, F. Fajula, *Stud. Surf. Sci. Catal.*, **2002**, 142, 1057.
- ²² V. Alfredsson and M. W. Anderson, *Chem. Mater.*, **1996**, 8, 1141.

Chapter 6. Preparation and characterization of ordered mesoporous films.

6.1. Introduction

6.2. Experimental

6.2.1. Preparation of ordered mesoporous films

6.2.2. Characterization of the mesoporous films

6.3. Results and discussion

6.3.1. Mesophase structure - influence of the relative humidity, composition of the coating solution and post-synthesis thermal treatments

6.3.1.1. CTABr-templated mesoporous films

6.3.1.2. Pluronic123 - templated mesoporous films

6.3.2. Sorption properties of the mesoporous films – N₂ sorption studies with a QCM device

6.3.3. Surface morphology and thickness of the mesoporous films

6.4. Conclusions and Perspectives

6.1. Introduction

The methods for the preparation and the techniques for characterization of ordered mesoporous films were discussed in Chapter 2.2.4 and Chapter 4. The evaporation-induced self-assembly (EISA) method performed by spin- or dip-coating has been proven to be advantageous when smooth and continuous films with nanometer thickness are desirable. It has been shown in the literature that this method is strongly dependent on the initial silica to surfactant ratio, the nature of the prehydrolyzed silica species, type of surfactant, dilution of the initial solution, humidity in the deposition chamber, deposition speed and post-synthesis treatments (see Chapter 2.2.4 and references therein). These parameters can influence the mesophase structure, pore size and pore accessibility, the stability of the films, film thickness and roughness. The goal was to find optimum preparation conditions for the deposition of mesoporous films by the EISA method. This includes investigation of the composition of the precursor solutions (silica/surfactant ratio, pH, solvent, etc), coating conditions, humidity in the deposition chamber, and post-synthesis thermal treatments. At the same time the

techniques that can be used to characterize thin mesoporous films are very limited and in many cases give only partial characterization information (see Chapter 4. and references therein). Therefore surface sensitive techniques, such as grazing-incidence diffraction (GID), absorption-reflection FT-IR, cross-sectional TEM, gravimetric measurements with a QCM device, AFM, and SEM, should be used to characterize the structure and surface morphology of the mesoporous films. Here the application of these techniques to mesoporous thin films is shown.

The dynamic conditions for the preparation of mesoporous films by the EISA method made it difficult to predict and follow the formation mechanism since the synthesis proceeds for no more than about one minute. It has been shown in several publications that the formation of mesostructured silica/surfactant films is a delicate and complex process that involves several intermediate phases and competing processes leading to a variety of mesophase structures (see Chapter 2.2.4 and references therein). Certainly the three-dimensional cubic or hexagonal mesophase structures assembled in thin-film architectures are preferable for our purposes because of the accessible porosity that can be further functionalized and used for surface-confined chemistry. Another structure that can give easy accessibility to the mesophase system is the hexagonal arrangement of mesoporous channels, aligned perpendicular to the substrate surface. Unfortunately, up to this point it is not clear if such a structure can be made over extended areas. There are promising initial results suggesting that an electric field applied perpendicular to the sample surface can be used to macroscopically align the hexagonal mesophase structure with its *c*-axis normal to the substrate surface.

6.2. Experimental

6.2.1. Preparation of ordered mesoporous films

Coating solutions were prepared by applying a two step synthesis procedure. First, 2.08 g tetraethoxy orthosilicate (TEOS - Aldrich) was mixed with 3 g 0.2 M HCl, 1.8 g H₂O and 5 mL EtOH and heated at 60 °C for 1h. In the second step, ethanol solutions of cetyltrimethylammonium bromide (CTABr - Aldrich) or PEO-PPO-PEO tri-block copolymer (Pluronic 123 - BASF) were added to the prehydrolyzed silica sols and stirred for

2 h. Namely, NPF1 and NPF2 coating solutions were prepared by addition of 0.546 g and 0.655 g CTABr each dissolved in 25 ml EtOH, to the as-prepared prehydrolyzed TEOS. Similarly, 15 mL and 20 mL 5 % Pluronic 123 solutions in EtOH were added to the prehydrolyzed silica and diluted with 10 ml and 5 ml of EtOH, respectively.

The final molar ratios of the coating solutions were:

NPF1: 1 TEOS: 0.15 CTABr: 0.06 HCl: 48.8 EtOH: 26.6 H₂O

NPF2: 1 TEOS: 0.18 CTABr: 0.06 HCl: 48.8 EtOH: 26.6 H₂O

NPF3: 1 TEOS: 0.013 Pluronic123: 0.06 HCl: 48.8 EtOH: 26.6 H₂O

NPF4: 1 TEOS: 0.017 Pluronic 123: 0.06 HCl: 48.8 EtOH: 26.6 H₂O

The mesoporous films were deposited on acetone pre-cleaned silicon wafers (25 x 25 mm) with a SCS P6700 spin coater at a rotation speed of 2000 rpm at room temperature. Similarly, mesoporous films were deposited on the gold surface of the QCM device after modification of the gold surface with 17 μ g 3-mercaptopropyltrimethoxy silane (MPS - Fluka) dissolved in 10 ml toluene for 6 h under nitrogen atmosphere. The relative humidity in spin-coating the deposition chamber was controlled with calibrated gas-flow system and was checked with a portable gas-chromatograph (Agilent 3000A Micro GC). Films were deposited at different relative humidity ranging from 20% to 80%. Finally, the films were thermally stabilized at 120 °C for 6 h and calcined at 500 °C for 2 h (0.5 °C/min ramping) following calcination procedure B (Figure 1, Chapter 5.3.2.). In order to obtain thermally stable mesoporous films that can be used for high temperature growth of carbon materials, calcination procedure D (Figure 1, Chapter 5.3.2.) was applied.

6.2.2. Characterization of the mesoporous films

The mesophase structure of the as-synthesized and calcined films was determined by X-ray diffraction in the θ - θ scan mode (Scintag XDS 2000 cooled Ge detector, Cu K α radiation). Grazing-incidence diffraction experiments were performed at beam-line ID01 at the ESRF (www.esrf.fr) in Grenoble, France. The geometry of the two XRD experiments and the comparison between them is given in Chapter 4.2. Further structural information was

obtained by TEM images taken as plan views. Samples for plan-view TEM investigations were obtained by thinning the Si-wafer or glass substrate till the sample is transparent for TEM measurements or by delaminating the film from the substrate and depositing the scratches directly on carbon coated copper grids. The thinning process is performed by applying Gatan instruments that include: disk cutter, disk grinder and dimple grinder. Finally, in order to obtain samples several hundred nanometer thin an Ar-ion milling was used (Gatan – Precision Ion Polishing System 691).

The calcination of the mesoporous films was followed by reflection-absorption FT-IR spectroscopy. The measurements were carried out at an incidence angle of 55 degrees on silicon supported samples after collecting the background with a Bruker IFS 66v/S spectrometer equipped with a grazing-incidence module.

Quartz crystal microbalance devices (10 MHz QCM, Cold Springs R&D, Marcellus, NY) were used to monitor the sorption properties of the mesoporous films. The mass changes of the films caused by sorption of gas were recorded as a frequency change of the QCM devices (1 Hz correlates to 26.4 ng/cm²). Typically, the calcined mesoporous films were outgassed at 120 °C for 48 h and then the mass of the deposited film was measured at room temperature. Nitrogen sorption isotherms of the calcined films were obtained at –196 °C by recording the change in the frequency at every sorption step. The nitrogen partial pressure in helium was regulated by a computer controlled gas flow system (MKS Instruments) in the range of 0 – 95%.

6.3. Results and discussion

6.3.1. Mesophase structure - influence of the relative humidity, composition of the coating solution, and post-synthesis thermal treatments

6.3.1.1. CTABr-templated mesoporous film.

The structure of the mesoporous films was determined using X-ray diffraction in two different geometries – reflection ($\theta - \theta$) and grazing-incidence geometry. As outlined before, grazing-incidence geometry gives much more structural information but requires use of

Synchrotron radiation (see Chapter 4.1). Here the results of both techniques will be presented.

Figure 6.1. shows the GID pattern of the as-deposited cubic mesoporous film prepared with coating solution NPF1 at a relative humidity in the deposition chamber of 70%. The Bragg spots on the pattern can be indexed in the cubic ($Pm\bar{3}n$) symmetry as previously proposed by Grosso¹. The most intensive spots in the GID pattern are due to {210} and {211} planes parallel to the substrate surface (diffraction intensity along the q_z vector, see Chapter 4.1). The cubic ($Pm\bar{3}n$) films have a structure that is similar to powder SBA-1 material where the extended three-dimensional order is obtained by close packing of spherical and cylindrical micellar structures². The fact that we observe diffraction spots rather than continuous diffraction rings indicates that the mesoporous films have preferential orientation, or so-called single-crystal orientation. The initial micellar cubic structure has a unit cell parameter of $a_0 = 9.1$ nm calculated based on the position of the (211) reflection ($a = 6^{1/2} \cdot d_{sp(211)}$). The diffraction spots are localized on three ellipses that are found to result from one-dimensional contraction occurring during the drying process in the direction normal to the substrate surface. This phenomenon has been well studied and explained by the slow and continuous condensation of the inorganic network.³

The degree of distortion δH calculated using formula:

$$\delta H = d_{sp(211)} - d_{sp(121)}/d_{sp(-121)} \quad (6.1.)$$

is found to be 22% for the as-deposited sample. It has also been suggested that the ($Pm\bar{3}n$) cubic mesoporous films are mono-oriented with the {211} lattice planes parallel to the substrate surface and that they show only one diffraction peak in the direction of the out-of-plane diffraction³. The intensity profile corresponding to the out-of-plane diffraction (similar to the diffraction patterns obtained in RXRD) shows two distinct reflections that correspond to (210) and (211) diffraction peaks and indicate that the texture along the direction of the [211] zone axis is not extended along the whole film (Figure 6.1 inset). Therefore other domains should co-exist that show orientations with {210} lattice planes parallel to the substrate surface. This fact suggests that mesoporous films showing a mosaic structure with

two different orientations of domains having ($Pm3n$) cubic mesostructure are formed during the coating process.

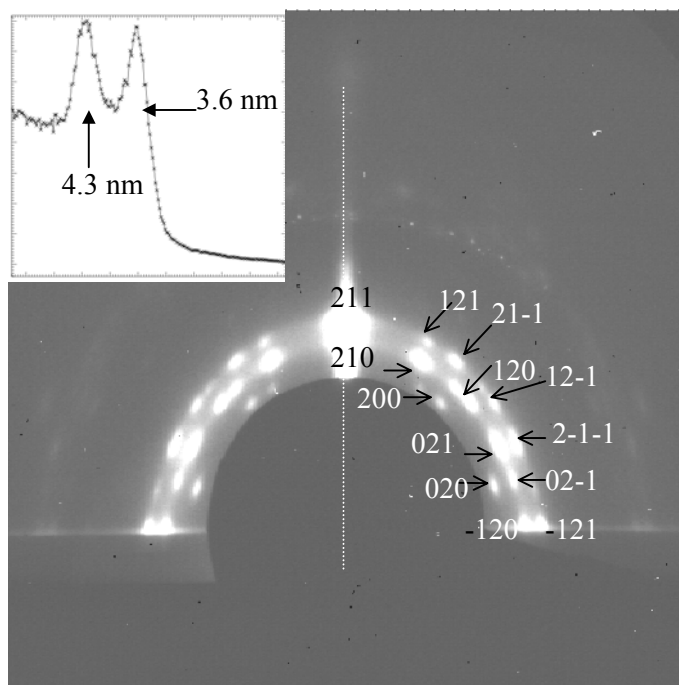


Figure 6.1. GID pattern of as deposited cubic ($Pm3n$) mesoporous film prepared at relative humidity of 70% from coating solution NPF1 (inset: intensity distribution along q_z vector).

In order to further characterize the mesophase structure of the as-deposited cubic ($Pm3n$) films, TEM measurements were undertaken. Figure 6.2. shows the TEM image of the NPF1 sample taken as a plan-view (incident electron beam perpendicular to the film surface) at two different magnifications.

The models of the two possible orientation of the ($Pm3n$) cubic domains in respect to the substrate surface are shown in Figure 6.3.a and b with the corresponding plan-views in directions of the $[210]$ and $[211]$ zone axes (Figure 6.3.c and d). Two distinct domain structures with different orientation towards the electron beam (shown with arrows) are seen in Figure 6.2.a. Taking into account the models shown in Figure 6.3. these domains are assigned to cubic ($Pm3n$) mesophase structures oriented with the $\{210\}$ and $\{211\}$ lattice planes perpendicular to the electron beam (parallel to the substrate surface). Figure 2b shows

a magnified domain having ($Pm3n$) mesophase structure imaged along the [211] zone axes and confirms the excellent order of the ($Pm3n$) cubic mesoporous film. It was also observed that in plane the domains are not preferentially oriented as shown schematically in Figure 3e.

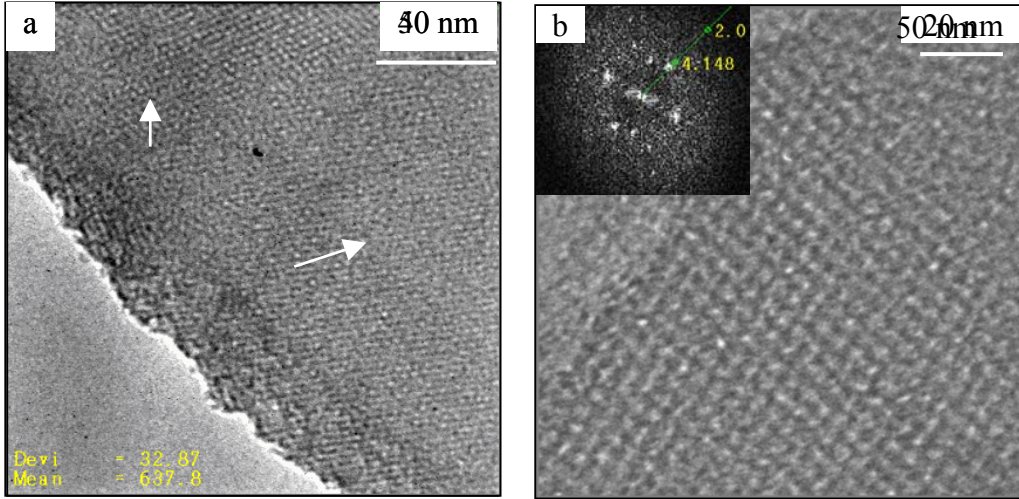


Figure 6.2. a) Plan-view TEM image of NPF1 mesoporous film showing two different domains of the ($Pm3n$) cubic mesophase (shown with arrows) and b) higher resolution TEM image of a domain imaged along the [211] zone axes (inset: corresponding power spectrum).

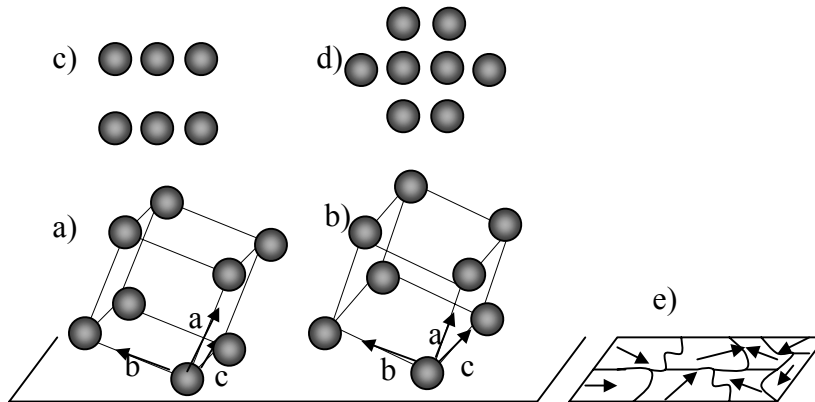


Figure 6.3. Schematic representation of the ($Pm3n$) cubic mesophase oriented with a) [210] and b) [211] zone axes perpendicular to the substrate, c) and d) corresponding plan-views parallel to the substrate surface, and e) mosaic structure of the mesoporous film showing no in-plane orientation.

It is suggested that the disorder-to-order transformation (nucleation of the ordered mesoporous domains) is completely random and is not affected by the shear forces (in-plane forces) developed during the spin-coating process. It is suggested that the film/surface and the film/air interfaces are the driving force governing the alignment of the most densely packed {210} and {211} planes in the cubic lattice. This is supported by the fact that the mesostructuration process of the mesoporous films deposited by EISA takes place slightly after the drying of the film and enables alignment of the porous system to both interfaces.¹

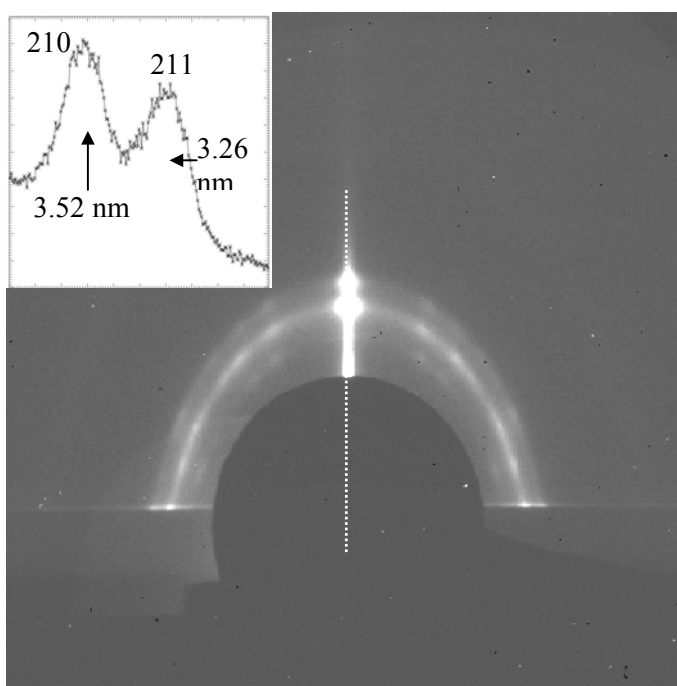


Figure 6.4. GID pattern of calcined cubic ($Pm3n$) mesoporous film prepared at a relative humidity of 70% from coating solution NPF1 (inset: intensity distribution along q_z vector).

The GID pattern of the cubic mesoporous film treated following calcination procedure B (Figure B, Chapter 4.3.2.) is shown in Figure 6.4. The mesophase structure is preserved upon calcination as seen from the large number of diffraction spots typical for the cubic ($Pm3n$) mesophase. The cubic unit cell size as calculated from the position of the (211) reflection is 6.6 nm. The diffraction spots are again localized on three ellipses, and the distortion of the structure in the direction perpendicular to the surface is estimated to be $\delta H =$

38% (6.1). The structural changes before and after calcination are attributed to the increased shrinkage of the structure upon template removal and increased siloxane condensation after thermal treatment. The diffraction spots appear attenuated and show lower intensity that may be attributed to decreased mesostructural order. The intensity profile corresponding to the out-of-plane diffraction (inset in Figure 6.4.) shows two reflection indexed in ($Pm3n$) mesophase that are coming from two different domain orientations with [210] and [211] zone axis perpendicular to the substrate surface.

When the deposition of the mesoporous film is performed at different relative humidity the mesophase structure is expected to change because of the different concentration of water molecules in the condensing film during the evaporation. This will influence the mesophase structure because of the i) swelling effects (changing surfactant packing parameter g) and ii) the changed silica hydrolysis/condensation process.

Figure 6.5. shows the GID pattern of a mesoporous film deposited with the same coating solution NPF1 at a relative humidity of 40%.

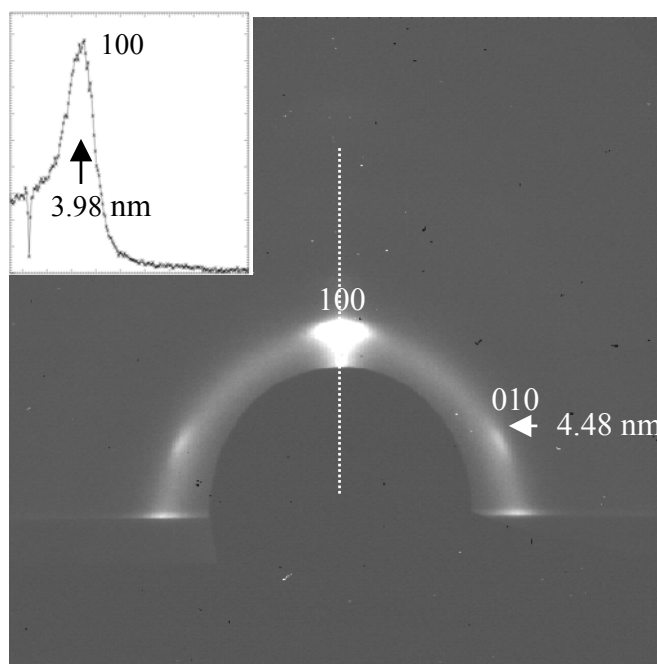


Figure 6.5. GID pattern of mesoporous film prepared at relative humidity of 40% from coating solution NPF1 (inset: intensity distribution along q_z vector).

The pattern shows three diffraction spots that are indexed in the hexagonally ordered ($p6m$) mesophase structure.¹ The diffraction spots are superimposed over a diffraction ellipse showing weak intensity. The real structure of these films has already been evaluated assuming the one-directional contraction in the direction normal to the substrate during the rapid evaporation of the solvent. As a result a two-dimensional centered rectangular structure showing ($c2m$) space group, textured with the b -axis perpendicular to the film surface is formed (see below). The unit cell size of the initial hexagonal mesophase structure calculated from the position of the (010) reflection is 5.17 nm.

The distortion of the initial hexagonal mesophase structure calculated according to the equation (6.2) is 12%.

$$\delta H = d_{sp(100)} - d_{sp(010)}/d_{sp(100)} \quad (6.2.)$$

Additionally, continuous ellipsoidal diffraction with lower intensity is observed. This fact is attributed to the existence of disordered domains corresponding to worm-like structure. The vague intensity of the diffraction ring comes from the scattering from micellar structures with the same characteristic dimensions as those forming the hexagonally ordered structure:

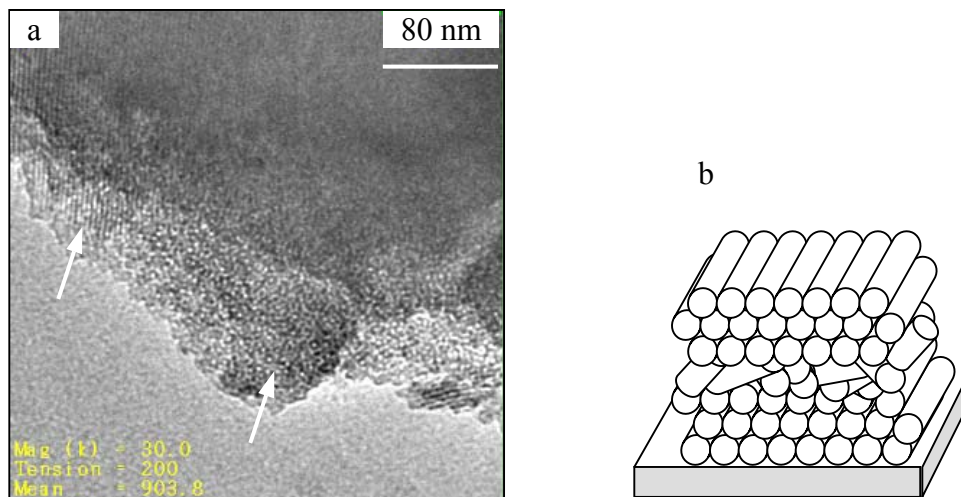


Figure 6.6. a) TEM image of the worm-like- $(p6m)$ mesophase films prepared from coating solution NPF01 at relative humidity of 40% and b) schematic representation showing the

existence of two types of mesoporous domains – hexagonally ordered and worm-like shown with arrows in the TEM image.

Additional, TEM investigations suggest that such kind of domains co-exist with well ordered hexagonal structures that are localized at the two interfaces of the film¹. Figure 6.6 shows that different domain structures can be observed in the plan-view image (shown with arrows).

It is clear that the relative humidity during the deposition plays a decisive role for the mesostructurization process. For CTABr-templated mesoporous films prepared by dip-coating with similar coating mixtures it was recognized that a modifiable steady state exists that is highly influenced by the humidity conditions.⁴ It has been observed that relative humidity in the range 70 – 80% favor formation of the cubic ($Pm3n$) mesophase even if a hexagonal ($p6m$) mesophase is first formed. Our results also suggest that by changing humidity in the atmosphere, water is encouraged to stay inside the coating favoring formation of micelles of high curvature ($Pm3n$ cubic mesophase); during this dynamic equilibrium state silica condensation takes place (probably also influenced by the higher water content), stabilizing the inorganic framework around the spherical (or semi-spherical) micelles. At the same time this local dilution at high humidity allows for viscosity to be lowered, resulting in greater mobility of non-volatile silica species and facile supramolecular self-assembly. Further time-resolved XRD experiments using CCD detection and Synchrotron radiation that follow the formation mechanism of CTABr-templated mesoporous films prepared by spin-coating are planned, these will help with the full characterization and understanding of the mesostructurization process at different humidities.

Another possibility to gain control over the mesostructurization process during the deposition of mesoporous films is to use different surfactant/silica ratios in the coating solutions. It is expected that in this way it could be possible to move along the CTABr/water/ethanol phase diagram and observe different liquid-crystal like mesophases. Figure 6.7 shows the GID pattern of the mesoporous film deposited from coating solution NPF2 (CTABr/silica = 0.18) at a relative humidity of 70%. The pattern is indexed in the hexagonal ($p6m$) mesophase structure with tubular channels running parallel to the sample

surface.¹ A hexagonal unit cell of 4.3 nm is calculated from the position of the (100) reflection ($a = 2/3^{1/2} \cdot d_{sp(100)}$)

In contrast to the mesoporous films deposited with the NPF1 coating solution (CTABr/silica = 0.15) at a relative humidity of 40% the three reflections typical for the ($p6m$) mesophase structure appear at higher intensities (see inset Figure 6.7). Barely any ellipsoidal diffraction ring showing disordered domains is observed. This suggests that a highly ordered mono-oriented hexagonal mesophase structure is formed. As for the NPF1 film deposited at a relative humidity of 40% the diffraction spots are localized on an ellipse associated with the one-dimensional contraction in the direction normal to the substrate and giving rise to a centered rectangular ($c2m$) mesophase structure.

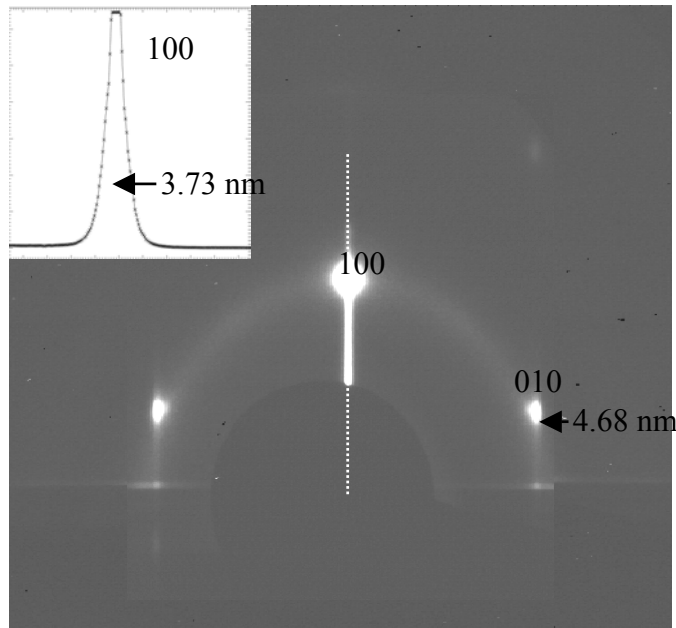


Figure 6.7. GID pattern of mesoporous film prepared at relative humidity of 70% from coating solution NPF2 (inset: intensity distribution along q_z vector).

The relationship between hexagonal ($p6m$) and center-rectangular ($c2m$) structures is given in Figure 6.8. The indexing of the structure can be done in center-rectangular ($c2m$) symmetry assuming that $a_r = 3^{1/2}b_r$ for the thermally not contracted structure. After one-dimensional contraction there is deviation of the shown relation due to the contraction of a_r .

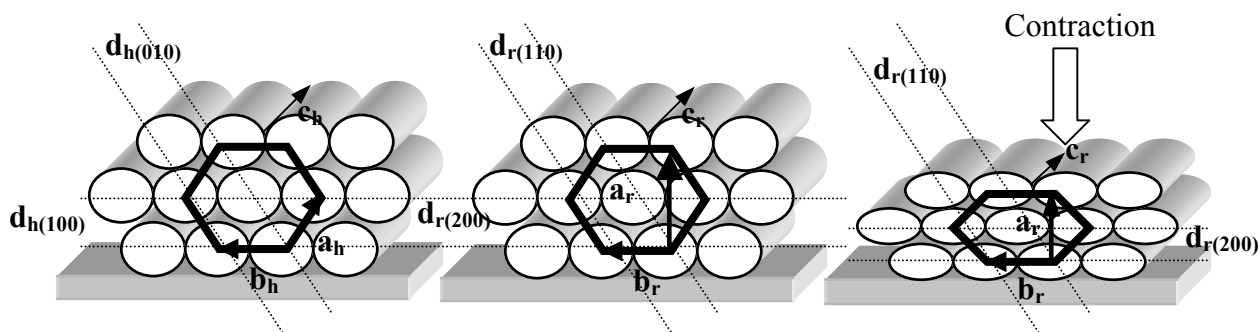


Figure 6.8. Schematic representation of the relationship between hexagonal ($p6m$) and center-rectangular ($c2m$) structures. The latter is considered to adequately describe the one-dimensional contraction.

For clarity the description “distorted hexagonal” ($p6m$) will be used for this structure in all cases when one-dimensional contraction normal to the substrate is evident. The distortion from the hexagonal mesophase structure is calculated to be 20% (6.2.) and is similar to that of the highly textured cubic ($Pm3n$) mesophase structure (22%). The organization of the mesophase structure after calcination (procedure B) is generally not preserved. In order to retain the mesostructural order after calcination the samples were additionally stabilized in vapor of 0.2M HCl at 60 °C for 6 h. Thus the silica framework is additionally condensed and therefore more thermally stable.

Figure 6.9. shows the plan-view TEM images of the NPF2 mesoporous films deposited at a relative humidity of 70%. Tubular mesopores aligned with the c -axis parallel to the surface (perpendicular to the electron beam) with pore-to-pore distance of about 4 nm are visible. This is in a good agreement with the d -spacing of 4.68 nm of the $\{010\}$ planes observed in the GID experiment (see above). The deviation in the results can come from the focusing conditions in the TEM, and the errors associated with the microscope optics (usually around 10%). More importantly, the TEM shows that different domain structures are formed with different in-plan orientation of the mesoporous channels (see Figure 6.7.a). The accepted mechanism of formation is similar to those proposed for the cubic ($Pm3n$) mesoporous films where the mosaic structure of domains with different in-plan orientations is observed (see Figure 6.3.e).

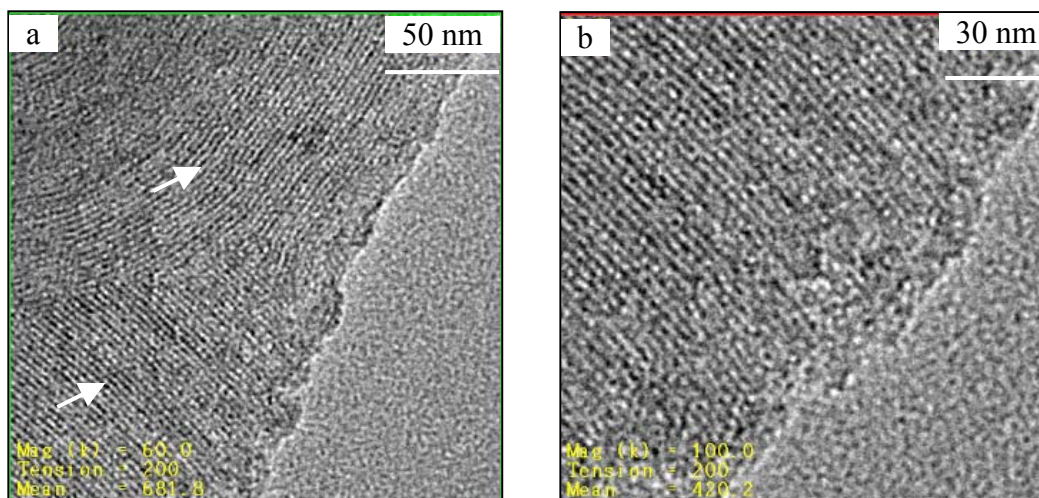


Figure 6.9. Plan-view TEM images taken at different magnifications of the NPF2 mesoporous film deposited at 70% relative humidity. Domains with different in-plane orientations are shown with arrows.

In contrast to the hybrid hexagonal-worm-like mesoporous film (NPF1 film deposited at 40% RH), here it is evident that the excellent out-of-plane (along the film thickness) hexagonal order is obtained. This is attributed to the increased surfactant concentration in the coating solution that drives the mesophase structure along the phase diagram from cubic (spherical micelles) to hexagonal (tubular micelles).

The structural information for the CTABr-templated mesoporous films based on the RXRD is summarized in Figure 6.10. It shows the RXRD patterns of the mesoporous films prepared from two different coating solutions, NPF1 (CTABr/silica = 0.15) and NPF2 (CTABr/silica = 0.18) at relative humidity of 40 and 70%, respectively. It should be noted that the scans in the RXRD experiment correspond to the intensity distributions along the q_z vector (see Chapter 4.1.) in the GID measurements. The RXRD pattern in Figure 6.10.a corresponds to the cubic ($Pm\bar{3}n$) mesophase structure prepared with CTABr/silica ratio of 0.15 at relative humidity of 70%. Using the same coating solution at relative humidity of 40% one-dimensional hexagonal + worm-like structure is formed (Figure 6.10.b). By increasing the CTABr/silica ratio to 0.18 highly ordered two-dimensional hexagonal mesophase structure is obtained in the whole interval of relative humidity 40 - 70%. By

increasing the relative humidity in the deposition chamber a small decrease in the d-spacing of the first-order reflection is observed. This is attributed to swelling effects due to the increased water content in the films.

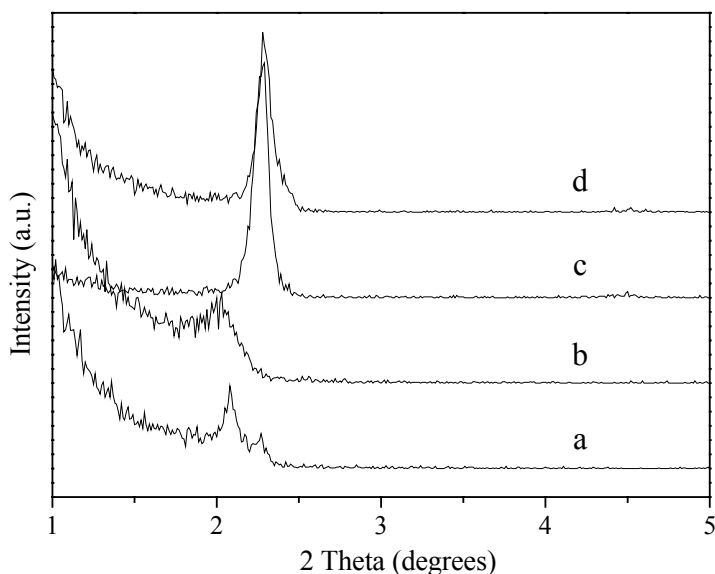


Figure 6.10. shows the XRD patterns of the mesoporous films prepared from NPF1 coating solution (CTABr/silica = 0.15) at a) 70% and b) 40%, relative humidity and NPF2 coating solution (CTABr/silica = 0.18) at c) 70% and d) 40% relative humidity.

It has been shown that the structure of the CTABr-templated mesoporous films can be controlled by varying the relative humidity in the deposition chamber and CTABr/silica ratios in the coating solutions. Thus, three types of mesophase structures were obtained, namely three-dimensional ($Pm3n$) cubic consisting of close-packed spherical and elliptical micelles, two-dimensional ($p6m$) hexagonal + worm-like structure and highly ordered two-dimensional ($p6m$) hexagonal structure with tubular channels aligned parallel to the substrate surface. Due to the successive drying and calcination process, these phases exhibit one-dimensional contraction in the direction normal to the substrate resulting in distortion of the initial liquid-crystalline structure. It is worth to mention that the immobilization of silica networks by the self-assembly mechanism resulting from rapid solvent evaporation of

CTABr/silica/ethanol/water coating solutions is a promising way to obtain mesophase structures like cubic ($Pm3n$) that have not been observed with CTABr using synthetic approaches other than EISA.

6.3.1.2. Pluronic123 - templated mesoporous films

As shown in Chapter 5, nonionic amphiphilic triblock copolymers like Pluronic123 can be used to direct the formation of mesostructures with larger pore sizes, thicker walls, and superior thermal stability. Mesostructured silica films prepared with nonionic surfactants have been less well studied but showed interesting structural characteristics⁶. Here the structural characterization of the Pluronic123-templated films is given combining the results of RXRD, GID and TEM measurements.

Figure 6.11. shows the GID patterns of a mesoporous film prepared from coating solution NPF3 at a relative humidity of 40%. The patterns are taken in the low 2θ region (close to the specularly reflected beam indicated with an arrow) without a beam stop for a very short exposition time in order not to saturate the CCD detector (Figure 6.11.a) and in the higher 2θ region (Figure 6.11.b) using the usual set-up.

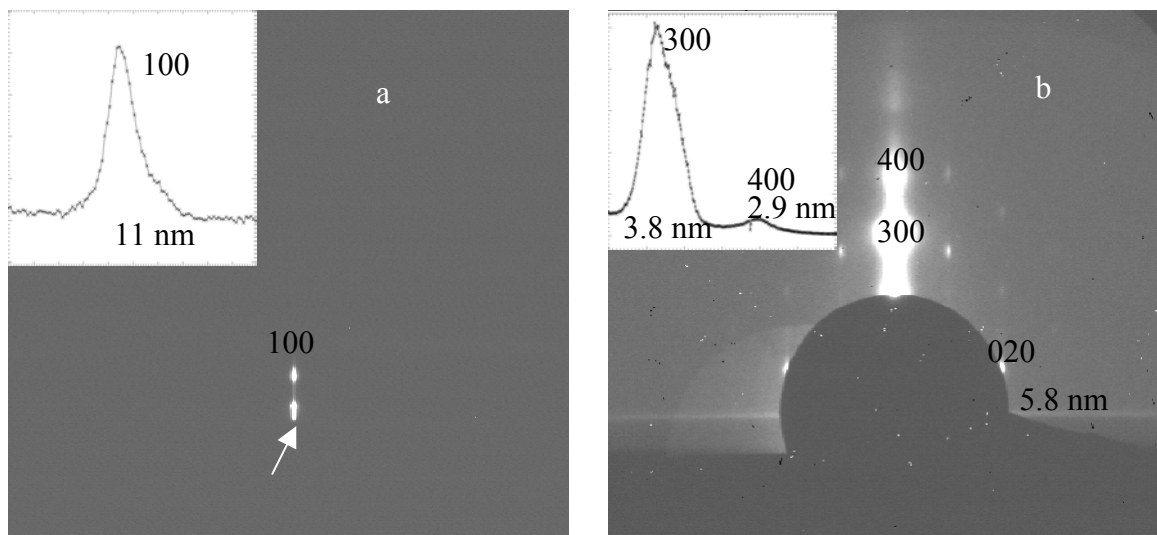


Figure 6.11. GID patterns of the as-deposited mesoporous film prepared at a relative humidity of 40% from coating solution NPF2 taken in a) low 2θ and b) high 2θ regions (inset: intensity distribution along q_z vector).

The pattern in Figure 6.11a shows only one reflection at $d_{sp} = 11$ nm, the next order reflections of the same film show several diffraction spots that can be indexed in the ($p6m$) mesophase structure with unit cell of 12.6 nm calculated from the position of the 100 reflection ($a = 2/3^{1/2} \cdot d_{sp(100)}$)^{5,6}. As expected, the unit cell size is considerably larger than that of the CTABr-templated hexagonal films (4.3 nm). The absence of the (010) reflection in the pattern shown on Figure 6.11.a is a result of the short exposure time. This fact hinders the evaluation of the degree of one-dimensional contraction normal to the substrate during the deposition. Most importantly, highly ordered two-dimensional hexagonal mesophase structure with larger mesoporous channels running parallel to the substrate surface is obtained as evidenced from the large number of high-order reflections (Figure 6.11.b).

Further characterization of the as-deposited NPF3 mesoporous film was obtained by TEM investigations. Figure 6.12. shows plan-view TEM images taken at two different magnifications.

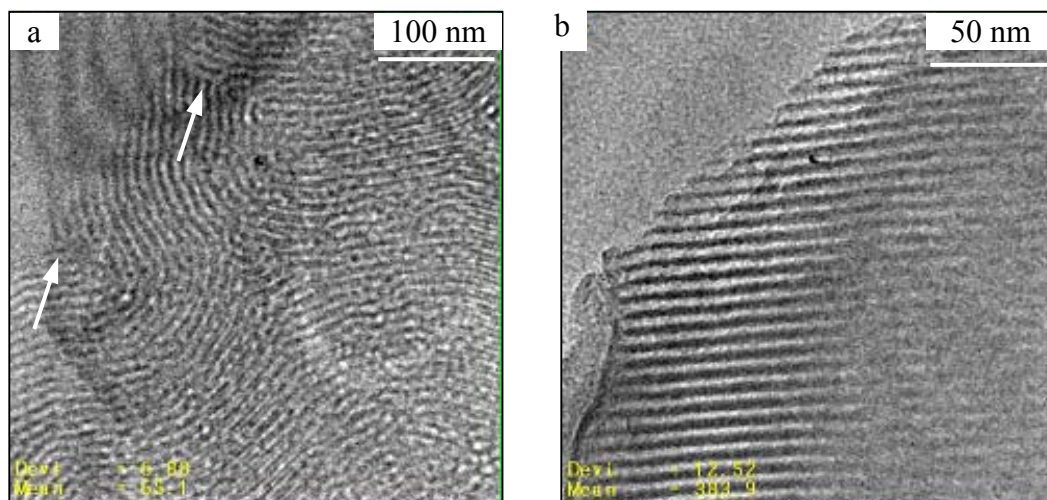


Figure 6.12. Plan-view TEM images taken at different magnifications of the NPF2 mesoporous film deposited at 40% relative humidity. Domains with different in-plane orientations having finger-print structure are shown with arrows.

Meandering channels oriented parallel to the substrate surface (perpendicular to the electron beam) forming finger-print structures can be observed. As for the CTABr-templated samples, it is suggested that disorder-to-order transformation is randomly initiated and is not

affected by the forces induced from the spin-coating process. It is accepted that a mosaic structure with hexagonally ordered domains having different in-plan orientations are formed. The pore-to-pore distance measured from Figure 6.12.b is 8.3 nm and corresponds to a hexagonal unit cell of 9.6 nm that is smaller than that calculated from the GID experiment. (about 12% deviation). Additionally, the mesopore walls of the as-deposited NPF3 film appear thicker in comparison to the hexagonal CTABr-templated film (NPF2).

After calcination (procedure B, Chapter 5.3.2) the mesophase structure is preserved (Figure 6.13.). The reflections are clearly localized on ellipses explained again by the one-directional contraction during the template removal resulting in the centered-rectangular mesophase structure. The comparison of the initial hexagonal ($p6m$) structure and resulting ($c6m$) center-rectangular structures is given in Figure 6.8.

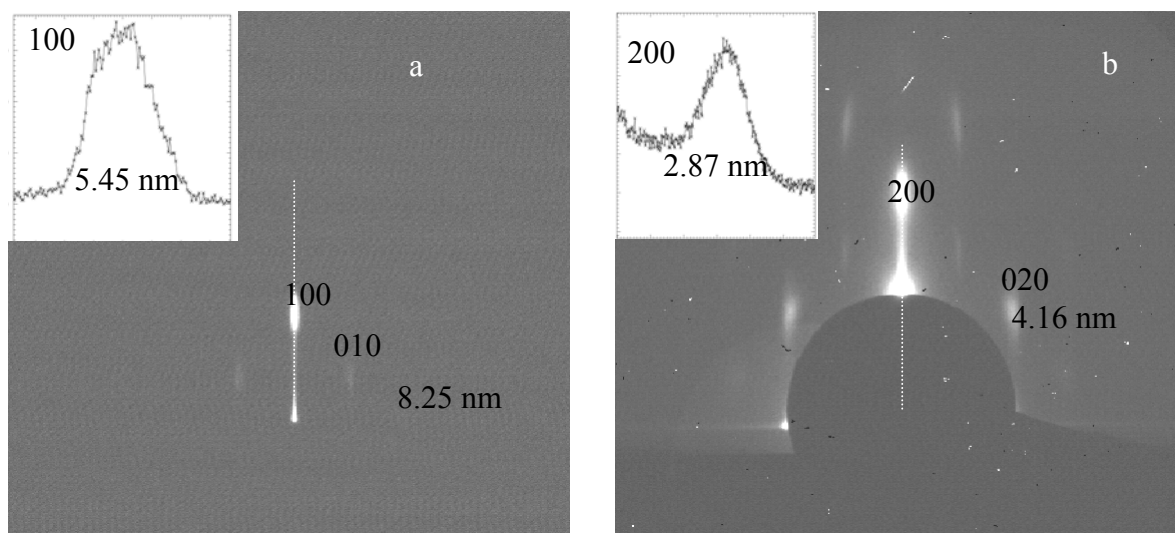


Figure 6.13. GID patterns of a calcined mesoporous film prepared at a relative humidity of 40% from coating solution NPF3 taken in a) low 2θ and b) high 2θ regions (inset: intensity distribution along q_z vector).

The distortion of the hexagonal mesophase structure calculated from $\delta H = d_{sp(100)} - d_{sp(010)}/d_{sp(100)}$ is 34% and is much higher than that of CTABr-templated films calcined at the same conditions. The diffraction spots appear attenuated, broader, and show lower intensity that may be attributed to decreased mesostructural order. The intensity distribution along the q_z vector (out-of-plane diffraction) show only two diffraction peaks (for comparison, the as-

deposited sample showed reflections till the fourth order) that are indexed as the first and second order reflections of the hexagonal structure.

Mesoporous films deposited with the same coating solution (NPF3) at different relative humidities of 40 – 70% show similar diffraction patterns with sharp and very intensive first-order reflections with its second and third order harmonics typical for highly ordered hexagonal mesophase structures. After calcination the mesophase structures were preserved for all samples.

The self-assembly process for the formation of surfactant/silica mesophases can be controlled, as shown for the CTABr-templated mesoporous films, by changing the surfactant/silica ratio in the coating solutions. In order to examine the effect of the Pluronic123/silica ratio on the mesophase structure, films were prepared from coating solution NPF4 (higher Pluronic123/silica ratio). Figure 6.14. shows the RXRD pattern of the as-deposited mesoporous film prepared from NPF4 coating solution at a relative humidity of 40%.

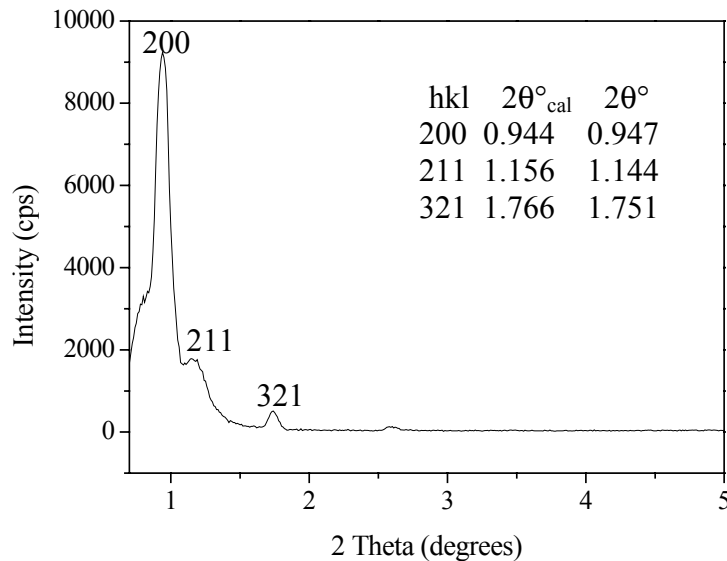


Figure 6.14. RXRD pattern of the as-deposited mesoporous film prepared from NPF4 coating solution at a relative humidity of 40% (inset: 2θ values of the calculated and measured Bragg peaks).

The pattern can be indexed in a cubic ($Im3m$) mesophase structure as first proposed by Stucky and co-workers⁷. It is assumed that this structure is equivalent to the SBA-16 powder mesoporous material. It consists of close-packed spherical micelles and is templated by Pluronic F127 surfactant (tri-block copolymer with increased molar ratio of the hydrophilic blocks). Here, for the first time, cubic ($Im3m$) mesoporous films templated with Pluronic123 and prepared *via* spin-coating are observed. The table of the observed and calculated 2θ values is shown as an inset in Figure 6.14. The calculated cubic unit cell is 18.7 nm and corresponds to that observed by Stucky and co-workers. Having in mind that in the RXRD experiment only the lattice planes oriented parallel to the substrate surface can be detected (see Chapter 4.1.) it is suggested that the ($Im3m$) mesoporous film is oriented with the (200) planes parallel to the substrate surface. The appearance of the (211) Bragg peak in the pattern of the NPF4 sample suggests that domains with (211) lattice planes parallel to the substrate surface may also co-exist. Figure 6.15. shows a schematic representation of the possible orientations of the body-centered cubic ($Im3m$) mesophase structure and the corresponding two-dimensional plan views parallel to the substrate surface.

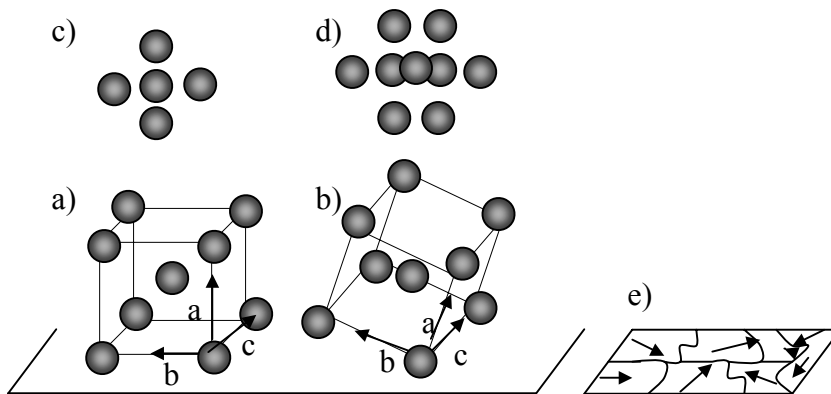


Figure 6.15. Schematic representation of the ($Im3m$) cubic mesophase oriented with a) [200] and b) [211] zone axes perpendicular to the substrate, c) and d) corresponding plan-views parallel to the substrate surface and e) mosaic structure of the mesoporous film showing no in-plane orientation.

The TEM images of the NPF4 mesoporous film taken at two different magnifications are shown in Figure 6.16. It can be seen that the structure is extended in two different domains (shown with arrows) corresponding to two different orientations with respect to the film surface as shown in Figure 6.15. The pore-to-pore distance (see Figure 6.16.b) is about 5 nm. The existence of different domain structures is explained by the appearance of different nucleation centers giving disorder-to-order transition during the film preparation that are unaffected from the shear forces induced during spin-coating.

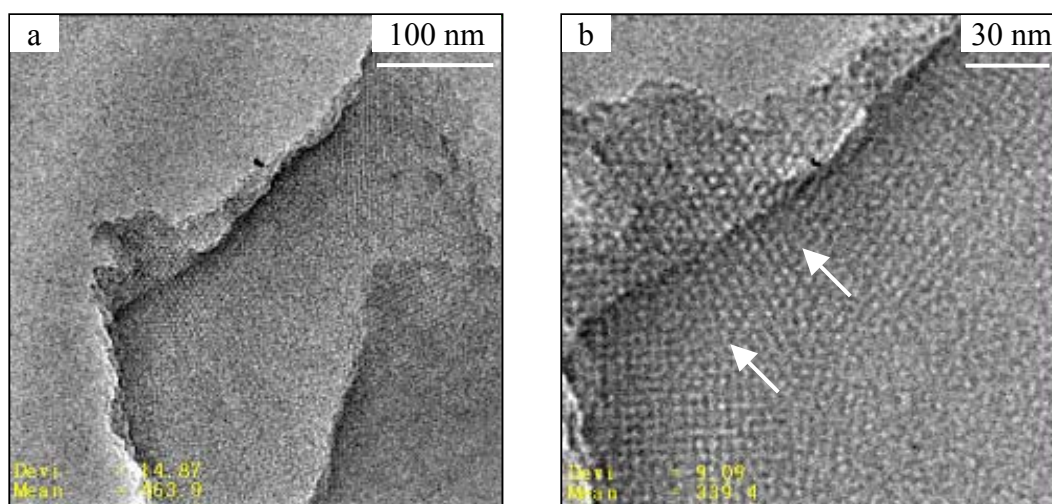


Figure 6.16. TEM images of NPF4 mesoporous film at two different magnifications. The arrows show two different domains of the $(Im3m)$ cubic mesophase.

After calcination the mesophase structure is preserved only in cases when calcination procedures with additional thermal stabilization steps are applied. Figure 6.17. shows the RXRD pattern of the calcined cubic $(Im3m)$ mesoporous film with a unit cell of 11.6 nm. The calculated one-dimensional contraction normal to the substrate plane is 37%. The results are consistent with the observed contraction of the mesophase structure for the hexagonally ordered film deposited from the NPF3 coating solution (see above).

Generally, it seems that the external conditions, especially the relative humidity is likely to be “the missing link” to the reproducible, controlled formation of mesostructured thin films that has been a challenge in the last few years. Therefore, the approach based on fixing the silica/surfactant ratio and the hydrolysis-condensation process of the silica source

should be complemented by a series of other variables such as relative humidity, and post-synthesis thermal and stabilization treatments in order to obtain reproducible results, independent of operational, geographical, or seasonal features.

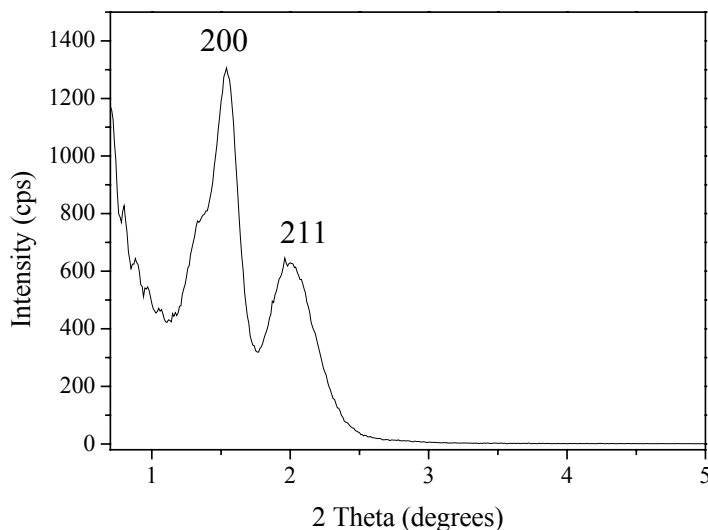


Figure 6.17. RXRD pattern of calcined mesoporous film prepared from NPF4 coating solution at relative humidity of 40%.

6.3.2. Sorption properties of the mesoporous films – N_2 sorption studies with a QCM device.

Pore accessibility of the ordered mesoporous films has long been a matter of debate due to the lack of a facile method for the characterization of the pore accessibility. Usually it is accepted that the mesoporous films having three-dimensional porous systems should give easy access to the internal surface⁸. In order to probe pore accessibility of the calcined mesoporous films and to obtain information on the specific surface area, pore size and total pore volume, N_2 sorption measurements were performed. The principle of the N_2 sorption experiments with the QCM device was explained in Chapter 4.4. The raw data (Figure 6.18.) are collected as frequency changes with time at liquid nitrogen temperature while by introducing small amounts of sorptive. At every relative pressure 300 s equilibration time is given resulting in the steps shown in Figure 6.18. After applying the Sauerbrey equation (Chapter 4.4.) the change in mass is calculated at every equilibration step, resulting in an isotherm as the one shown in Figure 6.19. Here, the N_2 sorption isotherm taken at $-196\text{ }^\circ\text{C}$ of

the calcined cubic ($Pm3n$) mesoporous film prepared from NPF1 coating solution is shown. The sorption isotherm shows strong adsorption between N_2 relative pressures of 0.0 and 0.4 and no significant sorption at higher relative pressures indicating no interparticle meso- or macroporosity.

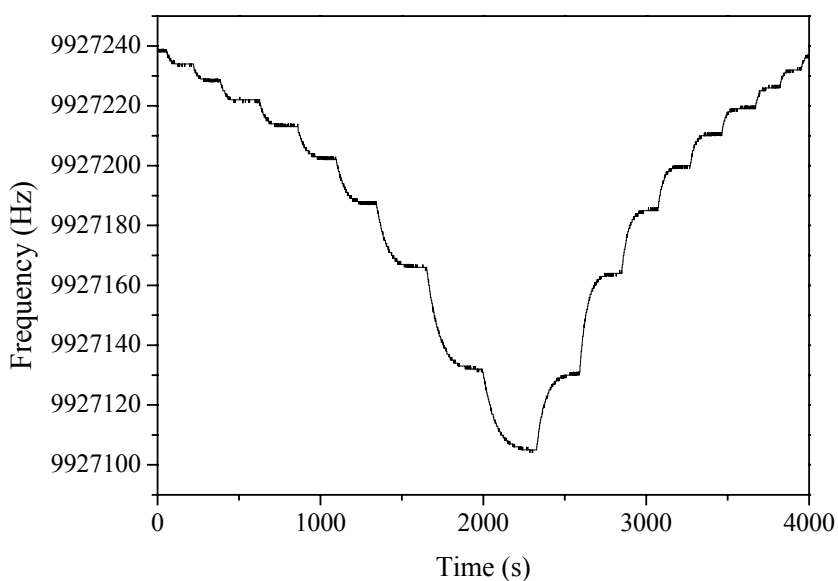


Figure 6.18. N_2 sorption raw data taken at different relative pressures at -196°C with the QCM device.

The lack of hysteresis and absence of any appreciable sorption at relative pressures above 0.4 is consistent with other sorption data of thin mesoporous films prepared with CTABr as a structure directing agent⁸. Using the BET and BJH models, the specific surface area and pore size distribution of the mesoporous film is calculated (see Chapter 4.4.). The total pore volume adsorbed is calculated from the sorption point at about 0.98 relative pressure. The calculated values are shown in Table 6.1. The pore size distribution of the CTABr-templated film is in agreement with that obtained for CTABr-templated mesostructured monoliths (Chapter 5.4.2.). The total pore volume adsorbed is slightly lower than that observed for the CTABr-templated mesostructured monoliths and MCM-48 material. This can be explained by the partial inaccessibility of the porous system due to the

preferred orientation of the mesoporous film. Most importantly, the cubic ($Pm3n$) mesoporous film shows considerable N_2 sorption capacity close to that of the powdered mesoporous materials that is due to the easy pore accessibility.

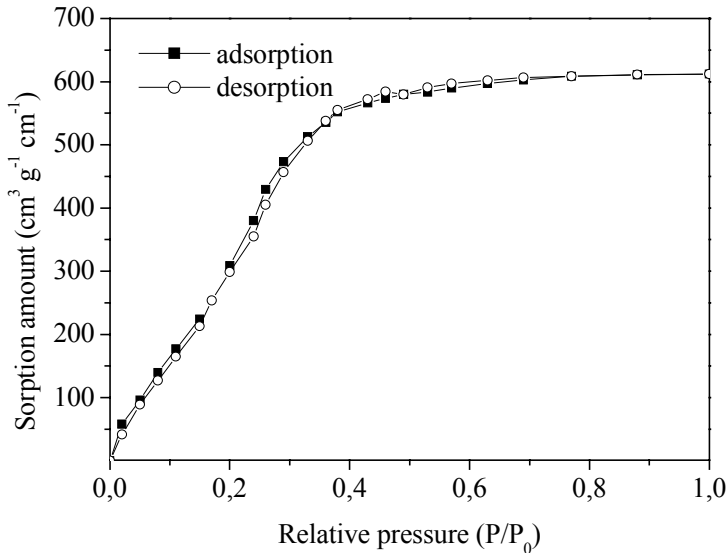


Figure 6.19. N_2 sorption isotherms of the ($Pm3n$) cubic mesoporous film deposited from NPF1 coating solution at 70% relative humidity measured with the QCM device at -196°C .

Table 6.1. Specific surface area (S_{BET}), total pore volume adsorbed (V_t), and pore size distribution (D_{BJH}) of different types of mesoporous materials prepared as powders and thin films.

Type of mesoporous material	S_{BET} (m^2g^{-1})	V_t (cm^3g^{-1})	D_{BJH} (nm)
CTABr-templated film	1462	0.94	2.1
MCM-48	1574	0.96	2.19
Pluronic123-templated film	174	0.57	4.5
SBA-15	845	1.42	6.3

Figure 6.20. shows the N_2 sorption isotherm of the calcined ($p6m$) hexagonal mesoporous film prepared from coating solution NPF3. The sorption isotherm shows

adsorption and desorption steps in the region 0.5 – 0.9 relative pressures characteristic for the capillary condensation in larger mesopores. Clear hysteresis between the adsorption and desorption branch of the isotherm is observed. This phenomenon is well known for the SBA-type powder materials templated with triblock polymers and is explained by the bottle-shaped tubular mesopores (see Chapter 4.4 and references therein). Apparently, the shape of the isotherm is typical for Pluronic123-templated mesoporous material. The calculated BET surface area, pore size distribution (BJH), and total pore volume adsorbed are shown in Table 6.1. Comparing the data in Table 6.1. to that for SBA-15 material, it is clear that BET and the total pore volume adsorbed are considerably decreased. This fact is explained by the decreased pore accessibility due to the preferential orientation of the mesoporous channels parallel to the substrate surface. In this case sorption is possible only through the interface between the ordered domains. The observed sorption step is evidence that such sorption is only feasible in a part of the film structure (smaller accessible volume) as compared to the three-dimensional mesoporous system. Till now no sorption isotherm of Pluronic123-templated films was discussed in the literature.

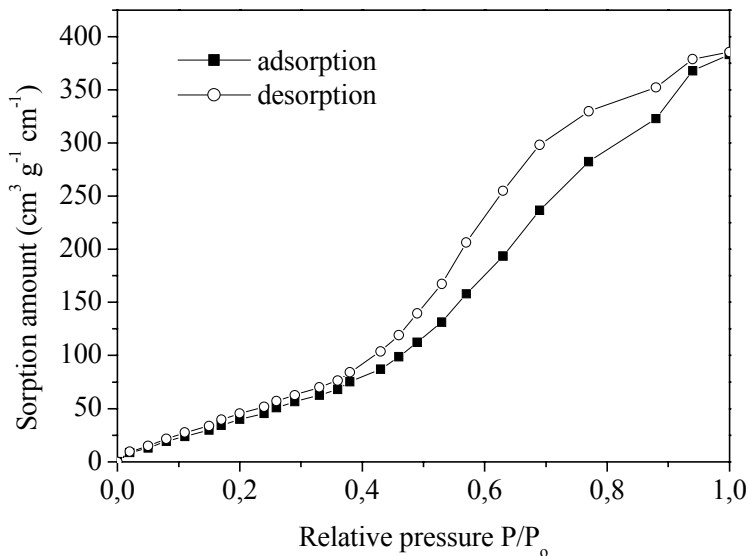


Figure 6.20. N₂ sorption isotherms of the (*Pm3n*) cubic mesoporous film deposited from NPF3 coating solution at 70% relative humidity measured with a QCM device.

6.3.3. Surface morphology and thickness of the mesoporous films – AFM and SEM studies.

Many nanotechnological applications require smooth and homogeneous film surfaces. In order to estimate the surface roughness and homogeneity of the deposited mesoporous films, an AFM investigation in contact mode was undertaken.

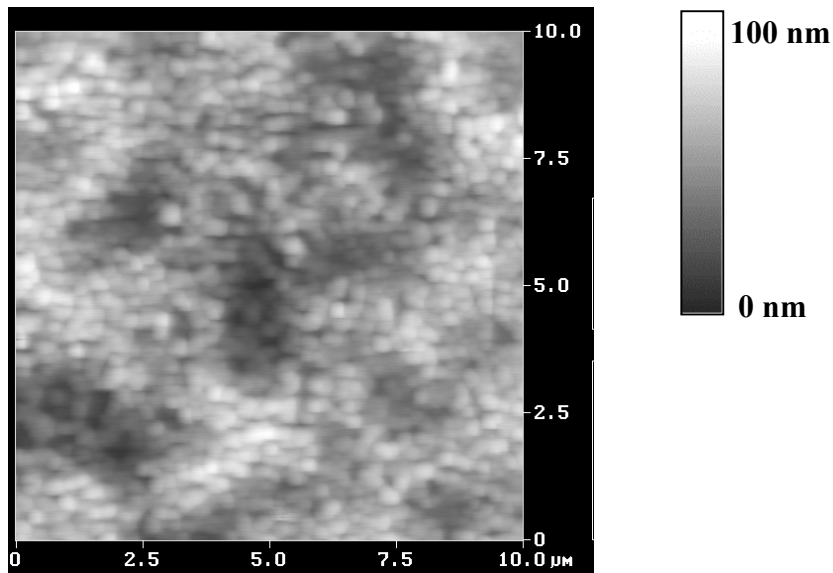


Figure 6.21. AFM image (contact mode) of the calcined mesoporous film deposited from NPF1 coating solution.

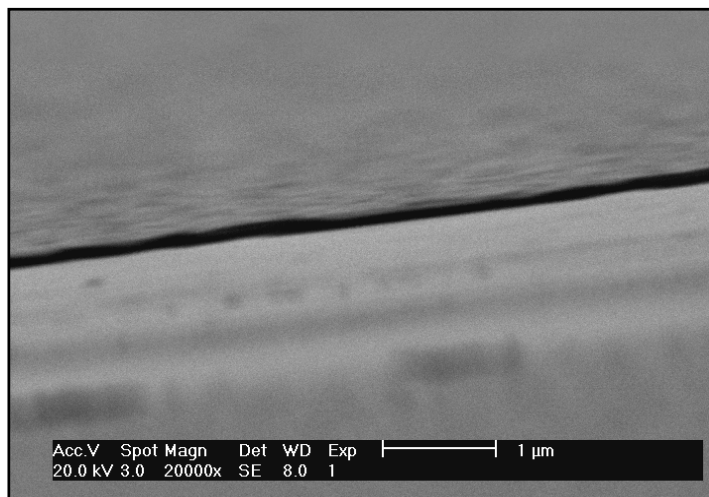


Figure 6.22. Side-view SEM image of the calcined mesoporous film deposited from NPF1 coating solution.

Figure 6.21. shows the AFM image of the calcined CTABr-templated mesoporous film prepared from the NPF1 coating solution. The calculated surface roughness from the whole image frame shown in Figure 6.21 is about 11 nm. The film surface shows spherical objects with diameters of less than 500 nm. The shape and form of these objects might be explained by the existence of a mosaic structure of the film composed of ordered domains (see above).

The corresponding side-view SEM image taken at a scratched part of the film is shown in Figure 6.22. The thickness is estimated to be around 120 nm. The film appears homogeneous and continuous over millimeter scale; no bumpy or uneven structures were observed.

The AFM image of the calcined Pluronic123-templated film prepared from coating solution NPF3 is shown in Figure 6.23. The surface roughness is about 9 nm. Clearly seen are worm-like type of surface objects curling over several micrometers. This kind of morphology is typical for the SBA-15 material and comes from hexagonally ordered domains that have worm-like shapes (see Chapter 5). Furthermore, the TEM images of the same sample showed curling, worm-like domains with characteristic dimensions of more than several microns in length. The thickness of the NPF3 film is around 100 nm as seen from the side-view SEM image (Figure 6.24.).

Generally, the thickness, surface roughness and homogeneity of the mesoporous films can be controlled by changing the deposition speed and the relative humidity in the deposition chamber. Films as thin as 60 – 70 nm can be prepared by increasing the deposition speed during the spin-coating to more than 4000 rpm (note that usually the films in this study are prepared at deposition speeds of 2000 rpm). Usually films deposited at higher relative humidities showed inferior optical quality with an uneven and inhomogeneous surface. Another possibility to change the thickness of the mesoporous films is to use different dilutions of the coating solutions or by altering the hydrolysis-condensation of TEOS in the first synthesis step. These parameters will change the viscosity of the coating solution and will affect the mesoporous film thickness.

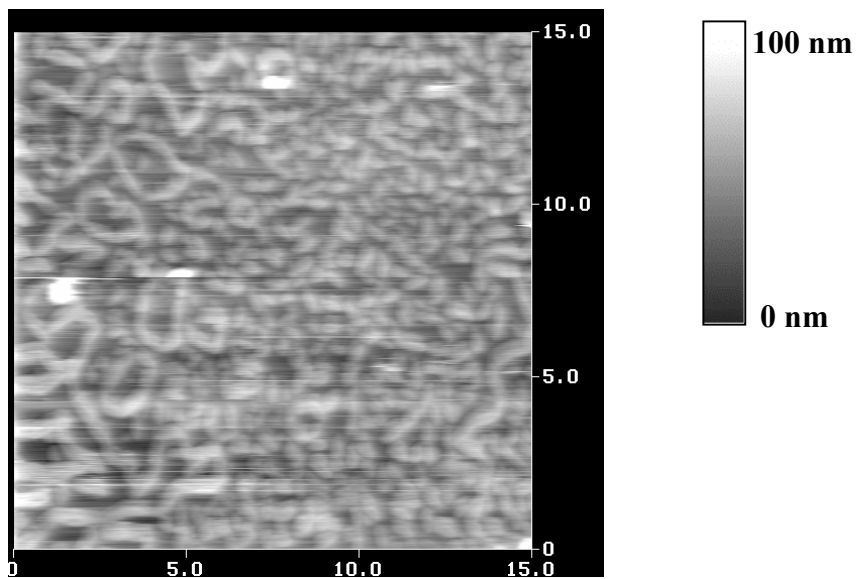


Figure 6.23. AFM image (contact mode) of the calcined mesoporous film deposited from NPF3 coating solution

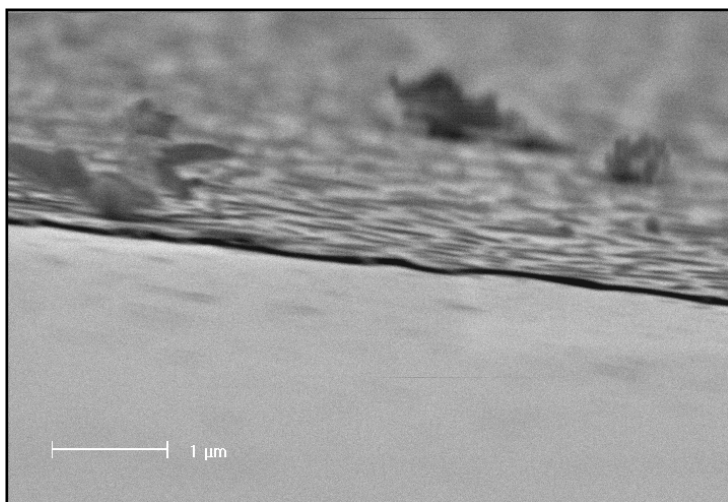


Figure 6.24. Side-view SEM image of the calcined mesoporous film deposited from NPF3 coating solution.

6.4. Conclusions and Perspectives

Thin mesoporous films have been prepared on different substrates (silicon wafer, glass, gold) by applying spin-coating of silica/surfactant/water/ethanol coating solutions under the conditions of the evaporation-induced self assembly method (EISA). Two types of established structure directing agents for bulk mesoporous phases, cationic CTABr surfactant and amphiphilic tri-block copolymer Pluronic123, have been applied. In both cases, well-ordered and stable silica mesoporous films have been obtained showing three-dimensional cubic or two-dimensional hexagonal structures. Typical for the mesoporous films is the preferred orientation (single-crystal orientation) of the domains that are arranged in a mosaic structure. It is shown that many different parameters, not only those based on the composition of the coating solution but also “external” parameters such as relative humidity are very important for the reproducible preparation of different mesophase structures. Furthermore, these “external” parameters can be used to tailor the mesophase symmetry and structure. A combination of GID, RXRD, and TEM analysis enabled rather complete structural characterization of the mesoporous films. N₂ sorption measurements with a QCM device were used to explore the pore accessibility of the mesoporous films. Certainly, additional structural in-situ studies such as in-situ GID measurements at different “external” parameters and specific compositions of the coating solution should be performed in the future. In this respect, it will be desirable to control the alignment of tubular mesophase structures (for example, hexagonal *p6m* structure) in orientations that allows easy access to the porous system (c-axis perpendicular to the substrate). For example, such an alignment may be possible in an electric field, assuming a re-orientation, can be caused by the differences in the dielectric constant at the silica/surfactant interface. Unfortunately, many other parameters (many of them discussed in this Chapter) are also playing an important role in the disorder-to-order transition and the exact experimental conditions for such an alignment may be still difficult to find.

References

- ¹ D. Grosso, F. Babonneau, P.-A. Albouy, H. Amentisch, A. R. Balkenende, A. Brunet-Bruneau, J. Rivory, *Chem. Mater.*, **2002**, 14, 931.
- ² D. Sakamoto, M. Kaneda, O. Terasaki, D. Y. Zhao, J. M. Kim, G. D. Stucky, H. J. Shin, R. Ryoo, *Nature*, **2000**, 408, 449.
- ³ M. Klotz, P.-A. Albouy, A. Ayrat, C. Menager, D. Grosso, A. Van der Lee, V. Caball, F. Babonneau, C. Guizard, *Chem. Mater.*, **2000**, 12, 1721.
- ⁴ F. Cagnol, D. Grosso, G. J. De A. A. Soler-Illia, E. L. Crepaldi, F. Babonneau, H. Amentisch, C. Sanchez, *J. Mater. Chem.*, **2003**, 13, 61.
- ⁵ D. Grosso, A. R. Balkenende, P.-A. Albouy, A. Ayrat, H. Amentisch, F. Babonneau, *Chem. Mater.*, **2001**, 13, 1848.
- ⁶ P. C. Alberius, K. L. Fridell, R. C. Hayward, E. J. Kramer, G. D. Stucky, B. F. Chmelka, *Chem. Mater.*, **2002**, 14, 3284.
- ⁷ D. Zhao, P. Yang, N. Melosh, J. Feng, B. Chmelka and G. D. Stucky, *Adv. Mater.*, **1998**, 10, 1380.
- ⁸ Y. Lu, R. Ganguli, C.A. Drewien, M.T. Anderson, C.J. Brinker, W. Gong, Y. Guo, J. I. Zink, *Nature* **1997**, 389, 364.

Chapter 7. Growth of carbon nanotubes by catalytic decomposition of acetylene on Fe-containing mesoporous films.

7.1. Introduction

7.2. Experimental

7.2.1. Preparation of Fe-containing mesoporous films and monoliths

7.2.2. Growth of carbon nanotubes

7.2.3. Characterization

7.3. Results and Discussion

7.3.1. Nature of precursor species in Fe-containing coating solutions

7.3.2. Mesophase structure and surface morphology of Fe-containing mesoporous films and monoliths

7.3.3. Growth of carbon nanotubes

7.4. Conclusions and Perspectives

7.1. Introduction.

The necessity of miniaturization of electronic devices motivates the development of new synthetic strategies for the construction of materials suitable for molecular electronics (see Chapter 1). The properties of carbon nanotubes and their fundamental importance as potential basic structural units for future nanotechnology have been covered in Chapter 3. An assembly of one-dimensional molecular wires such as carbon nanotubes with their unique electronic properties, embedded in an ordered channel matrix of an insulating material such as mesoporous silica represents an interesting architecture for nanoelectronics^{1,2}. Molecular sieves loaded with transition metals have been used as catalytic supports to prepare quasi-aligned carbon nanotubes by thermal decomposition of hydrocarbons^{3,4,5,6}. Depending on the type of catalytic metal center, carbon source, and molecular sieve used as a catalytic support, carbon nanotubes with different diameter and nanotube alignment were prepared. In this system, the templating role of the porous system is not yet understood in detail. It should be noted that all these structures were prepared as powders which limits the addressability and hinders the orientational alignment of the encapsulated nanostructures. Recently, aligned carbon nanotube

patterns were prepared on cubic mesoporous films by decomposition of acetylene⁷. In this study, patterned mesoporous films were deposited using the micromolding-in-capillaries technique (MIMIC) combined with preformed Fe-containing silica/surfactant solutions.

In this Chapter a synthetic approach that applies the conditions of the EISA method for the preparation of Fe-loaded mesoporous films and Fe-containing monoliths is presented together with other approaches for the introduction of the catalytically active Fe species such as wet impregnation or Fe-sputtering. The aim was to show that these supports are suitable for the growth of carbon nanotubes by catalytic decomposition of acetylene. In most cases, the preparation of the catalytic Fe-containing mesoporous support was performed by direct coating of preformed acidic silica/surfactant/ethanol/iron nitrate solutions following the conditions of the evaporation-induced self-assembly method. Important aspects addressed in this Chapter are: the nature of the coating solutions, structure and stability of the Fe-containing mesoporous films, different ways for the incorporation of Fe species, and optimal conditions for the growth of carbon nanotubes by decomposition of acetylene at 700°C.

7.2. Experimental

7.2.1. Preparation of Fe-containing mesoporous films and monoliths

Clear precursor silica/surfactant assemblies were prepared by mixing acid hydrolyzed tetraethoxy silane (TEOS 98%, Aldrich) at 60 °C with an ethanolic solution of PEO-PPO-PEO tri-block copolymer (Pluronic 123 - BASF) as described for pure silica mesoporous films (see Chapter 6.2.1.). Iron was introduced during the mixing of the two solutions as $\text{Fe}(\text{NO}_3)_3 \cdot 9\text{H}_2\text{O}$, and resulted in formation of a yellow transparent sol. The final molar ratio of the coating solutions were:

NPFe1: 1TEOS: 0.017Pluronic 123: 0.06HCl: 48.8EtOH: 26.6H₂O: 0.1Fe(NO₃)₃·9H₂O

NPFe2: 1TEOS: 0.017Pluronic 123: 0.06HCl: 48.8EtOH: 26.6H₂O: 0.2Fe(NO₃)₃·9H₂O

The coating solutions were aged at least 2 h prior to the preparation of the thin films. The mesoporous films were deposited on acetone cleaned silicon wafers (25 x 25 mm) by spin-coating (SCS P6700) at a rotation speed of 2000 rpm at room temperature and relative

humidity of 40%. For comparison, monoliths were also prepared by slow evaporation of the same coating solutions (deposited drop-wise on silicon wafers or glass petri-dishes and dried at room temperature for 24 h). To obtain thermally stable mesoporous films and monoliths that can be used for high temperature growth of carbon nanotubes calcination procedure D (Figure 5.1., Chapter 5.3.2.) was applied.

Other approaches for the incorporation of catalytically active Fe species are as follows. An Fe-layer was deposited on pre-cleaned silicon wafers by sputtering, using modular high vacuum coating system (BAL-TEC MCS 010). The thickness of the Fe layer (2 – 4 nm) was measured in-situ with a QCM device coupled to the coating system. Pure silica mesoporous films were deposited on this support by spin-coating employing the coating solutions NPF3 (two-dimensional hexagonally ordered films) and NPF4 (three-dimensional cubic films) (see Chapter 6.2.1.). The structural properties and surface morphology of these films do not differ from those reported in Chapter 6.3.

Fe species were also introduced by an incipient wetness impregnation technique. In a standard impregnation procedure, $\text{Fe}(\text{NO}_3)_3 \cdot 9\text{H}_2\text{O}$ was dissolved in technical ethanol resulting in a 3 wt% $\text{Fe}(\text{NO}_3)_3 \cdot 9\text{H}_2\text{O}$ solution and acidified with 2 M HCl till pH 1. Calcined pure silica mesoporous films (calcination procedure D, Figure 5.1., Chapter 5.3.2.) prepared from coating solutions NPF3 and NPF4 (see Chapter 6.2.1.) were impregnated for 24 h at room temperature. Finally the films were washed with ethanol and dried at room temperature.

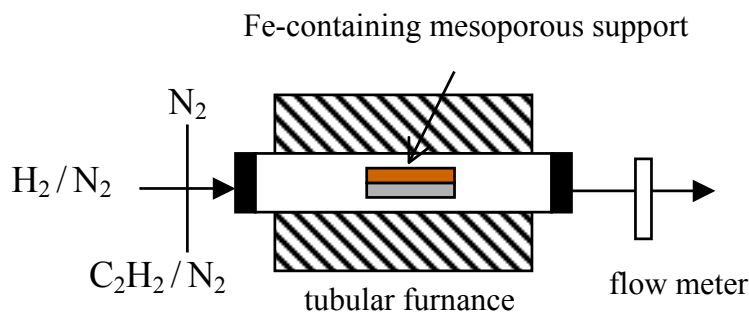


Figure 7.1. Set-up for the growth of carbon nanotubes by catalytic decomposition of acetylene at 700 °C.

7.2.2. Growth of carbon nanotubes.

The Fe-containing mesoporous films were reduced in a 5% H₂ in nitrogen flow in the temperature interval of 550 - 700 °C (0.5 °C/min ramping) for 4 h and were directly used for the carbon nanotube synthesis. The carbon nanotubes were grown from the Fe-loaded mesoporous films by catalytic decomposition of 10% acetylene in nitrogen in a tubular reactor (Figure 7.1.). The carbon nanotube growth was conducted at 700 °C for times ranging from 10 to 60 min at different flow rates of the hydrocarbon source (see below).

7.2.3. Characterization

The silica/Pluronic123/ethanol/Fe(NO₃)₃.9H₂O precursor solutions were investigated with liquid ¹³C and ²⁹Si NMR spectroscopy prior to the film deposition. The particle size distribution in the coating solutions was followed with dynamic light scattering (DLS). The structure of the as-prepared and calcined mesoporous films and monoliths was determined by X-ray diffraction in the θ - θ scan mode (Scintag XDS 2000). The surface morphology and the thickness of the mesoporous films were determined from the scratched parts of the films by scanning electron microscopy (SEM) (Philips XL 40). The growth of the carbon nanotubes was followed by SEM (Philips XL 40) and Raman spectroscopy (Bruker Equinox 55 - 106v/S spectrometer equipped with a Raman module - 9395 cm⁻¹ laser, 4 cm⁻¹ resolution, 10 mW laser power, 2000 scans). The structure of isolated carbon nanotubes was investigated with transmission electron microscopy TEM (JEM 2010 TEM operating at 200 kV).

7.3. Results and Discussion.

7.3.1. Nature of precursor species in Fe-containing coating solutions

The ²⁹Si NMR spectrum (Figure 7.2.) of the NPF₂ coating solution aged for 5 days is compared to the that of the silica/Pluronic123/ethanol coating solution (NPF₄, Chapter 5.2.1.) aged for the same time. The two signals at -90 ppm and -100 ppm in Figure 7.2.a are assigned to the Q² and Q³ silicon atoms of branched silica oligomers obtained after acidic hydrolysis-condensation of TEOS. The Fe-containing solution shows only one signal at -98 ppm of the Q³ silicon atoms that are usually associated with more condensed silica species (Figure 7.2.b).

Nevertheless, gelation of the precursor sols was not observed, thus enabling the formation of continuous mesoporous films by spin-coating.

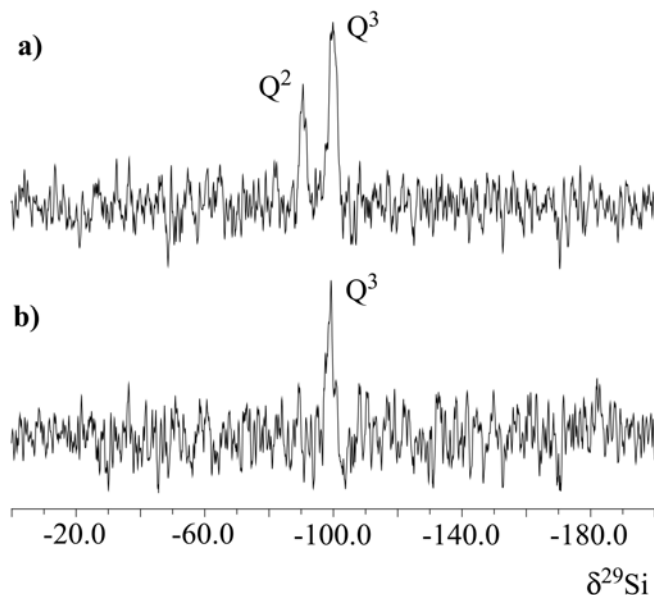


Figure 7.2. ^{29}Si NMR spectra of coating solutions a) NPF4 and b) NPFe2 coating solutions (at 79.42 MHz, 27°C, 15000 scans, pulse width 45°, relaxation delay 4 s, total time for each experiment 19 h).

In addition, the ^{13}C NMR spectra of the Pluronic123 in ethanol, pure silica NPF4 and NPFe2 solutions are shown in Figure 7.3. The signals of the surfactant in the spectrum of the NPF4 coating solution are shifted in comparison to the signals of the pure surfactant because of the interactions of the surfactant molecules with the components of the coating mixture: silica species, HCl and water. More importantly, after the introduction of the Fe species in the coating solution, the Fe(III) cations readily coordinate to the OH functions of the surfactant molecules indicated by the large broadening of the signal of the $-\text{CH}_2\text{-OH}$ carbon atom. The spectrum is shifted due to introduction of the paramagnetic Fe species. In this way, coordinated Fe(III) ions can be incorporated in the tri-block copolymer interiors of the amphiphilic template and can further self-assemble in liquid-crystal mesophase upon spin-coating..

Figure 7.4. shows the distribution of the particles radii in the coating solutions NPFe1 and NPFe2 aged for 5 days compared to those in coating solution NPF4. For the three coating solutions, a broad range of precursor species was detected, which implies diverse silica

precursor species with different degrees of condensation. The pure silica sample that was aged for 5 days showed particle radii in the range of 1 – 8 nm with a maximum population at 3 nm.

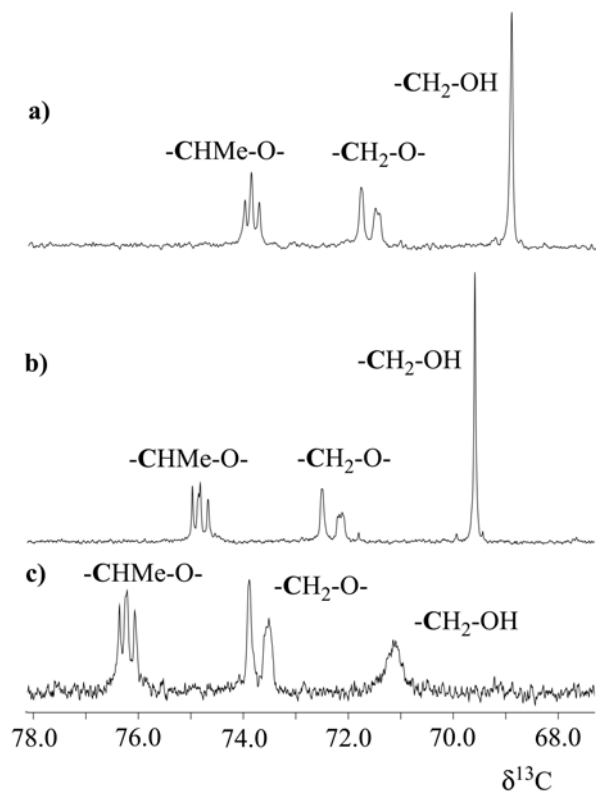


Figure 7.3. $^{13}\text{C}\{^1\text{H}\}$ NMR spectra of a) Pluronic123 in ethanol, b) NPF4 and c) NPF2 coating solutions.

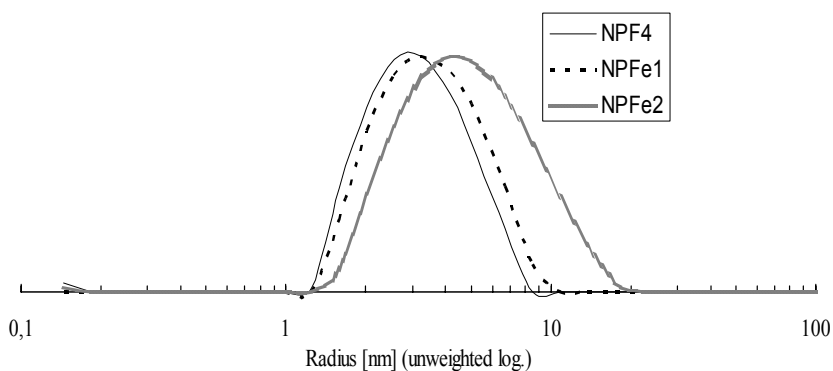


Figure 7.4. DLS data for pure silica NPF4, and Fe-containing NPF1 and NPF2 coating solutions.

Addition of $\text{Fe}(\text{NO}_3)_3 \cdot 9\text{H}_2\text{O}$ leads to a broader distribution of precursor species with the maximum of the population shifted to larger condensation products. Apparently, the concentration of different silica products resulting from the acid-catalyzed hydrolysis-condensation of TEOS was influenced by the addition of the Fe source. Due to highly diluted conditions and high acidity ($\text{pH} = 2$) bigger (more than 20 nm) condensation products have been not observed; this is essential for the formation of homogeneous and smooth thin mesoporous films by the EISA method.

7.3.2. Mesophase structure and surface morphology of Fe-containing mesoporous films and monoliths

The structure of the Fe-containing mesoporous films (Figure 7.5.) deposited on Si wafers was determined by reflection X-ray diffraction (see Chapter 4). The as-deposited NPF₁ film shows three reflections with decreasing intensity that can be indexed as (100), (200) and (300) reflections of a highly ordered one-dimensional hexagonal ($p6m$) mesophase structure with channels oriented parallel to the substrate surface (Figure 7.5.a). The unit cell ($a = d_{(100)} \cdot 2/3^{1/2}$) of the corresponding as-deposited one-dimensional hexagonal structure is $a = 10.8$ nm. Upon thermal treatment at 700°C in vacuum and followed by calcination at the same temperature (calcination procedure D, Chapter 5.3.2.) several reflections are observed that can be indexed in cubic ($Im3m$) mesophase symmetry (Figure 7.6.a). The cubic unit cell of the calcined NPF₁ film is $a = 11.5$ nm, similar to that of the pure silica NPF₄ sample (see Chapter 5.3.1.2). The as-deposited NPF₂ film shows one intensive and two low-intensity reflections that are consistent with a one-dimensional ($p6m$) hexagonal mesophase structure with unit cell size of $a = 9.6$ nm (Figure 7.5.b). In comparison to the NPF₁ film the unit cell is decreased, probably due to the introduction of a higher amount of Fe salt in the coating mixture that influences the self-assembly process during the formation of the mesoporous film. The calcined NPF₂ film shows only two very broad and low-intensity (200) and (210) reflections of the cubic ($Im3m$) mesophase structure (Figure 7.6.b).

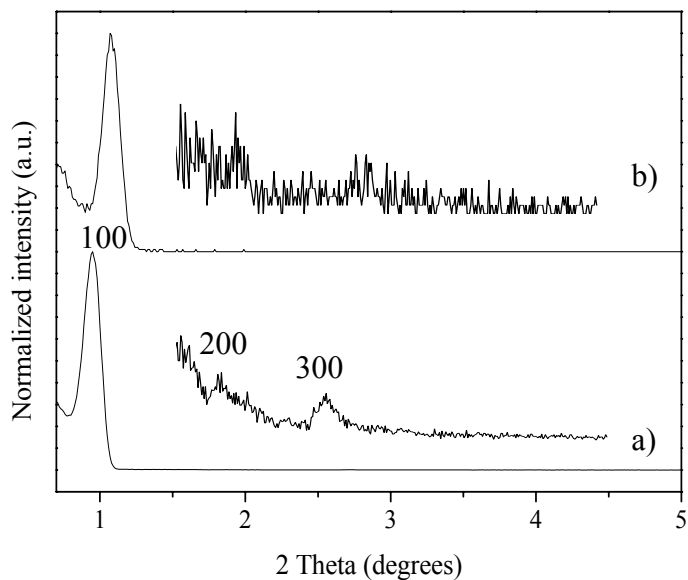


Figure 7.5. RXRD patterns of the as-deposited a) NPFel and b) NPF2 Fe-containing mesoporous films.

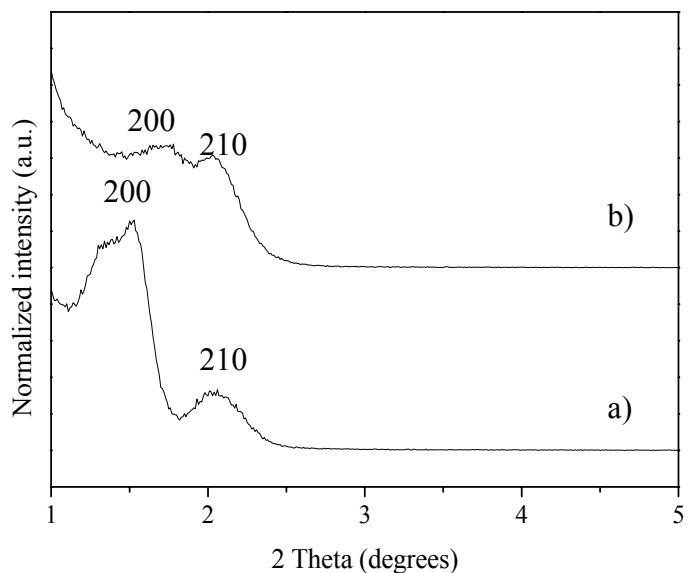


Figure 7.6. RXRD patterns of the calcined a) NPFel and b) NPF2 Fe-containing mesoporous films.

In contrast to the pure silica mesoporous films prepared with the same Pluronic123/silica ratio of 0.017 (NPF4, Chapter 6.3.1.2), the as-deposited Fe-containing films show a one-dimensional hexagonal ($p6m$) mesophase structure that is transformed into a three-dimensional cubic ($Im3m$) structure after calcination. The introduction of the Fe-source in the synthetic mixture apparently changes the self-assembly process by influencing the surfactant packing parameter g and thus manipulating the final curvature of the mesophase structure. Most probably, the Fe (III) cations (which are present in the stoichiometric excess) are coordinated to the ethylene oxide terminal OH groups of the hydrophilic blocks of the amphiphilic copolymer. In this way, the Fe (III) cations are participating actively in the surface charge matching process between the inorganic silica species and the templating copolymer molecules.

Apparently, the introduction of the Fe-source in the synthetic mixture provokes the formation of a one-dimensional hexagonal mesophase structure (as-deposited samples) in comparison to the three-dimensional cubic structures of the pure silica films prepared with the same silica/surfactant ratio. Due to the thermal transformation during the calcination process, formation of a three-dimensional cubic mesophase structure is possible. Similar mesophase transformation processes have been observed for the cubic mesoporous films prepared from silica/cationic surfactant solutions by dip-coating⁸.

Figure 7.7. shows the side-view SEM image of the Fe-containing mesoporous film deposited from NPF₁ coating solution. Similarly to the pure silica mesoporous films, the Fe-containing film shows homogeneous and very smooth surface morphology. The film thickness is estimated to be about 100 nm, similar to the pure silica films deposited at the same conditions with coating solution NPF₄. The mesoporous film deposited from the coating solution with increased Fe content (NPF₂) again shows a continuous and even surface with no bumps or corrugations (Figure 7.8.). The increased size of the precursor species in the Fe-containing coating solutions (see above) does not influence dramatically the surface morphology and thickness of the deposited films.

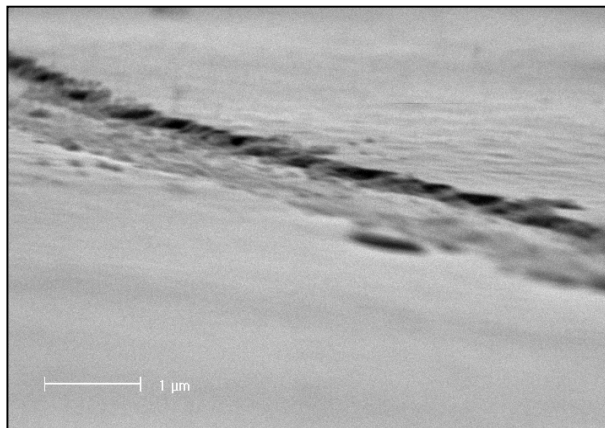


Figure 7.7. Side-view SEM image of the calcined mesoporous film prepared from NPFe1 coating solution.

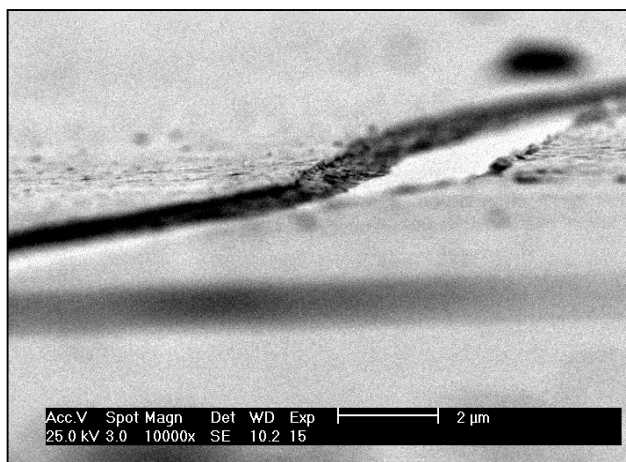


Figure 7.8. Side-view SEM image of the calcined mesoporous film prepared from NPFe2 coating solution.

Fe-containing mesoporous monoliths were also prepared by slow evaporation of the same coating solutions, by drop-wise deposition on silicon wafers at room temperature. The XRD patterns of the as-deposited films are presented in Figure 7.9.

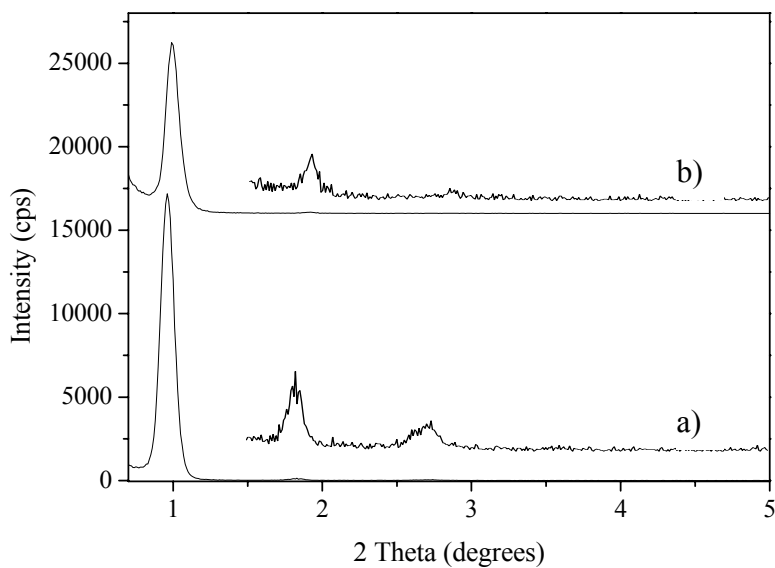


Figure 7.9. RXRD patterns of the as-deposited a) NPFel and b) NPFel2 Fe-containing mesoporous monoliths.

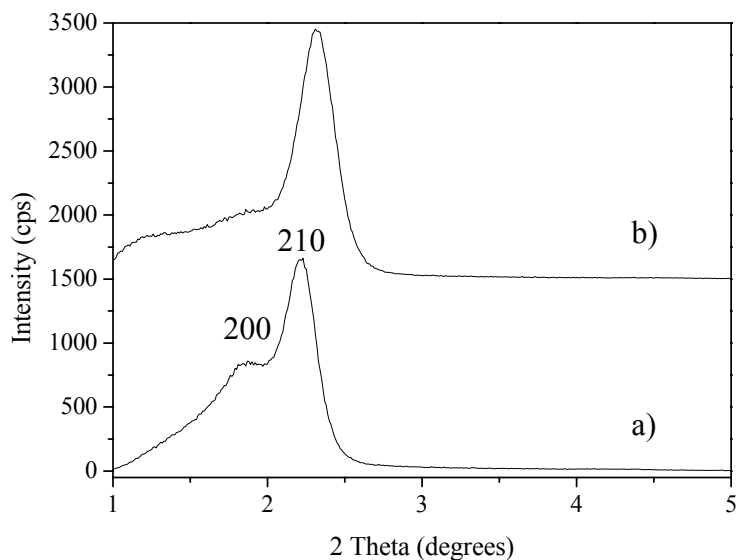


Figure 7.10. RXRD patterns of the calcined a) NPFel and b) NPFel2 Fe-containing mesoporous monoliths.

The results show that one-dimensional hexagonal ($p6m$) mesophase structures with channels running parallel to the substrate surface are formed from the two coating solutions. The corresponding unit cell size of the one-dimensional hexagonal mesophase structures are: $a_{\text{NPFel}} = 10.8$ nm and $a_{\text{NPF2}} = 10.3$ nm. The observed decrease in the hexagonal unit cell (as for the spin-coated samples) is attributed to the introduction of Fe salt in the synthetic mixture. The calcined NPFel film shows two reflections that are indexed as (200) and (210) reflections of the cubic ($Im3m$) symmetry (Figure 7.10.). Similarly to the thin mesoporous films, mesophase transformation process takes also place in the monoliths during the calcination. The cubic unit cell of the NPFel monolith is $a = 8.1$ nm. The calcined NPF2 monolith shows two broad reflections shifted to higher 2θ values that are assigned to the same cubic mesophase structure (Figure 7.10.b)

Figure 7.11. shows the side-view SEM image of a calcined NPFel mesoporous monolith deposited on a silicon wafer. The thickness of the monolith is about $40 \mu\text{m}$ and can be tuned by changing the amount of the deposited synthesis sols and by controlling the solvent evaporation rate. Before calcination, deposited monoliths show homogeneity and uniformity over centimeter ranges. After calcination micrometer long cracks were observed in the monoliths giving delaminated pieces with different dimensions.

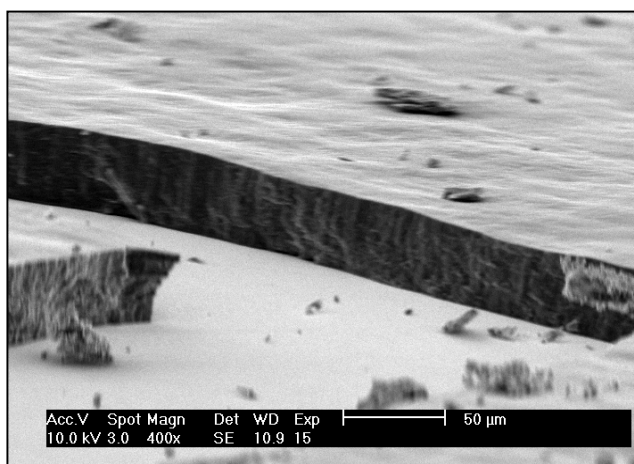


Figure 7.11. Side-view SEM image of calcined Fe-containing mesoporous monolith prepared from NPFel coating solution.

7.3.3. Growth of carbon nanotubes

The carbon nanotubes were prepared on the Fe-containing mesoporous films by thermal decomposition of acetylene in a flow reactor at 700 °C, and the growth was followed by SEM, TEM and Raman spectroscopy.

Table 7.1. Summary of the SEM and TEM results for the carbon nanotubes grown by thermal decomposition of acetylene at 700 °C.

Mesoporous sample	Flow rate of C ₂ H ₂ /N ₂ (mL/min)	Contact time (min)	SEM and TEM results
NPFe1	120	10	highly covered surface, high density CNT layer
		30	highly covered surface, high density CNT layer
NPFe1	60	10	sparsely covered surface, medium density CNT layer
		30	sparsely covered surface, medium CNT layer
NPFe2	120	10	highly covered surface, high density CNT layer
		30	fully covered surface, high density CNT layer
NPFe2	60	10	sparsely covered surface, medium density CNT layer
		30	sparsely covered surface, medium CNT layer
NPF4Fe-imp	120	10	sparsely covered surface, groups of CNT
NPF4Fe-imp	60	10	groups of several nanotubes
NPF4Fe-sp	120	10	sparsely covered surface, randomly distributed CNT
NPF4Fe-sp	60	10	several CNT

The mesoporous films used for the carbon nanotube growth were those obtained from coating solutions NPFe1 and NPFe2, and pure silica films prepared from coating solution

NPF4 on Fe sputtered supports or Fe-impregnated as explained above. Table 7.1. summarizes the type of Fe-containing mesoporous supports, conditions for carbon nanotube growth and the results obtained from SEM and TEM analysis.

Figure 7.12. represents the carbon nanotubes prepared at different flow rates of acetylene at 700 °C over NPFel mesoporous film.

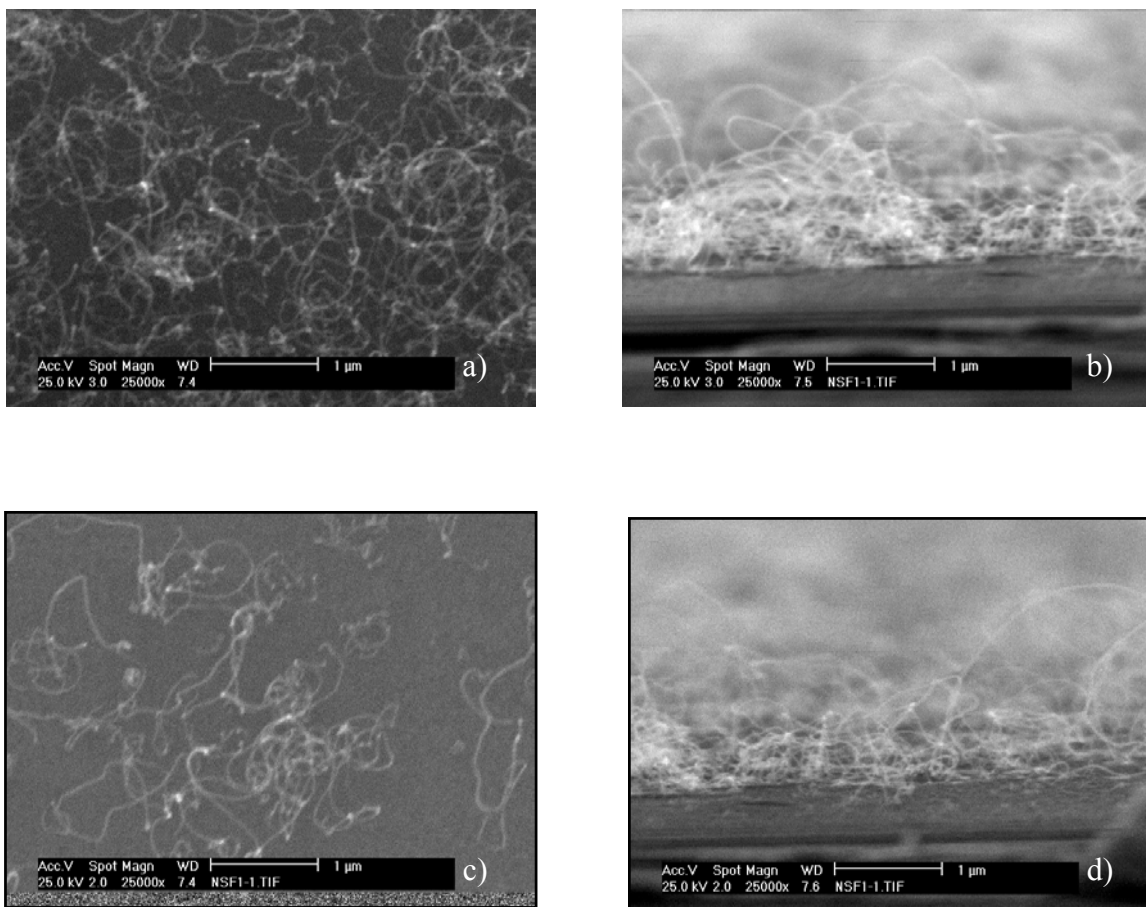


Figure 7.12. SEM images of carbon nanotubes grown at 700 °C on NPFel mesoporous film for 10 min with a flow rate of a) 120 mL/min (top-view), b) 120 mL/min (side-view), c) 60 mL/min (top-view) and d) 60 mL/min (side-view).

The micrographs show that carbon nanotubes grow on the Fe-loaded mesoporous film surface in a hairy fashion. In all cases carbon nanotubes curling up, several hundreds of nanometers long were obtained, no carbon fibers or other deposits including amorphous

carbon particles were monitored. The optimum conditions for the preparation of high coverage of carbon nanotubes without additional carbon nanoparticles or bigger carbon products were confirmed to be 10% acetylene in nitrogen at a flow rate of 120 mL/min for 10 min at 700 °C.

It has been observed that changing the flow rate of the carbon source different surface coverage with carbon nanotubes can be obtained (see Table 7.1.). At flow rates of acetylene as small as 40 mL/min, no carbon nanotubes were observed after the time given on the mesoporous film surface. In addition to the flow rate of the carbon source, the catalytic metal loading plays also an important role for controlling the growth of carbon nanotubes. For example, when the deposition is performed over NPF₂ mesoporous film at flow rates of 120 mL/min for 10 min or longer a very dense layer of carbon nanotubes is formed together with some carbon particles (Figure 7.13).

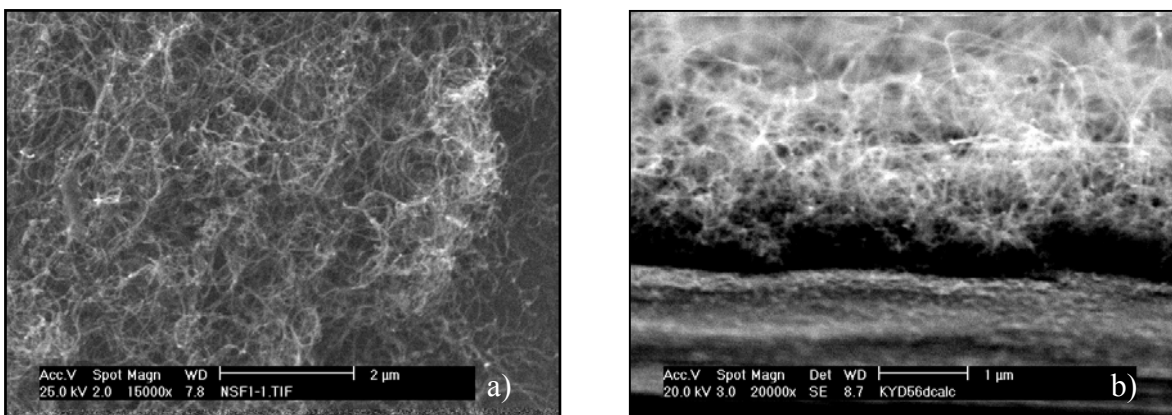


Figure 7.13. SEM images of carbon nanotubes grown at 700 °C on NPF₂ mesoporous film for 10 min with a flow rate of a) 120 mL/min (top-view) and b) 120 mL/min (side-view).

When the catalytic Fe species were introduced by impregnation into mesoporous films prepared from NPF₄ coating solution, the growth of carbon nanotubes was again observed to proceed in a hairy fashion but the tubes were only sparsely distributed on the film surface and grouped together (Figure 7.14.).

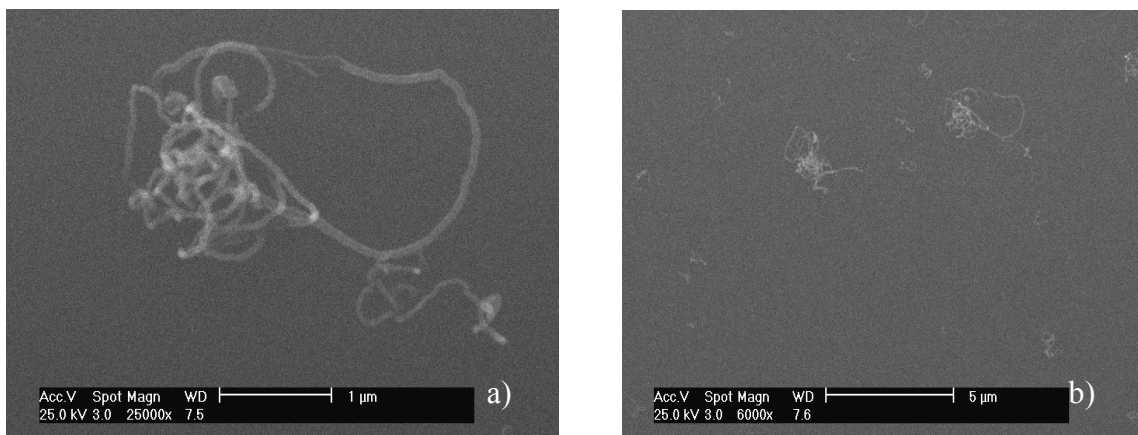


Figure 7.14. SEM images of carbon nanotubes grown at 700 °C on NPF4Fe-imp mesoporous film for 10 min with a flow rate of 120 mL/min; a) and b) different magnifications.

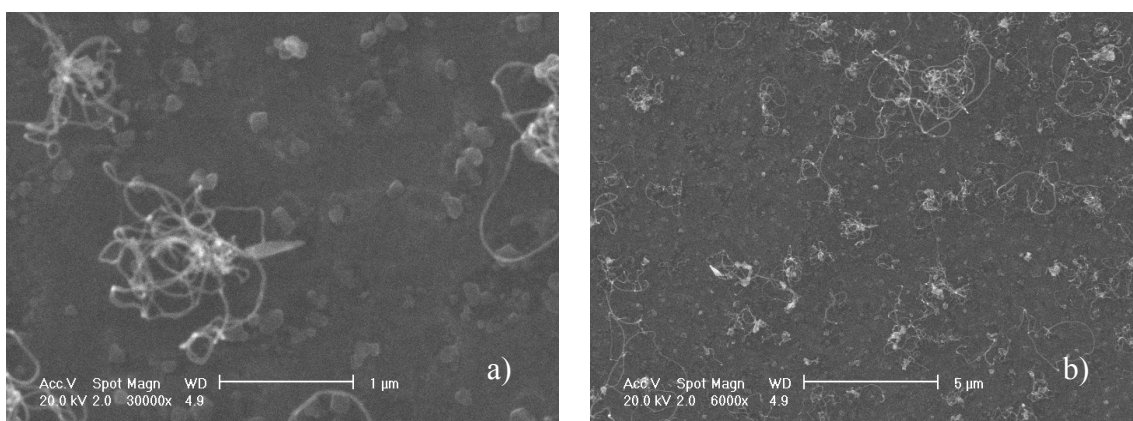


Figure 7.15. SEM images of carbon nanotubes grown at 700 °C on NPF4Fe-sp mesoporous film for 10 min with a flow rate of 120 mL/min; a) and b) different magnifications.

Growth of carbon nanotubes was also observed for the mesoporous films deposited on sputtered Fe surfaces. Since the catalytically active Fe species are positioned at the bottom of the film, the diffusion of the carbon source into the porous system of the mesoporous film is necessary in order to obtain carbon nanotube growth. Apparently, the three-dimensional cubic mesophase structure of the NPF4 film facilitates this process and allows the growth of

the carbon nanotubes to proceed (Figure 7.15.). The growth is again in a hairy fashion; the carbon nanotubes appear to be randomly distributed.

The SEM results show that carbon nanotubes can be grown on Fe-containing mesoporous films in a controlled fashion. In all cases, curling up, long carbon nanotubes were obtained, growing in a hairy fashion to several hundred nanometers. The growth process can be controlled by the deposition conditions such as hydrocarbon flow and exposure time.

The nature of the carbon nanotubes was further investigated by Raman spectroscopy and transmission electron microscopy. The Raman spectrum of the carbon nanotubes prepared on NPFe1 mesoporous film at a flow rate of 120 mL/min of acetylene for 10 min shows two bands at about 1614 cm^{-1} and 1345 cm^{-1} (Figure 7.16.). The first one at 1614 cm^{-1} corresponds to the Raman – active E_{2g} mode characteristic of single crystal graphite, while the second one at 1345 cm^{-1} shows the disorder in the graphitic sheets of the carbon nanotubes. The degree of the disorder affects the position, intensity and line-width of this peak. The Raman spectrum corresponds to the spectra of multiwalled carbon nanotubes (MWCNs) published in the literature^{1,2}.

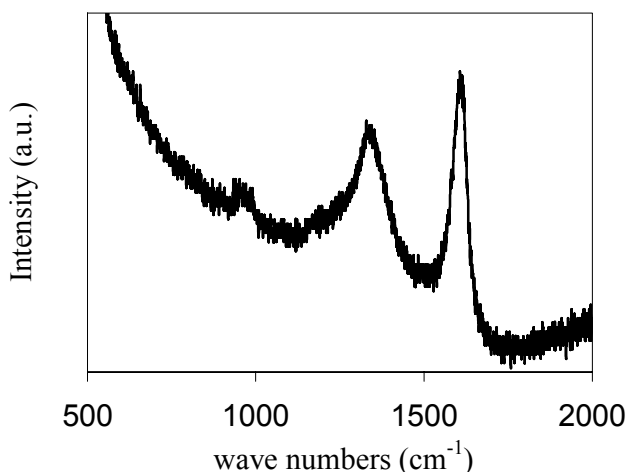


Figure 7.16. Raman spectrum of carbon nanotubes prepared on NPFe1 mesoporous film at 700 °C for 10 min with a flow rate of acetylene of 120 mL/min.

Carbon nanotubes from the NPFe1 sample were examined with transmission electron microscopy. The TEM image demonstrates that multiwalled carbon nanotubes with diameters in the range 15 – 20 nm were formed (Figure 7.17.a). The catalytic Fe nanoparticles are often integrated in the carbon nanotubes usually at the tips of the nanotubes (also seen in the SEM images) suggesting that they serve as a catalytic centers for the growth of the nanotubes. No amorphous carbon or other carbon products were observed on the carbon nanotube surface. The diameter of more than 15 nm of the nanotubes seen on the surface of the mesoporous films is far greater than that of the pore size in the film. (the pore size of Pluronic123-templated films does not exceed 5 nm). Furthermore, after the deposition of the carbon nanotubes at 700 °C no ordered mesophase structure was observed.

However, carbon nanotubes extracted from the film (Figure 7.17.b) reveal structures that have different diameters at the both ends; the larger diameter is around 15 nm, the same as the diameter of the nanotubes seen on the surface of the mesoporous film. The thinner part has a diameter of around 5 nm and a length of not more than several tens of nanometers. We argue that this part had been grown inside the porous system of the mesoporous film before the carbon nanotube started growing out of the porous support.

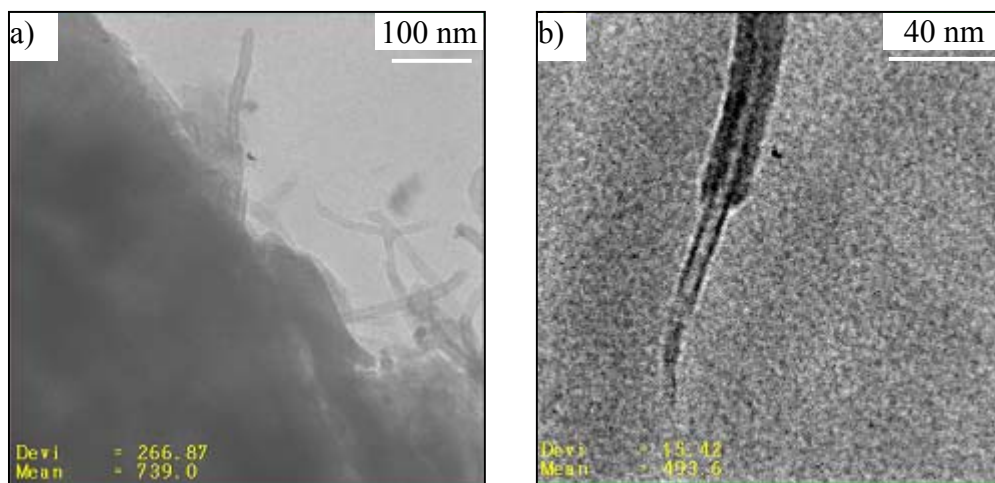


Figure 7.17. TEM image of a) carbon nanotubes prepared on NPFe1 mesoporous film at 700 °C for 10 min with a flow rate of acetylene of 120 mL/min and b) extracted carbon nanotube prepared at the same conditions.

The growth process could be such that the growth of a carbon nanotube starts in the catalytically loaded mesoporous structure where it is confined by the mesoporous walls, later it continues to grow out of the porous system and is no more restricted. The latter results in an increased wall thickness of the carbon nanotubes outside of the interior of the film.

Figure 7. 18. shows the TEM images of the carbon nanotubes prepared over NPF4Fe-imp mesoporous films. The diameter of the obtained carbon nanotubes is about 30 – 40 nm which is even larger than that of the carbon nanotubes grown over NPF₁ mesoporous film. Other structures besides nanotubes, such as carbon particles (Figure 7.18.a) were also observed. Figure 7.18.b shows that the same growth phenomenon was detected as before, with different diameters of the carbon nanotubes at both ends. Note that the diameter of the smaller part of the nanotube is again around 5 nm, similar to the pore diameter of the mesoporous system that, in this case, is preserved after the growth process of the carbon nanotubes. It is suggested that the same growth mechanism as above is involved in the formation of the carbon nanotubes over Fe-impregnated mesoporous films.

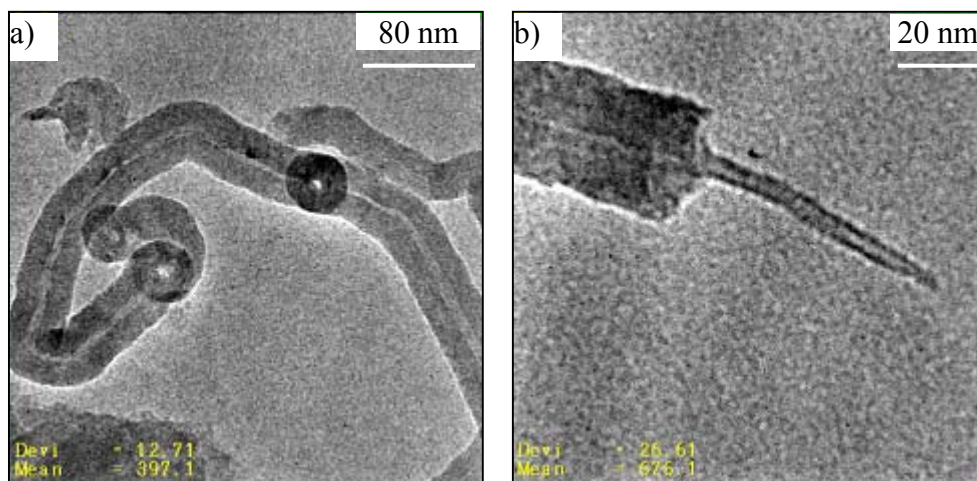


Figure 7.18. TEM image of a) carbon nanotubes prepared on NPF₄-imp mesoporous film at 700 °C for 10 min with a flow rate of acetylene of 120 mL/min and b) extracted carbon nanotubes prepared at the same conditions.

The lower number of the nanotubes (see SEM images) on the film surface and the larger tube diameter can be explained by the decreased number of catalytically active Fe

centers (usually the Fe content in the impregnated samples can not exceed that of the Fe species incorporated in-situ by direct synthesis). The unusual two-diameters morphology of the extracted carbon nanotubes suggests catalytic growth of carbon nanotubes in the interior of the channel system of the mesoporous films.

7.4. Conclusions and Perspectives

Evaporation induced self-assembly *via* spin-coating has been employed for the formation of Fe-loaded mesoporous films from Fe-containing silica/triblock copolymer/ethanol coating solutions. The rapid solvent evaporation of the coating mixture induces the formation of three-dimensional micellar interiors containing coordinated Fe (III) ions, which self-assemble in the hexagonal ($p6m$) mesophase structure (in comparison, at the same conditions with the same silica/Pluronic123 ratio, the pure silica films show cubic ($Im3m$) structure). The RXRD results reveal a transformation from one-dimensional hexagonal to the three-dimensional cubic mesophase structure during the calcination process.

The growth of carbon nanotubes on the Fe-containing mesoporous silica films was conducted by thermal decomposition of acetylene at 700 °C and resulted in multiwalled carbon nanotubes. The carbon nanotube growth rate was controlled by changing the hydrocarbon flow rate, exposure time and catalytic metal loading of the mesoporous support. Usually curling up, long carbon nanotubes protruding out of the film were obtained, growing in a hairy fashion. TEM studies of the isolated carbon nanotubes show the templating role of the mesoporous support for the formation of the carbon nanotubes.

Future work should be conducted on investigations of other transition metals as catalytically active centers for the growth of carbon nanotubes on mesoporous films prepared from silica/surfactant/ethanol/metal salt coating solutions. The influence of the mesophase structure on the growth process should be further examined by using thin films having different mesostructured configurations and loaded with transition metals. Oriented thin zeolite films prepared under hydrothermal conditions and loaded with transition metals can also be explored as catalytic supports for carbon nanotube growth. The reduced pore dimensions and high thermal stability of these supports may be advantageous when the synthesis of single-walled carbon nanotubes is targeted.

On the other hand, another type of hydrocarbon source such as methane or a mixture of several hydrocarbon sources at higher temperatures (around 1000 °C) are necessary if the growth of single walled-carbon nanotubes is desirable. At those temperatures the thermal stability of the porous host becomes an important issue.

References

- ¹ P. M. Ajayan, *Chem. Rev.*, **1999**, 99,1787.
- ² M. S. Dresselhaus, G. Dresselhaus, M. Pimenta, *Eur. Phys. J. D*, **1999**, 9 69.
- ³ K. Mukhopadhyay, A. Koshio, T. Sugai, N. Tanaka, H. Shinohara, Z. Konya, J. B. Nagy, *Chem. Phys. Lett.*, **1999**, 303, 117.
- ⁴ A. Zhang, C. Li, S. Bao, Q. Xu, *Micropor. Mesopor. Mater.*, **1999**, 29, 383.
- ⁵ N. He, Y. Kuang, Q. Dai, Y. Miao, A. Zhang, X. Wang, K. Song, Z. Lu, C. Yuan, *Mater. Sci. Eng. C*, **1999**, 8-9, 151.
- ⁶ W. Z. Li, S. S. Xie, L. X. Qian, B. H. Chang, B. S. Zou, W. Y. Zhou, R. A. Zhao, G. Wang, *Science*, **1996**, 274, 1701.
- ⁷ G. Zheng, H. Zhu, Q. Luo, Y. Zhou, D. Zhao, *Chem. Mater.*, **2001**, 13, 2240.
- ⁸ Y. Lu, R. Ganguli, C.A. Drewien, M.T. Anderson, C.J. Brinker, W. Gong, Y. Guo J.I. Zink, *Nature*, **1997**, 389, 364.

Chapter 8. Growth of carbon filaments in ferrocene-modified SBA-15 rods and mesoporous thin films.

8.1. Introduction

8.2. Experimental

8.2.1. Modification of the SBA-15 rods and mesoporous films

8.2.2. Growth of carbon filaments

8.2.3. Characterization

8.3. Results and Discussion

8.3.1. Amino- and ferrocene-modified SBA-15 rods

8.3.2. Carbon filaments in ferrocene-modified SBA-15 rods

8.3.3. Carbon filaments in ferrocene-modified mesoporous films

8.4. Conclusions and Perspectives

8.1. Introduction

Solid supports with ordered porosity offer potential as template-matrices for guided growth of a variety of conductive structures, resulting in patterned arrays of aligned nanowires (see Chapter 3). Among the nanowires, carbon nanotubes (CNs) have attracted considerable attention during the last few years because of their remarkable electronic properties; they are recognized to be some of the most promising materials to impact future nanotechnologies¹. The preparation of carbon nanotubes *via* catalytic decomposition of hydrocarbons over transition metal-loaded porous supports has been accomplished over molecular sieves including both mesoporous silica and zeolites (Chapter 7 and references therein). It has been shown in this Thesis that mesostructured Fe-containing silica films prepared by the evaporation-induced self-assembly method on silicon substrates can be used to grow multiwalled carbon nanotubes (MWCNs) by the catalytic decomposition of acetylene (Chapter 7). Unfortunately, in these systems, the templating role of the porous substrates is not yet understood in detail, and usually the growth process results in quasi-aligned arrays of MWCNs growing out of the templating support in a hairy fashion.

Most of the nanotechnological applications of carbon nanotubes will require a fabrication method capable of producing uniform carbon nanotubes with well-defined and controllable properties. In addition, electronic and photonic devices, such as field emission

displays and data storage devices, will require high-density and well ordered nanotube arrays². Highly ordered MWCN have been previously prepared by the catalytic decomposition of hydrocarbons using anodic alumina as a support that contains hexagonally close-packed nanochannels^{3,4}. Following a related template approach for growing carbon nanotubes, Tang et al. prepared the smallest possible 0.4 nm single-walled carbon nanotubes (SWCNs) by simply pyrolyzing organic template molecules employed in the synthesis of the microporous aluminophosphate molecular sieve AlPO₄-5 with one-dimensional 0.73 nm channels^{5,6}. Mesoporous silica template material has also been used as a host matrix to grow conductive carbon wires in ordered nanometer-sized channels by pyrolysis of polyacrylonitrile filaments prepared in the MCM-41 host⁷. For the bulk synthesis of MWCNs, pyrolysis has been used, using a so-called flow-catalysis method⁸. For example, pyrolysis of ferrocene/hydrocarbon mixtures at high temperatures resulted in the controllable synthesis of well aligned carbon nanotubes^{9,10}.

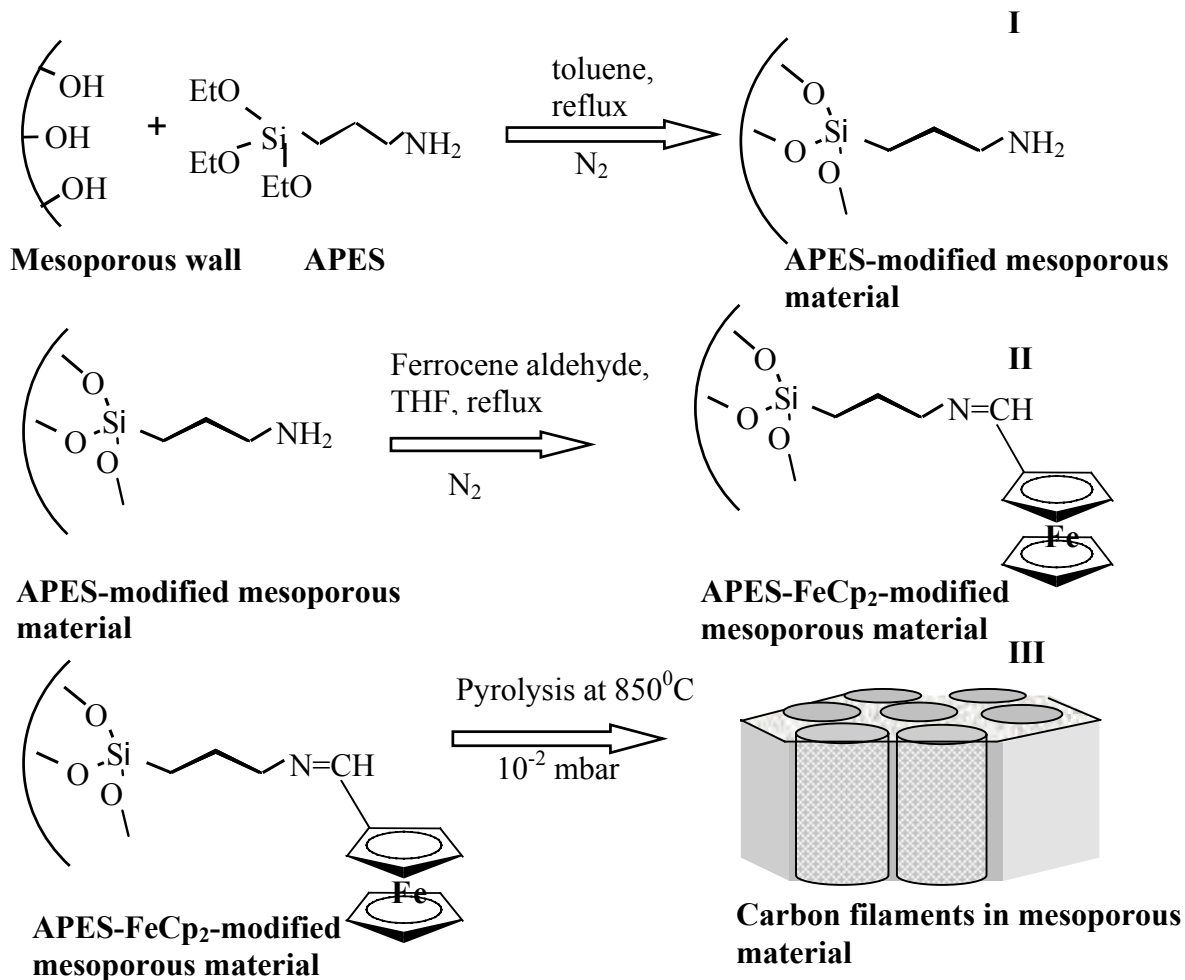
In this Chapter a new synthetic approach is presented for the preparation of carbon filaments by vacuum pyrolysis of ferrocene-modified mesoporous silica (SBA-15) rods and thin mesoporous films. Our approach relies on a selective functionalization with ferrocene of the inner surface of the highly ordered nanometer-sized channels of mesoporous material and subsequent pyrolysis under dynamic vacuum conditions. The ferrocene moieties were introduced through covalent bonding to the amino-functionalized walls of mesoporous materials (see Scheme 8.1.).

8.2. Experimental

8.2.1 Modification of the SBA-15 rods and mesoporous films

SBA-15 rods were synthesized as explained in Chapter 5.3.2. CTABr- and Pluronic123-templated mesoporous films were prepared following the conditions of the EISA method (Chapter 6.2.1.). Template removal was achieved by first treating the sample at 700°C under vacuum (10^{-2} mbar) for 1 h followed by calcination in flowing air at the same temperature for 1 h (ramping 0.75 deg/min) as explained before (see Figure 5.1.D, Chapter 5.3.4). Conventional calcination at 700°C without additional thermal treatment in non-oxidative atmosphere usually resulted in a considerable loss of the mesostructural order. A

high thermal stability of the host is necessary for the subsequent growth of carbon filaments at temperatures as high as 850°C.



Scheme 8.1. Graphical representation of the modification steps of the mesoporous materials and growth of carbon filaments.

Calcined SBA-15 rods and mesoporous films were modified with 3-aminopropyltriethoxysilane (APES - Fluka) in order to introduce amino functionalities on the silica walls (Scheme 8.1, step I). A sample of 50 mg of mesoporous silica SBA-15 material was dehydrated at 120°C in vacuum to remove water molecules absorbed on the surface and then stirred in 10 mL dry toluene (Fluka) containing 700 μL (0.003 mol) of APES under refluxing conditions applying standard Schlenk-line techniques. The reaction time was varied

from 6 to 22 h. The sample reacted for 22 h was designated SBA-15-APES. The powder was collected by filtration, washed with excess amounts of the solvent, and dried at 60°C for at least 24 h. 40 mg of amino-functionalized SBA-15-APES material was further reacted with 5 mg (0.003 mol) ferrocene aldehyde in 10 mL THF at 60 °C for 3 h under inert conditions resulting in imine-coupled ferrocene functionalities (Scheme 8.1, step II). The resulting orange composite SBA-15-APES-FeCp₂ material was separated by filtration, washed with THF, and dried at 60°C overnight. The identification of the samples used in this Chapter is shown in Table 8.1.

Table 8.1. SBA-15 samples with codes used in the study.

Sample names	Manipulation
SBA-15	thermally treated and calcined
SBA-15-APES	modified with APES
SBA-15-APES-FeCp ₂	modified with ferrocene aldehyde
SBA-15-APES-FeCp ₂ – 850°C	pyrolysed at 850°C

Table 8.2. Modified mesoporous film samples with codes used in the study.

Manipulation	NPF1	NPF3
	CTABr-templated	Pluronic 123-templated
	Cubic	hexagonal
Thermally treated and calcined	NPF1-calc	NPF3-calc
APES-modified	NPF1-APES	NPF3-APES
Ferrocene-modified	NPF1-APES-FeCp ₂	NPF3-APES-FeCp ₂
Pyrolysed at 850°C	NPF1-APES-FeCp ₂ -850°C	NPF3-APES-FeCp ₂ -850°C

Similarly, calcined mesoporous films showing different mesophase structures (see Table 8.2) were dehydrated at 120°C in vacuum to remove water molecules absorbed on the surface, and then stirred in 10 mL dry toluene (Fluka) containing 700µL (3 µmol) of APES under refluxing conditions applying standard Schlenk-line techniques under N₂. After 20 h

the functionalized mesoporous films were washed with excess amounts of the solvent and dried at 60°C for at least 24 h. Finally, amino-modified mesoporous films were reacted with 5 mg (0.03 mmol) ferrocene aldehyde in 10 mL THF at 60°C for 3 h (Scheme 8.1, step II).

8.2.2. Growth of carbon filaments

The SBA-15-APES-FeCp₂ sample and ferrocene-modified mesoporous films were evacuated in a tubular furnace and subjected to vacuum pyrolysis (10⁻² mbar) at temperatures between 750 and 900°C (Scheme 8.1, step III). Heating and cooling rates of 4.5 deg/min were used. Based on Raman-spectroscopic data a treatment temperature of 850 °C was selected for further studies. Free-standing carbon filaments were obtained by dissolving the silica matrix in 4% HF and washing in H₂O.

8.2.3. Characterization

The periodic structure of the parent SBA-15 mesoporous material and modified samples was confirmed with X-ray diffraction measurements (Scintag XDS 2000, CuK_α radiation). Nitrogen adsorption-desorption isotherms of the host structure and modified samples were recorded using a Micromeritics ASAP2010 instrument after evacuation of the samples at 120°C. The functionalization process of the SBA-15 material was followed by FT-IR spectroscopy using a Nicolet Avatar-360 FTIR spectrometer with a spectral resolution of 4 cm⁻¹. The powder was pressed in self-supporting disks (ca. 15-20 mg/cm²) that were directly mounted in a sample cell. Measurements were performed in transmission mode at room temperature after evacuation. FT-Raman spectra were recorded with a Bruker Equinox 55-106v/S spectrometer equipped with a Raman module (9395 cm⁻¹ laser, 4 cm⁻¹ resolution, 80 mW laser power, 2000 scans). Proton decoupled ¹³C and ²⁹Si solid-state NMR spectra were recorded on a Bruker DSX Avance spectrometer. The loading of the host support with organic functionality was followed by thermogravimetric analysis (TGA) (Du Pont 951, Thermal Analyzer). The surface morphology of the SBA-15 material was deduced from electron microscopy images taken on a Philips XL 40 microscope. The elemental composition was measured by EDX analysis (JEOL, JSM 65007, field emission SEM equipped with Oxford EDX detector). The growth process of the carbon filaments was

examined by FT-Raman spectroscopy (10 mW, 2000 scans) and compared to the spectrum of multiwalled carbon nanotubes MWCNs obtained by thermal decomposition of acetylene on Fe-loaded mesoporous silica at 700°C. TEM measurements were performed with a JEM 2010 transmission electron microscope operating at 200 kV. Samples for TEM were prepared by depositing a drop of a suspension of the solid in acetone on carbon-coated copper grids.

The mesophase structure of the calcined and modified mesoporous films was determined by X-ray diffraction in the θ - θ scan mode (Scintag XDS 2000 cooled Ge detector, Cu K α radiation). Grazing-incidence diffraction experiments were performed at beam-line ID01 at the ESRF (www.esrf.fr) in Grenoble, France. The modification process of the mesoporous films was followed by reflection-absorption FT-IR spectroscopy. The measurements were carried out at an incidence angle of 55 degrees on silicon-supported samples after collecting the background with a Bruker IFS 66v/S spectrometer equipped with a grazing-incidence module. Quartz crystal microbalance devices (10 MHz QCM, Cold Springs R&D, Marcellus, NY) were used to monitor the loading with molecular functionality and the N₂-sorption properties of the modified mesoporous films (Chapter 4). The measurements were performed as explained in Chapter 5.2.1. Further structural information concerning the mesoporous films and the grown carbon filaments was obtained by TEM images taken as plan views. Samples for plan views were obtained as described in Chapter 5.2.1.

8.3. Results and Discussion

8.3.1. Amino- and ferrocene-modified SBA-15 rods

The XRD analysis of the SBA-15 material confirms the preservation of the hexagonal structure after calcination, and of the amino- and ferrocene-modified samples (Figure 8.1.a, b, c). One very intensive and two weak reflections are recorded that correspond to the (100), (110), and (200) diffraction peaks of the two dimensional (*p6m*) mesophase structure. The corresponding unit cell ($a = 2/3^{1/2} \cdot d_{100}$) of the calcined and modified samples was calculated to be 11.6 nm. A slight decrease of the intensity of the (100) peak upon post-synthesis modification is observed and can be explained by the decreased scattering contrast between

the pores and the walls of the functionalized mesoporous material. Nevertheless, the (110) and (200) reflections are still observed.

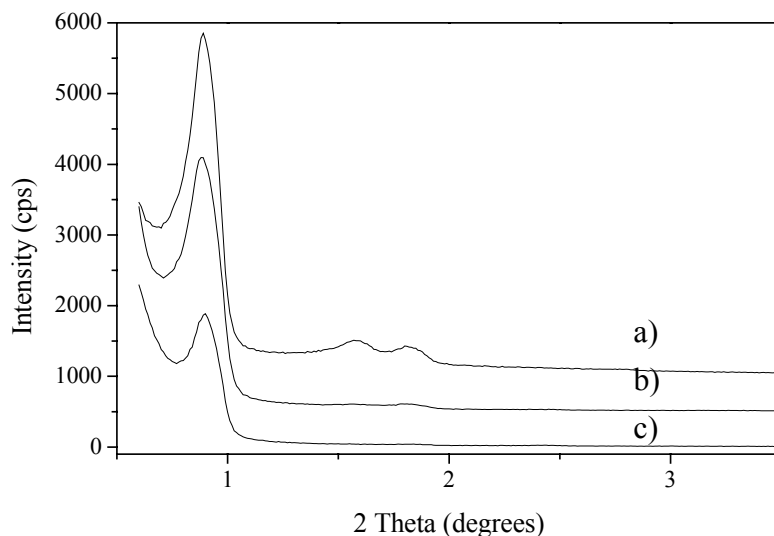


Figure 8.1. XRD patterns of a) calcined SBA-15, b) SBA-15-APES, and c) SBA-15-APES-FeCp₂ samples (the patterns are offset with 500 cps).

In Figure 8.2 the nitrogen-sorption isotherms of the calcined SBA-15, the amino-modified SBA-15-APES and ferrocene-modified SBA-15-APES-FeCp₂ samples are shown. Typical type IV nitrogen-sorption isotherms with distinct hysteresis loops and steep adsorption and desorption steps are recorded that indicate a narrow pore-size distribution.

These results together with the XRD data confirm the preservation of the mesostructural order of the samples after the modification steps. Table 8.3. summarizes the data from the nitrogen-sorption measurements and XRD analysis. After grafting the calcined SBA-15 material with amino-functionality, the BET surface area, the total pore volume (V_t), and the pore size (D_{BJH}) decreased, which is in agreement with the pore filling effect¹¹. However, the resulting surface area and the pore volume are still sufficient for a subsequent modification step with ferrocene aldehyde. The SBA-15-APES-FeCp₂ sample shows a further decrease in the aforementioned parameters as expected after the reaction of the ferrocene aldehyde with the amino groups in the mesoporous channels of the SBA-15 material.

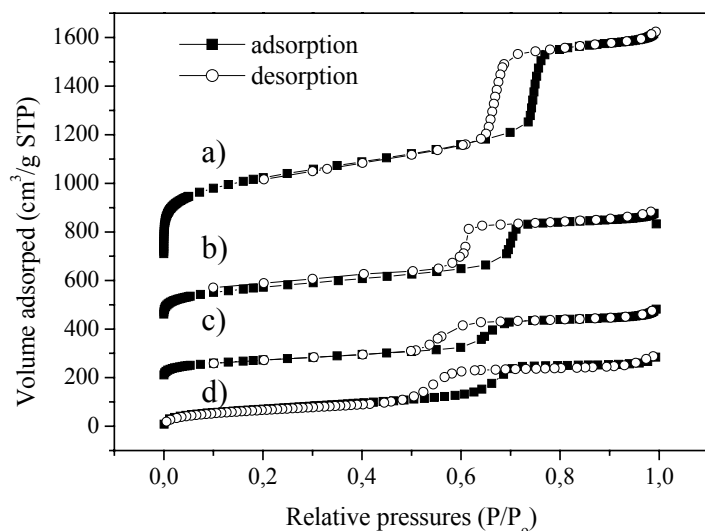


Figure 8.2. N₂-sorption isotherms of a) calcined SBA-15, b) SBA-15-APES, and c) SBA-15-APES- FeCp₂ materials (the isotherms are offset with 200 cm³/g).

Table 8.3. N₂-sorption data for the calcined SBA-15 and modified samples.

Sample	a(nm)	S _{BET} (m ² g ⁻¹)	V _t (cm ³ g ⁻¹)	D _{BJH} (nm)
SBA-15	11.6	926	1.42	5.4
SBA-15-APES	11.5	754	0.67	5.3
SBA-15-APES-FeCp ₂	11.5	290	0.43	5.0
SBA-15-APES-FeCp ₂ – 850°C	10.5	285	0.42	4.8

The surface area is calculated from the BET model, the total volume adsorbed is calculated from single point measurement at P/P₀ = 0.994, and the pore size is determined by the BJH model applied to the desorption branch of the isotherm.

The degree of loading of the mesoporous material with amino-functionalized organosilane was followed by TGA as a function of the reaction time of the silane grafting process. The loading is increased from 0.18 mmol/g for the sample reacted for only 6 h to 0.32 mmol/g for the sample reacted for 22 h. The latter corresponds to weight loss of 7 wt% (or about 17 wt% loading with APES, assuming that the weight loss is only due to the combustion of the organic part of the silane and that siloxane bonds are formed). The final

value corresponds to 0.76 mmol/g or 0.5 APES molecules per nm² of the mesoporous surface calculated from the following formula:

$$S = W\% \cdot N_A / M \cdot S_{\text{BET}} \cdot 10^{-20} \quad (8.1)$$

where W% represents the weight loss after silylation obtained from TGA, N_A is Avogadro's number, M is the molar mass of the silane molecules, and S_{BET} is the specific surface area of the parent material. No further increase in the loading level was observed with prolonged time of silane grafting. The calculated number of the APES molecules on the SBA-15 surface is lower than that observed for amino-modified SBA-1¹² material (0.93 molecules per nm²).

Assuming full coverage with APES molecules (with length of the APES molecule of about 0.41 nm, calculated from geometrical considerations) of the cylindrical mesopores with average diameter of 5.4 nm and specific surface area of 926 m²g⁻¹, the total decrease of mesoporous volume is estimated to be 0.41 cm³g⁻¹. This is less than the decrease of the total pore volume (V_t) measured by N₂ sorption (0.75 cm³g⁻¹). Possibly, the calculated decrease in the pore volume (after formation of a silane monolayer) is exceeded because of the existing microporosity in the walls that is more difficult to be functionalized with large silane molecules but is taken into account in the model calculations (contributing to the BET surface area).

The SBA-15-APES-FeCp₂ shows an increased TGA weight loss of about 5 wt% (or about 7 wt%, assuming that the weight loss is due only to the combustion of the organic part) in comparison to the SBA-15-APES sample that corresponds to 0.36 mmol/g of FeCp₂. This value corresponds to about 50% yield of the Schiff-base reaction (see Scheme 8.1, II). Furthermore, the calculated full coverage of the cylindrical mesoporous channels with a monolayer of ferrocene moieties linked to the APES molecules resulted in an expected decrease in the total pore volume of about 0.33 cm³g⁻¹ (at 100% yield of the Schiff-base reaction), which is higher than that measured by N₂ sorption (0.24 cm³g⁻¹). The latter corresponds to 72% of the theoretical full coverage with ferrocene molecules of the whole mesophase surface.

The modification steps of the SBA-15 material were followed by FT-IR and FT-Raman spectroscopies. Selected regions of interest of the FT-IR spectra of the calcined and the amino-modified samples are shown in Figure 8.3. The isolated Si-OH groups in the spectra of the calcined sample that are accessible for further functionalization give a sharp signal at 3750 cm^{-1} (Figure 8.3.a)¹³. In the high-frequency region, a broad envelope band between $3700 - 3000\text{ cm}^{-1}$ is recorded for the calcined and amino-modified samples that is assigned to residual silanol-bonded water¹². The removal of the template after the thermal treatment and the calcination step at 700°C is confirmed by the strong reduction of the C-H stretching vibrations (Figure 8.3.a). The amino-modified sample does not show any signal typical for the isolated Si-OH groups. In addition, vibrational bands at 2935 , 2866 , 1560 , and 1493 cm^{-1} are observed that are characteristic for -CH₂- asymmetric and symmetric stretching, -NH₂ bending, and -CH₂ scissoring vibrations, respectively. The band positions are similar to those reported in the literature for amino-functionalized mesoporous materials^{13,14}.

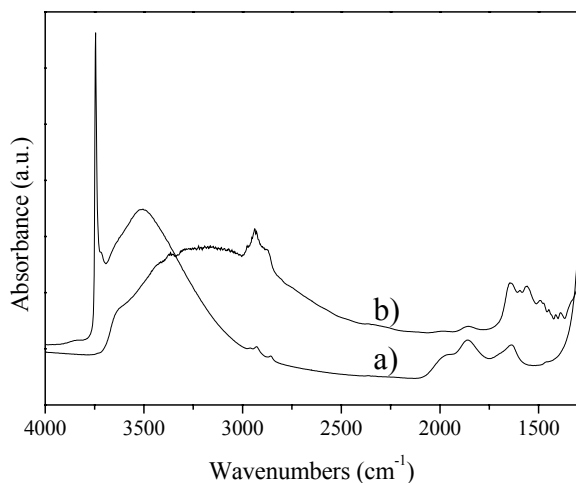


Figure 8.3. FT-IR spectra of a) calcined SBA-15 and b) SBA-15-APES samples.

The reaction of ferrocene aldehyde with primary amino groups leads to the formation of imines in the course of the well-known Schiff-base reaction¹⁵. In analogy, the heterogeneous reaction of ferrocene aldehyde with the covalently-grafted APES linker attached to the silica walls is expected. This is confirmed by the appearance of a sharp and

intense band at 1644 cm^{-1} assigned to the imine groups in the FT-Raman spectra (see below). The FT-Raman spectra of the calcined, the amino-, and the ferrocene-modified samples in the high- and low-frequency regions are shown in Figure 8.4. The calcined sample (Figure 8.4.A, a) did not show any Raman active modes in the region between $2500\text{--}3000\text{ cm}^{-1}$, in agreement with the complete removal of the surfactant. One intensive band recorded for the amino-modified sample in the high-frequency region at 2900 cm^{-1} is assigned to the $\text{-CH}_2\text{-}$ stretching vibrations. After covalent linking of the ferrocene functionality, a new band appeared at 3104 cm^{-1} , which is characteristic for the C-H stretching vibrations of the Cp-rings (Figure 8.4.A, c). The corresponding $\text{-CH}_2\text{-}$ scissoring vibrations are visible in the region between $1410\text{--}1470\text{ cm}^{-1}$ together with the C=C stretching vibration modes of the Cp-rings (Figure 8.4.B, c). The band at 1312 cm^{-1} in the spectrum of the amino-modified SBA-15 material (Figure 8.4.B, b) is likely to be assigned to the Si-C bond. A prominent band in the Raman spectra of the ferrocene-modified material (Figure 8.4.B, c) is the Cp-breathing mode that is recorded at 1107 cm^{-1} .

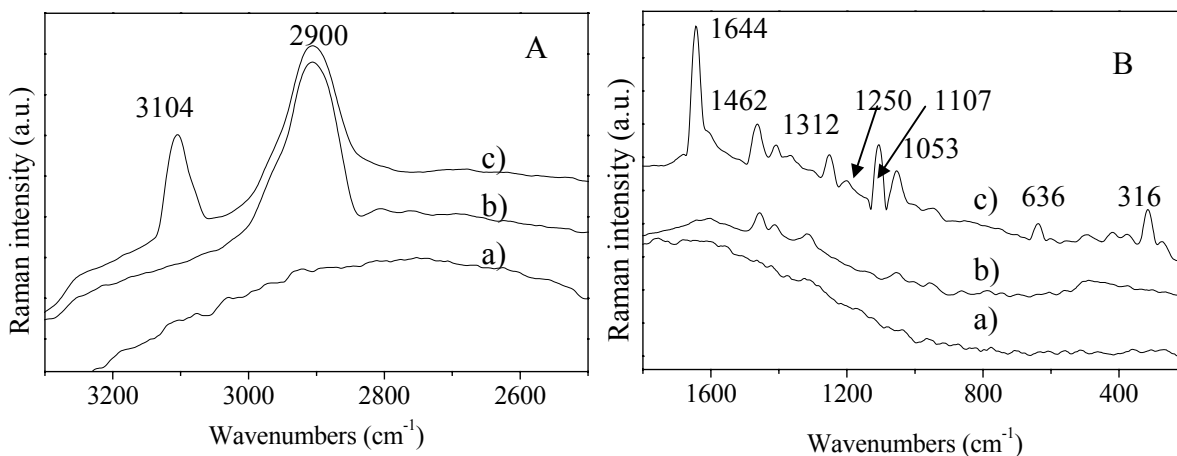


Figure 8.4. FT-Raman spectra of a) calcined SBA-15, b) SBA-15-APES, and c) SBA-15-APES-FeCp₂ samples recorded in the A) high- and B) low-frequency regions.

In addition, in the region around 1000 cm^{-1} Raman active C-H in-plane bending modes associated with the Cp-rings are observed. The C-H out-of-plane bending modes show low Raman intensity at $920\text{--}900\text{ cm}^{-1}$. The other vibration modes typical for metallocenes are

skeletal vibrations, namely Cp – tilt, Cp – Fe stretching, and Cp-Fe-Cp deformation bands. The Cp – tilt skeletal vibrations show a weak Raman band at 390 cm^{-1} accompanied by a more intensive Cp – Fe stretching mode at 316 cm^{-1} (Figure 8.4B, c). The positions of the Raman shifts measured for our samples are similar to those already published in the literature for ferrocene derivatives^{15,16,17}.

A direct confirmation of the covalent linking of the ferrocene aldehyde to the amino groups attached to the mesoporous walls is obtained through the observation of the Raman-active imine band at 1644 cm^{-1} (Figure 8.4.B,c and Figure 8.5.a). The comparison of the Raman spectra of neat ferrocene aldehyde with that of SBA-15-APES-FeCp₂ material (Figure 8.5.) shows that the high-intensity carbonyl band at 1671 cm^{-1} vanishes while the imine band at 1644 cm^{-1} appears.

In addition to vibrational studies, ¹³C solid-state NMR measurements were performed with sample SBA-15-APES-FeCp₂ in order to prove the successful modification of the mesoporous silica surface with ferrocene moieties (Figure 8.6.). The most prominent ¹³C NMR signal at 69.5 ppm in the spectrum is associated with the carbon atoms in the Cp rings¹⁶.

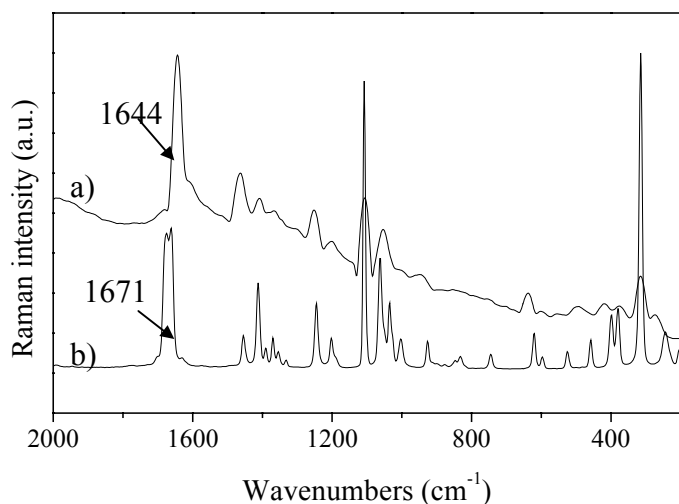


Figure 8.5. FT-Raman spectra of a) ferrocene aldehyde and b) SBA-15-APES-FeCp₂ material.

The chemical shifts that appear at 10.9, 24.9, and 43.6 ppm are not found in the ^{13}C NMR spectrum of pure ferrocene aldehyde and are assigned to the typical resonances of the carbon atoms in amino-modified mesoporous materials. The signal at 10.9 ppm is ascribed to the C^1 carbon atoms of the methylene groups, which are directly bonded to the silicon atom¹⁸. The other two signals are assigned to carbon atoms C^2 and C^3 of the propyl chain as shown in Figure 8.6.

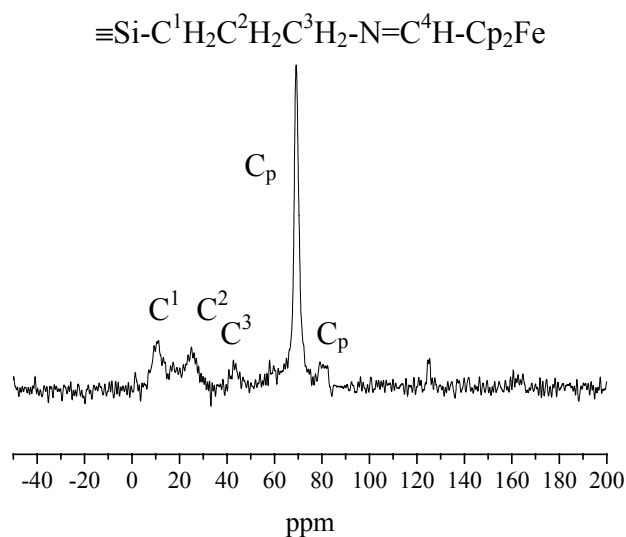


Figure 8.6. ^{13}C NMR spectrum of SBA-15-APES-FeCp₂ sample.

The nature of the molecular functionalities and the chemical bonding to the silica surface of the mesoporous material was studied with ^{29}Si solid-state NMR spectroscopy and compared with previously published results^{18,19}. The ^{29}Si spectra with peak assignments for the calcined SBA-15 and SBA-15-APES samples are shown in Figure 8.7. In the ^{29}Si NMR spectrum of the calcined SBA-15 material two distinct chemical shifts were recorded at -90.8 and -99.8 ppm, which are attributed to silicon in the siloxane binding environment with geminal silanol groups $[(\text{SiO})_2\text{Si}(\text{OH})_2]$ (Q^2 silicon atoms) and to isolated silanol groups $[(\text{SiO})_3\text{Si}(\text{OH})]$ (Q^3 silicon atoms). Only a shoulder of low intensity was detected at -110 ppm that is due to silicon atoms in a siloxane environment with no silanol groups $[(\text{SiO})_4\text{Si}]$ (Q^4 silicon atoms)¹⁸. The predominant appearance of Q^2 and Q^3 silicon atoms even after

treatment at 700°C suggests a high degree of coverage of silanol groups on the pore surface of the calcined SBA-15 material (having well known additional microporosity). It may be speculated that the former observation is due to a stabilizing effect of carbonized ethyleneoxide segments of the tri-block co-polymer on the silica walls during the first thermal stabilization step. The ^{29}Si NMR spectrum of the amino-modified SBA-15 material shows chemical shifts typical for Q^3 and Q^4 silicon atoms at -100.3 and -107.8 ppm, respectively, which are in agreement with a decreased population density of the silanol groups on the mesoporous silica surface and increased siloxane condensation *via* reaction of the organosilane with the surface silanols¹¹. In addition to the peaks of Q^3 and Q^4 silicon atoms, the spectrum of the SBA-15-APES sample also shows two resonances at -60 and -68.9 ppm that correspond to two different environments of the silicon atoms in the organosilane molecules^{11,18}. Specifically, T^2 silicon atoms are bound to one hydroxyl and one organic residue and form two siloxane bridges $[(\text{SiO})_2\text{Si}-(\text{OH})\text{R}]$, while T^3 silicon atoms form three siloxane bonds $[(\text{SiO})_3\text{Si}-\text{R}]$. The population of the T^2 species is larger than that of T^3 species, which implies that the organosiloxane molecules are more randomly distributed on the porous surface rather than being directly linked with each other in a continuous layer¹⁹.

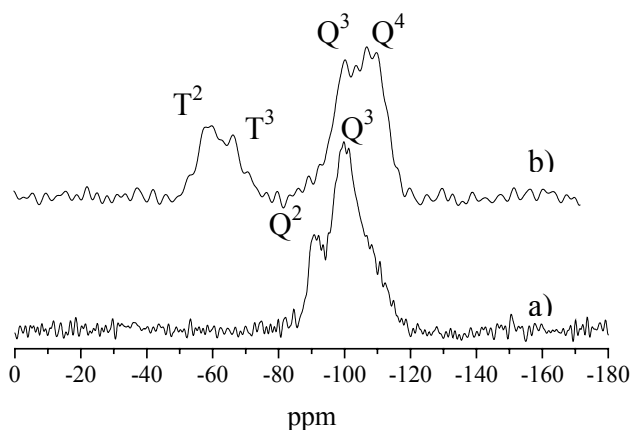


Figure 8.7. ^{29}Si NMR spectra of a) calcined SBA-15 and b) SBA-15-APES samples.

The relative integrated intensities of the NMR signals of the organosiloxanes (T^m) and siloxane species (Q^n) can be employed to estimate the incorporated amount of functional groups¹². The percentage of the reacted surface silanol groups with organosilane molecules

can be roughly estimated by taking into account the ratio of the integrated intensities of the NMR signals for $T^2 + T^3$ and those of $Q^3 + Q^4$. The calculated $(T^2 + T^3)/(Q^3 + Q^4)$ ratio is 0.36. Taking into account the density of the silica, $\sim 0.2 \text{ g/cm}^3$, and the wall thickness of the silica walls of about 5 nm (typical for SBA-15 material, see Chapter 5.3.2), the number of SiO_2 molecules per nm^2 is calculated to be 4. The density of silane molecules on the SBA-15 surface calculated from the TGA is 0.5 molecules per nm^2 (see before); the corresponding ratio of Si atoms in the silane and in the silica walls is 0.13. That is less than calculated from the ^{29}Si NMR data. It should be noted that the relative peak intensities in the ^{29}Si NMR spectra are not strictly quantifiable due to possible differences in the relaxation behavior.

The population density and the quality of the molecular functionality grafted on the surface of the mesoporous materials are generally affected by the nature of the silanol groups available on the surface. It is well known that free silanol groups are necessary to anchor the organic molecules to the silica surface by siloxane bonding. Although the mesoporous silica surface could have a significant population of silanols, most of them are hydrogen bonded to each other forming a hydrophilic net and are in this way non-reactive toward silane modification²⁰. A considerable increase in the number of free silanols that are reactive towards silane modification is obtained by evacuation at temperatures as high as 400°C ¹³. The density of free hydroxyl groups on mesoporous silica depends on the type of mesoporous material, synthesis route, and template-removal procedure. The density of free silanol groups on MCM-41, MCM-48, and amorphous silica has been reported²¹, and it is assumed that the density of the silanols on the surface of these materials is not high enough to fix silanes with more than two Si-O-Si bonds. That is in agreement with the preferential formation of randomly distributed organosiloxane molecules (high concentration of T^2) rather than a continuous layer of fully cross-linked organosiloxane molecules (T^3 signal) on the surface of the SBA-15-APES sample.

The morphology of the calcined and modified SBA-15 material was examined by scanning electron microscopy (Figure 8.8.). The calcined SBA-15 material contains rods with a typical diameter of 10 - 30 μm and lengths of up to 150 μm . The rods are assembled from worm-like structures (several micrometers long) that are running or curling along the long axis of the rod. It has been observed in TEM investigations that the hexagonally ordered

channels of the SBA-15 material are preferentially aligned with the long axes of the worm-like structures (see below). After several steps of modification the worm-like structure of the rods is essentially preserved although breakage leads to shorter lengths.

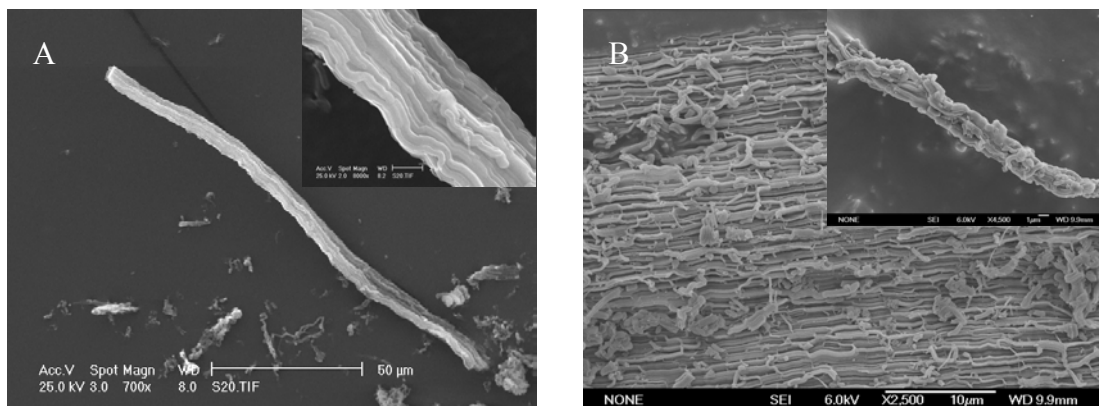


Figure 8.8. SEM images of A) calcined SBA-15 rods (inset shows the worm-like structure of the rods, scale bar 20 μm) and B) SBA-15-APES-FeCp₂ (inset shows small micrometer-sized rods, scale bar 1 μm).

8.3.2. Carbon filaments in ferrocene-modified SBA-15 rods

The mesostructural order of a ferrocene-modified sample that was subjected to vacuum pyrolysis for 1 h at 850°C (ramping rate 4.5 deg/min, 10^{-2} mbar) is still intact based on the first-order reflection in the X-ray diffractogram. The peak position is shifted to higher 2θ values (Figure 8.9.). The calculated cell parameter is 10.5 nm and corresponds to a shrinkage of 10% of the mesoporous structure due to the increased siloxane condensation and cross-linking in the mesoporous walls at higher temperatures. Vacuum pyrolysis at temperatures as high as 950°C with the same heating rate still showed retention of the mesostructural order, thus confirming the extreme thermal stability of the ferrocene-modified sample. This is notable since purely siliceous SBA-15 materials prepared by conventional routes (hydrolysis-condensation of TEOS) show low structural stability at those high temperatures and high heating rates. We suggest that the formation of the carbon filaments during the pyrolysis step serves as additional structure-stabilizing effect that prevents the

mesophase structure from collapsing. The as-synthesized SBA-15 sample that was treated in flowing air at 900°C (heating rate of 4.5 deg/min) did not show any mesophase structure.

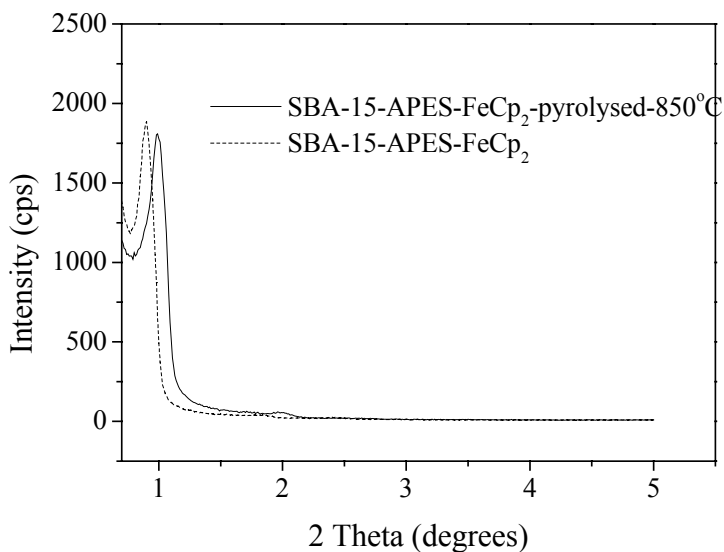


Figure 8.9. XRD patterns of SBA-15-APES-FeCp₂ material before and after pyrolysis at 850°C.

The Raman modes of carbon nanotubes and other sp² carbons, including carbon nanoparticles, disordered carbon, and graphite, have been studied in detail; they present an important tool for the characterization and prediction of the electronic properties of those materials^{1,22,23}. Figure 8.10 shows Raman spectra of the carbon filaments prepared by pyrolysis of the ferrocene-modified SBA-15 material at 750 and 850°C, and the spectrum of the MWCNs obtained by catalytic decomposition of acetylene over Fe-loaded mesoporous films at 700°C (see Chapter 7). A Raman-active E_{2g} mode at 1606 cm⁻¹ characteristic for graphite is observed in CVD-processed MWCNs and in the pyrolysed SBA-15-APES-FeCp₂ material (with increasing intensity at higher pyrolysis temperature) (Figure 8.10). A similar band, but at different position and line-width²², is also found in the Raman spectra of sp²-carbons, such as boron doped pyrolytic graphite, carbon nanoparticles, and even in glassy carbon. Since the line-width and the position of the E_{2g} mode in the sample pyrolysed at 850°C and that of the CVD-processed MWCNs are very similar it is suggested that the

obtained carbon filaments in the SBA-15 material have similar properties to multiwalled carbon nanotubes or pyrolytic graphite. Nevertheless, a considerable disorder in the graphene sheets is present as indicated by the D-band at 1330 cm^{-1} . The degree of the disorder affects the position, intensity, and line-width of this peak²². As can be seen for the sample pyrolysed at 750°C , the D-band is broader, more intense than the E_{2g} mode, and is shifted to lower frequencies. This indicates that at a lower pyrolysis temperature carbon material similar to glassy carbon is formed.

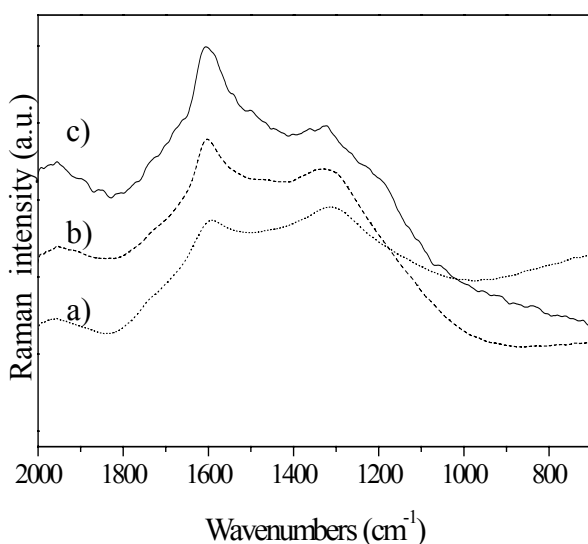


Figure 8.10. FT-Raman spectra of SBA-15-APES-FeCp₂ sample pyrolysed at a) 750°C and b) 850°C in vacuum, and c) MWCNs prepared by catalytic decomposition of acetylene at 700°C in a flow reactor.

EDX analysis was performed in order to probe the iron content in the samples before and after pyrolysis and to examine possible sublimation of ferrocene into the gas phase. A similar Fe/Si atomic ratio of 0.06 was found in both cases that corresponds to ferrocene loading of the mesoporous silica material of about 7 wt% (for comparison, the TGA also showed loading of about 7 wt%, see above). Furthermore, the thermogravimetric data of the ferrocene-modified SBA-15 material in inert gas atmosphere showed no significant weight loss up to temperatures as high as 600°C . The synthesis of carbon nanotubes by pyrolysis of ferrocene/hydrocarbon mixtures is already an established technique for the mass production

of MWCNs⁹. The role of ferrocene in the production of the MWCNs by pyrolysis of ferrocene/hydrocarbon mixtures is to act as a floating catalyst in the gas phase and to nucleate the growth of carbon nanotubes on porous surfaces⁸. The necessity of introducing an additional hydrocarbon source instead of using only ferrocene is based on the low carbon-to-iron content in the ferrocene. Nevertheless, pyrolysis of ferrocene in a flow reactor without additional hydrocarbon flow was shown to give small amounts of single-walled nanotubes and carbon particles¹⁰. In this study the carbon content is enhanced by the selective functionalization of the silica walls of the SBA-15 material with organosilane; the latter also serves as a coupling agent for the ferrocene moieties. It appears that the selective inclusion of ferrocene through covalent bonding to the organosilane linker molecules, and the precise tuning of the vacuum-pyrolysis conditions are critical for the production of carbon filaments by the method described here.

Pure carbon material was obtained by dissolving the templating SBA-15 matrix in 4% hydrofluoric acid at room temperature for 12 h. The complete dissolution of the silica matrix was confirmed by EDX analysis (removal of the Si signal). SEM images of the pyrolysed SBA-15-APES-FeCp₂ material before and after HF treatment are shown in Figure 8.11.

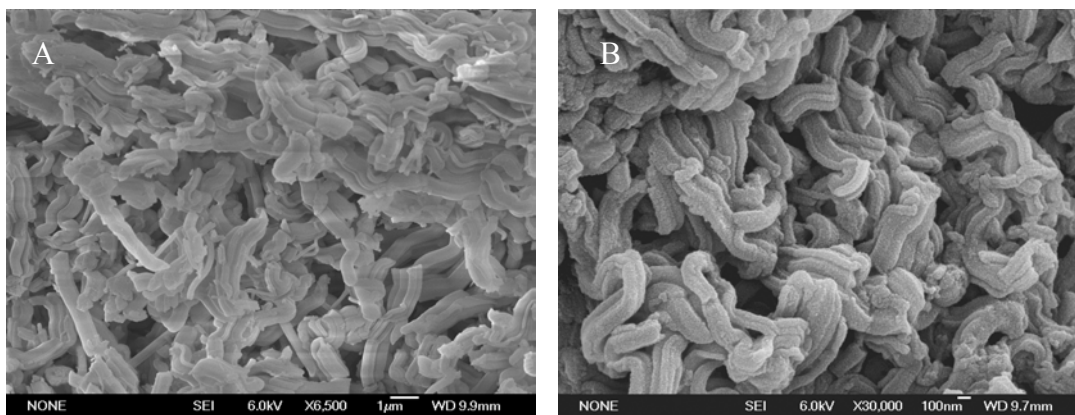


Figure 8.11. SEM images of pyrolysed ferrocene-modified SBA-15 material A) before (scale bar 1 μm) and B) after removal of silica matrix (scale bar 100 nm).

Ferrocene-modified SBA-15 material subjected to pyrolysis shows the same worm-like morphology as that observed for the SBA-15-APES-FeCp₂ material. The preservation of

the morphology of the carbon material after removal of the silica matrix suggests that the carbon filaments are interconnected. Similar results have already been observed for Pt wires prepared in SBA-15 host and have served as an indirect proof for the suggested microporosity in the SBA-15 walls²⁴.

The synthesis of ordered mesoporous carbons (CMK-materials) by carbonization of an infiltrated carbon precursor (sucrose) in the pores of mesoporous silica and subsequent removal of the silica template is already a well established technique²⁵. The carbon filaments prepared by the method proposed here are obtained due to the selective introduction of ferrocene functionalities in the mesoporous channels combined with the ferrocene-based catalytic method for the production of bulk amounts of carbon nanotubes. Since the Raman spectrum of the SBA-15-APES-FeCp₂ sample pyrolysed at 850°C is very similar to that of the MWCNs we suggest that the carbon filaments have analogous properties to the MWCNs or nanosized graphite.

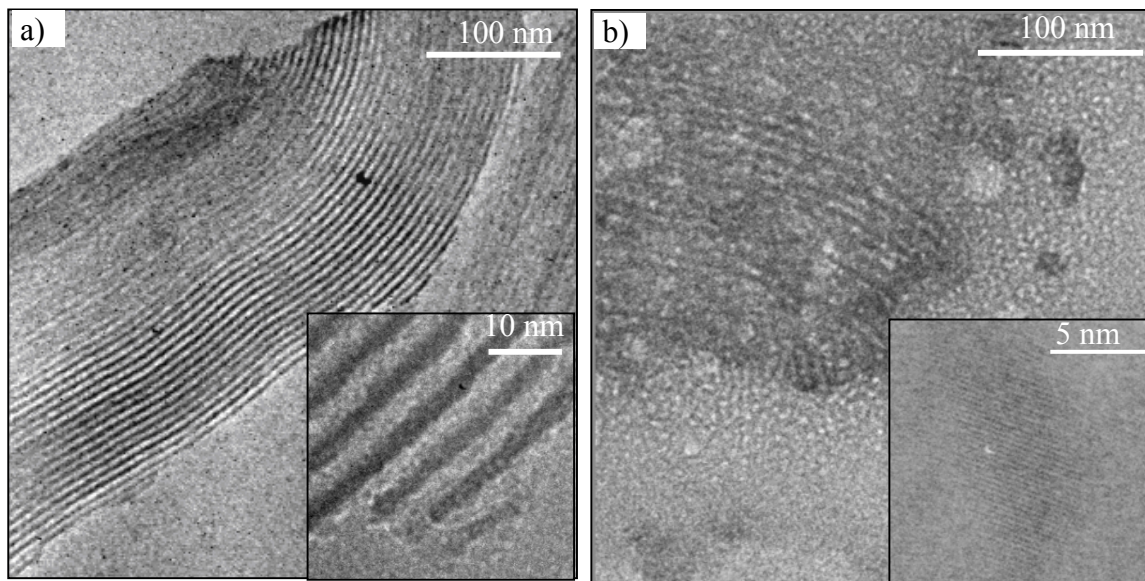


Figure 8.12. TEM images of a) pyrolysed SBA-15-APES-FeCp₂-850°C (inset: scale bar 10 nm) and b) isolated carbon filaments after removal of the silica matrix (inset: showing graphitic parts of the carbon filaments, scale bar 5 nm).

Additional TEM investigations were undertaken to probe the structure of the included carbon filaments. Figure 8.12 shows the TEM images of SBA-15-APES-FeCp₂ sample pyrolysed at 850°C and extracted carbon filaments after dissolving the silica matrix. Figure 8.12.a confirms the excellent mesostructural order of the host material. The mesoporous channels with diameter of about 5 nm are oriented parallel to the long axis of the worm-like structures. After modification with APES-FeCp₂ and pyrolysis at 850°C the mesostructural order is still intact (Figure 8.12.a). After extraction from the host silica matrix, continuous carbon filaments were observed showing a one-dimensional tubular structure with diameters of about 5 nm and lengths of more than 100 nm. Removal of the silica framework distorts the alignment of the carbon filaments but they still show quasi-parallel arrangement similar to that of the channels in the parent SBA-15 matrix (Figure 8.12.b). The HRTEM images of the carbon filaments showed small domains with a graphite-like structure (inset Figure 8.12.b).

8.3.3. Growth of carbon filaments in mesoporous films

The functionalization steps described in Scheme 8.1 were applied to mesostructured thin films prepared by the EISA method. Two types of mesoporous films showing three-dimensional cubic ($Pm3n$) (templated by CTABr surfactant) and two-dimensional ($p6m$) mesophase structure (templated by tri-block copolymer Pluronic123) were modified with APES (see Table 8.2.), reacted with ferrocene aldehyde, and subjected to vacuum pyrolysis. It is expected that a three-dimensional array of carbon filaments with diameters of less than 2 nm will form due to the confinement in the cubic silica mesoporous film (see Figure 8.13.). Furthermore, due to the pore accessibility offered by the three-dimensional cubic structure it is assumed that the inclusion chemistry in this porous system is much facilitated, and easy access of reagents would be allowed at every modification step. Oppositely, if the two-dimensional channel system of the ($p6m$) mesoporous films is used as a template, nanometer-sized carbon wires oriented parallel to the substrate surface would be expected (see Figure 8.13.). The orientation of the mesoporous channels parallel to the substrate surface would probably restrict the access of the reagents to the host, except by using the boundaries between the mesostructured domains (see Chapter 6.3.1.1).

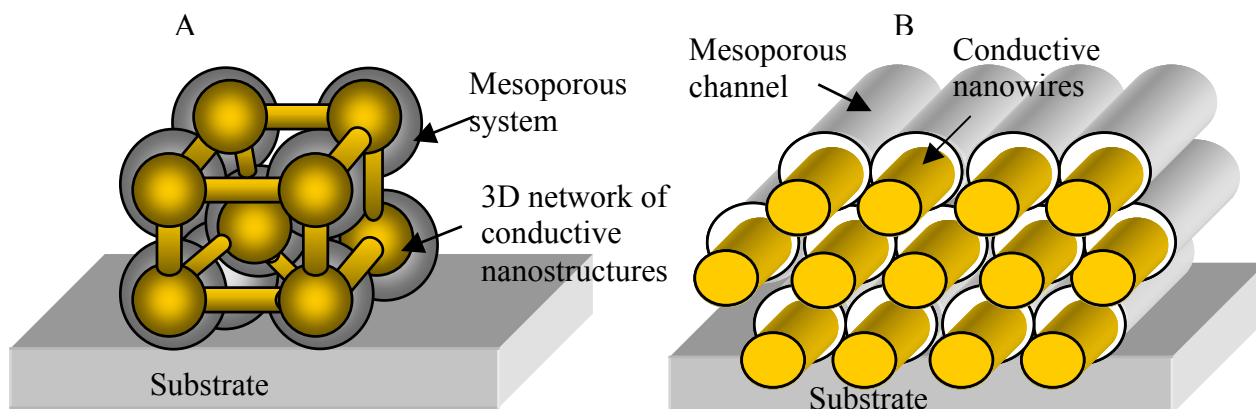


Figure 8.13. Schematic representation of the conductive nanostructures prepared in the thin mesoporous films having A) three-dimensional cubic and B) two-dimensional hexagonally ordered mesoporous systems.

Figure 8.14 shows the RXRD patterns for the cubic ($Pm3n$) mesoporous film (NPF1 sample) subjected to different modification steps. It can be seen that the cubic ($Pm3n$) mesophase structure is preserved at every modification step. The indexing of the mesophase structure is done as described in Chapter 6.3.1.1.

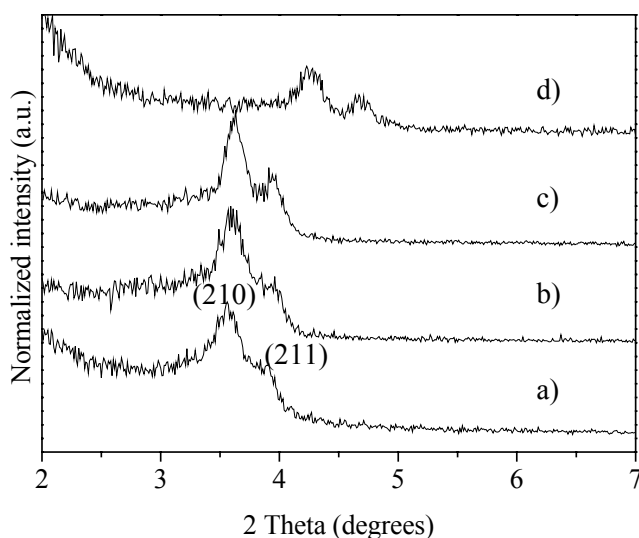


Figure 8.14. RXRD patterns of a) NPF1-calc, b) NPF1-calc-APES, c) NPF1-calc-APES-FeCp₂, and d) NPF1-calc- APES-FeCp₂-850°C.

The cubic unit-cell parameter of the NPF1-calc, NPF1-APES, NPF1-APES-FeCp₂ is 5.5 nm calculated from the position of the (211) reflection. The cubic unit cell of the NPF1-APES-FeCp₂-850°C sample decreases to 4.3 nm due to the increased condensation of the silica framework at the high pyrolysis temperature.

The GID pattern of the NPF1-APES-FeCp₂-850°C sample shown in Figure 8.15 gives additional information about the three-dimensional cubic structure of the sample. As for the as-deposited NPF1 and NPF1-calcined samples, the diffraction spots in the pattern of the NPF1-APES-FeCp₂-850°C sample are localized on three diffraction ellipses rather than rings, indicative for the one-dimensional contraction of the silica framework. At the pyrolysis temperature of 850°C the contraction calculated from eqn. 6.1. (Chapter 6.3.1.1.) is $\delta H = 49\%$ (in comparison $\delta H_{\text{as-deposited}} = 22\%$ and $\delta H_{\text{calc}} = 38\%$). The intensity distribution in the direction of the out-of-plane diffraction (inset in Figure 8.14.) similar to the RXRD experiment, shows two reflections indexed as (210) and (211) reflections of the (*Pm3n*) cubic mesophase. For additional discussion on the mesophase structure see Chapter 6.3.1.1.

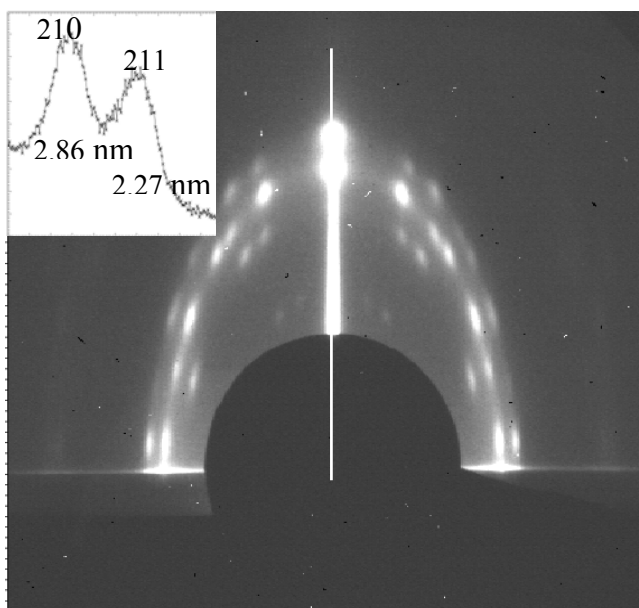


Figure 8.15. GID pattern of the NPF1-APES-FeCp₂-850°C sample (inset: intensity distribution in the direction of the out-of-plane diffraction).

The functionalization process with APES and ferrocene aldehyde of the NPF1 film was followed with reflection-absorption FT-IR spectroscopy. Figure 8.16. shows the reflection-absorption FT-IR spectra of NPF1-calc, NPF1-APES, NPF1-APES-FeCp₂ samples, respectively. In the high-frequency region a broad envelope band between 3700 – 3000 cm⁻¹ is recorded for the calcined and amino- and ferrocene-modified samples that is assigned to residual silanol-bonded water. Note that the experiments were performed in an evacuated sample chamber at room temperature. As shown before high-temperature activation of the mesoporous material is needed to remove all silanol-bonded water. Nevertheless, it was possible to record the signal at 3750 cm⁻¹ in the spectra of the calcined sample that is assigned to isolated Si-OH groups that are accessible for further functionalization.

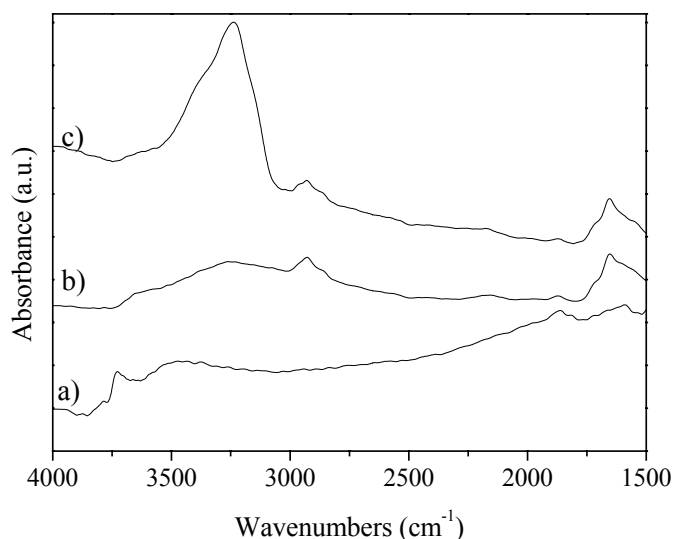


Figure 8.16. Reflection-absorption FTIR spectra of a) NPF1-calc, b) NPF1-APES, and c) NPF1-APES-FeCp₂ samples.

After modification with silane molecules and due to the covalent bonding to the free Si-OH groups of the mesoporous silica walls, the band at 3750 cm⁻¹ disappears (see Figure 16b). Additional bands typical for the grafted silane molecules appear at 2925, 2860, and 1655 cm⁻¹, which are attributed to -CH₂- asymmetric and symmetric stretching of the propyl chains and -NH₂ bending vibrations, respectively. Besides the -CH₂- stretching vibrations the

ferrocene-modified sample shows also a band at 1647 cm^{-1} that is assigned to the imine groups formed after Schiff-base reaction (see Scheme 1, III). The results are in good correspondence with the FT-IR and FT-Raman spectroscopy data obtained for the functionalized powder SBA-15 material.

In order to further characterize the mesoporous films and to follow the modification of the mesoporous surface with molecular functionality, measurements with QCM devices covered with the cubic mesoporous films were performed. The XRD patterns of the films deposited on the MPS-functionalized gold surface show the pattern characteristics similar to those of the cubic ($Pm3n$) mesoporous films prepared on silicon wafers (see Chapter 6.3.1.1). After functionalization of the calcined mesoporous films and full removal of the solvent, a drop of the frequency was measured by the QCM device. This is related to the effective mass loading of the mesoporous film due to the covalently grafted organosilane molecules.

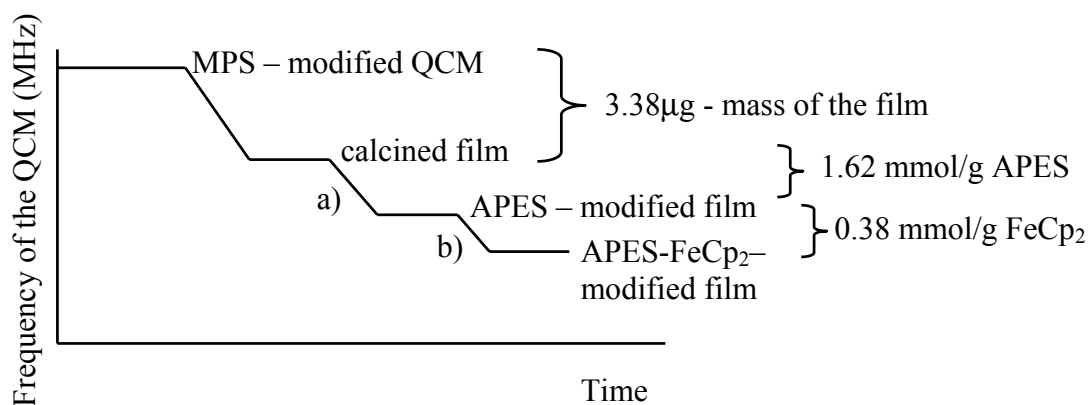


Figure 8.17. QCM gravimetric data for the modification of the NPF1-calc film with a) APES and b) FeCp₂

For example, it was calculated (using the Sauerbrey equation, for details see Chapter 4.4) that APES-modified films show a loading of about 1.62 mmol/g (see Figure 8.17.a). This value is higher than that obtained for the SBA-15-APES material (0.76 mmol/g) calculated from the TGA data. After modification with ferrocene aldehyde an additional drop in the frequency of the QCM device is observed (see Figure 8.17.b) that corresponds to an additional 0.38 mmol/g of FeCp₂. This value results in 24% yield of the Schiff-base reaction. Lower reaction yield in comparison to the SBA-15 material may be due to the partial

blockage and pore clogging in the porous system of NPF1-APES (see below). These results show that careful gravimetric-QCM measurements can be used to follow the modification process of thin mesoporous films.

Additionally, nitrogen-sorption measurements of the calcined and APES-modified sample were performed at liquid-nitrogen temperature. N₂-sorption data for the NPF1-calc and NPF1-APES are shown in Figure 8.18. The isotherm of the NPF1-calc film was already discussed in Chapter 6.3.2. The nitrogen-sorption data for the APES modified film shows considerable reduction of the amount of the adsorbed nitrogen (figure 8.18.b). This result can be attributed to the blockage of the porous system by introduction of molecular functionality. Nevertheless, drastically decreased accessibility of the porous system is higher than that found in the organically modified powder mesoporous materials. This lower sorption could be associated with partial blocking of the porous system by the thin organosilica overlayer plus a loss of flexibility of the organic groups at the liquid-nitrogen temperature.

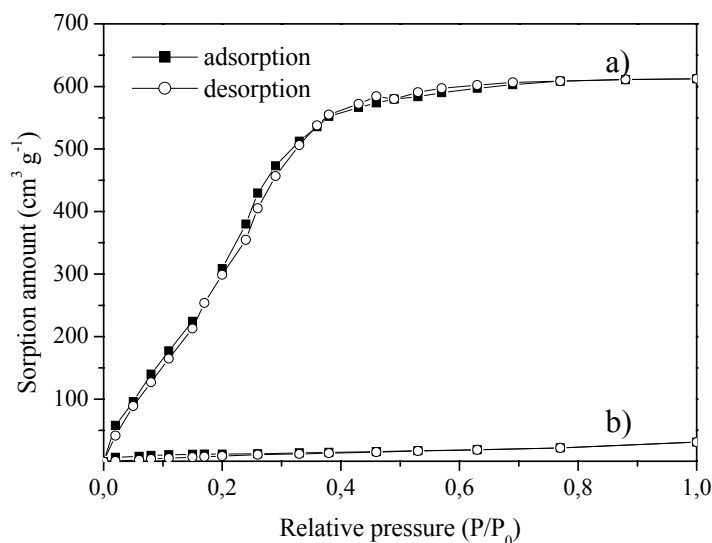


Figure 8.18. N₂-sorption isotherms measured with QCM device of a) NPF1-calc and b) NPF1-APES mesoporous films.

Similarly, hexagonally ordered mesoporous films prepared with Pluronic123 as a structure directing agent were subjected to modification with APES and FeCp₂ (see Table 8.2.). The RXRD patterns taken at different modification steps are shown in Figure 8.19. The

ordered mesostructure of the NPF3-calc sample was preserved at every modification step as confirmed from the appearance of the first-order (100) reflection in the RXRD patterns of the modified films shown in Figure 8.19. The shift in the position of the (100) reflection in the pattern of the pyrolyzed NPF1-calc-APES-FeCp₂ sample (Figure 8.19.d) is due to the increased siloxane condensation in the silica walls at the high pyrolysis temperature.

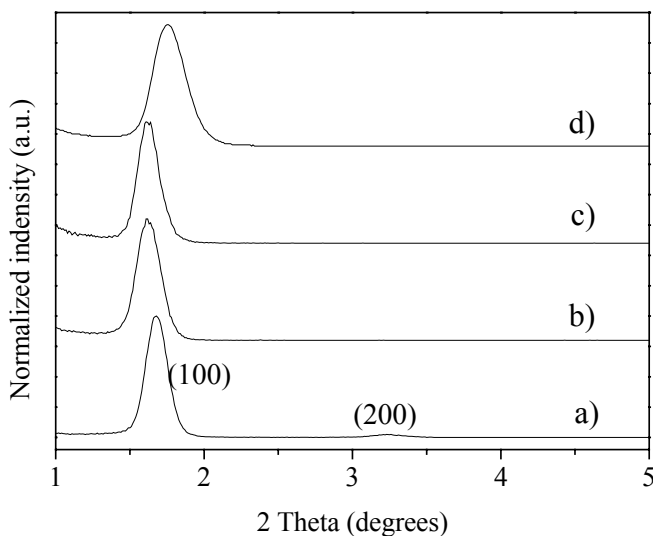


Figure 8.19. RXRD patterns of a) NPF3-calc, b) NPF3-calc-APES, c) NPF3-calc-APES-FeCp₂, and d) NPF3-calc-APES-FeCp₂-850°C.

The modification of the mesophase surface with APES-silane molecules and subsequent reaction with ferrocene aldehyde was proven by reflection-absorption FT-IR spectroscopy (see Figure 8.20.). The band at 3750 cm⁻¹ in the spectrum of NPF3-calc sample is assigned to free silanol groups and disappears in the spectrum of the APES-modified sample due to the silylation of the silica surface. Additionally, the -CH₂ stretching vibrations at 2935 and 2870 cm⁻¹ were recorded in the spectra of the NPF3-calc-APES and NPF3-calc-APES-FeCp₂ samples. The imine band at 1648 cm⁻¹ is evident in the spectrum of the NPF3-calc-APES-FeCp₂ sample proving successful modification of the silica surface with ferrocene functionality. Similar results have been obtained for the cubic NPF-1 film and SBA-15 rods (see above).

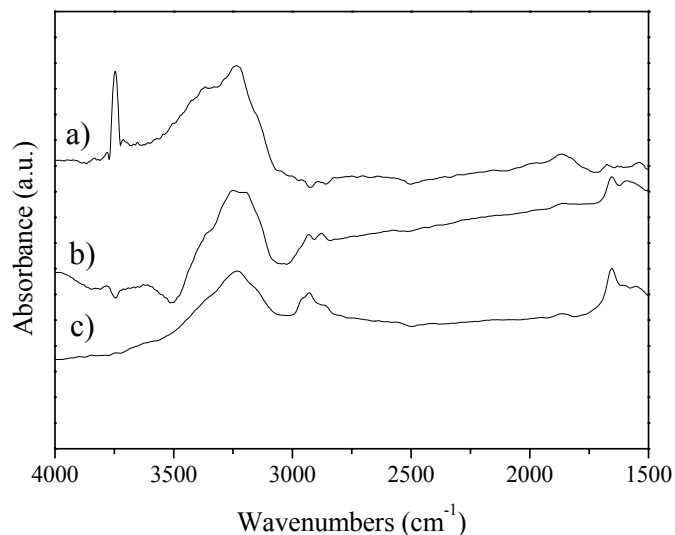


Figure 8.20. Reflection-absorption FTIR spectra of a) NPF3-calc, b) NPF3-APES, and c) NPF3-APES-FeCp₂ samples.

The formation of the carbon filaments in mesoporous films was followed by TEM measurements. Because of the low contrast between the carbon material and the mesoporous silica material direct visualization of the carbon filaments in the mesoporous channel system is difficult. Figure 8.21 shows the TEM images of the NPF1-APES-FeCp₂-850°C and NPF3-APES-FeCp₂-850°C samples. It is seen that the excellent cubic (*Pm3n*) order and the hexagonal order of the mesoporous channels is preserved after pyrolysis at high temperature. Usually unmodified silica films treated at those high temperatures (with high heating rates) result in full loss of the mesostructural order. It is difficult to resolve the carbon material deposited in the channel system of the mesoporous films. Attempts to isolate carbon material for imaging with TEM by dissolving the silica host were not yet successful.

The functionalization steps described in Scheme 8.1 were successfully applied to mesostructured thin films prepared by EISA method. After the final pyrolysis step at 850°C, the mesostructural order of the films was preserved. Unfortunately, the lack of characterization methods, such as Raman and NMR spectroscopies, or standard TGA and N₂-sorption measurements, makes it very difficult to fully follow the modification process of the films and to get more knowledge of the carbon material prepared in these hosts.

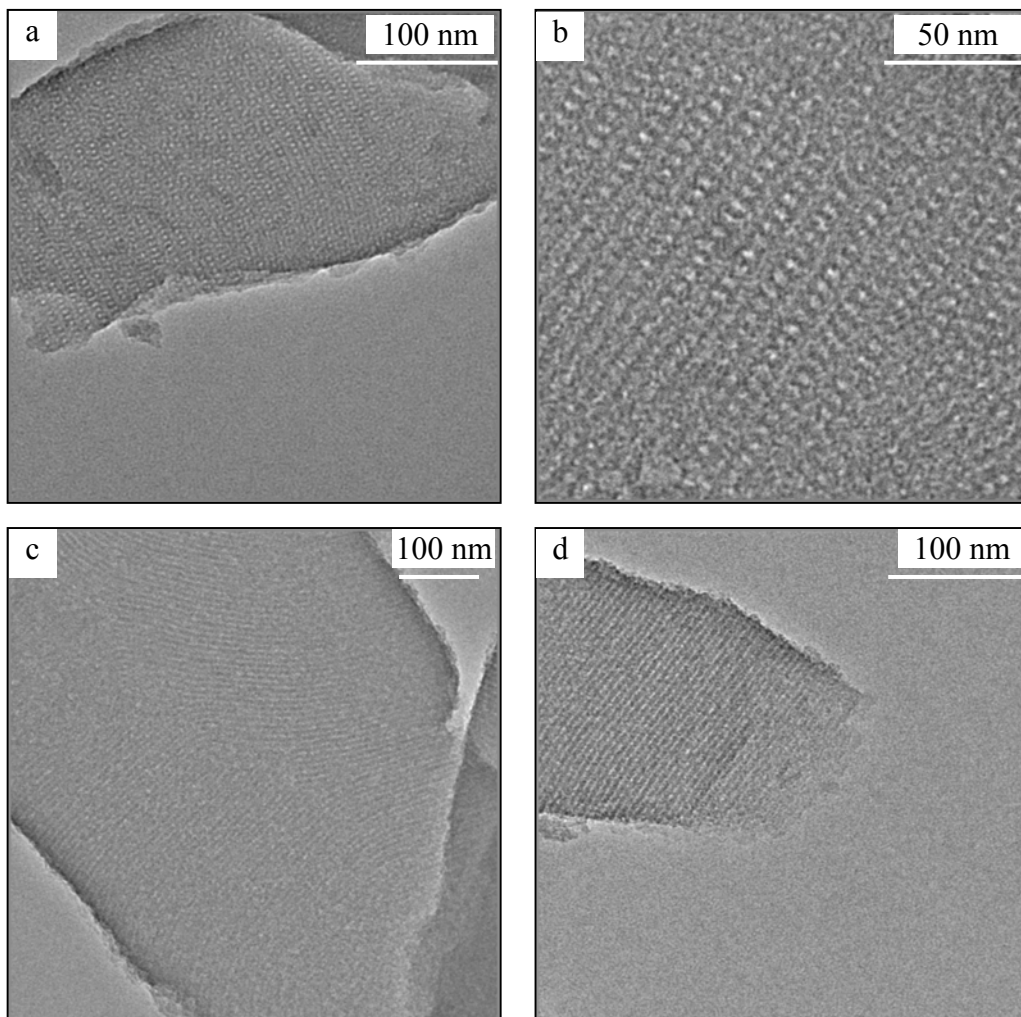


Figure 8.21. a) and b) TEM images of the NPF1-APES-FeCp₂-850°C at two different magnifications, and c) and d) TEM images of the NPF3-APES-FeCp₂-850°C at two different magnifications.

8.4. Conclusions and Perspectives

A new method for the growth of carbon filaments in ferrocene-modified SBA-15 rods and thin mesoporous films by vacuum pyrolysis at elevated temperatures is reported. The synthesis of carbon filaments is possible by the selective inclusion of the ferrocene through covalent bonding to organosilane molecules that serve as linking functionality to the silica walls and by the precise tuning of the vacuum-pyrolysis conditions. The mesophase structure

of the host/guest system was retained after pyrolysis at 850°C. Upon pyrolysis, 5 nm thin carbon filaments with tubular morphology generated within the channels of the SBA-15 host were extracted.

In this study, surface-sensitive techniques, such as GID, reflection-adsorption FT-IR spectroscopy, and QCMs measurements, were applied together in order to follow the post-synthesis functionalization process of thin mesostructured films. The vacuum-pyrolysis conditions and the selective inclusion of the catalytic ferrocene functionalities are critical for the growth of the carbon filaments in ferrocene-modified mesoporous films by the method described here.

Nevertheless, further characterization studies, such as Raman spectroscopy or GID measurements of the carbon filaments in the thin mesoporous films, could be conducted in order to gain more knowledge about the nature of the carbon material obtained. Most importantly, it is desirable to find synthetic methods to prepare hexagonally ordered mesoporous films that will facilitate the transport of reagents to the mesophase surface. Such approaches are discussed in the Outlook. Conductivity measurements performed with an STM of the hybrid carbon filaments/mesostructured silica material prepared as thin films are also envisioned, which will increase our knowledge about their electrical properties.

References

- ¹ V. Derycke, R. Martel, J. Appenzeller, Ph. Avouris, *NanoLetters*, **2001**, 1, 453.
- ² S. Fan, G. Chapline, N. R. Franklin, T. W. Tombler, A. M. Cassell, H. Dai, *Science*, **1999**, 283, 512.
- ³ J. S. Suh, J. S. Lee, *Appl. Phys. Lett.*, **1999**, 75, 2047.
- ⁴ J. Li, C. Papadopoulos, J. M. Xu, *Appl. Phys. Lett.*, **1999**, 75, 367.
- ⁵ Z. K. Tang, H. D. Sun, J. Wang, J. Chen, G. Li, *Appl. Phys. Lett.*, **1998**, 73, 2287.
- ⁶ N. Wang, Z. K. Tang, G. D. Li, J. S. Chen, *Nature*, **2000**, 408, 50.
- ⁷ C-G. Wu, T. Bein, *Science*, **1994**, 266, 1013.
- ⁸ B.C. Satishkumar, A. Govindaraj, C. N. R. Rao, *Chem. Phys. Lett.*, **1999**, 307, 158.
- ⁹ R. Andrews, D. Jacques, A. M. Rao, F. Derbyshire, D. Qian, X. Fan, E. C. Dickey, J. Chen, *Chem. Phys. Lett.*, **1999**, 303, 467.

- ¹⁰ H. Hou, A. K. Schaper, F. Weller, A. Greiner, *Chem. Mater.*, **2002**, 14, 3990
- ¹¹ C. Yang, P. Liu, Y. Ho, C. Chiu, K. Chao, *Chem. Mater.*, **2003**, 15, 275.
- ¹² H. Yoshitake, T. Yokoi, T. Tatsumi, *Chem. Mater.*, **2002**, 14, 4603.
- ¹³ A. Jentys, K. Kleestorfer, H. Vinek, *Micropor. and Mesopor. Mater.*, **1999**, 27, 321.
- ¹⁴ A. Cauvel, G. Renard, D. J. Brunel, *Org. Chem.*, **1997**, 62, 749.
- ¹⁵ E. Z. Hecht, *Anorg. Chem.*, **2001**, 627, 2351.
- ¹⁶ P. K. Dutta, M. A. Thomson, *Chem. Phys. Lett.*, **1986**, 131, 435.
- ¹⁷ J. Shimei, W. Yue, *Spectrochimica Acta A*, **1999**, 1025.
- ¹⁸ A. M. Liu, K. Hidajat, S. Kawi, D. Y. Zhao, *Chem. Commun.*, 2000, 1145.
- ¹⁹ X. Feng, G. E. Fryxell, L.-Q. Wang, A. Y. Kim, J. Liu, K. M. Kenner, *Science*, **1997**, 276, 923.
- ²⁰ X. S. Zhao, Q. G. J. Lu, *Phys. Chem. B*, **1998**, 102, 1556.
- ²¹ D. Kumar, K. Schumacher, C. du Fresne von Hohenesche, M. Grün, K. K. Unger, *Colloids and Surfaces A*, **2001**, 187, 109.
- ²² P. C. Eklund, J. M. Holden, R. A. Jishi, *Carbon*, **1995**, 33, 959.
- ²³ A. M. Rao, A. Jorio, M. A. Pimenta, M. S. S. Dantas, R. Saito, *Phys. Rev. Lett.*, **2000**, 84, 1820.
- ²⁴ Z. Liu, O. Terasaki, T. Ohsuna, K. Hiraga, H. J. Shin, R. Ryoo, *ChemPhysChem*, **2001**, 4, 229.
- ²⁵ S. Ryoo, S. H. Joo, M. Kurk. M. Jaroniec, *Adv. Mater.*, **2001**, 13, 677.

Chapter 9. Gold nanostructures in mesoporous SBA-15 rods and mesoporous films prepared by electroless reduction.

9.1. Introduction

9.2. Experimental

9.2.1. Modification of the SBA-15 rods and mesoporous films

9.2.2. Preparation of gold nanoparticles

9.2.3. Assembly of gold nanoparticles on MPS- and AEPMS-modified mesoporous materials and electroless reduction

9.2.4. Characterization

9.3. Results and Discussion

9.3.1. MPS- and AEPMS-modified SBA-15

9.3.2. Preparation of gold nanoparticles

9.3.3. Assembly of gold nanoparticles and electroless reduction of gold in SBA-15 rods

9.3.4. Au nanostructures in MPS-modified mesoporous films

9.4. Conclusions and Perspectives

9.1. Introduction

Nobel-metal nanostructures prepared as one-dimensional nanowires or arrays of ordered nanosized particles are considered to be key elements for the development of bottom-up technology in nanoscience (see Chapter 1). Among these, considerable attention has been paid to gold nanostructures because of their appealing electrical properties that are essential when the preparation of interconnections and functional units for electronic, optoelectronic, electrochemical, and electromechanical devices is required^{1,2}. The preparation of metal nanostructures applying templating methods within the confined spaces of host materials, such as anodic alumina, carbon nanotubes, or mesoporous solids is an attractive opportunity (see Chapter 3.1. and references therein).

Metal infiltration through wet impregnation or metalorganic chemical vapor deposition in the hollow channels of different porous supports are popular techniques used

to load porous materials with metallic particles for different catalytic applications^{3,4}. This approach has been expanded to the preparation of continuous metal wires. Stucky and co-workers demonstrate a general synthetic route for the preparation of noble metal nanowires (Au, Ag, Pt) encapsulated in SBA-15 materials⁵. In order to incorporate the metal precursors inside the mesoporous channels, calcined mesoporous SBA-15 was impregnated with aqueous solutions containing noble metal salts, such as $\text{Pt}(\text{NH}_3)_4(\text{NO}_3)_2$, HAuCl_4 , and AgNO_3 . The average length of a single nanowire was 500 nm with a uniform diameter of 6 nm, consistent with the channel dimensions. Chemical vapor infiltration is another approach used to prepare metal nanowires inside the mesoporous host matrix. Cheon and co-workers demonstrated the synthesis of Pd-nanoballs and nanowires in MCM-48, MCM-41, and SBA-15 materials, respectively, by chemical vapor infiltration with the organometallic precursor $\text{Pd}(\text{hfac})_2$ (hfac = 1,1,1,5,5,5-hexafluoroacetylacetonate)^{6,7}.

Unfortunately, electrical conductivity measurements were not performed in any of the studies discussed here, but potential applications of the metal nanostructures as conductive devices suitable for molecular electronics are occasionally mentioned. Recently, the preparation of RuO_2 nanowires in disordered mesoporous silica aerogels by cryogenic decomposition of RuO_4 was reported⁸. Two-point probe conductivity tests between various points in the center and on the outer surfaces of the loaded aerogel show metallic conductivity after annealing the composite material at 150 °C.

Gold nanostructures, nanowires, or nanoarrays can be prepared in mesoporous hosts by applying a direct wet impregnation technique with $\text{H}[\text{AuCl}_4]$, or in situ by complexation of the gold precursor on the organically modified mesoporous surface^{5,9,10,11,12}. Recently, co-assembly one-pot synthesis of ordered mesoporous material with gold nanoparticles was reported where the $\text{H}[\text{AuCl}_4]$ was directly added to the initial synthesis sol¹³. In these cases it is expected that mesoporous hosts with tubular mesoporous system (MCM-41, MCM-48, or SBA-15) will template gold nanowires whereas three-dimensional cubic mesoporous materials with spherical porous system can give templated growth of ordered gold nanoarrays. Usually the gold reduction was performed in hydrogen flow at elevated temperatures^{5,9,10} or by using chemical reducing agents, such as NaBH_4 or citrate^{11,12}. A prerequisite for the successful impregnation of the $\text{H}[\text{AuCl}_4]$ in the mesoporous solid is to

adjust the isoelectric point of the host matrix so that anionic $\text{Au}(\text{OH})_x\text{Cl}_{4-x}$ complexes are coordinated on the mesoporous surface. For example, at pH 6-10 where the usual wet impregnation is done, the mesoporous silica surface is negatively charged (isoelectric point of silica is around 2) and no coordination of the gold precursors is expected. A useful strategy is to modify the mesoporous surface with cationic functional groups that will enhance the interaction between the anionic gold complex and the silica surface^{9,10}. On the other hand, thiol-functionalized mesoporous materials were used to directly assemble gold nanoarrays by size-selective extraction of gold nanoparticles from nanosized colloidal gold suspensions¹⁴.

An important factor that influences the synthesis of gold nanostructures in host matrices is the choice of the reducing agent. When high temperature reduction in hydrogen is used the mobility of gold is usually high enough to form bigger clusters on the outer surface of the host matrix⁵. To overcome this problem mild chemical reduction conditions were suggested that make the final size of the gold nanostructures only dependent on the pore size of the host matrix¹¹.

For the future applications in nanotechnology it is desirable that the metal nanostructures are encapsulated in host templates prepared on a variety of substrates, such as thin layers or films. Recently, Ag nanoparticles assembled in nanosized arrays in the three-dimensional hexagonally ordered films have been made by wet impregnation of the mesoporous film with AgNO_3 , followed by hydrogen reduction¹⁵. Similarly, Au nanoparticles were prepared in hexagonally-ordered CTAC-templated films¹⁶.

A significant disadvantage of all these strategies is the low continuity of the final gold nanowires or nanoarrays. Usually only several tens of nanometers of gold nanowires or a mesoporous surface sparsely covered with gold nanoparticles is obtained. A promising approach to obtain continuous metal nanowires is electroless reduction. The electroless reduction methods use metal ions or catalyst nanoparticles to nucleate and guide the growth of continuous metal nanowires. It has been shown that chiral lipid tubules can be metallized by electroless reduction giving nanometer thin metal wires¹⁷. Metallized DNA molecules were also subjected to electroless reduction, resulting in a metal nanowire between two metal electrodes^{18,19}.

In this Chapter, a two-step procedure for the preparation of gold nanostructures in SBA-15 hosts and mesoporous films is demonstrated. First, the assembly of catalytically active gold nanoparticles is achieved followed by electroless reduction in a gold plating bath to obtain continuous gold nanostructures. Different methods for the preparation of the catalytically active gold nanoparticles were explored, namely direct assembly of gold particles on thiol-modified mesoporous materials from different gold colloids (5 - 6 nm and 1.5 - 3 nm gold particles) and impregnation-complexation of H[AuCl₄] on ethylenediamino-modified mesoporous materials (see below). The aim was to find optimal synthetic conditions for selective loading of the inner surface of the mesoporous materials with gold nanoparticles and to use these supports for catalytic electroless reduction. The methods investigated for the inclusion of gold nanostructures in SBA-15 material were extended to mesostructured films prepared by the EISA method.

9.2. Experimental

9.2.1. Modification of the SBA-15 rods and mesoporous films

SBA-15 rods were synthesized as explained in Chapter 5.3.2. CTABr- and Pluronic123-templated mesoporous films were prepared following the conditions of the EISA method (Chapter 6.2.1.). Template removal was achieved by first treating the sample at 120 °C for 6 h in air followed by calcination in flowing air at 500°C for 4 h (ramping at 0.75 deg/min), calcination procedure B (Chapter 5.3.2.).

Calcined SBA-15 rods and mesoporous films were modified with thiol groups. A sample of 50 mg of mesoporous silica SBA-15 material was dehydrated at 120 °C in vacuum to remove water molecules absorbed on the surface, and then stirred in 10 mL dry toluene (Fluka) containing 500 μL (0.003 mol) of 3-mercaptopropyltrimethoxysilane (MPS – Fluka) (Scheme 9.1., step IA) under refluxing conditions applying standard Schlenk-line techniques for 20 h. Similarly, 50 mg of dehydrated SBA-15 material in 10 ml dry toluene (Fluka) was reacted with 700 μL (0.003 mol) of 3-(2-aminoethylamino) propyltrimethoxysilane (AEPMS - Fluka) under N₂ for 20 h in order to introduce ethylenediamino functionalities on the silica walls (Scheme 9.1., step IB). The powder was

collected by filtration, washed with excess amounts of the solvent, and dried at 60 °C for at least 24 h. The identification of the samples used in this Chapter is shown in Table 9.1.

Calcined mesoporous films showing different mesophase structures (see Table 9.2.) were dehydrated at 120 °C in vacuum to remove water molecules absorbed on the surface, and then stirred in 10 mL dry toluene (Fluka) containing 500 μ L (3 μ mol) MPS under refluxing conditions applying standard Schlenk-line techniques under N₂. After 20 h the functionalized mesoporous films were washed with excess amounts of the solvent and dried at 60 °C for at least 24 h. The identification of the samples is given in Table 9.2.

9.2.2. Preparation of gold nanoparticles

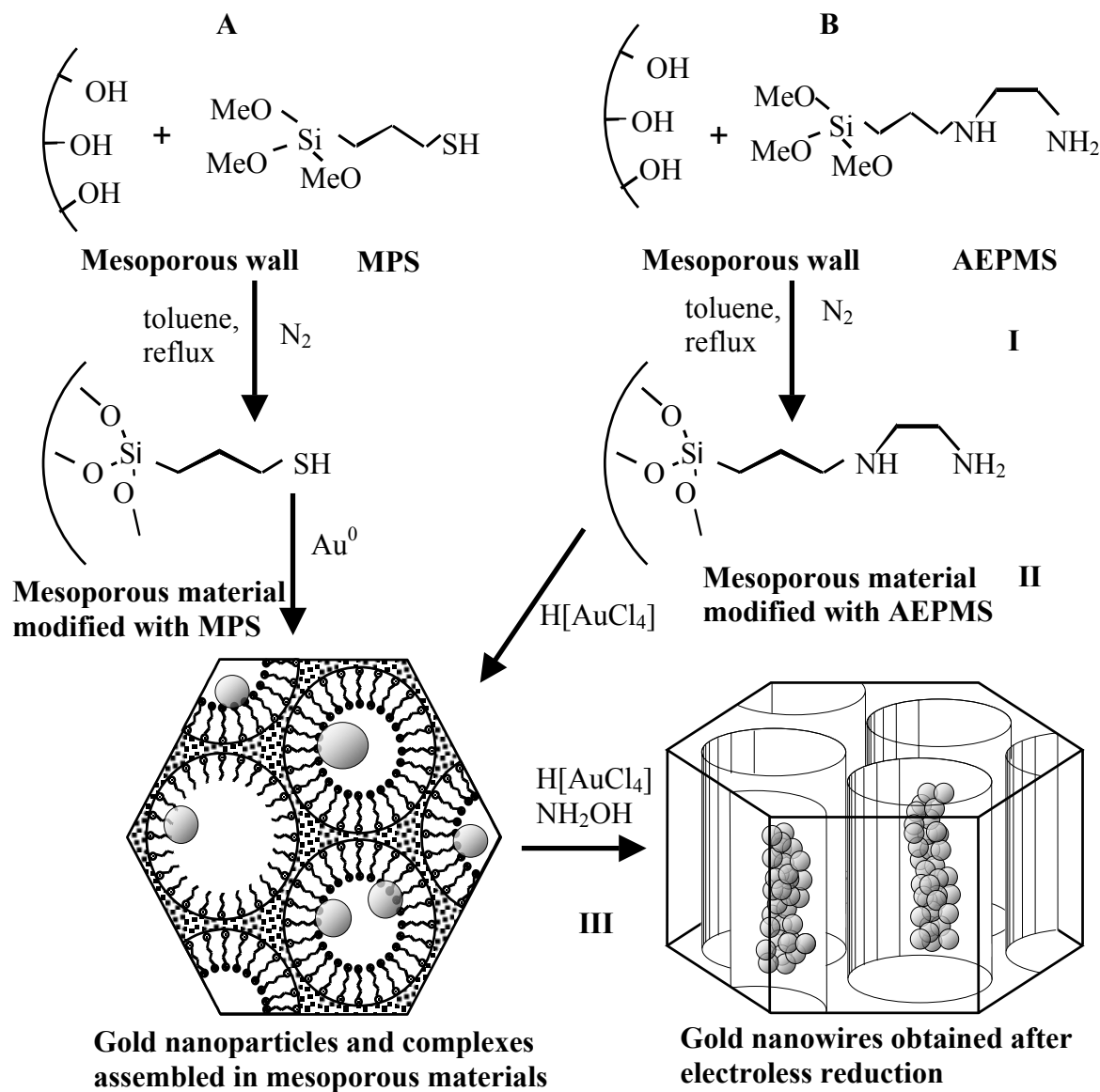
Three types of gold colloids were prepared in this study that are referred to as Au1, Au2, and Au3. Special attention was paid that clean glassware (aqua-regia) is used in all synthesis.

Au1 colloidal gold was synthesized according to literature methods and is expected to give 4 - 5 nm gold nanoparticles²⁰. 1.5 mL (0.045 mmol) of a 30 mM aqueous solution of hydrogen tetrachloroaurate H[AuCl₄].3H₂O (Aldrich) were mixed with 4 mL (0.2 mmol) of a 50 mM solution of tetraoctylammonium bromide TOAB (Aldrich) in toluene and shaken vigorously in a separation funnel. After quantitative transfer of the tetrachloroaurate to the organic phase, 1.75 mL (0.875 mmol) of freshly prepared 0.5 M sodium borohydride NaBH₄ (Aldrich) was added at once under stirring and reacted for 15 min. Finally, the ruby-colored organic phase was separated carefully, washed once with 0.1 M sulphuric acid to remove access of borohydride, and used for further studies.

Au2 solution was prepared similar to Au2 but the NaBH₄ reduction step was omitted. The final orange-brown toluene solution was further used to directly assemble gold precursors in the MPS-modified mesoporous hosts.

Au3 colloidal gold with 1.5 - 3 nm gold particles was prepared following literature methods²¹. To 45.5 ml distilled water were added in the following order: 1.5 mL (0.3 mmol) of 0.2 M NaOH, 1 mL of 0.96% tetrakis(hydroxymethyl)phosphonium chloride THPC (1.2 mL of 80% THPC diluted to 100 mL with distilled water), and 1 mL (0.03 mmol) of 30 mM hydrogen tetrachloroaurate H[AuCl₄].3H₂O. Two minutes were allowed between the

addition of the THPC and that of the tetrachloroauric acid. The final orange-brown hydrosols were used for further experiments.



Scheme 9.1. Graphical representation of the synthetic steps to obtain gold nanostructures in the mesoporous materials.

9.2.3. Assembly of gold nanoparticles on MPS- and AEPMS-modified mesoporous materials and electroless reduction

Usually, a sample of 40 mg of MPS-modified SBA-15 material (SBA-15-MPS) were stirred for 20 h at room temperature with 5 mL of Au1, Au2, and Au3 gold colloids, respectively (see Scheme 9.1., IIA). After the assembly of the gold nanoparticles the powder was collected by filtration, washed with excess amounts of solvent, and dried at 60 °C for at least 24 h. The identification of the samples is given in Table 9.1. Similarly, 40 mg AEPMS-modified SBA-15 material (SBA-15-AEPMS) was stirred with 5 mL (0.15 mmol) of 30 mM H[AuCl₄].3H₂O at room temperature for 24 h (see Scheme 9.1., IIB). Finally, the SBA-15-AEPMS-Au sample was separated by filtration, washed with water, and dried at 60 °C.

In the same way, MPS-modified mesoporous films were immersed up-side down for 24 h at room temperature in 5 mL of Au2 gold solution. After washing with access amounts of solvent, the films were dried and used for further studies. The identification of the samples is given in Table 9.2.

Table 1. SBA-15 samples with codes used in the study.

Sample name	Manipulation
SBA-15-calc	Calcined SBA-15
SBA-15-MPS	MPS-modified SBA-15
SBA-15-MPS-Au1	Assembly of Au1 in SBA-15-MPS
SBA-15-MPS-Au2	Assembly of Au2 in SBA-15-MPS
SBA-15-MPS-Au3	Assembly of Au3 in SBA-15-MPS
SBA-15-MPS-Au1-red	Subjected to electroless reduction
SBA-15-MPS-Au2-red	Subjected to electroless reduction
SBA-15-MPS-Au3-red	Subjected to electroless reduction
SBA-15-AEPMS	AEPMS-modified SBA-15
SBA-15-AEPMS-Au	Complexing of H[AuCl ₄]
SBA-15-AEPMS-Au-red	Subjected to electroless reduction

The third step of the synthetic procedure involves electroless reduction (see Scheme 9.1., III). 30 mg of SBA-15 material modified with gold precursors were immersed in gold electroless reduction bath²² consisting of 3 mL (0.016 mmol), 4 mM NH₂OH.HCl, and 3 mL (0.09 mmol), 30 mM H[AuCl₄].3H₂O for 10 min (see Table 9.1.). Similarly, Au-

modified mesoporous films were reacted in an electroless reduction bath consisting of 1.5 mL 0.4 mM NH₂OH.HCl and 1.5 mL 3 mM H[AuCl₄].3H₂O (electroless reduction 1) for 6h followed by repeated electroless reduction in a plating bath consisting of 3 mL 4 mM NH₂OH.HCl and 3 mL 30 mM H[AuCl₄].3H₂O (electroless reduction 2) for 30 min. Finally all samples were washed with water and dried at 60°C overnight.

Table 9.2. Modified mesoporous film samples with codes used in the study.

Manipulation	NPF1	NPF3
	CTABr-templated cubic	Pluronic 123-templated hexagonal
Thermally treated and calcined	NPF1-calc	NPF3-calc
MPS-modified	NPF1-MPS	NPF3calc-MPS
Assembly of Au ₂	NPF1-MPS-Au ₂	NPF3-MPS-Au ₂
Subjected to electroless reduction 1	NPF1-MPS-Au ₂ -red1	NPF3-MPS-Au ₂ -red1
Subjected to electroless reduction 2	NPF1-MPS-Au ₂ -red2	NPF3-MPS-Au ₂ -red2

9.2.4. Characterization

The mesophase structure of the host materials and the samples loaded with gold nanostructures were confirmed by X-ray diffraction measurements (Scintag XDS 2000, CuK_α radiation). Nitrogen adsorption-desorption isotherms were recorded using a NOVA 4000e Surface Area & Pore Size Analyser after evacuation of the samples at 120 °C. The functionalization process of the SBA-15 material was followed by FT-IR spectroscopy using a Nicolet Avatar-360 FTIR spectrometer with a spectral resolution of 4 cm⁻¹. The powder was pressed into self-supporting disks (ca. 15 - 20 mg/cm²), that were directly mounted in a sample cell. Measurements were performed in transmission mode at room temperature after evacuation. FT-Raman spectra were recorded with a Bruker Equinox 55 -

106v/S spectrometer equipped with a Raman module (9395 cm^{-1} laser, 4 cm^{-1} resolution, 80 mW laser power, 2000 scans). The modification processes of the mesoporous films were followed by reflection-absorption FT-IR spectroscopy. Proton-decoupled ^{13}C and ^{29}Si solid-state NMR spectra were recorded on a Bruker DSX Avance spectrometer. The loading of the host support with organic functionality was followed by thermogravimetric analysis (TGA; Du Pont 951, Thermal Analyzer). The elemental composition and surface morphology of the powder and film samples were determined with SEM (JEOL, JSM 65007, field emission SEM equipped with Oxford EDX detector). TEM measurements were performed with a JEOL JEM 2010 transmission electron microscope operating at 200 kV. Samples for TEM were prepared by depositing a drop of a suspension of the solid in acetone on carbon-coated copper grids. Samples for plan views of the mesoporous films were obtained as described in Chapter 5.2.1.

9.3. Results and Discussion

9.3.1. MPS- and AEPMS-modified SBA-15

The XRD patterns of the calcined, MPS- and AEPMS-modified SBA-15 samples show that the mesophase structure is preserved after the silylation of the mesophase surface. As discussed earlier, this pattern corresponds to ($p6m$) hexagonal mesophase structure with highly intense first-order (100) reflections and second-order (110) and (200) reflections (see Figure 9.1.). After post-synthesis modification, the intensity of all reflections decreases due to the decreased scattering contrast between the silica wall and the porous system; this is typical for the pore filling of porous materials.

The nitrogen-sorption isotherms of the calcined, MPS- and AEPMS-modified samples are shown in Figure 9.2. This type of isotherms has already been discussed in Chapter 8.3.1. Most importantly, after post-synthesis silylation the type of the isotherms is preserved; no pore blocking or mesophase distortion is observed. The specific surface area, S_{BET} , total pore volume, V_{t} , and mean pore size calculated from the BJH model, D_{BJH} , show decreased values for silane-grafted samples in comparison to the parent SBA-15 materials in correspondence to the pore-filling effect (see Table 9.3.).

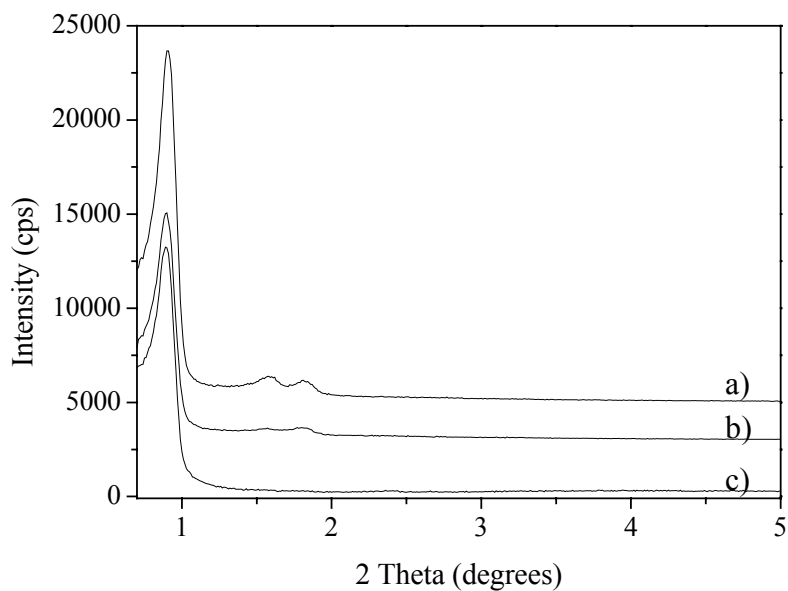


Figure 9.1. XRD patterns of a) calcined SBA-15, b) SBA-15-MPS, and c) SBA-15-AEPMS samples (the patterns are offset with 7000 cps).

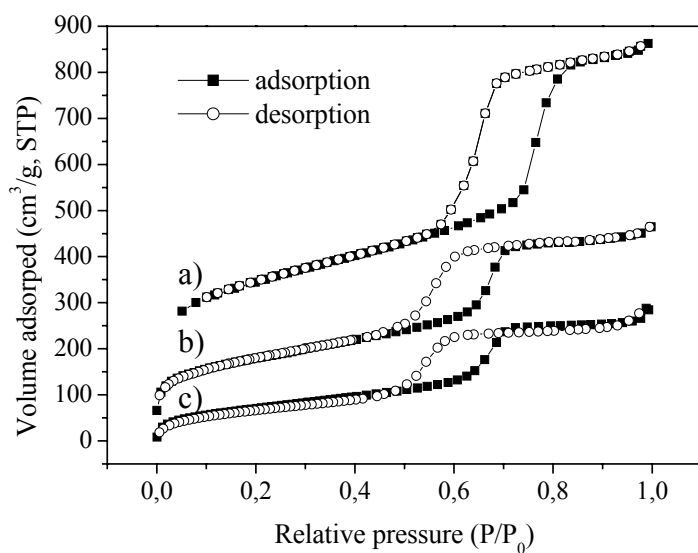


Figure 9.2. N₂-sorption isotherms of a) calcined SBA-15, b) SBA-15-MPS, and c) SBA-15-AEPMS samples (the isotherms are offset with 100 cm³/g).

Table 9.3. N₂-sorption data for the calcined SBA-15 and modified samples.

Sample	a(nm)	S _{BET} (m ² g ⁻¹)	V _t (cm ³ g ⁻¹)	D _{BJH} (nm)
SBA-15-calc	11.6	887	1.17	5.4
SBA-15-MPS	11.5	468	0.62	5.3
SBA-15-AEPMS	11.5	382	0.44	4.5

The surface area is calculated from the BET model, the total volume adsorbed is calculated from single point measurement at P/P₀ = 0.994, and the pore size is determined by the BJH model applied to the desorption branch of the isotherm.

Thermal analysis was used to evaluate the degree of loading with molecular functionality. The SBA-15-MPS sample shows a weight loss of 7 wt% (or about 14 wt% loading with MPS, assuming that the weight loss is only due to the combustion of the organic part of the silane and that siloxane bonds are formed) that corresponds to 0.63 mmol/g. This value stands for 0.45 MPS molecules per one nm² of mesoporous surface calculated from eqn. 8.1. (Chapter 8.3.1.) A fully dense monolayer of MPS molecules on an MCM-41 surface (S_{BET}~900 m²/g) has been evaluated to be 5 molecules per one nm²²³. Assuming full coverage with MPS molecules (with length of the MPS molecule of about 0.42 nm, calculated from geometrical considerations) of the cylindrical mesopores with average diameter of 5.4 nm and specific surface area of 887 m²g⁻¹, the total decrease of mesoporous volume is estimated to be about 0.68 cm³g⁻¹. This is more than the decrease of the total pore volume (V_t) measured by N₂ sorption (0.55 cm³g⁻¹) and suggests sparsely covered mesoporous surface with MPS molecules. These results are in accordance with the ²⁹Si NMR data shown below.

The SBA-15-AEPMS sample shows a thermal weight loss of 10% (or about 17 wt% loading with AEPMS, assuming that the weight loss is only due to the combustion of the organic part of the silane, and that siloxane bonds are formed) equivalent to about 0.77 mmol/g of silane molecules grafted on the mesoporous surface. This value corresponds to 0.5 AEPMS molecules per one nm² calculated from eqn. 8.1. (Chapter 8.3.1.). This value is lower than that obtained for AEPMS molecules grafted on MCM-41 and SBA-1 materials²⁴. Assuming full coverage with AEPMS molecules (with length of the AEPMS molecule of about 0.44 nm, calculated from geometrical considerations) of the cylindrical mesopores with average diameter of 5.4 nm and specific surface area of 887 m²g⁻¹, the total decrease of

mesoporous volume is estimated to be about $0.75 \text{ cm}^3\text{g}^{-1}$. This is slightly more than the decrease of the total pore volume (V_t) measured by N_2 sorption ($0.73 \text{ cm}^3\text{g}^{-1}$). The results are similar to those obtained for the APES modified SBA-15 material (Chapter 8.3.1).

Here we obtain a lower surface coverage of MPS and AEPMS molecules on the SBA-15 surface than theoretically estimated. On the other hand, as discussed in Chapter 8.3.1., the population density and the quality of the functionalized monolayers on the mesoporous materials is strongly affected by the population of the surface silanol groups that can participate in the silylation reaction. The type and density of the silanol groups on the mesoporous surface is influenced by the synthesis mechanism (type of surfactant, pH, etc.), post-synthesis treatments, and calcination procedure that are different for every type of mesoporous material.

Further characterization of the modification process with MPS and AEPMS functionalities was obtained with FT-IR and FT-Raman spectroscopy. The selected regions of interest in the FT-IR spectra of the SBA-15-calc and SBA-15-MPS samples are shown in Figure 9.3. The band positions in the spectrum of the calcined SBA-15 material and their assignment was already discussed in Chapter 8.3.1. Briefly, the sharp signal at 3750 cm^{-1} in the spectrum of the calcined SBA-15 is due to the free Si-OH that are accessible for silylation (see Figure 9.3.a). After MPS-modification, the intensity of this band is considerably decreased confirming silane grafting on the mesoporous surface through covalent bonding to the Si-OH groups. In comparison to the APES-modified (see Chapter 8.3.1) and AEPMS-modified samples (see below), the band at 3750 cm^{-1} of the MPS-modified sample is still evident. This can be explained by the less than complete siloxane linking of the organosilane molecules to the free Si-OH groups of the mesoporous surface. The bands at 2950 and 2855 cm^{-1} in Figure 9.3.b are characteristic for $-\text{CH}_2-$ asymmetric and symmetric stretching vibrations of the organosilane molecules.

The FT-IR spectra of the SBA-15-AEPMS sample are shown in Figure 9.5.b. The full disappearance of the band at 3750 cm^{-1} and the appearance of the bands at 2940 , 2880 , and 1657 cm^{-1} that are characteristic for $-\text{CH}_2-$ asymmetric and symmetric stretching and $-\text{NH}_2$ bending, respectively, prove the successful post-synthesis grafting of AEPMS

molecules on the mesoporous surface. The band positions are similar to those reported in the literature for thiol- and amino-functionalized mesoporous materials^{23,24,25}.

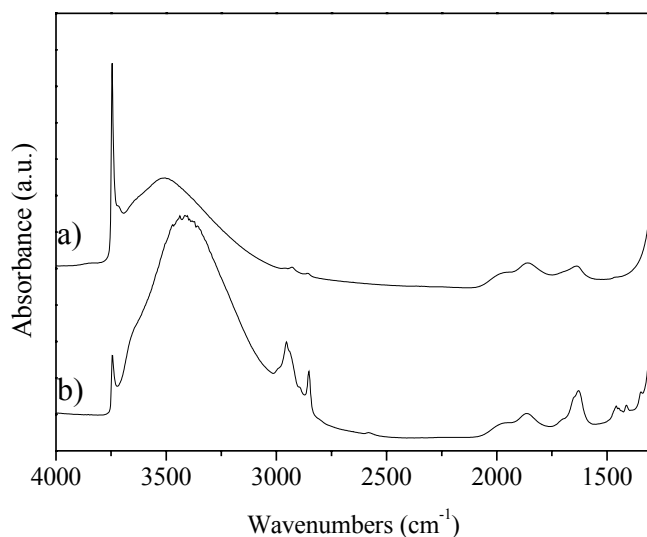


Figure 9.3. FT-IR spectra of a) calcined SBA-15 and b) SBA-15-MPS samples.

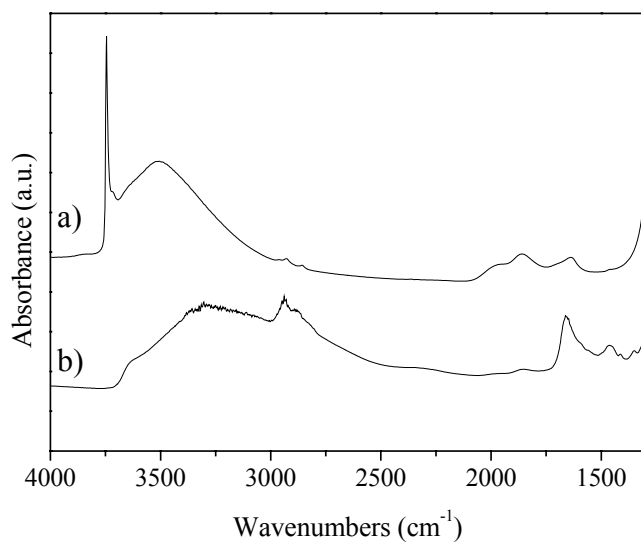


Figure 9.4. FT-IR spectra of a) calcined SBA-15 and b) SBA-15-AEPMS samples.

Additional evidence for the covalent bonding of the silane molecules is obtained by FT-Raman measurements. Figure 9.5 shows the Raman spectra of the SBA-15-calc, SBA-15-MPS, and SBA-15-AEPMS samples. As expected, the spectrum of the SBA-15-calc does not show any Raman peaks in the examined region in correspondence with the full template removal during the calcination process. In the high-frequency region, the bands that are typical for the $-\text{CH}_2-$ asymmetric- and symmetric-stretching vibrations are seen in the spectra of the SBA-15-MPS and SBA-15-AEPMS samples. The band at 2584 cm^{-1} in the spectrum of the MPS-modified sample (Figure 9.5.b) is assigned to the S-H stretching vibrations. The bands that are typical for the $-\text{CH}_2$ scissoring vibrations and Si-C bonds are seen at 1462 and 1307 cm^{-1} , respectively (Figure 9.5.b and c).

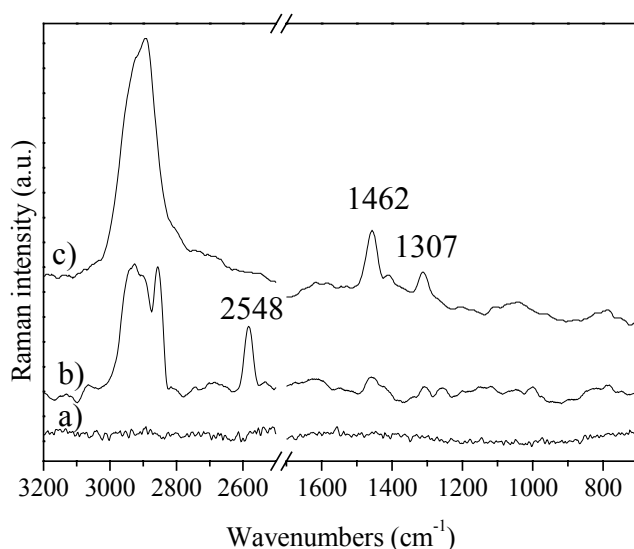


Figure 9.5. FT-Raman spectra of a) calcined SBA-15, b) SBA-15-MPS, and c) SBA-15-AEPMS samples.

^{13}C NMR solid-state NMR studies were performed to further identify organic functionality grafted to the mesoporous surface. Figure 9.6.a shows the ^{13}C NMR spectra of the SBA-15-MPS sample. The peak at 9.3 ppm was attributed to the C^1 carbon atoms (see inset Figure 9.7.a) of the methylene groups that are directly bonded to the Si atoms. The signals at about 27.2 and 49.1 ppm were assigned to the other two carbon atoms (C^2 and C^3)

from the propyl chain. The identification of the carbon atoms for the SBA-15-AEPMS sample is shown in the inset in Figure 9.7.b. Analogously, the signal at 9.5 ppm is attributed to C¹ carbon atoms from the methylene groups directly bonded to the silicon atoms, and the signals at about 21.8, 41.1 and 51.1 ppm are assigned to the carbon atoms in the propylene and ethylene chains, as shown in the inset. The assignments correspond to other results shown in the literature^{23,25,26}.

Additionally, the nature of the molecular functionalities and the chemical bonding to the silica surface of the mesoporous material can be studied by solid-state ²⁹Si NMR experiments. The peak assignment and the indexation of the silicon atoms according to their chemical environment in the amino-modified sample SBA-15-APES were shown in Chapter 8.3.1.

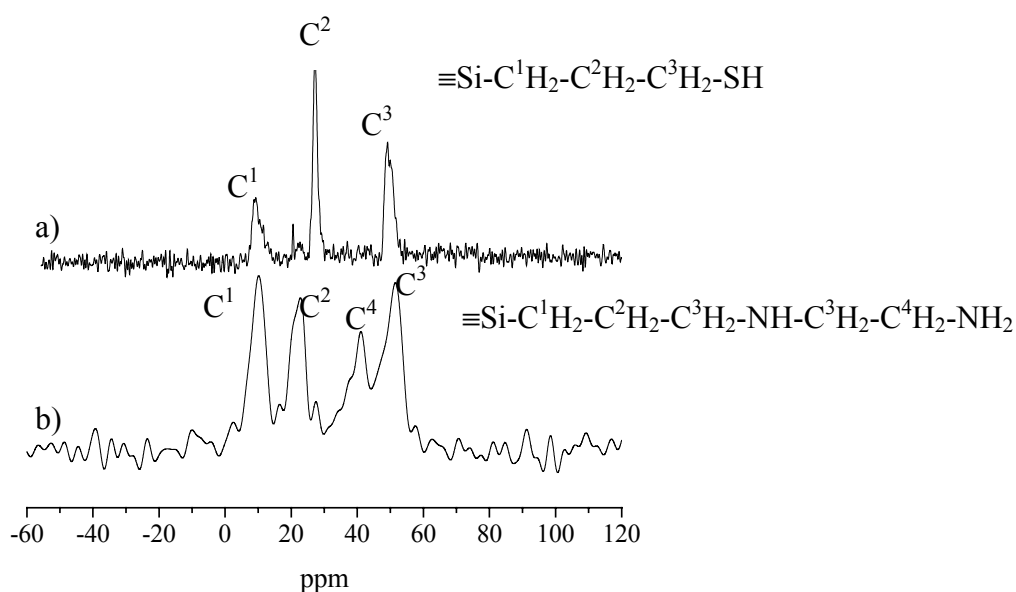


Figure 9.6. ¹³C NMR spectra of a) SBA-15-MPS and b) SBA-15-AEPMS samples.

Similarly, in the spectra of the SBA-15-calc, SBA-15-MPS, and SBA-15-AEPMS samples (Figure 9.7) the peaks at about -101 ppm and -109.7 are assigned to the Q³ and Q⁴ silicon atoms (see Chapter 8.3.1 for assignments) that are representative for the cross-linked silica framework. In the spectrum of the SBA-15-calc and SBA-15-MPS sample, a resonance at about -91.5 ppm is observed that is assigned to Q² silicon atoms. In comparison to the ²⁹Si NMR spectra of the calcined SBA-15 material (Figure 9.7.a), the

appearance of fully cross-linked Si atoms (Q^4) and the disappearance of the Q^2 silicon atoms in the spectrum of the SBA-15-AEPMS material, and the considerable decrease of the Q^2 species in the spectrum of the SBA-15-MPS material is indicative for the increased siloxane condensation *via* reaction of the organosilane with the surface silanols. The appearance of the residual Q^2 species in the spectrum of the MPS-modified sample suggests the existence of Si bearing OH groups that did not participate in the cross-linking of the organosilane molecules, in agreement with residual free silanols observed in the FT-IR spectra (see above).

Signals from the T^n silicon atoms (silicon atoms in the organosilane molecules, see Chapter 8.3.1) were also detected in the SBA-15-MPS and SBA-15-AEPMS samples. Figure 9.7.b shows signals at about 49.1, 56.7, and 65.5 ppm that are attributed to the T^1 (silicon atoms that are bound to two hydroxyl, one organic residue, and one siloxane bridge $[(SiO)Si-(OH)_2R]$, T^2 and T^3 silicon atoms (for assignments see Chapter 8.3.1). The predominant appearance of the T^1 and T^2 silicon atoms suggests the formation of a sparsely covered mesoporous surface with mostly isolated MPS molecules (Figure 9.7.b). Oppositely, the SBA-15-AEPMS sample shows only signals of the T^2 and T^3 silicon atoms (Figure 9.7.c) with a major contribution of the T^3 silicon atoms, which implies that more fully cross-linked siloxane networks are formed resulting in a denser organosilane layer on the mesoporous surface.

As explained in Chapter 8.3.1., the quantification of the degree of surface coverage with organosilane molecules in the course of the grafting process based on the NMR data is difficult. It is controlled by the surface coverage with reactive (non-hydrogen bonded) silanols and the conditions of the post-synthesis condensation process. Nevertheless, the relative integrated intensity of the signals for the $T^n = (T^1+T^2+T^3)$ and $Q^n = (Q^3 + Q^4)$ silicon atoms, the T^n/Q^n ratio, can give a good estimate of the percentage of reacted silanols and thus give the loading with silane molecules. For example, for the SBA-15-MPS and SBA-15-AEPMS samples the T^n/Q^n ratio is 0.27 and 0.52, respectively. In comparison, the calculated ratios of silicon atoms in the silane layers and in the silica walls taking into account TGA results (for details see Chapter 8.3.1) are 0.12 and 0.13, respectively. That is less than calculated from the ^{29}Si NMR data. It should be noted that the relative peak

intensities in the ^{29}Si NMR spectra are not strictly quantifiable due to possible differences in the relaxation behavior.

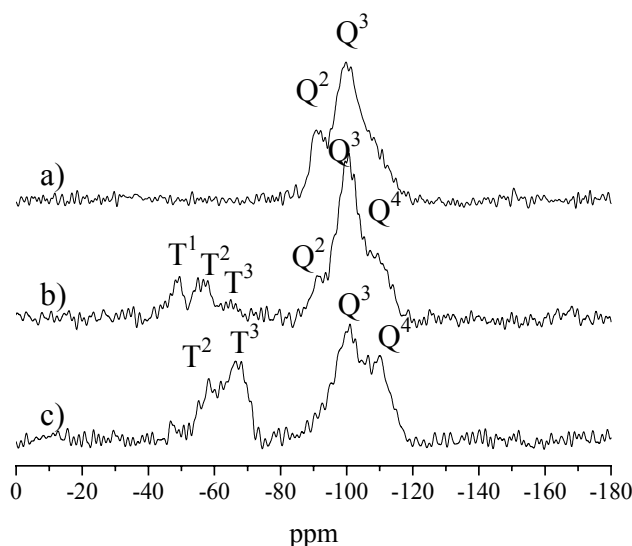


Figure 9.7. ^{29}Si NMR spectra of a) calcined SBA-15, b) SBA-15-MPS, and c) SBA-15-AEPMS samples.

9.3.2. Preparation of gold nanoparticles

The synthesis of the gold colloids was followed with DLS and TEM measurements. The Au1 colloid was prepared in a reverse micellar solution formed by extraction of the $\text{H}[\text{AuCl}_4]$ into an organic phase with tetraoctylammonium bromide followed by reduction with NaBH_4 . This is already a well established technique for the preparation of 4 - 5 nm gold nanoparticles²⁰. The growth of the crystalline gold nanoparticles is controlled by the reverse tetraoctylammonium bromide micelles and the growth of large gold crystals is prevented by the repulsive forces between the alkyl chains of the surfactant. The particle-size distribution in the Au1 colloid is shown in Figure 9.8. The distribution shows an approximately Gaussian shape for particles with monomodal size distribution. The mean particle radius is estimated to be about 2.6 nm. Additionally, TEM measurements were performed to investigate the particle sizes and crystallinity of the Au1 particles. Figure 9.9 shows TEM images of the Au1 colloid taken at two different magnifications. It is seen that the Au particles are almost monodispersed with mean diameter of about 4.5 - 5 nm that is in

a good agreement with the DLS data. HRTEM shows fringes typical for crystalline gold nanoparticles (Figure 9.8.b). The results obtained for the Au₁ colloid agree with those reported in the literature²⁰.

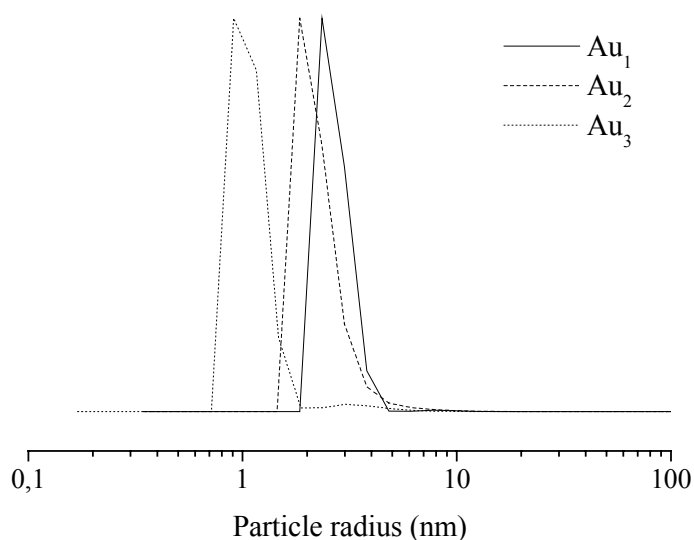


Figure 9.8. Particle size distribution in Au₁, Au₂, and Au₃ gold colloids determined from DLS data.

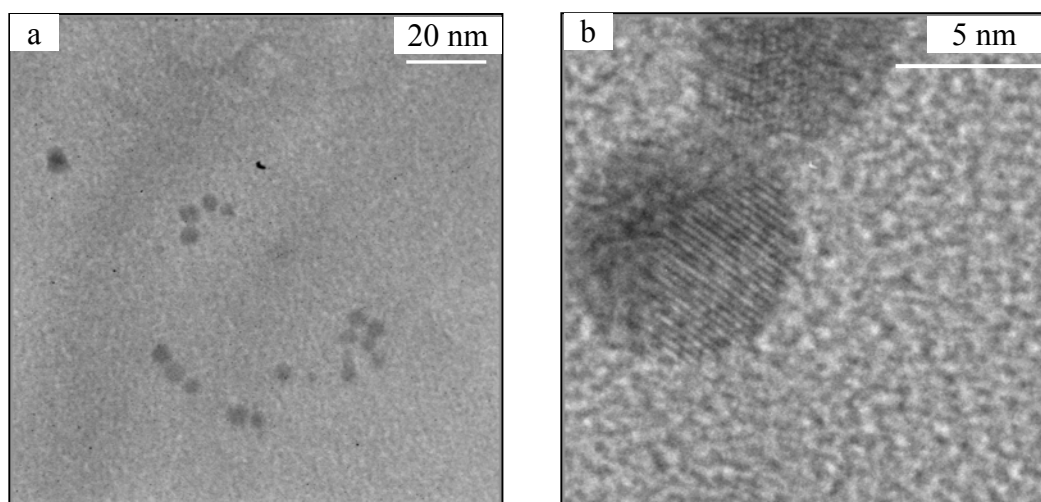


Figure 9.9. TEM images of Au₁ nanoparticles at two different magnifications a) and b).

The Au₂ gold solution was obtained by extraction of the H[AuCl]₄ into the organic phase by the tetraoctylammonium bromide. This resulted in a change of the color of the

solution from yellow to orange-brown that is probably due to the partial reduction of the $\text{H}[\text{AuCl}]_4$ to Au^0 in the organic phase. The organic phase was subjected to DLS measurements and the results show that particles with a radius of about 2 nm were formed showing monomodal size distribution (Figure 9.8.). It should be noted that the gold precursors prepared with these two synthesis methods are dispersed in organic solvent (toluene) and are used for further assembly.

The third preparation procedure used to obtain colloidal gold nanoparticles is based on the method that uses formaldehyde-substituted phosphine of the formula $\text{P}(\text{CH}_2\text{OH})_4\text{Cl}$ (THPC) as a reducing agent in basic media. Duff et al. first reported the synthesis and characterization of the tris(hydroxymethyl)phosphine-capped gold nanoparticles (THPC-Au)²¹. It was observed that the gold nanoparticles are negatively charged and can be absorbed easily to positively charged surfaces²⁷. Amino- and to a smaller extent thiol-functionalized silica particles were successfully modified with THPC-Au colloids²⁸. Furthermore, assembled THPC-Au were used as active catalysts for the metallization of DNA molecules¹⁹. The mechanism of the Au reduction with this method is still not clear but the known chemistry of the THPC²⁹ would suggest that the first step is the generation of an active reducing agent by the alkaline elimination of one formaldehyde molecule as shown:



Formaldehyde, which is liberated by the reaction of THPC, is a well-known reducing agent for gold ions. Figure 9.8 shows the DLS data for the Au3 sol. Particles with a mean radius of about 1.1 nm showing a monomodal size distribution were detected in the aqueous solution. The TEM image of the particles deposited on the carbon-covered copper grids are shown in Figure 9.10. The images show particles with diameters of about 1.5 – 2 nm in accord with the DLS results. The gold nanoparticles obtained here have the same dimensions as those reported in literature²¹.

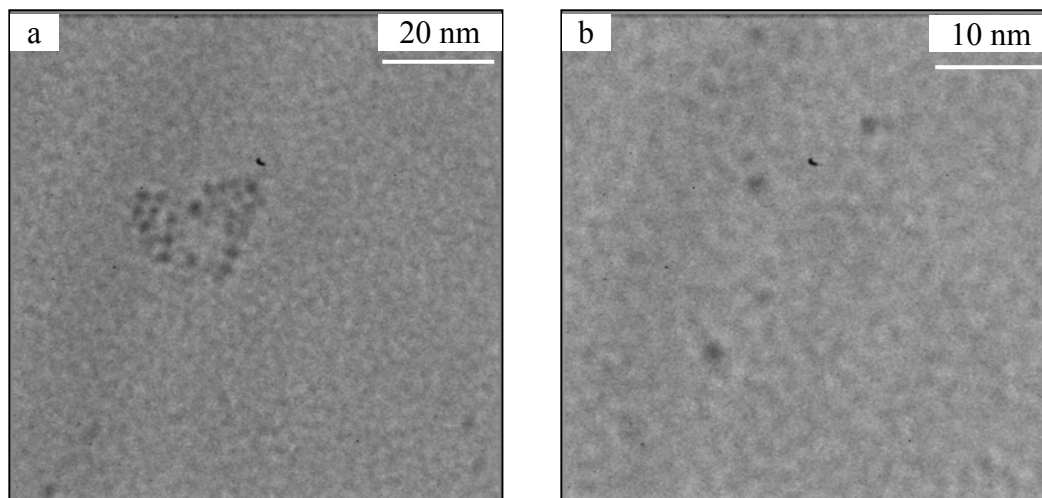


Figure 9.10. TEM images of Au₃ nanoparticles at two different magnifications a) and b).

9.3.3. Assembly of gold nanoparticles and electroless reduction of gold in SBA-15 rods

Figure 9.11 shows small-angle and wide-angle (inset in Figure 9.11) XRD patterns of the MPS-modified SBA-15 sample subjected to co-assembly with the Au1 colloid in toluene followed by electroless reduction of gold. The mesophase structure is preserved at every modification step as seen from the small-angle XRD patterns. The decrease in the intensity of the first order reflection is attributed to the decreased scattering contrast due to the pore filling effect. The wide-angle XRD patterns show that after the co-assembly of the small gold nanoparticles (~5 nm) very low intensity, broad diffraction peak at about 38.1° 2θ is recorded that can be assigned to (111) reflection of the crystalline gold. The particle size of the gold nanostructures assembled from Au1 colloidal gold suspension, calculated from the Scherrer equation, is 5.7 nm (see Table 9.3.). After electroless reduction the wide-angle XRD pattern shows distinct (111) and (200) reflections of crystalline gold that correspond to particles with more than 20 nm in diameter calculated using the Scherrer equation.

To further confirm the pore-filling effect due to the incorporation of gold nanostructures in the mesoporous host N₂-sorption measurements were undertaken. Figure 9.12 shows N₂-sorption isotherms for the SBA-15-MPS, SBA-15-MPS-Au1, SBA-15-MPS-Au1-red materials.

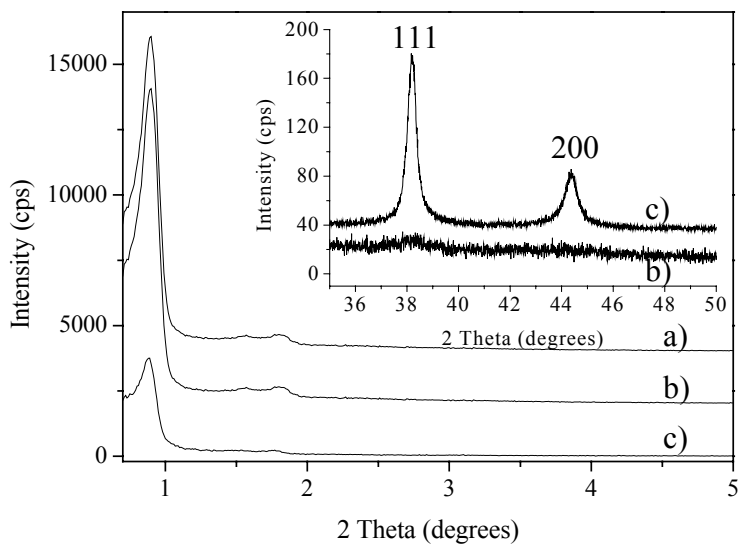


Figure 9.11. XRD patterns of a) SBA-15-MPS, b) SBA-15-MPS-Au1, and c) SBA-15-MPS-Au1-red materials (inset shows the wide-angle XRD patterns of SBA-15-MPS-Au1 and SBA-15-MPS-Au1-red samples).

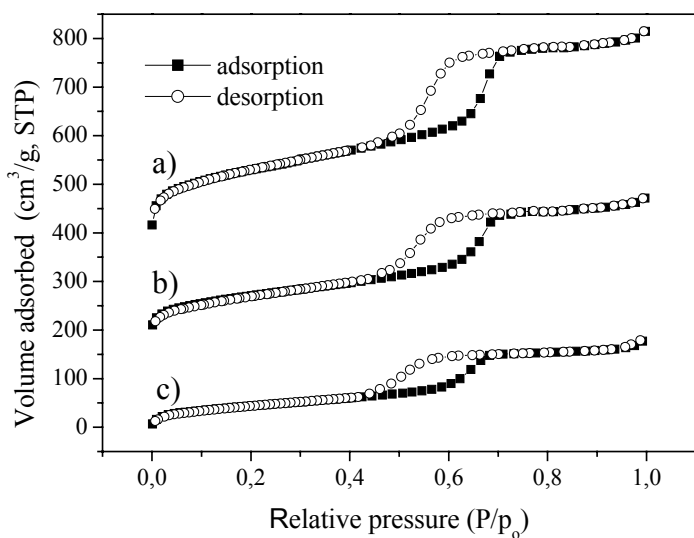


Figure 9.12. N₂-sorption isotherms of a) SBA-15-MPS, b) SBA-15-MPS-Au1, and c) SBA-15-MPS-Au1-red materials (the isotherms are offset with 200 cm³/g).

Generally, the shape of the isotherm is preserved after every modification step in agreement with the preserved mesostructural order of the samples. Hysteresis loops with similar shapes were obtained for all samples showing absence of pore clogging. Most importantly, the calculated surface area (S_{BET}), mean pore size diameter (D_{BJH}), and total pore volume (V_t) show a continuous decrease from the values obtained for the SBA-15-MPS sample to the sample subjected to electroless reduction (see Table 9.3). The decrease of the aforementioned parameters is very small in comparison to the increased dimensions of the gold nanostructures after electroless reduction calculated from the XRD experiment. Therefore, direct confirmation for the templating role of the SBA-15 host material for the preparation of the gold nanostructures can be obtained only by applying transmission electron microscopy.

Table 9.3. N₂-sorption data and Au particle size for the gold-modified SBA-15 samples.

Sample	S_{BET} (m ² g ⁻¹)	V_t (cm ³ g ⁻¹)	D_{BJH} (nm)	Size of Au (nm)*	Size of Au (nm)#
SBA-15-MPS-Au1	266	0.42	4.4	spheres: 3 – 7 nm	5.7
SBA-15-MPS-Au1-red	168	0.27	4.1	spheres: 20 – 70 nm	20.8
SBA-15-MPS-Au2	328	0.48	4.5	-	-
SBA-15-MPS-Au2-red	191	0.32	4.2	wires: 5 nm thick, several microns long	22.7
SBA-15-MPS-Au3	-	-	-	-	-
SBA-15-MPS-Au3-red	-	-	-	spheres 5 – 30 nm	14.5
SBA-15-AEPMS-Au	310	0.56	5.3	nanometer long wires; 5-30 nm spheres	14.1
SBA-15-AEPMS-Au-red	290	0.5	5.2	nanometer long wires; 5-30 nm spheres	14.5

The surface area is calculated from the BET model, the total volume adsorbed is calculated from single point measurement at $P/P_0 = 0.994$, and the pore size is determined by the BJH model applied to the desorption branch of the isotherm. * Au particle size is determined by TEM measurements, # Au particle size is determined from Scherrer equation (see Chapter 4).

Figure 9.13 shows the TEM images of the SBA-15-MPS-Au1 and SBA-15-MPS-Au1-red samples. After assembly of the Au1 colloid the mesophase structure is preserved (in agreement with the XRD results) and gold nanoparticles (shown with arrows in the image) are visible on the mesophase surface (may be only on the outer surface). Usually isolated gold nanoparticles with diameters corresponding to those observed in the initial

Au1 colloid were observed (see above). In some cases, gold aggregates were also seen (see Figure 9.13.b), which could be responsible for the increased particle size determined with the Scherrer equation. The number density of the gold nanoparticles in the mesoporous host is low.

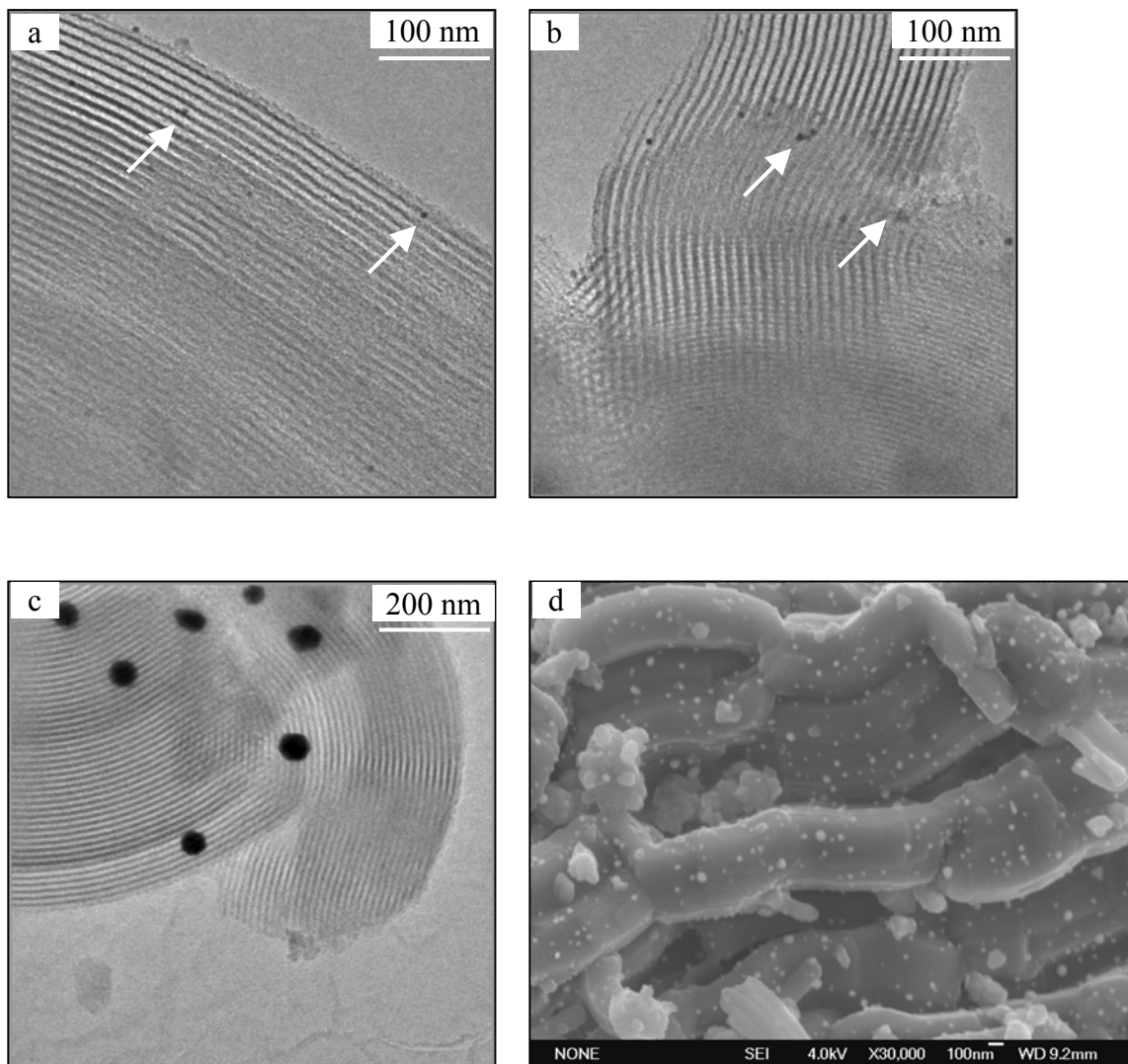


Figure 9.13. TEM images of a) and b) sample SBA-15-MPS-Au1, c) sample SBA-15-MPS-Au1-red, and d) FE-SEM of sample SBA-15-MPS-Au1-red.

After the electroless reduction of gold (Figure 9.13.c) the TEM images show the formation of bigger gold nanoparticles with diameters of more than 30 nm, in

correspondence with the XRD results. It appears that the growth of the gold nanoparticles is not templated by the mesophase structure. The particles are randomly distributed over the whole outer surface of the mesoporous material (Figure 9.13.d). The density of the gold nanoparticles seems to be similar to that before electroless reduction suggesting that the 5 nm gold nanoparticles served as nucleation centers for the further growth of bigger gold nanoparticles. The gold loading before and after electroless reduction was determined with EDX (Figure 9.14.). The gold loading in the SBA-15-MPS-Au1 was below the detection limit of EDX at the experimental conditions used in this study. The signals of the Si and S atoms appear with a S/Si atom ratio of 0.05. After electroless reduction the signal of the Au atoms was detected with a Au/Si atom ratio of 0.07. The estimated loadings of Au, based on the EDX results, before and after the electroless reduction is about 1.5 wt% and about 2.1 wt%, respectively.

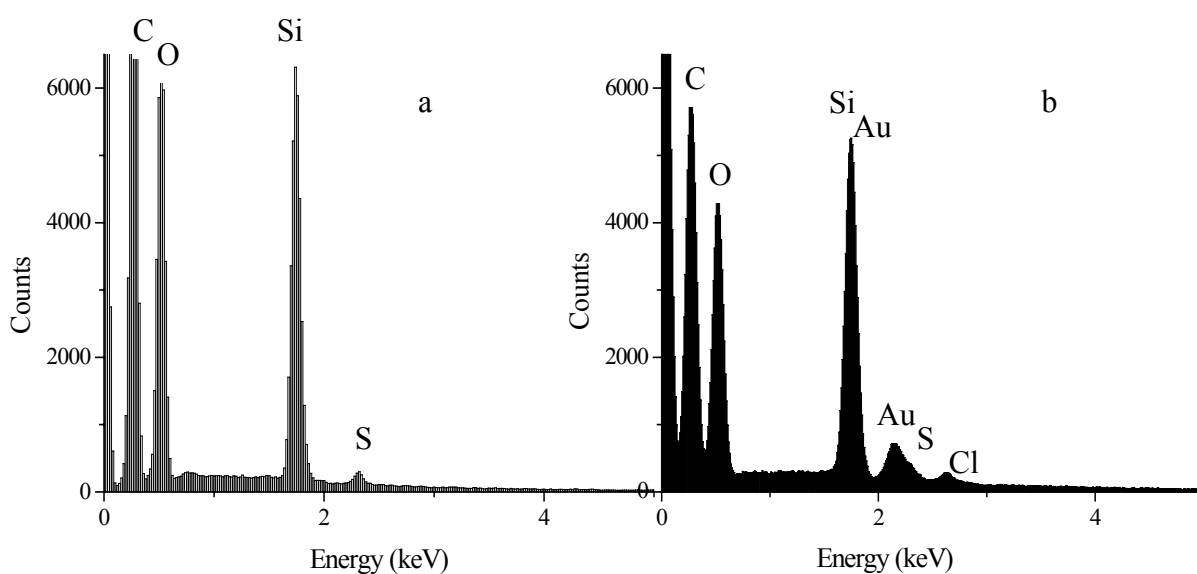


Figure 9.14. EDX analysis of a) SBA-15-MPS-Au1 and b) SBA-15-MPS-Au1-red samples.

The second synthetic approach to assemble gold nanostructures in the SBA-15-MPS material relies on the impregnation with the Au²⁺ solution in toluene followed by electroless reduction with the same gold plating bath. The small-angle XRD patterns, taken after these

modification steps, show that the mesophase structure is preserved (Figure 9.15.). The decreased intensity of the Bragg peaks is indicative of the pore filling effect due to the decreased scattering contrast between the walls and the pores of the SBA-15 material. In the wide-angle XRD patterns of the SBA-15-MPS-Au₂ sample no crystalline gold was detected suggesting that very small (less than 1 nm) gold species are present. After electroless reduction, the wide-angle XRD pattern shows the appearance of crystalline gold with an average particle size determined from the Scherrer equation of about 22 nm.

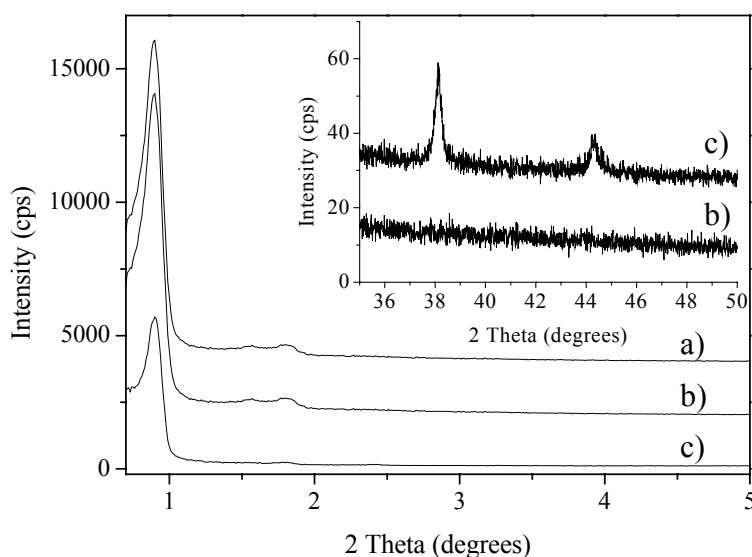


Figure 9.15. XRD patterns of a) SBA-15-MPS, b) SBA-15-MPS-Au₂, and c) SBA-15-MPS-Au₂-red materials (inset shows the wide-angle XRD patterns of SBA-15-MPS-Au₂ and SBA-15-MPS-Au₂-red samples).

Nitrogen sorption measurements were performed to further examine the pore filling effect after the assembly of the gold nanostructures. The shape of the sorption isotherms typical for the SBA-15 material is preserved after every modification step showing that the mesophase structure is retained (Figure 9.16.). The specific surface area (S_{BET}), total pore volume (V_t), and the pore size (D_{BJH}) decrease after assembly of the Au₂ structures and gold electroless reduction in agreement with the pore-filling effect (see Table 9.3.). The

degree of decrease of the aforementioned parameters is similar to that observed for the samples modified with Au1 colloid followed by electroless reduction. As discussed earlier, the XRD and N₂-sorption results alone do not give a definite conclusion about the templating role of the mesoporous support in the growth of the gold nanostructures. Furthermore, the particle size calculated from the XRD experiment and the similarity between the N₂-sorption data for the structures prepared with Au1 and Au2 solutions followed by electroless reduction suggest that similar results are to be expected from the latter synthetic approach.

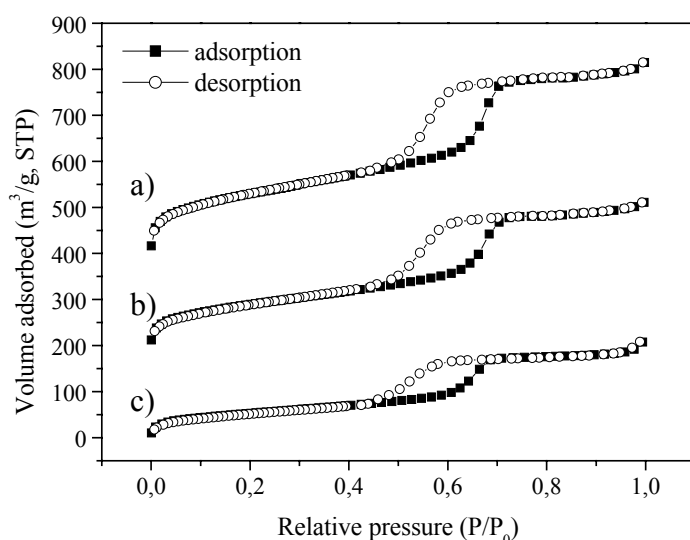


Figure 9.16. N₂-sorption isotherms of a) SBA-15-MPS, b) SBA-15-MPS-Au₂, and c) SBA-15-MPS-Au₂-red materials (the isotherms are offset with 200 cm³/g).

Surprisingly, the TEM results show completely different gold nanostructures (Figure 9.17.). The TEM results for the SBA-15-MPS-Au₂ show that no crystalline gold nanostructures can be observed at the used magnification (Figure 9.17.a) in agreement with the XRD results (inset Figure 9.15.b). Probably, a very thin gold layer of several tens of nanometer was formed on the internal mesophase surface (see N₂-sorption results). After electroless reduction continues, several micrometer long gold nanowires with a diameter of about 5 nm were observed. Very few other gold nanostructures, such as gold spheres or

agglomerates, were observed. These are not templated by the host matrix and might be the reason for the bigger average particle size determined from the Scherrer equation (see Table 9.3.). Figure 9.17.c clearly shows that the growth of the gold nanowires is templated by the channel structure of the SBA-15 material. The FE-SEM image shows that no gold nanoparticles can be observed on the outer surface of the mesoporous material (Figure 9.17.d). To the best of our knowledge these are the longest continuous gold nanowires prepared with mesoporous material as solid template.

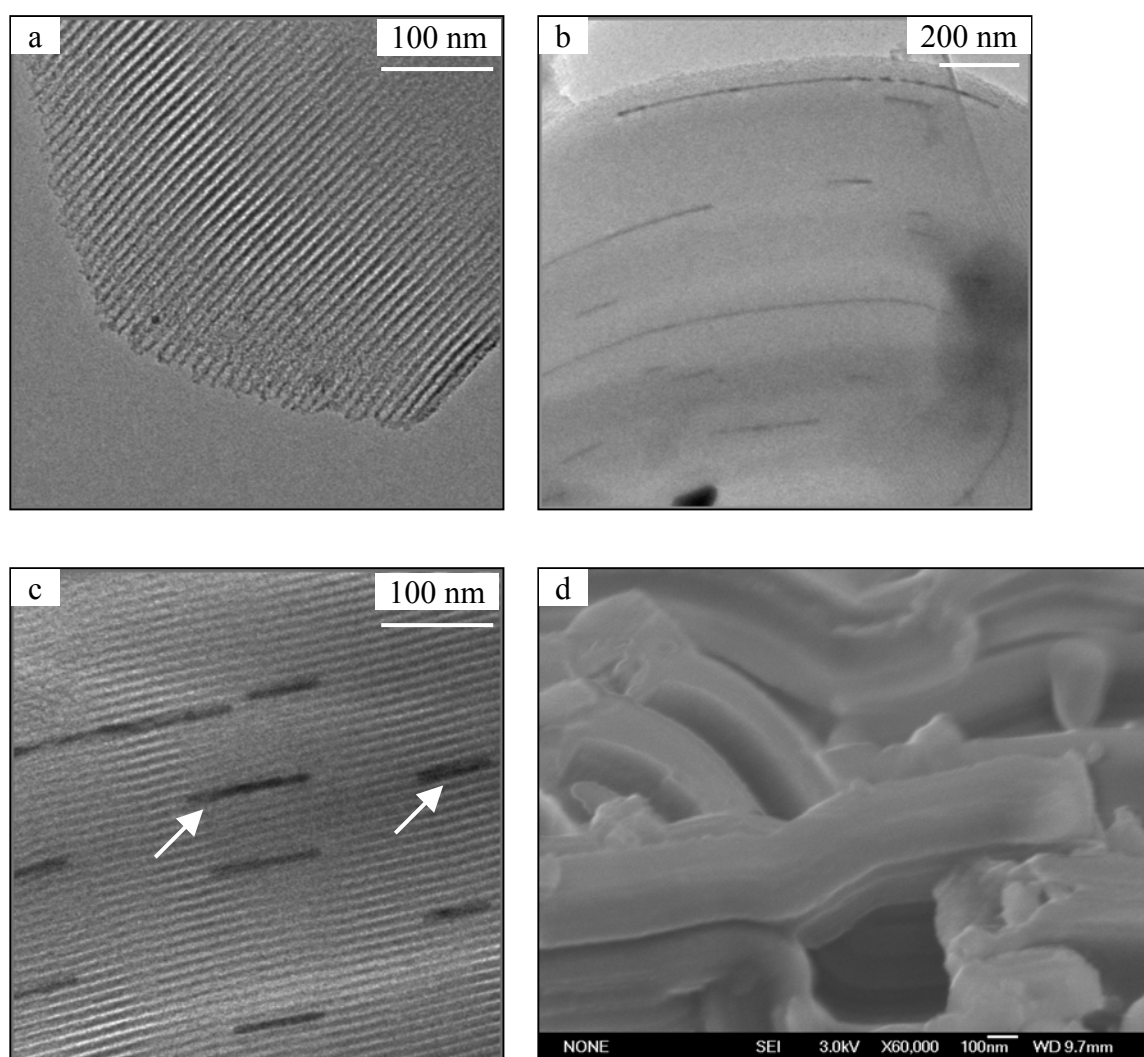


Figure 9.17. TEM images of a) sample SBA-15-MPS-Au2, b) and c) sample SBA-15-MPS-Au2-red at two different magnifications, and d) FE-SEM of sample SBA-15-MPS-Au2-red.

The loading with gold nanowires was estimated from the EDX analysis (Figure 9.18). Before electroless reduction no gold was detected (close to the detection limit of the EDX), whereas afterwards the Au/Si atom ratio was measured to be 0.05 corresponding to about 1.5 wt%. This is less than that observed for the SBA-15-MPS-Au1-red sample.

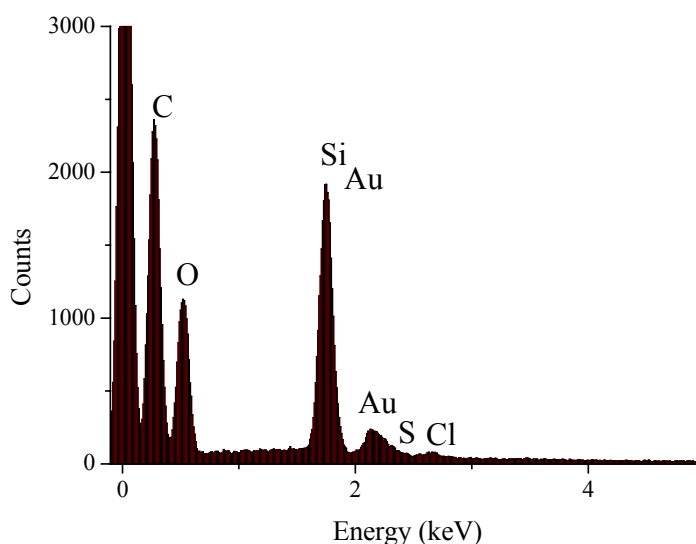


Figure 9.18. EDX analysis of SBA-15-MPS-Au2-red sample.

Comparing the results from the first synthetic approach (with Au1 as a precursor for the electroless reduction) and the second synthetic approach (with Au2 as a precursor for the electroless reduction) it is clear that the first step, namely the assembly of the gold precursors, is critical for the further growth of continuous gold nanowires. In the first case 3 – 5 nm gold nanoparticles were assembled preferentially on the outer surface of the MPS-modified mesoporous material and gave rise to the growth of 20 – 70 nm gold spheres where no templating role of the mesoporous support could be observed. It can be argued that the diffusion of these 3 – 5 nm gold precursors into the channel system of the SBA-15 material is hindered because of the almost equal pore size of the host matrix. Even if some of the Au1 nanoparticles gain access to the channel system of the SBA-15 material, the necessary diffusion of the AuCl_4^- precursors during the electroless reduction would be considerably restricted. Thus, the nucleation sites for the electroless reduction are preferentially formed on the outer surface of the mesoporous material and result in

unrestricted growth of bigger gold particles. In contrast, during the assembly of the Au²⁺ solution into the MPS-modified SBA-15 material a very thin layer of gold precursors is formed on the mesoporous surface that allows easy diffusion of the AuCl₄⁻ and the reducing agent into the channel system of the host material and results in the formation of continuous gold nanowires after the electroless reduction, templated by the mesoporous support.

The similarity of the XRD and N₂-sorption results for both synthetic approaches shows that often in inclusion chemistry such results must be interpreted with great care because alternative models or explanations might provide different conclusions. For example, the decreased intensity of the mesoporous Bragg peaks is in most cases explained by the decreased scattering contrast between the pores and the walls due to the pore filling effect, but another reasonable explanation could be the decreased structural order in the mesoporous material. It seems that TEM measurements are essential for such investigations although in many cases TEM is considered to be a local probe measurement.

In order to overcome the problems with the diffusion of the 3 – 5 nm gold nanoparticles into the mesoporous host, gold nanoparticles with smaller diameters, i.e. 1.5 – 3 nm were prepared (Au³⁺ solution). It is worth mentioning here that those gold nanoparticles are prepared in aqueous media and are negatively charged (see above).

The small-angle XRD results show that the mesophase structure is preserved after adsorption of the Au³⁺ colloid and after the subsequent electroless reduction (Figure 9.19.). The wide-angle XRD pattern of the SBA-15-MPS-Au³⁺ sample shows that no crystalline gold can be detected probably because of the very small gold particle size. Nevertheless, after electroless reduction gold nanostructures are formed as shown by the appearance of the (111) and (200) reflections of crystalline gold. The particle size calculated from the Scherrer equation is about 14 nm.

The TEM images of the SBA-15-MPS-Au³⁺ sample show that the mesophase surface is sparsely covered with 1 – 3 nm gold nanoparticles (Figure 9.20.a). This is in agreement with the literature results where poor or no coverage of the MPS-modified silica surface was observed in comparison to an amino-modified silica surface. In comparison to the coverage of the SBA-15-MPS material with Au¹⁺ nanoparticles, it is clear the Au³⁺ precursor gives considerably decreased mesoporous surface coverage. This can be explained by the

negative charge of the Au³ nanoparticles that are difficult to assemble to the negatively charged mesoporous silica surface (at the pH = 8 the silica surface is negatively charged) due to repulsive electrostatic forces. Nevertheless, after electroless reduction, 5 nm gold nanoparticles were formed in the channels of the mesoporous material (shown with arrows, Figure 9.20.b), accompanied by bigger 20 nm gold structures on the outer surface of the mesoporous material. The latter can explain the bigger particle size calculated from the XRD data (see Table 9.3.).

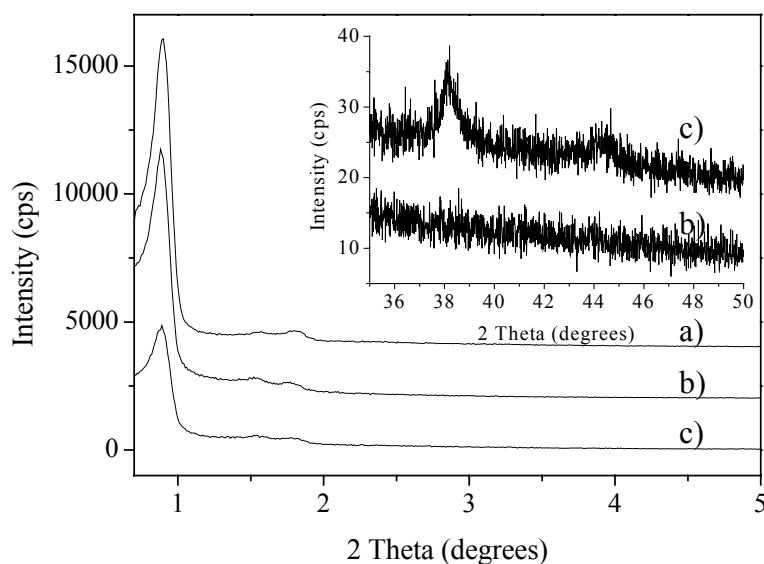


Figure 9.19. XRD patterns of a) SBA-15-MPS, b) SBA-15-MPS-Au₃, and c) SBA-15-MPS-Au₃-red materials (inset shows the wide-angle XRD patterns of SBA-15-MPS-Au₃ and SBA-15-MPS-Au₃-red samples).

No extended one-dimensional gold nanostructures were observed. The loading of the mesoporous surface with gold nanoparticles is smaller than that obtained with the previous two approaches (close to the detection limit in the EDX). The formation of gold nanoparticles that are sparsely distributed on the outer and inner mesoporous surface after electroless reduction is associated with the poor coverage of SBA-15 material with the 1 – 3 nm gold precursors. Apparently, a modification of the first gold assembly step is necessary

in order to obtain higher surface coverage with gold nanostructures. For example, assembly of the 1–3-nm Au³⁺ nanoparticles conducted at different pH into the amino-modified mesoporous material might be an interesting approach²⁸.

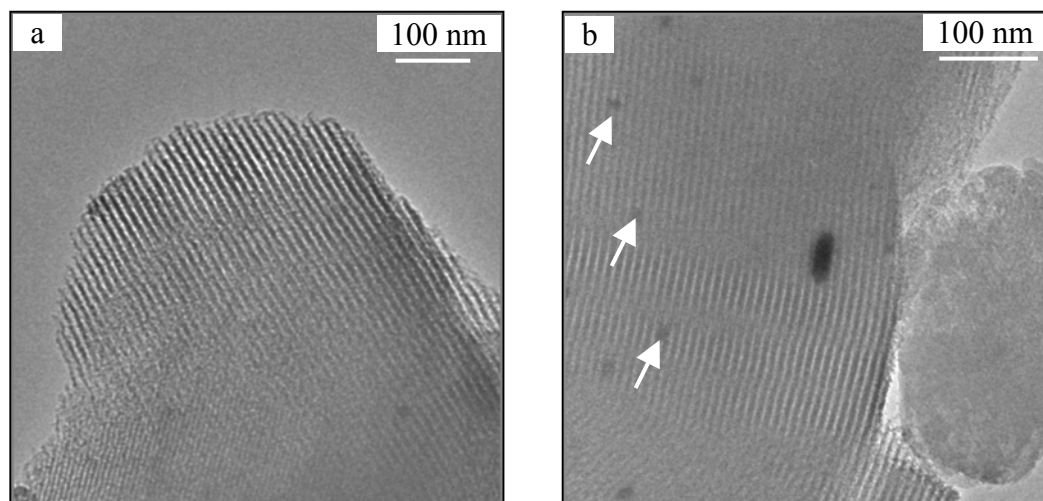


Figure 9.20. TEM images of a) SBA-15-MPS-Au³⁺ and b) SBA-15-MPS-Au³⁺-red samples.

The fourth approach to prepare Au nanostructures in SBA-15 material relies on the modification of the mesoporous surface with ethylenediamine groups followed by selective coordination of [AuCl₄]⁻ to the protonated amino groups in acidic media (see Scheme 9.1.B). Subsequently, Au electroless reduction was performed following the same conditions as in the first three cases. It has been reported that Pt and PtAu nanostructures can be prepared in MCM-41 and MCM-48 hosts by complexing [PtCl₆]²⁻ and [AuCl₄]⁻ to the mesoporous surface modified with ammonium groups^{9,10} and subsequent reduction in flowing hydrogen at elevated temperatures.

Figure 9.21 shows the small-angle XRD patterns of the SBA-15-AEPMS, SBA-15-AEPMS-Au, and SBA-15-AEPMS-Au-red samples together with the wide-angle XRD patterns (see inset). The mesophase structure is preserved at every modification step and the decrease in the intensity of the first order reflection is attributed to the decreased scattering contrast between the walls and the filled pores of the mesoporous material. The presence of gold nanostructures was verified from the wide-angle XRD patterns where (111) and (200) reflections were detected. The average particle size determined based on the Scherrer

equation is 14 and 15 nm for the SBA-15-AEPMS-Au and SBA-15-AEPMS-Au-red, respectively (see Table 9.3.). The XRD results show that small nanometer-sized Au particles have been formed on the mesophase surface without further reduction after the first complexing step. It is assumed that spontaneous in-situ reduction takes places on the amino-modified mesoporous surface. These Au nanoparticles were than directly used for additional electroless reduction. We note that no dramatic increase in the size of the Au nanoparticles was observed after electroless reduction based on X-ray line broadening (see inset in Figure 9.21.).

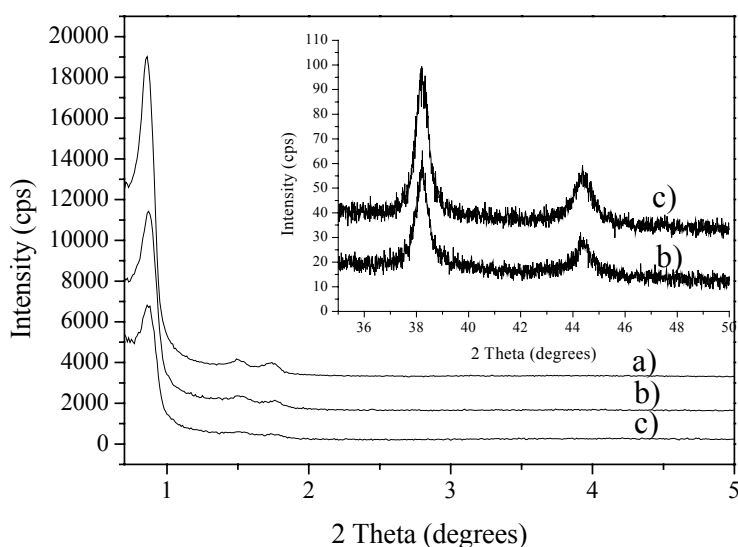


Figure 9.21. XRD patterns of a) SBA-15-AEPMS, b) SBA-15-AEPMS-Au, and c) SBA-15-AEPMS-Au-red materials (inset shows the wide-angle XRD patterns of SBA-15-AEPMS-Au and SBA-15-AEPMS-Au-red).

The nitrogen-sorption measurements (Figure 9.22.) with the corresponding data for the specific surface area (S_{BET}), pore size distribution (D_{BJH}), and total pore volume (V_t) (see Table 9.3.) show that the mesoporous character of the samples is preserved at every modification step, and that the above parameters decrease with every modification step in agreement with the pore filling effect. However, the decrease in the S_{BET} , D_{BJH} , and V_t for

the SBA-15-AEPMS-Au-red samples in comparison to the SBA-15-AEPMS-Au sample is smaller than that observed for the samples prepared with the first two approaches after the electroless reduction step. A possible explanation might be reduced access of the $\text{H}[\text{AuCl}_4]$ to the inner mesoporous surface during the electroless reduction due to the formation of bigger Au nanoparticles in the mesoporous channels during the initial coordination/reduction step.

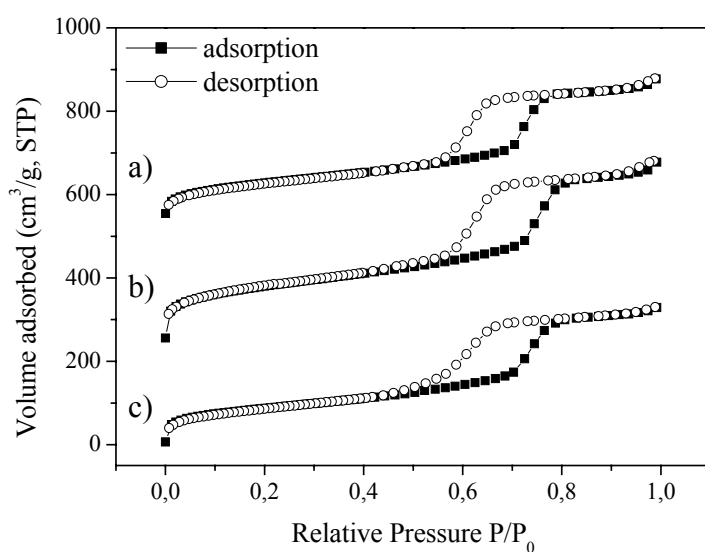


Figure 9.22. N_2 sorption isotherms of a) SBA-15-AEPMS, b) SBA-15-AEPMS-Au and c) SBA-15-AEPMS-Au-red materials (the isotherms are offset with $220 \text{ cm}^3/\text{g}$).

The TEM images of the SBA-15-AEPMS-Au and SBA-15-AEPMS-Au-red samples are shown in Figure 9.23. After complexation/autoreduction of $\text{H}[\text{AuCl}_4]$ on the AEPMS-modified mesoporous channel surface, nanometer long wires (ellipsoids) confined in the mesoporous channels are formed accompanied by small, about 5 nm in diameter, spheres (shown with arrows) and bigger, about 30 nm in diameter, particles on the outer surface of the mesoporous host. The observed loading with Au nanostructures is higher than that obtained for the MPS-modified samples treated with Au1, Au2, Au3 colloids (see above). This can be explained by the easy diffusion of $\text{H}[\text{AuCl}_4]$ in the mesoporous channels coupled with the higher complexing capacity of the ethylenediamino groups. After

electroless reduction a slight increase in the dimensions of the observed Au nanostructures was detected.

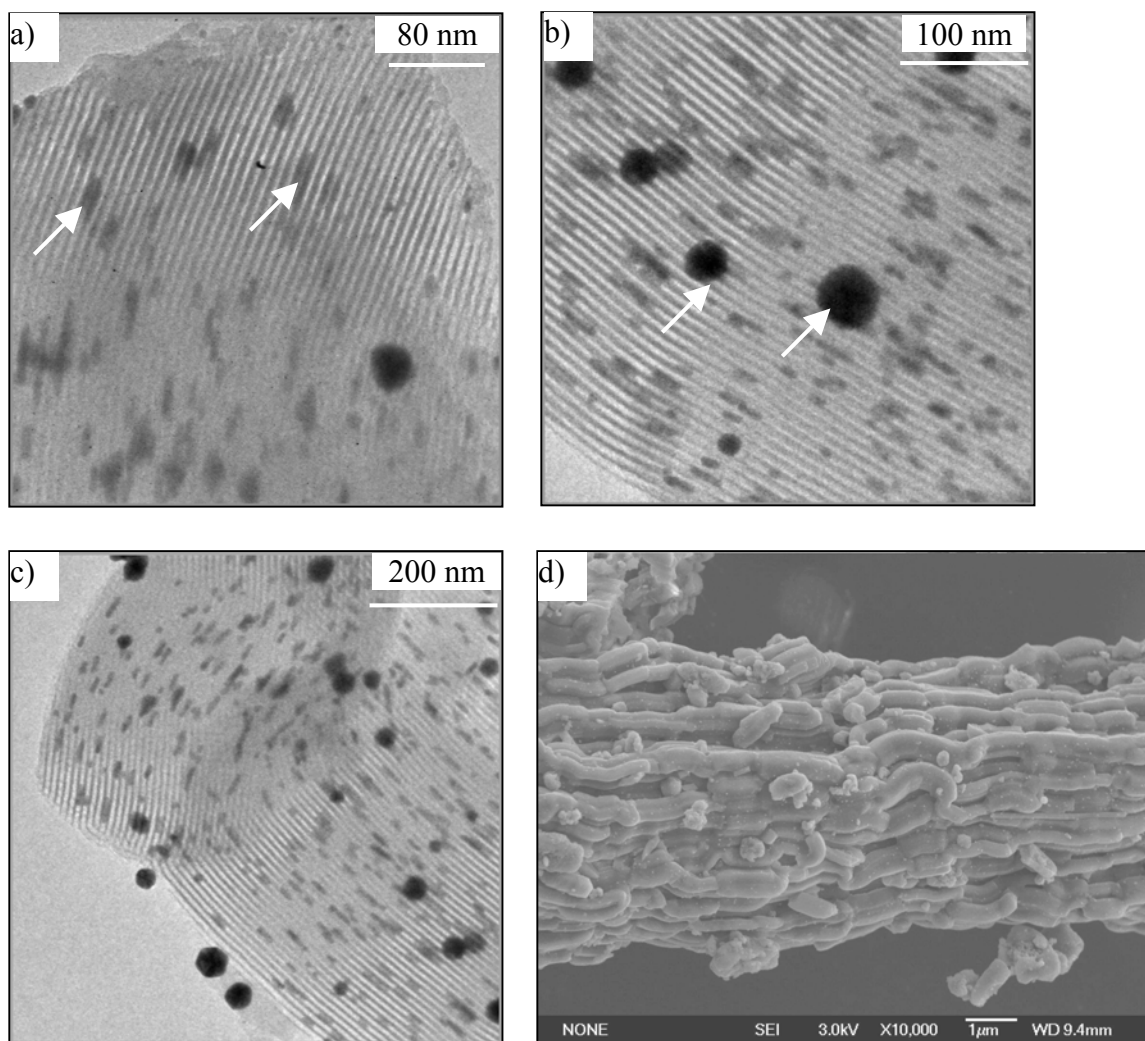


Figure 9.23. TEM images of a) sample SBA-15-AEPMS-Au, b) and c) sample SBA-15-AEPMS-Au-red at two different magnifications, and d) FE-SEM of sample SBA-15-AEPMS-Au-red.

The highest increase was registered for the non-confined bigger Au spheres (shown with arrows, Figure 9.23.b), whereas Au nanowires and small spheres were not affected

drastically. No Au nanowires longer than 80-100 nm were observed. This is in agreement with the XRD and sorption measurements and supports the claim that the diffusion of the reagents for the Au electroless reduction is hindered by the high loading of the mesoporous channels with Au nanostructures before the electroless reduction.

The loading of the mesoporous support with Au nanostructures was investigated with EDX. Figure 9.24 shows the EDX analysis of the SBA-15-AEPMS-Au before and after electroless reduction. The calculated Au/Si atom ratios are 0.07 and 0.08, which corresponds to about 2.1 and 2.4 wt%, respectively. The difference in the Au loading is negligible and supports the fact that the Au electroless reduction does not substantially increase the Au loading. It may be concluded that the fourth synthetic approach results in both, 80-100 nm long Au nanowires included in the SBA-15 support that are grown in-situ during the coordination/reduction of AuCl_4^- to the ammonium modified mesoporous surface, and larger Au spheres on the outer mesoporous surface. Further Au electroless reduction does not promote the formation of longer Au nanowires but leads to growth of the non-confined Au spheres on the mesoporous surface.

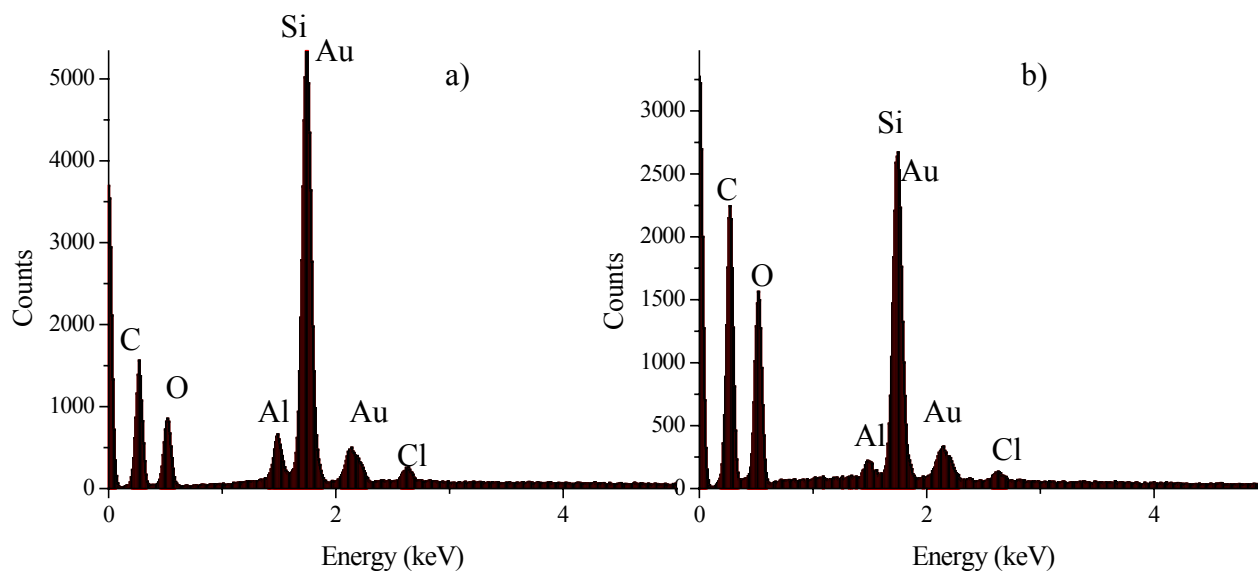


Figure 9.24. EDX analysis of a) SBA-15-AEPMS-Au and b) SBA-15-AEPMS-Au-red samples (Al signals are due to the glass supports).

9.3.4. Au nanostructures in MPS-modified mesoporous films

The second synthetic approach for the incorporation of Au nanostructures in mesoporous hosts, utilizing the Au²⁺ solution as precursor for electroless reduction, was also extended to thin mesoporous films. Two types of mesoporous films, showing the three-dimensional cubic (*Pm3n*) (templated by CTABr surfactant) and two-dimensional (*p6m*) mesophase structure (templated by tri-block copolymer Pluronic 123), were modified with MPS (see Table 9.2.), treated with Au²⁺, and subjected to electroless reduction. As shown in Figure 8.13, Chapter 8.3.3. in the first case a three-dimensional array of gold spheres with diameters of less than 2 nm would be expected. The increased pore accessibility offered by the three-dimensional cubic structure should offer fast transport of the reagents and facile inclusion chemistry. In contrast, Pluronic123-templated films with channels oriented parallel to the substrate surface are expected to template nanometer-sized gold wires (see Figure 8.13, Chapter 8.3.3.). The boundaries between the mesostructured domains forming the mosaic structure of the films should provide access for the incorporation of the Au nanostructures (see Chapter 6.3.1.1.).

The reflection-absorption FTIR spectra of the NPF1calc and NPF1calc-MPS samples are shown in Figure 9.25. The assignment of the peaks is given in Chapter 6.3.1.1.

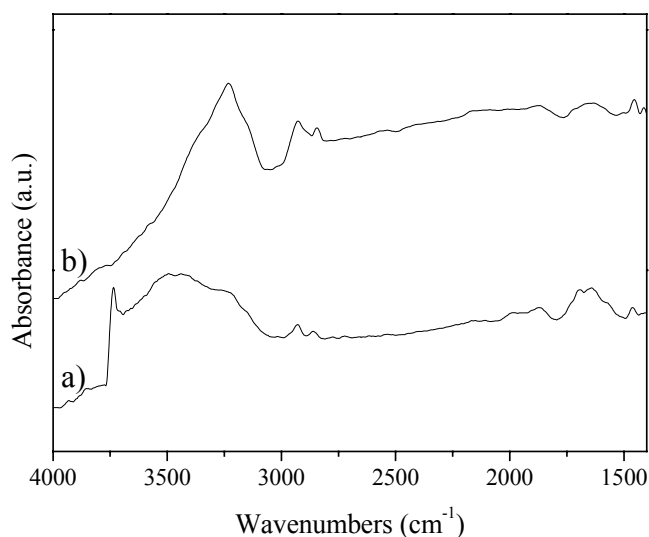


Figure 9.25. Reflection-absorption FTIR spectra of a) NPF1-calc and b) NPF1-MPS films.

Briefly, the peak at about 3750 cm^{-1} in the spectrum of the calcined sample is due to isolated Si-OH groups that are accessible for further functionalization. As discussed before the degree of surface coverage of those groups determines the density and nature of the molecular layers formed in subsequent molecular modification from reaction with organosilane molecules. After reaction of the mesoporous film with the MPS molecules the band at 3750 cm^{-1} disappears due to the condensation process between the free silanols and organosilane molecules. Additionally, in the $-\text{CH}_2$ stretching region two bands appear that are indicative for the organic functionality grafted to the mesoporous film surface. These results are in a good agreement with data obtained for the MPS-functionalized SBA-15 material and confirmed the successful modification of the mesoporous film surface with MPS molecules.

The small-angle RXRD patterns of the NPF1calc-MPS, NPF1calc-MPS-Au2, NPF1calc-MPS-Au2-red1, NPF1calc-MPS-Au2-red2, are shown in Figure 9.26 together with the wide-angle RXRD patterns.

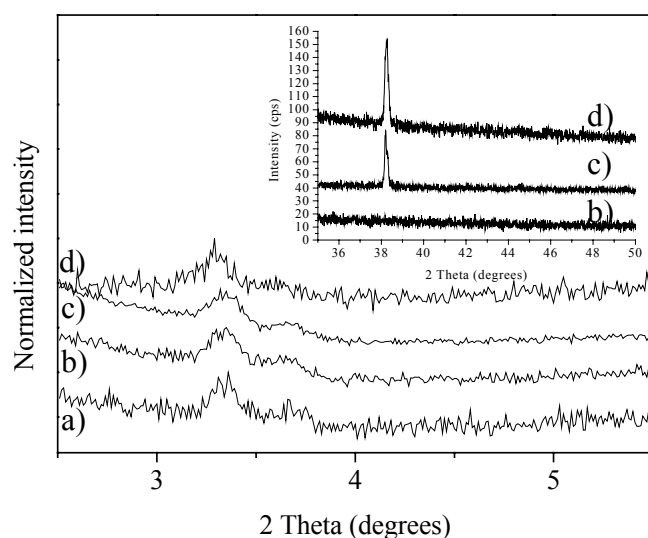


Figure 9.26. RXRD patterns of film samples a) NPF1-calc-MPS, b) NPF1-calc-MPS-Au2, c) NPF1-calc-MPS-Au2-red1, and d) NPF1-calc-MPS-Au2-red2 (inset wide-angle RXRD patterns).

The mesostructural order of the NPF1calc sample is preserved after subsequent modification with MPS, assembly of Au₂ colloid, and subsequent Au electroless reduction, shown by the presence of the two Bragg peaks indexed as (210) and (211) reflections typical for cubic (*Pm3n*) films (see Chapter 6.3.1.1.). In the wide-angle XRD pattern of the NPF1calc-MPS-Au₂ sample no crystalline gold was detected in agreement with the results obtained for the SBA-15-MPS-Au₂ material (see above). After electroless reduction with plating baths with two different concentrations the Bragg reflection typical for the (111) planes of crystalline gold appears. The peak width at half maximum was used to estimate the size of Au crystallites using the Scherrer equation and found to correspond to 59 and 60 nm, respectively. These values are much higher than that expected for nanocrystalline gold in mesoporous channels. A possible explanation could be that large micrometer-size particles of gold are formed on the film surface during the electroless reduction. The absence of the (200) reflection can be explained by the preferred orientation of the Au particles on the film surface with the (111) planes parallel the substrate surface.

To further characterize the nature of the gold structures prepared on NPF1calc-MPS films, TEM studies were performed on samples that were directly scratched from the substrate surface. Figures 9.27.a and b show the images taken at two different magnifications from the sample NPF1calc-MPS-Au₂-red1. The images indicate excellent cubic mesostructural order of the template matrix that serves as host to accommodate 1.5 – 2 nm gold particles (shown with arrows). The arrangement of the gold nanoparticles follows the cubic arrangement of the spherical pores of the NPF1 film. However, the high-magnification TEM image clearly shows that the loading of the film with gold nanostructures is quite low (Figure 9.27.b), suggesting that an effective transport of the reagents for the electroless reduction in the mesoporous film was not possible. To enhance the loading with gold nanoparticles, a successive reaction in the electroless bath with higher concentration of the reagents was conducted (see Experimental part). This resulted in the formation of a higher number of large micron-sized gold particles on the film surface such as those shown in Figure 9.30.a (see also XRD results), and also promoted a higher loading of nanometer gold particles in the pores of the mesoporous film (Figure 9.27.d). There are areas clearly visible with a cubic arrangement of gold nanoparticles, forming a three-

dimensional array of 2 nm gold nanocrystals encapsulated in an isolating silica matrix. However, the filling is far from being complete.

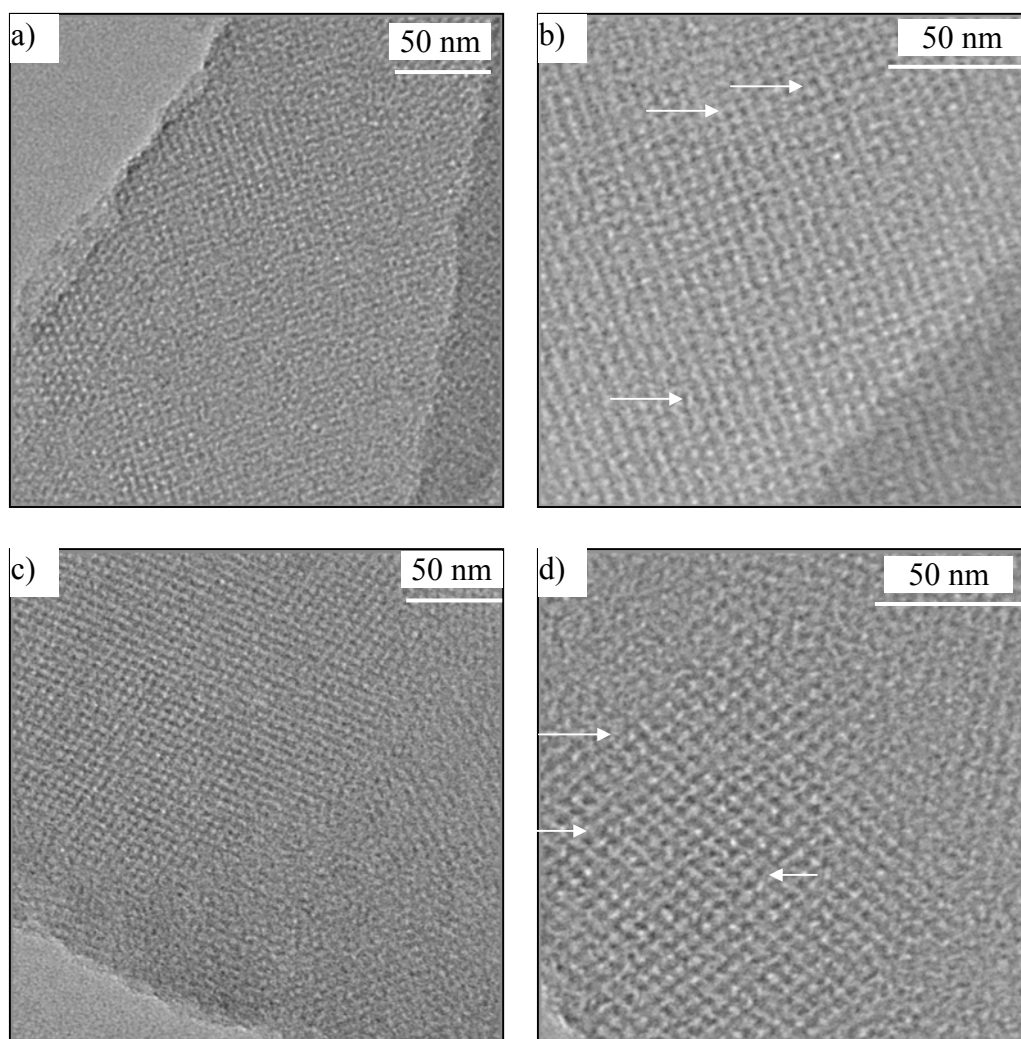


Figure 9.27. TEM images of scratched parts of sample NPF1calc-MPS-Au2-red1 at two different magnifications a) and b), and of sample NPF1calc-MPS-Au2-red2 at two different magnifications c) and d).

Hexagonally ordered mesoporous films prepared with Pluronic123 were subjected to the same sequence of modification processes as described above. The reflection-absorption FT-IR spectra of the calcined and MPS-modified samples are shown in Figure 9.28. The

assignment of the vibrational bands is similar to that shown for the NPF1calc and NPF1calc-MPS samples. Again the disappearance of the band at 3750 cm^{-1} can be used as an indirect indication for the covalent bonding of the organosilane molecules to the mesoporous surface in the course of the siloxane condensation. This result is further supported by the detection of the $-\text{CH}_2$ stretching vibrations at about 2935 and 2870 cm^{-1} and the $-\text{NH}_2$ bending vibrations at 1680 cm^{-1} .

The RXRD patterns taken in the small-angle region show the retention of the highly ordered hexagonal mesophase structure as confirmed by the presence of the intense first-order and the much less intense second-order diffraction peaks (Figure 9.29.). The formation of the gold structures was followed with RXRD in the wide-angle region and showed that no crystalline Au can be detected after neither the assembly process with Au2 solution nor after the first gold reduction step. After the second electroless reduction at higher concentrations of the plating bath, a highly intense Bragg reflection was recorded corresponding to gold particles with average dimensions of about 60 nm (Scherrer formula) that are grown on the film surface. These results can be explained by the restricted access of reagents into the two-dimensional mesoporous system due to its preferred orientation with the channels parallel to the substrate surface.

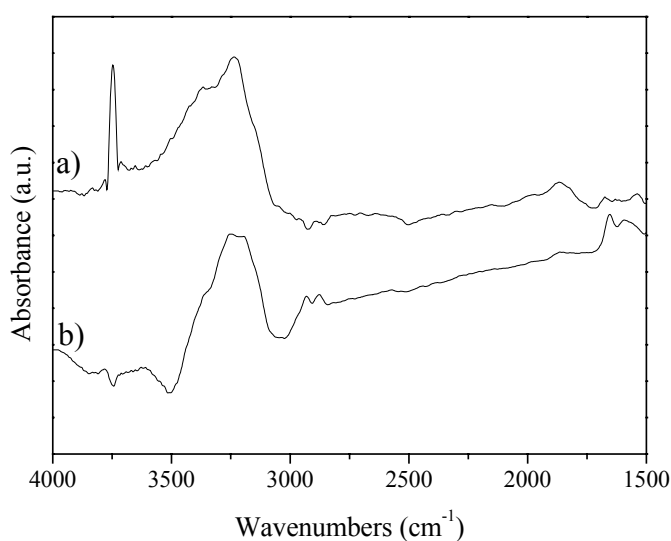


Figure 9.28. Reflection-absorption FTIR spectra of a) NPF3-calc and b) NPF3-MPS films.

Further TEM measurements provided detailed information of the gold structures on sample NPF3calc-MPS after electroless reduction. Figure 9.30.a shows the gold particles together with the mesoporous silica host (shown with arrow) imaged at low magnification. Gold particles greater than one micron are seen that are nucleated on the film surface (the same are seen on the NPF1calc-MPS-Au2-red1 film surface).

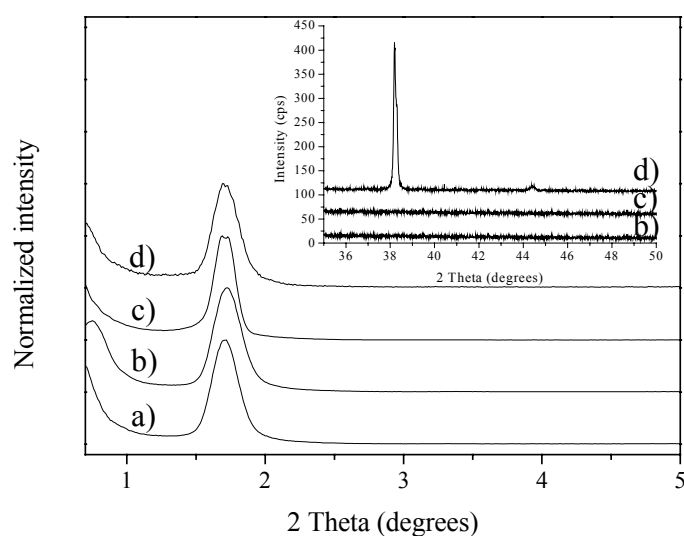


Figure 9.29. RXRD patterns of a) NPF3-calc-MPS, b) NPF3-calc-MPS-Au2, c) NPF3-calc-MPS-Au2-red1, and d) NPF3-calc-MPS-Au2-red2 (inset wide-angle RXRD patterns).

The images taken of the silica host films showed gold nanowire structures templated in the mesoporous channels (gold nanostructures are shown with arrows in Figures 9.30.b, c, and d). The gold nanowires are less than 100 nm long with about 5 nm in diameter corresponding to the dimensions of the mesoporous channels. It is clear that the loading is very low and the wires are usually distributed at the ends of the mesostructured domains. It is suggested that the growth of these wires is conducted through the transfer of reagents (nuclei for electroless reduction and the components of the plating bath themselves) through the domain boundaries into the porous system. Such a mechanism of Au growth is fairly restricted and will not allow for the formation of densely packed metal nanowires (at least at the conditions used in this study). Further improvement would be expected in the re-orientation of the porous system with hexagonally ordered channels having the long axis

perpendicular to the substrate surface or finding another deposition procedure that allows higher loading with the gold nanostructures without formation of bulky gold particles on the film surface.

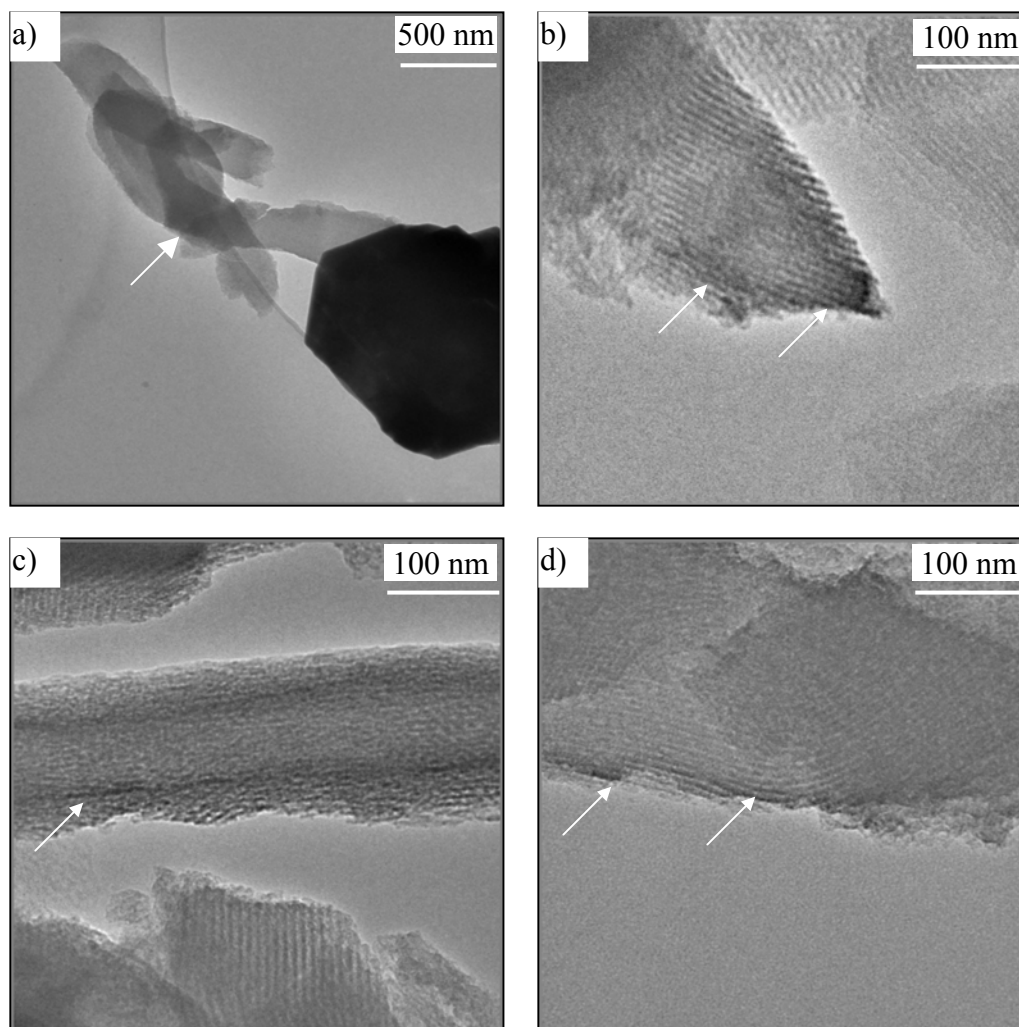


Figure 9.30. TEM images of scratched parts of sample NPF3calc-MPS-Au2-red2 at a) low and b), c), and d) high magnifications.

9.4. Conclusions and Perspectives

A novel synthetic method for the preparation of Au nanostructures in mesoporous hosts relying on the electroless reduction of gold was developed. Particularly, systematic investigation of the inclusion of Au nanostructures by electroless reduction in

functionalized SBA-15 material is presented. Four different approaches for the introduction of the seed species for the electroless reduction were investigated with emphasis on the different modification of the mesoporous surface with organic functionality (thiol- and ethylenediamino functional groups), different particle size of the Au precursors (ranging from 5-6 gold nanoparticles to ionic AuCl_4^- precursor) and Au particles with different surface charge. It has been shown that Au nanostructures stabilized in tetraoctylammonium bromide in toluene, assembled in MPS-modified mesoporous support are the best precursors for subsequent gold electroless reduction and resulted in formation of several micrometer long gold nanowires with diameter of about 5 nm. The experimental results clearly show that the growth of the gold nanowires is templated from the channel structure of the SBA-15 material. To the best of our knowledge these are the longest continuous gold nanowires prepared with mesoporous material as solid template. The coordination/reduction of aqueous AuCl_4^- on AEPMS-modified SBA-15 host resulted in in-situ formation of nanometer long Au nanowires accompanied by the larger Au particles on the mesoporous surface. Further electroless reduction does not increase substantially the dimensions of the Au nanostructures. A variety of characterization methods were applied to get information on the inclusion of Au nanostructures in SBA-15 mesoporous host. It is proven that TEM measurements are essential for such investigations; nevertheless, in many cases TEM is considered to be a local probe measurement.

Two types of thin mesoporous films, showing three-dimensional cubic ($Pm3n$) (templated by CTABr surfactant) and two-dimensional ($p6m$) mesophase structure (templated by tri-block copolymer Pluronic123), were modified with MPS, treated with Au nanostructures stabilized in tetraoctylammonium bromide in toluene and subjected to electroless reduction. Due to the templating effect of the host support three-dimensional array of less than 2 nm Au particles were obtained in the first case and several nanometer long Au nanowires with low density in the second case. To the best of our knowledge these are the first examples of Au nanostructures prepared in thin mesoporous films by an electroless reduction method.

Nevertheless, further characterization studies, such as GID or GI-SAXS measurements, of the Au structures imbedded in the thin mesoporous films can be

performed aiming to gain more knowledge of their microstructural order. On the other hand, methods for construction of hexagonally ordered mesoporous films that allow easy access to the channel system are desirable in order to obtain higher loading of the encapsulated material. Different approaches to achieve this are discussed in the Outlook. Conductive measurements performed with a STM of the those conductive structures in an isolating ceramics are also envisioned. This will open new avenues to real examples of nanoscale electronic devices.

References

- ¹ P. Schwerdtfeger, *Angew. Chem. Int. Ed.*, **2003**, 42, 1892.
- ² Z. L. Wang, *Adv. Mater.*, **2003**, 15, 1497
- ³ R. Kohn, M. Froba, *Catal. Today*, **2001**, 68, 227.
- ⁴ C. P. Mehnert, D. W. Weaver, J. Y. Ying, *J. Am. Chem. Soc.*, **1998**, 120, 12289
- ⁵ Y.-J. Han, J. M. Kim, G. D. Stucky, *Chem. Mater.*, **2000**, 12, 2068.
- ⁶ H. Kang, Y. W. Jun, J. I. Park, K.-B. Lee, J. Cheon, *Chem Mater.*, **2000**, 12, 3530.
- ⁷ K.-B. Lee, S.-M. Lee, J. Cheon, *Adv. Mater.*, **2001**, 13, 517.
- ⁸ J. V. Ryan, A. D. Berri, M. L. Anderson, J. W. Long, R. M. Stroud, V. M. Cepak, V. M. Browning, D. R. Rolison, C. I. Merzbacher, *Nature*, **2000**, 406, 169.
- ⁹ C. Yang, H. Shue, K. Chao, *Adv. Funct. Mater.*, **2002**, 12, 143.
- ¹⁰ C. Yang, P. Liu, Y. Ho, C. Chiu, K. Chao, *Chem. Mater.*, **2003**, 15, 275.
- ¹¹ Y. Guari, C. Thieuleux, A. Mehdi, C. Reye, R. J. P. Corriu, S. Gomez-Gallardo, K. Philippot, B. Chaudret, R. Dutartre, *Chem. Commun.*, **2001**, 1374.
- ¹² Y. Guari, C. Thieuleux, A. Mehdi, C. Reye, R. J. P. Corriu, S. Gomez-Gallardo, K. Philippot, B. Chaudret, *Chem. Mater.*, **2003**, 15, 2017.
- ¹³ H. Zhu, B. Lee, S. Dai, S. H. Overbury, *Langmuir*, **2003**, 19, 3974.
- ¹⁴ P. Mukherjee, M. Sastry, R. Kumar, *PhysChemCommun.*, **2000**, 4.
- ¹⁵ S. Besson, T. Gacoin, C. Ricolleau, J.-P. Boilot, *ChemCommun.*, **2003**, 360.
- ¹⁶ A. Fukuoka, H. Araki, Y. Sakamoto, N. Sugimoto, H. Tsukada, Y. Kumai, Y. Akimoto, M. Ichikawa, *NanoLetters*, **2002**, 2, 793.

- ¹⁷ M. S. Spector, R. R. Price, J. M. Schnur, *Adv. Mater.*, **1999**, 11, 337.
- ¹⁸ E. Braun, Y. Eichen, U. Sivan, G. Ben-Yoseph, *Nature*, **1998**, 391, 775.
- ¹⁹ O. Harnack, W. E. Ford, A. Yasuda, J. M. Wessels, *NanoLetters*, **2002**, 2, 919.
- ²⁰ M. Brust, D. Bethell, C. J. Kiely, D. J. Schiffrin, *Langmuir*, **1998**, 14, 5425.
- ²¹ D. G. Duff and A. Biaker, *Langmuir*, **1993**, 9, 2301.
- ²² H. Menzel, M. D. Mowery, M. Cai, C. E. Evans, *Adv. Mater.*, **1999**, 11, 131.
- ²³ X. Feng, G. E. Fryxell, L.-Q. Wang, A. Y. Kim, J. Liu, K. M. Kenner, *Science*, **1997**, 276, 923.
- ²⁴ H. Yoshitake, T. Yokoi, T. Tatsumi, *Chem. Mater.*, **2002**, 14, 4603.
- ²⁵ A. Cauvel, G. Renard, D. J. Brunel, *Org. Chem.*, **1997**, 62, 749.
- ²⁶ A. M. Liu, K. Hidajat, S. Kawi, D. Y. Zhao, *Chem. Commun.*, **2000**, 1145.
- ²⁷ W. Vogel, D. G. Duff, A. Baiker, *Langmuir*, **1995**, 11, 401.
- ²⁸ S. L. Westcott, S. J. Oldenburg, T. R. Lee, N. J. Halas, *Langmuir*, **1998**, 14, 5396.
- ²⁹ A. Hoffman, *J. Am. Chem. Soc.*, **1930**, 52, 2995.

Chapter 10. Preparation of semiconductor PbS nanostructures in functionalized mesoporous SBA-15 rods and mesoporous thin films.

10.1. Introduction

10.2. Experimental

10.2.1. Synthesis of PbS nanostructures in functionalized mesoporous materials

10.2.2. Characterization

10.3. Results and Discussion

10.3.1. PbS nanostructures in SBA-15 rods

10.3.2. PbS nanostructures in mesoporous films

10.4. Conclusions and Perspectives

10.1. Introduction

The miniaturization of devices for the semiconductor industry applying bottom-up approaches is a promising avenue to nanoscaled electronics (see Chapter 1). Different types of one-dimensional semiconductor nanostructures have been prepared by templating using existing nanoporous solids (see Chapter 3).

Two main synthetic strategies toward templated growth of semiconductors into mesoporous materials have been explored: metalorganic chemical vapor deposition (MOCVD) or wet chemical loading. For example, InP and GaAs direct-gap semiconductors were prepared in MCM-41 material from trimethylindium and phosphine, and trimethylgallium and tert-butylarsine, respectively, in continuous flow MOCVD reactors.^{1,2} In both cases a broad size-distribution of semiconductor particles grown on the internal and external surfaces of the MCM-41 material was obtained. Recently, several different wet chemical techniques were applied for the preparation of semiconductor heterostructures in mesoporous hosts. GaN was synthesized in a boron-doped MCM-41 mesoporous host by first impregnating the support with triazido(trimethylamine)gallium followed by heating in ammonia at 500°C.³ CdSe quantum dots were confined in an MCM-41 host by wet impregnation of dimethyl cadmium and Se dissolved in tributylphosphine under vacuum, followed by heating at 325°C in trioctylphosphine oxide to initiate growth of CdSe

nanoparticles.⁴ CdS semiconductor nanoparticles were incorporated into a thiol-modified MCM-41 matrix by immersion of the mesoporous support in a reactive solution that gave nanosized CdS particles.⁵ The wide-band semiconductor ZnO was prepared in ethylenediamine-functionalized MCM-41 by wet impregnation-complexing of Zn(II) to the ethylenediamine groups of the mesoporous support.⁶ Subsequent calcination led to ZnO nanoparticles encapsulated in the mesoporous host, the former showing a blue shift in their absorption spectra. Optical absorption spectra provide evidence for the nanoscale encapsulation of the semiconductor particles inside the mesoporous channels. However, in many cases bulk growth of semiconductor particles on the outer surface was observed. Aiming to overcome these problems selective functionalization of the mesoporous surface was applied.⁷ Furthermore, approaching nanoscale functional materials for device applications, CdS quantum dots were prepared for the first time in the three-dimensional hexagonal channel structure of mesoporous silica films prepared by EISA.⁸ The incorporation of the CdS nanoparticles was achieved by repeated wet impregnation with Cd salt, followed by reaction with gaseous H₂S. TEM images and UV-Vis absorption measurements demonstrate that the size confinement and the three-dimensional arrangement of the ordered porous structure (prepared as a 300 nm film) both control the growth of a CdS superlattice.

As one of the IV-VI semiconductors, PbS in its bulk form has a near-infrared band gap of 0.41 eV. Its band gap can be widened to the visible region by forming nanoclusters. Consequently, PbS nanocrystals and nanowires are potentially useful in electroluminescent devices, such as light-emitting diodes. In the limit of strong confinement, the third-order non-linear optical response of PbS nanocrystals is expected to be huge, thus making PbS highly desirable for photonic and optical switching devices. The templating approach for the growth of PbS nanostructures was applied by using polymers^{9,10}, glasses¹¹, block copolymer nanoreactors¹², and in Langmuir-Blodgett matrices¹³. PbS-nanowires with a uniform diameter of 6 nm were prepared in a thiol-functionalized SBA-15 host. A structural transition from nanocrystals to nanowires was achieved by increasing the loading of the inorganic compound in the host through -SH functionalization of the walls of the

mesoporous material. TEM images show that PbS nanowires are incorporated preferentially inside the channel system of the SBA-15 mesoporous host⁷.

These and other examples show that in most cases nanoscale semiconductor particles were prepared in powder mesoporous materials showing interesting optical properties. Size-quantization in three-dimensional space controlled by a mesoporous host system may lead to different optoelectronic effects, such as shifting of the semiconductor band gap, enhanced nonlinear optical properties, etc. The preparation of these nanoscale composite structures in the form of thin films on appropriate substrates is expected to offer added functionality. Nevertheless, a number of shortcomings, such as the lack of continuity of the nanoscale semiconductor structures and the restricted loading of the mesoporous host, are still to be overcome.

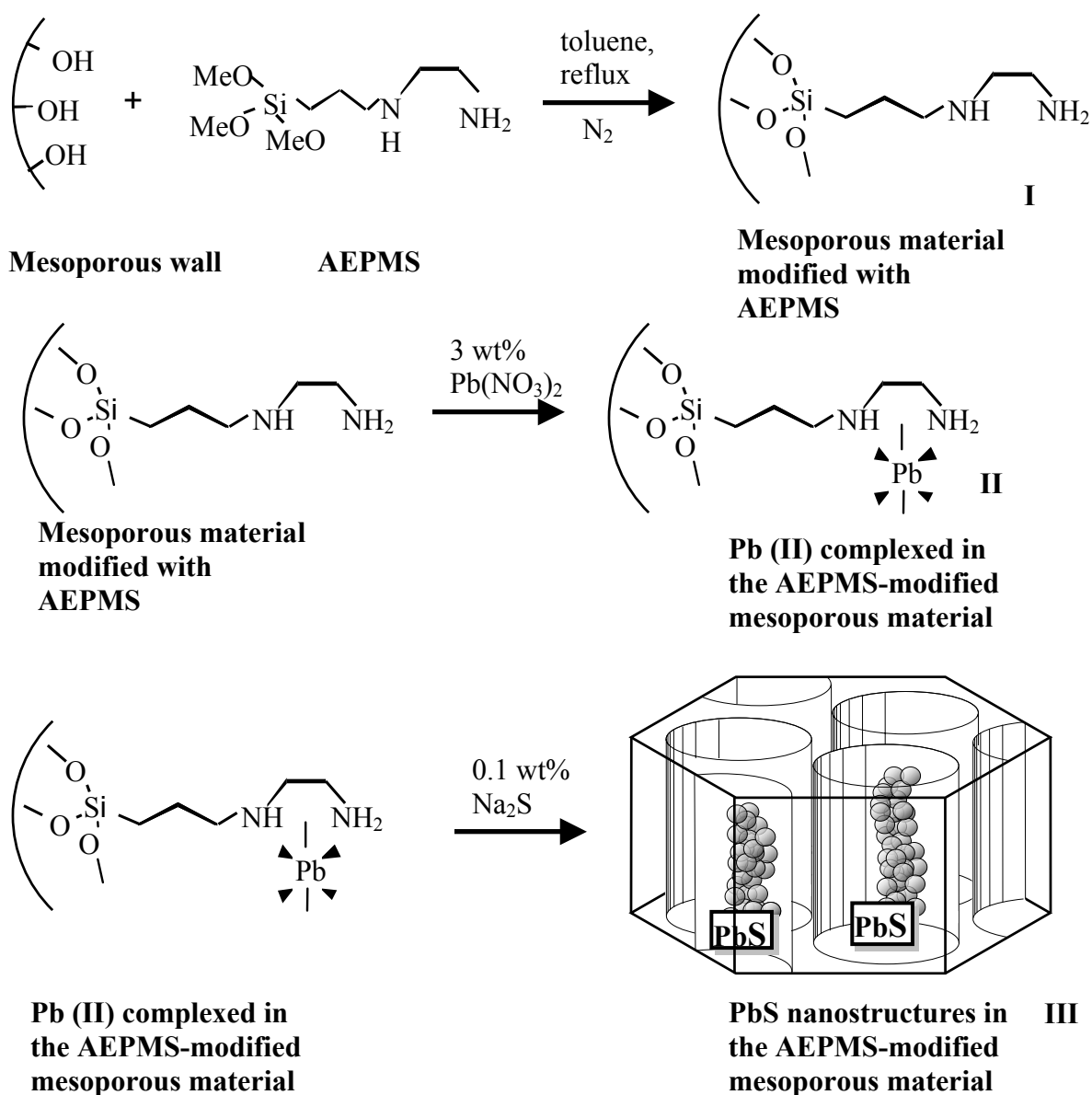
The aim of this Chapter is to show a new synthetic approach for the preparation of continuous PbS semiconductor nanostructures confined in a mesoporous matrix by applying surface modification of the mesoporous support and chemical wet impregnation technique. In contrast to the approach presented by Gao et al., here we use the good complexing properties of ethylenediamino functionalities towards Pb(II) cations that are further reacted with excess of S^{2-} to obtain the PbS material (see Scheme 10.1.). This approach is extended to the synthesis of thin film architectures consisting of hybrid semiconductor/mesoporous silica structures.

10.2. Experimental

10.2.1. Synthesis of PbS nanostructures in functionalized mesoporous materials

SBA-15 rods were synthesized as explained in Chapter 5.3.2. CTABr- and Pluronic 123-templated mesoporous films were prepared following the conditions of the EISA method (Chapter 6.2.1.). Template removal was achieved by first treating the sample at 120°C for 6 h in air followed by calcination in flowing air at 500°C for 4 h (ramping 0.75 deg/min), with the calcination procedure B (Chapter 5.3.2.)

Chapter 10. Preparation of semiconductor PbS nanostructures in functionalized mesoporous SBA-15 rods and mesoporous thin films



Scheme 10.1. Graphical representation of the reaction steps used to prepare PbS nanostructures in mesoporous materials.

Calcined SBA-15 rods were modified with 3-(2-aminoethylamino)propyltrimethoxysilane (AEPMS - Fluka) as described in Chapter 9.2. (Scheme 10.1., step I). The identification of the samples is given in Table 10.1. After

Chapter 10. Preparation of semiconductor PbS nanostructures in functionalized mesoporous SBA-15 rods and mesoporous thin films

silylation, 50 mg of the AEPMS-modified SBA-15 was impregnated with 10 mL (0.9 mmol) of an aqueous 3 wt% solution of $\text{Pb}(\text{NO}_3)_2$ for 12 h in order to form a complex of the Pb(II) with the ethylenediamine groups grafted to the mesoporous silica surface (see Scheme 10.1., step II). After washing with excess amounts of water and drying at 60°C for at least 24 h, the Pb-loaded mesoporous material was reacted with 10 mL of 0.5 wt% (0.6 mmol) Na_2S for 10 min (see Scheme 10.1., step III). Finally, the product was washed with excess amounts of water and dried at 60°C over night.

Table 10.1. SBA-15 samples with codes used in the study.

Sample names	Manipulation
SBA-15	thermally treated and calcined
SBA-15-AEPMS	modified with AEPMS
SBA-15-AEPMS-PbS	growth of PbS

Similarly, two types of mesoporous films (see Table 10.2.) were modified with AEPMS, treated with $\text{Pb}(\text{NO}_3)_2$, and subjected to the growth of PbS structures. The mesoporous films were dehydrated at 120°C in vacuum to remove water molecules absorbed on the surface, and then stirred in 10 mL dry toluene (Fluka) containing 700 μL (3 μmol) AEPMS under refluxing conditions applying standard Schlenk-line techniques. After 20 h the functionalized mesoporous films were washed with excess amounts of the solvent and dried at 60°C for at least 24 h. The films were impregnated with 5 mL (0.45 mmol) of an aqueous 3 wt% solution of $\text{Pb}(\text{NO}_3)_2$ for 24 h, followed by treatment with 5 mL (0.3 mmol) of 0.5 wt% Na_2S for 24 h. The identification of the samples is given in Table 10.2.

10.2.2. Characterization

The methods used for characterization of the PbS nanostructures prepared in powder SBA-15 material and different types of mesoporous films are already discussed in the previous chapters (see Chapter 4, 8 and 9).

Table 10.2. Modified mesoporous film samples with codes used in the study.

Manipulation	NPF1	NPF3
	CTABr-templated cubic	Pluronic 123-templated hexagonal
Thermally treated and calcined	NPF1-calc	NPF3-calc
AEPMS-modified	NPF1-AEPMS	NPF3-AEPMS
Growth of PbS	NPF1-AEPMS-PbS	NPF3-AEPMS-PbS

10.3. Results and Discussion

10.3.1. PbS nanostructures in SBA-15 material

The modification of the SBA-15 material with AEPMS was already discussed in Chapter 9.3.1. Here, only the results from modification steps II and III (Scheme 1) will be considered.

Figure 10.1. shows the small-angle and wide-angle XRD patterns (inset in Figure 10.1.) of the SBA-15-AEPMS and SBA-15-AEPMS-PbS samples. The mesophase structure is preserved after forming a complex with the Pb(II) and growth of PbS. The decreased intensity of the Bragg peaks in the small-angle region after growth of the PbS is assigned to the pore filling effect due to the decreased scattering contrast between the walls and the pores of the templating SBA-15 material. The wide-angle XRD shows several reflections that are typical for the crystalline cubic ($Fm\bar{3}n$) PbS material. The particle size of the grown PbS structures can be estimated using the Scherrer equation (see Chapter 4.4.). For example, fitting a Lorentzian function to the (220) reflection and calculating the full width at half maximum, it is estimated that the average size of the PbS structures is about 6 nm.

Figure 10.2. shows the TEM images of the SBA-15-AEPMS-PbS sample taken at different magnifications. It was observed that PbS nanowires, more than several micrometers long, were templated in the channel system of the SBA-15-AEPMS material.

Note that the PbS nanowires are following the curvature of the worm-like morphology of the SBA-15 material.

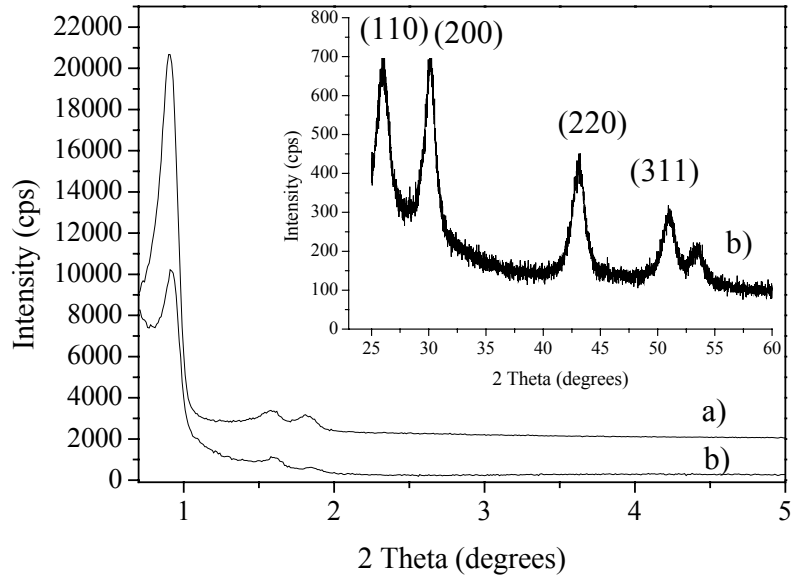


Figure 10.1. XRD patterns of a) SBA-15-AEPMS and b) SBA-15-AEPMS-PbS samples (inset shows the wide-angle XRD pattern of the SBA-15-AEPMS-PbS sample).

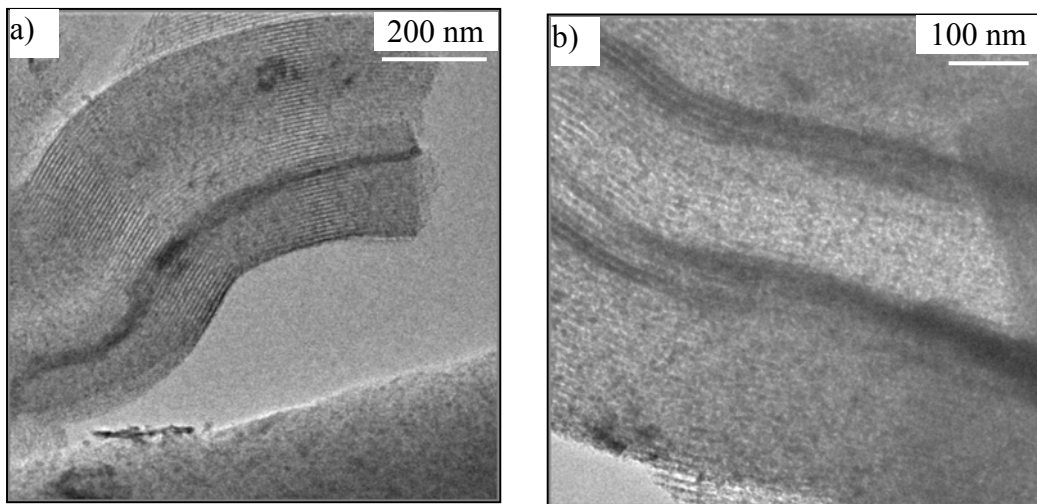


Figure 10.2. TEM images of the SBA-15-AEPMS-PbS material at two different magnifications a) and b).

The high-magnification image (Figure 10.2.b) provided direct proof of the templating role of the host structure; the diameter of the encapsulated wires is about 5 nm. It is seen that several nanowires are aligned parallel in the mesoporous channel. No big, micron-sized PbS particles were observed on the outer surface of the mesoporous material. This result is in an agreement with the particle size calculated from the XRD experiment. Nevertheless, the loading with PbS wires is still not complete. However, to the best of our knowledge these are the longest nanowires of semiconductor structures produced in mesoporous hosts. A few small particles of PbS encapsulated in the SBA-15 were also observed.

The loading with PbS was examined with EDX. The resulting signals are shown in Figure 10.3. The Pb/Si and S/Si atomic ratios are 1.1 and 0.9, respectively. The Pb/S atomic ratio is 1.2., close to the expected stoichiometry and imply that not all coordinated Pb^{+2} are consumed during the reaction with S^{-2} . The estimated loading of PbS in the SBA-15 mesoporous silica based on the EDX results is about 25 wt%. Repeated treatment with Na_2S would possibly increase the loading with PbS nanostructures in the SBA-material.

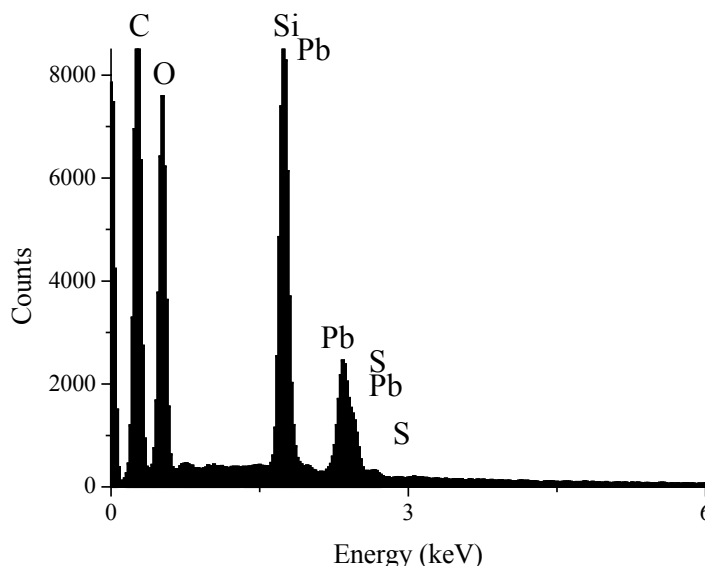


Figure 10.3. EDX analysis of the SBA-15-AEPMS-PbS material.

10.3.2. PbS nanostructures in mesoporous films

Two types of mesoporous films were investigated as host for the encapsulation of PbS nanostructures following the synthetic scheme applied to SBA-15 rods (see Table 10.2.). As already pointed out, in the first case an array of semiconductor particles forming a three-dimensional superlattice is to be expected whereas in the latter case one-dimensional nanostructures similar to those in the SBA-15 material are anticipated (see Figure 8.13., Chapter 8).

The modification with molecular functionality of the thin mesoporous films was followed by reflection-adsorption FT-IR spectroscopy. Figure 10.4. shows the spectra of the NPF1calc and NPF1-AEPMS samples. The peak assignment is similar to those already discussed in previous Chapters.

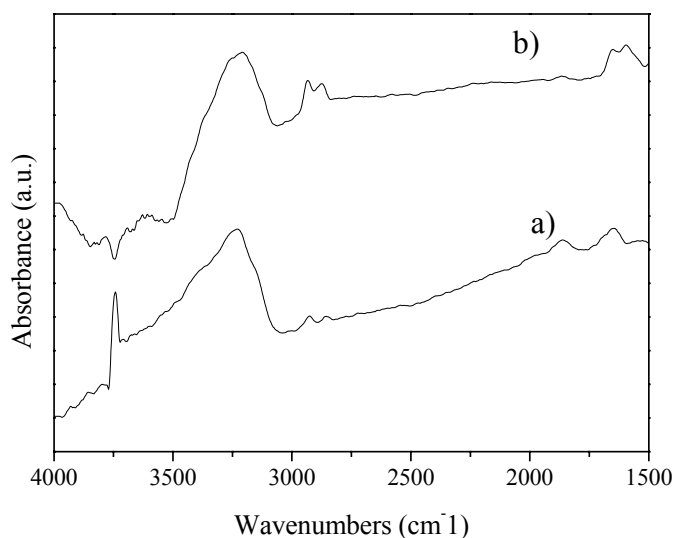


Figure 10.4. Reflection-absorption FT-IR spectra of a) NPF1-calc and b) NPF1-calc-AEPMS samples.

Briefly, the band at 3750 cm^{-1} in the spectrum of the calcined sample is due to isolated Si-OH groups that are accessible for further functionalization and is absent in the spectrum of the AEPMS modified sample. This result comes from the silylation process between the free surface silanols and organosilane molecules and is used as confirmation of

the successful grafting of the mesoporous silica surface with AEPMS molecules. Additionally, the bands typical for the CH₂ stretching vibrations (symmetric and asymmetric) and NH₂ banding are recorded at 2932, 2875, and 1590 cm⁻¹, respectively. Similar results were obtained for the NPF3-calc and NPF3-AEPMS samples (Figure 10.5.) proving the successful modification of the mesoporous film with AEPMS functionality. Unfortunately, the lack of characterization techniques, such as solid-state ¹³C and ²⁹Si NMR, Raman spectroscopy, or TG analysis, limit the full characterization of the film samples.

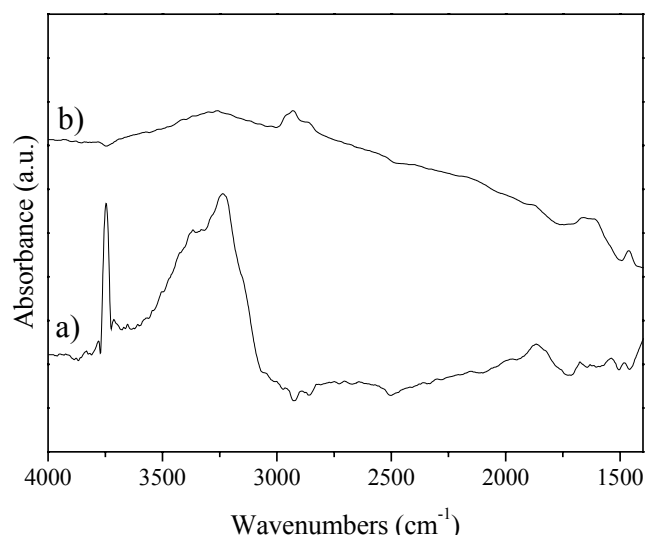


Figure 10.5. Reflection-absorption FT-IR spectra of a) NPF3-calc and b) NPF3-calc-AEPMS samples.

The growth of PbS nanostructures in NPF3-calc-AEPMS was followed with RXRD and TEM measurements. It was observed that the mesophase structure of the NPF1-calc-AEPMS sample is destroyed after treatment with Pb(NO₃)₂ and N₂S even for long contact times (more than 12 h). It is suggested that the lower stability of the cubic mesophase structure is due to the small domain sizes that are distorted at the low acidity.

The small- and wide-angle RXRD patterns of the NPF3-calc-AEPMS and NPF3-calc-AEPMS-PbS samples are shown in Figure 10.6. The two-dimensional hexagonal mesophase structure is preserved after the modification of the AEPMS, coordination of the Pb(II), and subsequent growth of the PbS nanostructures evidenced from the (100) reflection. It can be suggested that partial mesophase disordering was observed after the growth of the PbS nanocrystals indicated by the increased broadening of the (100) reflection. The wide-angle RXRD pattern of the NPF3-calc-AEPMS-PbS sample does not show any reflections of the PbS nanocrystals. It is suggested that the PbS nanoparticles are too small to be detected. The possible reflections are very broad and disappear in the signal noise. Apparently, the loading of the hexagonally ordered NPF3-calc-AEPMS film with PbS structures is very low in contrast to the SBA-15 material.

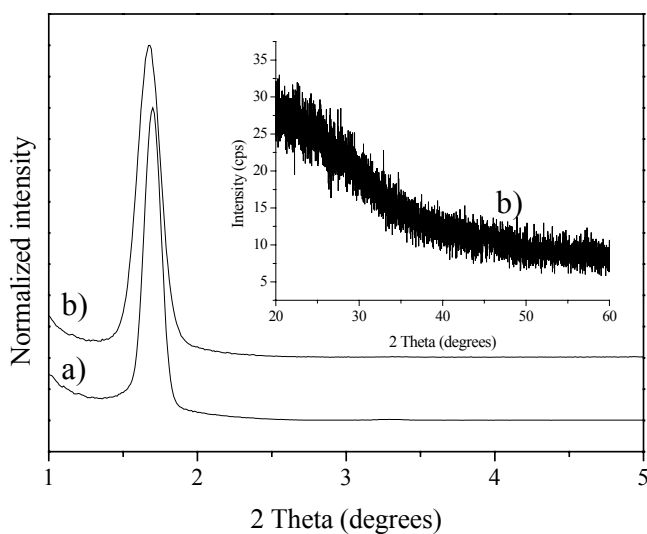


Figure 10.6. RXRD patterns of a) NPF3-calc-AEPMS and b) NPF3-calc-AEPMS-PbS samples (inset: wide-angle RXRD pattern of NPF3-calc-AEPMS-PbS sample).

Further insight on the PbS nanostructures in NPF3 films was obtained by TEM images of the scratched parts of the films (Figure 10.7). No dense arrays of nanowires were observed. It is clear that the loading with PbS nanostructures is very low; probably very small 1 – 2 nm clusters were formed on the mesoporous surface. These results correspond

to the RXRD data and suggest that, due to the poor diffusion of the reagents in the porous system with channels oriented parallel to the substrate surface, the growth of continuous PbS nanowires is considerably limited. Further increase in the reaction time or the concentration of the Na₂S in the last reaction step resulted in almost full mesostructural disordering due to high acidity of the solution.

No signals of Pb or S were detected in the EDX spectra, confirming that the amount of PbS is lower than the detection limit of the EDX.

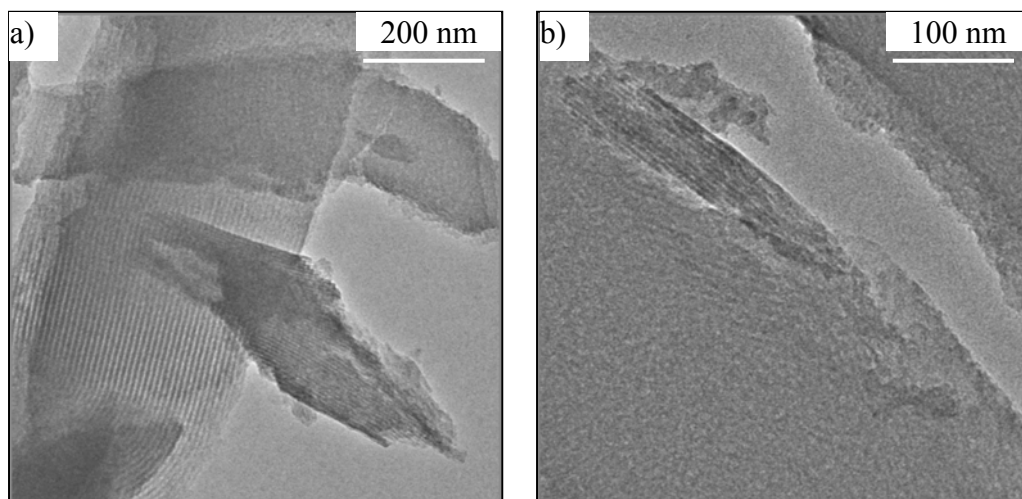


Figure 10.7. TEM images of the scratched parts of the NPF3-calc-AEPMS-PbS sample at two different magnifications a) and b).

These results can be related to the nitrogen sorption measurements where it has been shown that the adsorption of nitrogen is significantly lowered after silylation (Chapter 8). It is suggested that a very thin silane layer is formed that limits further diffusion of reagents. This is even more important for films that show orientation of the mesoporous channels parallel to the surface and where access to the channel system is only possible through the domain boundaries.

10.4. Conclusions and Perspectives

A novel synthetic method for preparation of one-dimensional nanostructures of PbS semiconductor in an isolating mesoporous silica matrix has been developed. Due to the selective modification of the mesoporous surface with ethylenediamino functionality, followed by coordination of Pb(II) and reaction with Na₂S, it was possible to obtain micrometer long nanowires in hexagonally ordered SBA-15 material. To the best of our knowledge these are the longest nanowires of semiconductor structures produced in the pore system of mesostructured hosts. Further characterization applying absorption spectroscopy or conductive measurements will facilitate the understanding of the physical properties of these and related semiconductor nanostructures encapsulated in the mesoporous silica matrix. CdS or ZnO nanowires are planned to be prepared in the SBA-15 following similar methods.

Approaching the creation of the nanostructured materials for device applications, PbS nanocrystals were also tried to be prepared in thin mesoporous films synthesized with the EISA method. Unfortunately, due to the lower stability of the cubic films (NPF1-calc-AEPMS sample) at high acidity and restricted diffusion of reagents in the hexagonally ordered films (NPF3-calc-AEPMS sample) no confined growth of PbS was observed. To overcome these problems it is envisioned to use different thiol sources at mild reaction conditions, but most importantly it is needed to allow easy access to the channel system of the hexagonally ordered mesoporous films to obtain higher loading of the encapsulated material. Different approaches to achieve this are discussed in the Outlook.

References

-
- ¹ J. R. Agger, M. W. Anderson, M. E. Pemble, O. Terasaki, Y. Nozue, *J. Phys. Chem. B*, **1998**, 102, 3345.
 - ² V. I. Srdanov, I. Alxneit, G. D. Stucky, C. M. Reaves, S. P. DenBaars, *J. Phys. Chem. B*, **1998**, 102, 3341.

- ³ H. Winkler, A. Birkner, V. Hagen, I. Wolf, R. Schmechel, H. von Seggern, R. A. Fischer, *Adv. Mater.*, **1999**, 11, 1444.
- ⁴ H. Parala, H. Winkler, M. Kolbe, A. Wohlfart, R. A. Fischer, R. Schmechel, H. von Seggern, *Adv. Mater.*, **2000**, 12, 1050.
- ⁵ T. Hirai, H. Okubo, I. Komasaawa, *J. Phys. Chem. B*, **1999**, 103, 4228.
- ⁶ W.-H. Zhang, Y.-L. Shi, L.-Z. Wang, D.-S., Yan, *Chem. Mater.*, **2000**, 12, 1408.
- ⁷ F. Gao, Q. Lu, X. Liu, Y. Yan, D. Zhao, *NanoLetters*, **2001**, 12, 743.
- ⁸ S. Besson, T. Gacoin, C. Ricolleau, C. Jacquiod, J.-P. Boilot, *NanoLetters*, **2002**, 2, 409.
- ⁹ S. Wang, S. Yang, *Langmuir*, **2000**, 16, 389.
- ¹⁰ L. Bakueva, S. Musikhin, M. A. Hines, T.-W. F. Chang, M. Tzolov, G. D. Scholes, E. H. Sargent, *Appl. Phys. Lett.*, **2003**, 82, 2895.
- ¹¹ R. S. Silva, F. Qu, A. M. Alcalde, N. O. Dantas, *Microelectronics Journal*, **2003**, 34, 647.
- ¹² R. S. Kane, R. E. Cohen, R. Silbey, *Chem. Mater.*, **1996**, 8, 1919.
- ¹³ A. G. Milekhin, L. L. Sveshnikova, S. M. Repinsky, A. K. Gutakovsky, M. Friedrich, D. R. T. Zahn, *Thin Solid Films*, **2002**, 422, 200.

Conclusions and Outlook

An assembly of nanosized wires, switches, or connections could be addressed by constructing an ordered channel matrix of insulating material of metal oxide in which these structures are encapsulated and therefore isolated. On the other hand, solid supports with ordered porosity can offer a template matrix for guided growth of a variety of conductive structures, giving patterned arrays of aligned nanowires and connections. Such solid supports with ordered porosity ranging from several Angstroms to several nanometers are silica-based micro- or mesoporous materials, also called molecular sieves. Sol-gel chemistry provides different approaches for preparation of such structures in a variety of special morphologies ranging from bulky materials to thin films and fibers.

The topic of this Thesis is the design of nanoporous solids prepared by liquid-crystal templating in form of thin films, rods, or spheres that are used for growth of carbon nanotubes, metal and semiconductor nanowires, and nanoparticle arrays.

In the course of this work, powder mesoporous materials such as three-dimensional cubic (*Ia3d*) MCM-48 spheres, two-dimensional hexagonally ordered (*p6m*) SBA-15 rods, and surfactant-templated mesostructured monoliths were prepared (Chapter 5). It was aimed to gain basic knowledge of the physico-chemical characteristics of the mesoporous solids and to access differences in their bulk and surface properties that can be essential for further functionalization and modification. It has been shown that the preparation of MCM-48 material is very sensitive and depends on variety of synthetic parameters. Among them silica-to-surfactant ratio is critical and determines the final mesophase structure. Applying the proposed procedure for the preparation of MCM-48 material, spherical particles with several hundreds nanometer in diameter can be prepared. SBA-15 rods having hierarchical structure composed of nanometer-sized worm-like structures have also been prepared. Applying an additional thermal curing step during the calcination process, SBA-15 rods with improved thermal stability were obtained. Mesostructured monoliths showing two-dimensional hexagonal structures have been deposited by using a simple solvent-evaporation method. The characterization of the mesostructured monoliths gave additional information that was very useful as starting point for the characterization of thin mesoporous films.

Thin mesoporous films have been prepared on different substrates (silicon wafer, glass, gold) by applying spin-coating of silica/surfactant/water/ethanol coating solutions under the conditions of the evaporation-induced self-assembly method (EISA) (Chapter 6). A combination of grazing-incidence diffraction (GID), reflection XRD, and TEM analysis enabled rather complete structural characterization of the mesoporous films. N₂-sorption measurements with quartz-crystal microbalances (QCMs) were used to explore the pore accessibility of the mesoporous films. Two types of structure directing agents, cationic CTABr surfactant and amphiphilic tri-block copolymer Pluronic123, which are well-established for the synthesis of powdered mesoporous materials, have been applied. In both cases, well ordered and stable silica mesoporous films have been obtained showing three-dimensional cubic or two-dimensional hexagonal structures. Typical for the mesoporous films is the preferred orientation (single-crystal orientation) of the domains that are arranged in a mosaic structure. It is shown that many different parameters, not only those coming from the composition of the coating solution but also “external” parameters, such as, for example, relative humidity, are very important for reproducible preparation of different mesophase structures.

Growth of carbon nanotubes on the Fe-containing mesoporous silica films was conducted by thermal decomposition of acetylene at 700 °C and resulted in multiwalled carbon nanotubes (Chapter 7). Evaporation-induced self-assembly *via* spin-coating has been employed for the formation of Fe-loaded mesoporous films from Fe-containing silica/triblock copolymer/ethanol coating solutions. The carbon nanotubes growth rate was controlled by changing the hydrocarbon flow rate, exposure time, and catalytic metal loading of the mesoporous support. Usually curling up, long carbon nanotubes protruding out of the film, growing in a hairy fashion were obtained.

A new synthetic approach is presented for the preparation of carbon filaments by vacuum pyrolysis of ferrocene-modified mesoporous silica SBA-15 rods and thin mesoporous films (Chapter 8). This approach relies on a selective functionalization with ferrocene of the inner surface of the highly ordered nanometer-sized channels of mesoporous material and subsequent pyrolysis under dynamic vacuum conditions. The ferrocene moieties were introduced through covalent bonding to the amino-functionalized walls of the

mesoporous materials through the Schiff-base reaction. Upon pyrolysis, 5 nm thin carbon filaments with tubular morphology generated within the channels of the SBA-15 host were extracted. HRTEM results showed that the carbon filaments have nanometer-sized domains with graphite-like structure. Surface-sensitive techniques, such as GID, reflection-adsorption FT-IR spectroscopy, and gravimetric QCMs measurements, were applied together in order to follow the post synthesis functionalization process of thin mesostructured films.

A novel two-step procedure for the preparation of gold nanostructures in SBA-15 host and mesoporous films is demonstrated (Chapter 9). First, the assembly of catalytically active gold nanoparticles is achieved followed by electroless reduction in a gold plating bath to obtain continuous gold nanostructures. Four different approaches for the introduction of the seed species for the electroless reduction were investigated with emphasis on the different modification of the mesoporous surface with organic functionality (thiol- and ethylenediamino functional groups), different particle size of the Au precursors (ranging from 5-6 gold nanoparticles to ionic AuCl_4^- precursor) and Au particles with different surface charge. It has been shown that Au nanostructures stabilized in tetraoctylammonium bromide in toluene, assembled on MPS-modified SBA-15 mesoporous support are the best precursors for subsequent gold electroless reduction and resulted in formation of several micrometer long gold nanowires with a diameter of about 5 nm. The experimental results clearly show that the growth of the gold nanowires is templated from the channel structure of the SBA-15 material. To the best of our knowledge these are the longest continuous gold nanowires prepared with mesoporous material as the solid template. Two types of thin mesoporous films showing three-dimensional cubic ($Pm3n$) (templated by CTABr surfactant) and two-dimensional ($p6m$) (templated by tri-block copolymer Pluronic123) mesophase structure were modified with MPS, treated with Au nanostructures stabilized in tetraoctylammonium bromide in toluene and subjected to electroless reduction. Due to the templating effect of the host support three-dimensional arrays of less than 2 nm large Au particles were obtained in the first case and several nanometer long Au nanowires with low density in the second case. A considerable decrease in the loading with Au nanostructures in the case of hexagonally ordered films was observed. Nevertheless, to the best of our knowledge these are the first

examples of Au nanostructures prepared in thin mesoporous films by electroless reduction method.

A new synthetic approach for preparation of continuous PbS semiconductor nanostructures confined in the mesoporous matrix by applying surface modification of the mesoporous support and chemical wet-impregnation technique (Chapter 10). There, we use the good complexing properties of ethylenediamino functionalities towards Pb(II) cations that are further reacted with excess of S^{2-} to obtain the PbS material. XRD and TEM results showed that it is possible to obtain micrometer long PbS nanowires in hexagonally ordered SBA-15 material. To the best of our knowledge these are the longest nanowires of semiconductor structures produced in the pores system of mesostructured hosts. It was attempted to extend this approach to thin film architectures. It was observed that due to the lower stability of the cubic films and restricted diffusion of reagents in the hexagonally ordered films the growth of continuous PbS nanostructures was not possible.

Approaching the creation of the nanostructured materials for device applications, the preparation of conductive nanostructures will require fabrication methods capable of producing uniform nanostructures with well defined and controllable properties. The templating approach described in this Thesis, takes advantage of the high density, continuity, and uniformity of nanochannels. The potential of using uniform nanochannels in device applications is given from the ability for preparation of thin-film architectures. At this point, the desirable alignment of nanochannels with long axis perpendicular to the surface of the film is not achieved. Alignment in an electric field, assuming a re-orientation caused by the differences in the dielectric constant at the silica/surfactant interface, has been tried in our group (see Diploma Theses of Martin Kuba and Barbara Fieres). Unfortunately, many other parameters (many of them discussed in Chapter 6) are also playing an important role in the disorder-to-order transition and the exact experimental conditions for such an alignment may still be difficult to find. Another possible approach is to use already existing one-dimensional macroporous templates (anodic alumina membrane, AnodiscTM) to cast/extrude mesoporous material that can possibly show aligned nanochannels parallel to the long axis of the membrane. Other possibility is to interrupt the preferred alignment of the mesoporous channels parallel to film surface by introduction of nanosized silica particles during the

coating process or to cut fine grooves in the film by ion bombardment that will be used as entrances for inclusion chemistry.

The encapsulation methods for incorporation of conductive structures used in this study are in most cases proof-of-principle methods. The detailed problems and possible solutions regarding every synthetic method are discussed separately in the preceding Chapters. Generally, the electroless reduction method, impregnation/complexing approach and selective modification with desirable molecular functionality can be further extended to other metal nanostructures, conductive polymers, semiconductor nanocrystals, optically active molecules, etc.

Finally, when the desired nanoscale architecture is achieved (Figure 1), the aim is to probe the electrical properties of an individual conducting entity, assumed to be isolated from its neighbors by the silica walls, by approaching the surface with an STM tip.

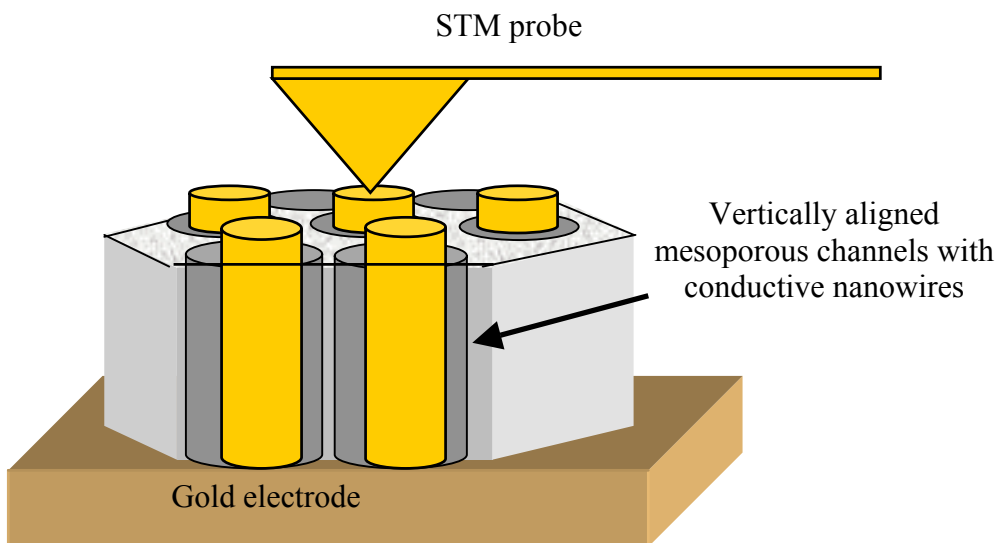


Figure 1. Schematic representation of the addressing of a single conductive nanowire.

CURRICULUM VITAE

Name: Nikolay Petkov

Date and place of birth: 05.04.1974, Sofia, Bulgaria

Nationality: Bulgarian

Family status: single

EDUCATION

July 2000-

present

Ph.D. Candidate in the group of Prof. Dr. Thomas Bein

Ludwig Maximilians Universität (University of Munich), Germany

1993 - 1998

Master of Science, Inorganic Chemistry, (With Distinction)

Sofia University, Bulgaria

1988 – 1993

English language school, Vidin, Bulgaria

RESEARCH EXPERIENCE

July 2000-

present

Ludwig Maximilians Universität, Munich, Germany

Doctoral student in the laboratory of Prof. Dr. Thomas Bein, Department of Physical Chemistry

- Research interests include: nanotechnology, nanoporous films, one-dimensional conductive nanostructures (carbon nanotubes, metal and semiconductor nanowires), composite materials, inclusion chemistry.
- Participated in the establishment and functioning of the electron microscopy research laboratory.
- Mentored two undergraduate and Master students.
- Teaching assistant for introductory and advanced physical chemistry (labs and classes), and inorganic chemistry for medical and chemistry students.

1998-2000

Institute for Nuclear Research and Nuclear Energy – Bulgarian Academy of Sciences, Sofia, Bulgaria

Graduate Research Assistant in the laboratory of Radioecology and Radiochemistry

- Designed radiopharmaceutical markers for radiodiagnostics, developed systems for solid-liquid chromatography, extraction chromatography, and other separation techniques for radiochemistry.

Date: 19.02.2004

Signature: _____

PUBLICATIONS AND PRESENTATIONS

1. N. Petkov and T. Bein, **Conductive structures in mesoporous materials**, review in press
2. N. Petkov, S. Mintova, B. Jean, T. H. Metzger and T. Bein, **Functionalized cubic mesostructured silica films**, *Materials Science and Engineering C 23* (2003), 827.
3. T. Bein, K. J. Hoekstra, M. Kuba; S. Mintova, N. Petkov, J. Reder, B. Schrick, **Hybrid conducting nanostructures in inorganic channel hosts**, *Abstracts of Papers, 226th ACS National Meeting*, New York, NY, United States, September 7-11, 2003 (2003):
4. N. Petkov, S. Mintova, T. H. Metzger and T. Bein, **Stable mesostructured silicate films containing nanosized zeolite**, *Chem. Mater.*, (2003), 15(11), 2240.
5. N. Petkov, S. Mintova, T. Bein, **Fe-containing mesoporous films for carbon nanotubes**, *Materials Science and Engineering C 23* (2003), 145.
6. N. Petkov, S. Mintova, T. Bein, **Spin coating induced self-assembly of pure silica and Fe-containing mesoporous films**, *Studies in Surface Science and Catalysis, 142 B*, (2002), 1465.
7. S. Mintova, N. Petkov, K. Karaghiosoff, T. Bein, **Crystallization of nanosized MEL-type zeolite from colloidal precursors**, *Materials Science and Engineering C 19* (2002) 111.
8. S. Mintova, N. Petkov, K. Karaghiosoff, T. Bein, **Transformation of amorphous silica colloids to nanosized MEL zeolite**, *Microporous and Mesoporous Materials 50* (2001) 121
9. A. Jordanova, A. Strezov, M. Ayranov, N. Petkov, T. Stoilova, **Heavy metal assessment in algae, sediments and water from the Bulgarian Black Sea coast**, *Water Science and Technology* (1999), 39(8), 207.
10. A. Strezov, T. Stoilova, A. Jordanova, M. Ayranov, N. Petkov, **Determination of cesium and natural radionuclide concentrations in sediments, algae and water on the Bulgarian Black Sea coast**, *Water Science and Technology* (1999), 39(8), 21.

Presenter and corresponding author for six oral and six poster presentations at national and international scientific conferences, such as E-MRS meetings, 13th International Zeolite Conference, CeNS international conference.

Member of the International Zeolite Association.

Member of [CeNS](#) (Center for Nanoscience).